Robust spectroscopic quantification in turbid media.

Francis W.L. Esmonde-White

Ph.D. Thesis

Department of Chemistry

McGill University

Montreal, Quebec, Canada

Dec. 01, 2008

A thesis submitted to McGill University in partial fulfilment of the requirements of the degree of Doctor of Philosophy

Dedication

This thesis is dedicated to: my wife, Karen, whose emotional support and scientific advice has been invaluable; my brothers, Emmett and Steve, without whom the world would have been much less colourful; and my parents, who instilled in me curiosity and perseverance.

Abstract

This thesis explores four methods for improving quantitative diffuse reflectance spectroscopy in light scattering media. To begin, an introduction is given outlining theories of light propagation in scattering media, relevant instrumentation for measuring light scattering properties, spectral data processing methods, and spectroscopically active bioanalytes. Four novel contributions to science are made. Each is described in a chapter. The improvements consist of two novel instruments for practical scattering measurements, and two novel data processing techniques. Finally, directions for future research into diffuse reflectance spectroscopy are suggested.

A novel photon time-of-flight device is first presented. This portable instrument is used to measure scattering coefficients in tandem with a portable diode spectrometer. The measured scattering coefficients are then used to correct the co-measured near infrared spectra for scattering and for improving quantification. Reduced scattering coefficients were measured with coefficients of variation of 11.6% at 850 nm and 14.1% at 905 nm. This simplified photon time-of-flight instrument allows for practical correction of light scattering in point-spectra. Using scattering-correction, estimates of dye concentration were improved by 35%. Applications

include integration with handheld spectrometers for development of handheld near-infrared medical diagnostic equipment.

A novel device for imaging annular patterns is presented. This imaging instrument is used to measure reduced scattering coefficients and absorption coefficients. This simple imaging system measures the optical properties using small source-detector spacings, resulting in high spatial resolution. Potential applications include correction of imaging spectroscopy in surgery and clinical applications. Reduced scattering coefficients were measured with a coefficient of variation of 12.6%, and absorption coefficients were measured with a coefficient of variation 50% lower than using traditional imaging methods.

A novel method for using parsimony in the development of data processing methods using genetic algorithms is presented. Genetic algorithms have been used to identify spectroscopic data processing methods for complex samples. A problem in the automated identification of processing models is that genetic algorithms tend to select unnecessarily complex models, which may fit noise. Parsimony methods are used to guide the selection process towards smaller models. Previous works have typically used custom parsimony penalty functions. Rather than custom penalties appropriate for particular data sets, a method using

penalization based on the number of incorporated wavelengths or pre-processing options was developed. This technique has applicability in the development of future spectrometric hardware, particularly for the development of simplified multiwavelength probes. Using the parsimonious genetic algorithm, a data processing model was found for estimating lactate concentration in tissue with a 41% improvement in standard error as compared to the best expert developed model.

A novel method is presented using multivariate curve resolution to measure myoglobin oxygen saturation from diffuse reflectance spectra of cardiac tissue. Multivariate curve resolution algorithms are used to simultaneously estimate the pure component profiles and the relative component weightings directly from recorded data. Changes in spectral shape due to scattering and the local chemical environment are modeled using multivariate curve resolution to estimate the hemoglobin and myoglobin component spectra from the recorded data. Oxygen saturation estimates using the multivariate curve resolution algorithm were compared to oxygen saturation estimates using a classical least squares approach. Multivariate curve resolution estimated myoglobin oxygen saturation better than the classical least squares method. Simulations also show that spectral data spanning the upper 15% oxygen saturation range should

allow for estimates of myoglobin oxygen saturation using multivariate curve resolution. The multivariate curve resolution algorithm was tested with spectra of guinea pig hearts perfused with blood, and showed a 100% improvement in accuracy as compared to the classical least squares approach.

The four methods developed in this thesis each showed improvement in the quantification of components using diffuse reflectance spectra. The photon time-of-flight and genetic algorithm methods are particularly applicable in point-measurements, and in the development of simplified portable instrumentation. The annular-beam imaging and multivariate curve resolution methods have use in spectral imaging for mapping chemical properties across a surface. Further applications and suggestions for future work are given in the conclusions chapter.

Résumé

Cette thèse explore quatre méthodes pour l'amélioration de la spectroscopie de réflectance diffuse quantitative dans des milieux qui diffusent la lumière. En introduction, une description des théories de la propagation de la lumière dans des médias qui diffusent celle-ci, des instruments pour mesurer les propriétés de diffusion, des méthodes de traitement des données spectrales, et des bioanalytes avec activité optique est donné. Quatre contributions à la science (une par chapitre) sont décrites. Les améliorations sont composées de deux nouveaux instruments facilitant la mesure de la dispersion, et de deux nouvelles techniques de traitement des données. Enfin, plusieurs perspectives sur la spectroscopie de réflectance diffuse sont suggérées.

Un nouvel appareil à «temps de vol de photon» est présenté. Cet instrument portatif est utilisé pour mesurer le coefficient de dispersion en tandem avec un spectromètre à diode portable. Les coefficients de diffusion mesurés sont ensuite utilisés pour corriger la dispersion dans les spectres infrarouges co-mesurée, ainsi que l'amélioration de la quantification. Les coefficients de dispersion ont été mesurés avec une variation de 11,6% à 850 nm et 14,1% à 905 nm. Cette approche simplifiée par un instrument à «temps de vol de photon» permet une

approche pratique pour la correction de la diffusion de la lumière dans les spectres. En prenant en compte la dispersion, les estimations de la concentration de teinture ont été améliorées de 35%. Les applications incluent l'intégration avec des spectromètres portatifs pour créer de nouveau équipement pour diagnostiques médicaux.

Un nouvel appareil utilisant les modes d'imagerie annulaire est présenté. Cet instrument est utilisé pour mesurer les coefficients de dispersion et d'absorption. Ce système d'imagerie optique simple mesure les propriétés de dispersion et absorption de la lumière à l'aide de petits espacements entre la source et le détecteur, conduisant à une haute résolution spatiale. Les applications potentielles incluent la correction de l'imagerie spectroscopique dans l'application clinique. Les coefficients de dispersion ont été mesurés avec un coefficient de variation de 12,6%, et les coefficients d'absorption ont été mesurés avec un coefficient de variation amélioré de 50% par rapport aux méthodes d'imagerie traditionnelle.

Une nouvelle méthode pour améliorer l'utilisation des mesures de simplicité dans le développement de méthodes de traitement des données via des algorithmes génétiques est présentée. Les algorithmes génétiques ont été utilisés pour identifier les méthodes de traitement de données

spectroscopiques pour des échantillons complexes. Un problème dans le traitement automatisé d'identification des modèles est que les algorithmes génétiques ont tendance à sélectionner les modèles complexe inutile, qui peuvent par exemple correspondre le bruit de fond. Des mesures de simplicité sont utilisées pour guider le processus de sélection vers des modèles plus petits. Les travaux précédant ont généralement utilisé des fonctions faite sur mesure. Plutôt que ces fonctions fait sur mesure, des sanctions appropriés pour différentes séries de données ont été élaboré en utilisant une méthode fondée sur la pénalisation du nombre d'ondes ou incorporés «pre-processing options» inclus. Cette technique est applicable dans le développement de nouvelles méthodes spectroscopiques, en particulier pour le développement des nouveaux appareils simplifiés. Un modèle de traitement des données a été déterminé par l'utilisation de l'algorithme génétique parcimonieuse pour l'estimation de la concentration de lactate avec une amélioration de 41% de la marge d'erreur standard par rapport au meilleur modèle d'expertise déjà développe.

Une nouvelle méthode a été développée en utilisant la «multivariate curve resolution» pour mesurer la saturation en oxygène de la myoglobine par spectres réflexion diffuse des tissus cardiaques. Les algorithmes «multivariate curve resolution» sont utilisés pour estimer

simultanément les profils de corps pur et de la composante relative directement à partir des données enregistres. Les changements de forme spectrale en raison de la diffraction et de l'environnement chimique local sont modélisés en utilisant la «multivariate curve resolution» pour estimer le taux d'hémoglobine et de myoglobine dans les échantillons. La saturation de l'oxygène mesurée en utilisant le «multivariate curve resolution» a été comparées aux estimations de la saturation de l'oxygène au moyen d'une approche classique des moindres carrés. «Multivariate curve resolution» a estimée la saturation d'oxygène en myoglobine supérieure à la méthode classique des moindres carrés.

Les simulations montrent également que les données spectrales couvrant la partie supérieure de la saturation en oxygène de 15% devraient permettre des estimations de la myoglobine saturation de l'oxygène en utilisant la courbe de résolution multivariée. La algorithme «multivariate curve resolution» a été testé avec des spectres de cœurs Cochon d'Inde perfusés avec du sang, et a montré une amélioration de 100% par rapport à la précision de la méthode classique des moindres carrés.

Les quatre méthodes développées dans cette thèse ont montré l'amélioration de quantification avec la spectroscopie de réflectance

diffuse. L'appareil à «temps de vol de photon» et l'algorithme génétique sont notamment applicables aux mesures poindre, pour le développement de simples appareils portatif pour diagnostiques médicaux. Les méthodes d'imagerie de la lumière annulaire et la «multivariate curve resolution» ont recours à l'imagerie spectrale pour la cartographie des propriétés chimiques à travers d'une surface. D'autres demandes et des suggestions pour les travaux futurs sont présentées dans le chapitre consacré aux conclusions.

Table of Contents

List of Figures

List of Tables

List of Commonly Used Symbols

- μ_s – scattering coefficient (typically in mm^{-1} or cm^{-1})
- μ_s' – reduced scattering coefficient (typically in mm^{-1} or cm^{-1})
- μ_a – absorption coefficient (typically in mm^{-1} or cm^{-1})
- g – anisotropy
- I – intensity
- I_0 – absorption-free reference intensity
- g – anisotropy
- ε – molar absorptivity
- c – concentration
- L – pathlength
- A – absorption or attenuation

Original Contributions to Knowledge

1. Development of a portable, hand-held photon time-of-flight instrument to measure optical scattering properties and improve near infrared reflectance quantification of scattering media.

2. Development of a novel diffuse reflectance imaging system using a ring-patterned laser to estimate optical scattering and absorption properties of scattering media with high spatial resolution.

3. Development of a novel parsimony method for guiding the selection of regression and classification spectral processing methods using genetic algorithms.

4. Development of a novel multivariate curve resolution algorithm for measuring myoglobin oxygen saturation in cardiac tissue without endpoint measurements.

Contribution of Authors

Listed below are articles included in this thesis and an outline of the responsibilities of each author. For all chapters, Dr. Burns was thesis supervisor and reviewer to Francis Esmonde-White.

Chapter 3

Francis W.L. Esmonde-White and David H. Burns, "Portable instrumentation for multi-wavelength NIR photon time-of-flight measurement of light scattering", *submitted.*

Mr. Esmonde-White proposed construction of a miniaturized version of photon time-of-flight (TOF) instrument. Mr. Esmonde-White conceptualized and built the TOF instrument, including all electronics and optics. Mr. Esmonde-White prepared tissue phantoms and calibrated the portable photon time-of-flight instrument. Data analysis was carried out by Mr. Esmonde-White. The document prepared for publication was written by Mr. Esmonde-White and edited by Dr. Burns.

Chapter 4

Francis W.L. Esmonde-White and David H. Burns, "Steady-state diffuse reflectance imaging of annular beams for quantification of scattering and absorption in turbid media", *to be submitted.*

Mr. Esmonde-White developed and assembled an amplitude-filter based system to generate a ring-shaped laser pattern and recorded measurements of tissue phantoms. Mr. Esmonde-White mathematically modeled the behaviour of ring-shaped light and its interaction with a tissue phantom. Data analysis was carried out by Mr. Esmonde-White. The document prepared for publication was written by Mr. Esmonde-White and edited by Dr. Burns.

Chapter 5

Francis W.L. Esmonde-White and David H. Burns, “Parsimony in Genetic Algorithms for Selection of Spectral Processing Models in Regression and Classification”, *to be submitted.*

Dr. Burns suggested the use of a genetic algorithm for classification models. Mr. Esmonde-White expanded the scope of the genetic algorithm to include regression models. Mr. Esmonde-White adapted the original generational genetic algorithm to a non-generational genetic algorithm. Mr. Esmonde-White developed measures of parsimony and implemented parsimony functions for development of both regression and classification models. Mr. Esmonde-White proposed and developed a Bayesian classification algorithm as part of the genetic algorithm. The genetic algorithm was written by Mr. Esmonde-White, and adapted for

development of both classification and regression models. Data analysis was carried out by Mr. Esmonde-White. The document prepared for publication was written by Mr. Esmonde-White and edited by Dr. Burns.

Chapter 6

Francis W.L. Esmonde-White, Lorilee S.L. Arakaki, Kenneth A. Schenkman, Wayne A. Ciesielski, David H. Burns, "Estimation of Myoglobin Oxygen Saturation from Spectra of Cardiac Tissue using Multivariate Curve Resolution", *submitted*.

Spectra of individual components were obtained by Dr. Arakaki and Dr. Schenkman. Animal protocols were developed by Dr. Ciesielski and approved by the University of Washington. *In-situ* cardiac tissue measurements were performed by Dr. Arakaki, Dr. Ciesielski and Dr. Schenkman at the University of Washington, and methods for processing visible and near infrared tissue spectra were discussed between all of the authors. An alternating least squares multivariate curve resolution program was developed by Mr. Esmonde-White at McGill University. Spectra of cardiac tissue were analyzed by Mr. Esmonde-White. The document prepared for publication was written by Mr. Esmonde-White and edited by all of the authors.

I certify that the above author contributions section is accurate and give permission for the publication of the corresponding manuscripts as part of Francis Esmonde-White's dissertation.

Name	Signature	Date
Kenneth Schenkman	_____	
Lorilee Arakaki	_____	
Wayne Ciesielski	_____	
David Burns	_____	
Francis Esmonde-White	_____	

Copyright Waivers

A copyright waiver for inclusion of the previously published manuscript entitled "Visualization of N-way data using two-dimensional correlation analysis" in this thesis was obtained electronically through the Copyright Clearance Center, Inc. as representatives of Elsevier Limited. Details of the copyright waiver follow.

Aug 31, 2007

This is a License Agreement between Francis W.L. Esmonde-White ("You") and Elsevier Limited ("Elsevier Limited"). The license consists of your order details, the terms and conditions provided by Elsevier Limited, and the payment terms and conditions.

License Number: 1779590898742

License date: Aug 31, 2007

Licensed content publisher: Elsevier Limited

Licensed content publication: Vibrational Spectroscopy

Licensed content title: Visualization of N-way data using two-dimensional correlation analysis

Licensed content author: Francis L. W. Esmonde-White and David H. Burns

Licensed content date: 6 December 2004

Volume number: 36

Issue number: 2

Pages: 6

Type of Use: Thesis / Dissertation

Portion: Full article

Format: Print

You are an author of the Elsevier article: Yes

Are you translating?: No

Purchase order number:

Expected publication date: Nov 2007

Acknowlegements

I thank the various members of the Burns lab for their advice and encouragement: Dirk Bandilla, Lucy Botros, Amila De Silva, Jonathan Dion, Julie Filion, Claudia Gributs, Shing Kwok, Fabiano Pandozzi, Kristin Power, David Troiani, He Xiao, and many summer research students. Je voudrais remercier Sylvestre Toumieux, un post-doc dans le laboratoire Moitessier, pour les corrections du résumé français. I also thank our Italian exchange students: Alberto Bonomi, Franchesca Patruno, and Marta Gaia Zanchi.

I thank the chemistry department instrument makers for building various optical mounts and mechanical adapters for my instruments: Bill Bastian, Jean-Philipe Guay, and Alfred Kluck. On more than one occasion parts were manufactured that didn't match my initial plans- however, they were always far better than expected. I would also like to thank the chemistry department electronics technicians, Rick Rossi and Weihua Wang, for patient help in troubleshooting various quirky experimental designs; the graduate studies coordinators, Renee Charron and Chantal Marotte, who kindly reminded me of deadlines and helped to keep the bureaucratic avalanche at bay; and other staff, Sandra Aerssen,

Jan Hamier, Alison McCaffrey, Fay Nurse, Mario Perrone, Claude Perryman, Michael Reece, Frank Rothwell, and Nadim Saade.

I also thank the other graduate students here at McGill who have enriched my studies, with particular thanks to Ed (Edward) Hudson, Daniel Tisi, Christina Georgiadis, and Erin Dodd.

I thank professors Steven Rosenfield and Helena Dedic for their continued support over the last 10 years. They helped me through a dark episode in my life, and gave me the courage and confidence to reach for my goals. Also, professors Joe Schwarcz and Ariel Fenster unknowingly led me to select chemistry as my field of study, for which I am very grateful.

I thank professors Parisa Ariya, Ian Butler, Masad Damha, Bruce Lennox, Joan Power, Eric Salin, Cameron Skinner, and Theo van de Ven for additional guidance and assistance at various points during my studies.

Finally, I acknowledge the guidance of my advisor, Dr. David Burns, who has overseen my studies with unparalleled insight, creativity, patience and optimism.

Chapter 1. Research Objectives and Overview

Spectroscopy is used for the analysis of many materials because it is rapid, precise, and non-destructive. Applications of quantitative optical spectroscopy are typically limited by the assumption that the sample should not scatter light. In practice, many analytes of interest scatter light. In this thesis several practical methods for improving quantification in scattering media are demonstrated. The methods discussed here have potential for use in many applications including medical diagnostics, industrial analysis and basic scientific research.

Quantitative spectroscopy in turbid media is currently limited in three main areas: mathematical processing models, instrumentation and sample complexity. In non-invasive medical applications, sample complexity cannot be reduced. Instead, improvements can be made in processing models and instrumentation. Medical applications using optical spectroscopy are limited by the concentration and optical response of both the components of interest, and of the many other components contributing to the background. In the high concentration range are water, proteins, and lipids. Hemoglobin and myoglobin are present at approximately one-tenth the concentration. Many additional components are present in lower concentrations, including lactate, glucose,

cytochromes, and other metabolic species. Using the best current methodology these species can be detected *in vivo*, however the detection limits, quantification accuracy, and robustness of the methods are not yet sufficient for most commercial clinical applications.

Quantification problems necessitate many different approaches for overcoming methodological limitations in turbid material spectroscopy. Four such methods were examined in this thesis to improve the accuracy of quantification in turbid media. These methods included two data processing and two instrumentation approaches. The approaches demonstrated in this work are complementary. They can be used in combination to effect greater improvements in quantification accuracy than any method alone, to reduce detection limits and increase quantification accuracy. The ultimate goal is to allow practical clinical measurements of biochemical components which can currently only be quantified in laboratory settings. Through the reduction of detection limits, chemical constituents which can currently only be quantified *in vitro* using invasive methods should become viable targets for *in vivo* laboratory studies. Additional benefits of these methodological improvements abound. Current studies using human or animal models often require that specimens be sacrificed for collection at many time-points. Non-invasive

and non-destructive analytical methods (such as those developed in this work) do not require sample collection such as tissue biopsy or animal sacrifice at each study time-point. Additionally, improvements in longitudinal biological studies should arise because temporal variations in an individual should not suffer from the baseline variability expected between individuals who are inherently imperfectly matched.

1.1 Research Objectives

The goal of this research was to investigate and develop methods for improving quantitative spectroscopy in light scattering media, with particular applications for improving quantitative visible and near-infrared spectroscopy of biological tissue. Most materials encountered in daily life scatter light, and can be described as light scattering or turbid media. Common examples of turbid media include milk and orange juice, paper and chalk, and biological tissues such as skin. Near-infrared light penetrates more deeply into turbid media than visible light, because optical scattering decreases with increasing wavelength. Spectral absorption by water is lower in the near-infrared region than at longer wavelengths. Optical sampling depth increases with wavelength, leading to increased absorption by chromophores of interest because of increased sampling pathlength. However, chromophores tend to have broad and

overlapping absorption features in the visible and near-infrared. With applications ranging from microscope imaging to planetary observation, improvements in optical measurements of chemical concentrations in light scattering media (also called turbid media) represent important scientific advancements.

1.2 Project Overview and Thesis Layout

Biomedical spectroscopy is a burgeoning field with current clinical usage in pulse-oximetry, and research into other clinical uses including non-invasive monitoring of water content, lipids, melanin, myoglobin, glucose and lactate. The use of biomedical spectroscopy is limited by three main problems: limits with the mathematical methods used for processing data, limits with the instrumentation used to record the spectra and the massive complexity of biological samples which are in constant flux and contain an enormous number of different chemical components. While nothing can be done to simplify intact biological samples, improved data processing techniques and instrumentation can help overcome the factors limiting the use of biomedical spectroscopy. Using novel instrumentation and data processing methods allows improvements in the accuracy of component measurements, and also simultaneously lowers

detection limits to allow biochemical species of lower concentrations to be detected.

This thesis begins in chapter 2 with a background introduction to near-infrared (NIR) spectroscopy, tissue optics, instrumentation and data processing. The introduction is written with the expectation that the reader has a cursory understanding of visible transmission spectroscopy. Specific methods for improving quantitative spectroscopic measurements in turbid media are described in chapters 3 through 6. Finally, conclusions of the present research are summarized in chapter 7, and directions for future research are suggested.

In this research, two general approaches were examined for improving spectroscopic quantification in scattering media. The first approach was to develop practical instruments capable of measuring the scattering coefficient, because measured scattering coefficients can be used to improve spectroscopic quantification.[1] The second approach was to develop data processing methods for improving constituent quantification from spectra without knowledge of scattering.

In the first approach, two instruments were developed to measure scattering coefficients. To date, analytical instruments for measuring scattering have been complex and impractical for field measurements. In

Chapter 3 we test the hypothesis that a simplified photon time-of-flight instrument can measure and correct for scattering. A hand-held photon time-of-flight instrument was developed for rapid measurement of the scattering coefficient concurrently with collection of NIR absorption spectra, providing a point-measure of the optical properties. This instrument was tested using Intralipid tissue phantoms of known optical scattering and absorption levels. Near infrared reflectance spectra were corrected using scattering coefficients measured with the pulsed laser system.

Point-spectra are very useful when the sample is homogeneous or only a small region is of interest. Many samples are heterogeneous and require spectral imaging over a wider area to understand the chemical composition. The hypothesis tested in chapter 4 was that a simple imaging system could measure scattering from the reflectance of an annular laser beam. Advantages of this system include the potential for rapid non-contact mapping of scattering coefficient without translating the optical probe over the surface. Measured maps of scattering coefficient could then be used to correct for scattering in spectral images for mapping analyte concentration.

In the second approach for improving spectroscopic quantification in scattering media, two data processing methods were developed for constituent quantification from spectra without knowledge of scattering. In chapter 5 a new method was developed for incorporating generic parsimony into genetic algorithms in selecting data processing models. Data processing models for evaluating spectra from biomedical and agricultural samples were developed without user intervention, using different parsimony functions. The optimal scientific approach to developing data processing models uses knowledge of the system. However, systems under study are often not completely understood. Expert-knowledge based systems can suffer from unintentional biases due to incomplete understanding of the system. Automated model development can optimize for quantification in the presence of impurities and ensure that models are not unintentionally biased by experimenters. Genetic algorithms tend to select complex models. Parsimony functions are used to bias the genetic algorithm to select simple models over complex ones. Generic parsimony functions investigated in chapter 5 are shown to improve quantification using the selected data processing models.

An alternate data processing approach is to determine the underlying components in a mixture directly from the recorded spectra. In light scattering systems pure component spectra are modified by scattering. Component spectra can be estimated from a series of measured spectra using multivariate curve resolution. In chapter 6 we test the hypothesis that multivariate curve resolution algorithms adaptively model for scattering in spectra and improve quantification of myoglobin oxygen saturation without requiring measured endpoint spectra.

The approaches developed in the course of this dissertation are shown to reduce quantification errors by up to 50%. Reductions of quantification error lead to improved detection limits. Additionally, the simplified instrumentation used is amenable to practical clinical applications. To conclude the thesis, in chapter 7 we outline the improvements made to current technologies and provide suggestions for future research.

Supplemental materials relating to the thesis including source code for computer programs, circuit diagrams and board layouts, a publication reprint, and outlines of some mathematical concepts are also given as appendices. One additional side project explored in this thesis was a method for preliminary exploration and representation of multi-way (n-

dimensional) data sets. A reprint of the n-way data exploration work is included in Appendix E. This manuscript is not included in the main section of the thesis since it is tangential.

Chapter 2.

Introduction to Spectroscopy in Turbid Media

As a background for tissue spectroscopy, an understanding of several subjects is required. This chapter outlines the basic principles of spectroscopy in turbid media and describes the terminology used throughout the thesis. To begin with a brief overview of light scattering, optical diffusion theory and Monte-Carlo simulations are described. These theories are used to estimate how light travels through scattering media. Next, to link the theory and practice, instruments used for measuring the optical properties (scattering and absorption) are presented. Various data processing methods are used to quantify component concentration from optical measurements, depending on the type of information recorded. Following the instrumentation section, recently published data processing methods are reviewed. Finally, tissue optical properties and the quantification of spectroscopically active biomarkers are presented.

Light Scattering

Matter can absorb, scatter, and diffract light. Spectroscopy is a subset of analytical chemistry in which the interactions of light with matter are examined to better understand matter. Spectroscopy is a powerful

analytical tool because it can be used for both qualitative and quantitative analysis in a wide variety of chemical or biological analytes. The non-destructive nature of spectroscopy is appealing for *in situ* analysis of human tissue. Ideal samples such as translucent solids, liquids or gases with known dimensions can be quantified using absorption spectroscopy. Transmission spectroscopy is widely used for non-destructive quantitative analysis of many chemical species. Ideal samples are quantified based on the transmission of light using the Beer-Lambert relationship,[2, 3]

$$A = -\log_{10}\left(\frac{I}{I_0}\right) = \varepsilon c L \qquad (2.1)$$

Where A is the absorbance measured as the logarithmic ratio of the intensity of the light source (I_0) to the intensity of the light having passed through the sample of interest (I). Analyte concentration (c) is determined according to the combination of the molar absorptivity (ε) and path length (L). Although widely used for simple analytes, application of the Beer-Lambert relationship is subject to several constraints. Constraints for use of the Beer-Lambert relationship include: the assumption of monochromatic illumination, absorbing species concentrations should be dilute, and scattering should be negligible so that the path length is well defined. This is not the case in most tissue spectroscopy.

Light absorption, scattering and diffraction are often observed in complex materials, such as biological tissue. Scattering is significant in many samples. As a result, estimation of analyte concentration in complex materials using the Beer-Lambert relationship is inaccurate.

2.1 Overview and Theory of Light Scattering

In turbid media, such as biological tissue, the pathlength that light travels is greater than the measured linear distance between the source and detector. Light scattering is depicted in Figure 2.1, where scattering and absorption determine the observed transmission and reflection of

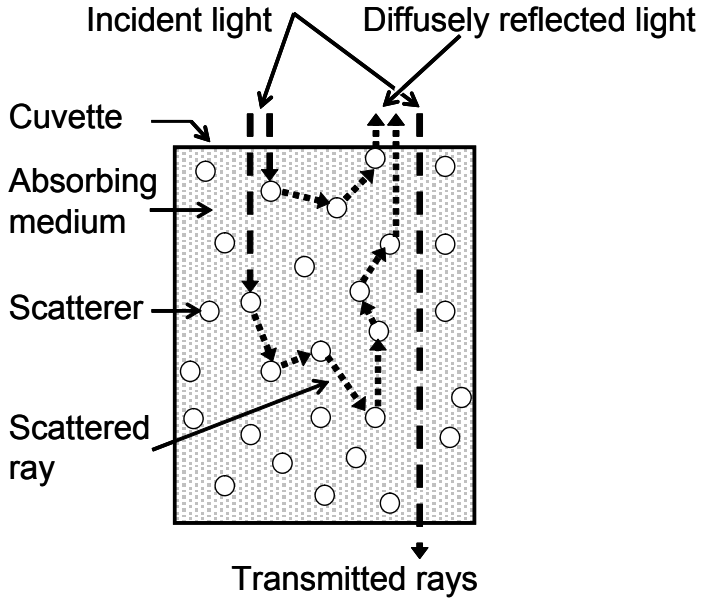

Figure 2.1: Light transport in scattering media. While some photons are transmitted through turbid media without scattering, most will be diffusely reflected (or diffusely transmitted), or absorbed by the medium.

light. In tissue, light is scattered strongly by small particles, macromolecules, tissue morphology, and boundaries with mismatched refractive indices.[4] When the light-scattering particle is much smaller than the wavelength (λ) of light, the scattering is best described by Rayleigh scattering theory in which the scattering is nearly isotropic and decreases as a function of λ^{-4}. When the scattering particle is larger than λ, the scattering is better described by Mie theory where the scattering is anisotropic and generally forward directed.

Three fundamental optical properties are used to describe turbid media: the scattering coefficient (μ_s), asymmetry parameter (g), and absorption coefficient (μ_a). Absorption coefficients can be related to traditional molar absorptivity through

$$A = \log 10(I_0 / I) = \varepsilon c L = \frac{1}{\ln(10)} \mu_a L$$

$$\mu_a = \ln(10) \cdot \frac{A}{L} \approx 2.3026 \cdot \frac{A}{L} \quad , \qquad (2.2)$$

where ε is the molar absorptivity, c is the concentration of the absorber, L is the pathlength, and A is the measured absorption. The absorption coefficient combines the molar absorptivity and concentration terms, having dimensions of inverse millimetres (mm^{-1}) or centimetres (cm^{-1}). Absorption coefficients are a measure of absorption events per unit distance. Corresponding to the absorption coefficient, the scattering

coefficient is the average number of scattering events per unit distance. Optical scattering and absorption coefficients can also be theoretically derived from the number density (concentration) and the molecular scattering cross sectional areas which are in turn determined from molecular volumes and scattering efficiency.[5-7] The asymmetry parameter, g, is used to describe the average scattering direction.[8] Also known as the anisotropy, g is calculated as the average cosine of the scattering angle. The amount of scattering with respect to the scattering angle can be plotted as a scattering diagram, also known as a phase function. The anisotropy varies from -1 to +1, for preferentially forward-directed scattering $g > 0$, for anisotropic scattering $g = 0$ (equal in all directions), and for preferentially backward-directed scattering $g < 1$. Scattering coefficients and anisotropy can be combined into the reduced scattering coefficient (μ_s'), based on the principle of similarity.[9]

$$\mu_s' = (1-g)\mu_s \qquad (2.3)$$

Reduced scattering coefficients are used because similar fluence distributions may be observed between systems with different optical properties, provided that particular anisotropic conditions are satisfied. This is illustrated in Figure 2.2. Highly forward directed scattering decreases the effective scattering coefficient because the average scattering event does not change the direction of propagation as greatly

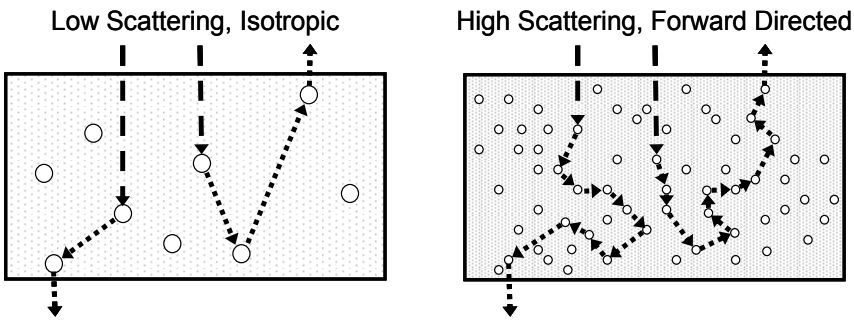

Figure 2.2: Principle of similarity: At left is a medium with anisotropic scattering and a low scattering coefficient. At right is a medium with forward directed scattering and a high scattering coefficient. Similar reflectance and transmittance may be observed for media with different optical properties. Reduced scattering coefficients can be used to correct scattering coefficients for anisotropy.

as for isotropic scattering. Scattering depends on wavelength. Scattering coefficients in tissue generally decrease with increasing wavelength, approximately linearly over short wavelength ranges.[10] Light scattering is predominantly modeled using either the diffusion equation or Monte Carlo simulations (Monte Carlo simulations are discussed in appendix G).

2.1.1 Radiative Transport Equation and the Diffusion Approximation

Boltzmann's radiative transport equation described the motion of a system of particles in space.[11] The radiative transport equation (r.t.e.) is[12]

$$s \cdot \nabla L(r,s) = -(\mu_a + \mu_s) L(r,s) + \mu_s \int_{4\pi} \rho(s,s') L(r,s') \partial\omega' \qquad (2.4)$$

where *L(r,s)* is the radiance at r travelling in the unit vector of direction s, and *ρ(s,s')* is the phase function (angular scattering profile). This states that changes in light intensity in a direction s are attributed to: 1) the light taken away from the incident beam by scattering and absorption, and 2) the light added to the beam from scattering of light into the direction s. Though difficult to do, various equations have been derived from the r.t.e. using different phase functions, source-detector geometries, boundary conditions and approximations.[13-20]

The diffusion approximation to the r.t.e. is often used, which assumes a semi-infinite sample medium where the reduced scattering coefficient is much greater than the absorption coefficient, and the source-detector spacing is at least several mean-free-paths. One transport scattering mean free path can be calculated as $mfp' = [(1-g)\mu_s]^{-1}$, and is the effective distance between scattering events. Succinct derivations of the diffusion approximation have been published.[6, 20-24] Most importantly, for the approximation to the diffusion equation uses a truncated Taylor series expansion in order to solve the radiative transport equation. In general the expansion of the scattering function is truncated to two terms (see Yoon[21], Appendix II). A first term describes the radial scattering and a second term

describes the forward peaked scattering. Because expansion terms have been truncated, quantification errors of up to 10% are observed when comparing theory to measurements.[25]

The diffusion equation models the transfer of light in both time and space, though particular solutions have been derived for steady-state (time-integrated) and time-dependent (spatially-integrated) solutions. These models of photon transport are most relevant to experimental observations, because most methods allow the measurement of intensity with respect to either time or position (but usually not both). In this thesis both the time-dependent and steady-state approaches were examined. Corresponding equations from diffusion theory are included here for reference. Equations 2.5 & 2.6 show two approximations of the diffusion equation, which have been solved for the time-independent case[26]

$$R(\rho) = \frac{a'\mu_t'}{4\pi}\int_0^{\infty}\left[z_0\left(\mu_{eff}+\frac{1}{r_1}\right)\frac{\exp\left(-\mu_{eff}r_1\right)}{r_1^2}+\left(z_0+2z_b\right)\left(\mu_{eff}+\frac{1}{r_2}\right)\frac{\exp\left(-\mu_{eff}r_2\right)}{r_2^2}\right]\exp\left(-\mu_t' z_0\right)\partial z_0 \tag{2.5}$$

and the time-dependent case[25]

$$R(\rho,t) = \frac{z_0}{\left(4\pi Dc\right)^{3/2}}t^{-5/2}\exp\left(-\frac{\rho^2+z_0^2}{2Dct}\right)\exp\left(-\mu_a ct\right) \tag{2.6}$$

where

$$D = \left[3\left(\mu_a+\mu_s'\right)\right]^{-1}, \tag{2.7}$$

$$\mu_{eff} = \left[3\mu_a\left(\mu_a + \mu_s^{'}\right)\right]^{1/2}, \quad (2.8)$$

$$a' = \mu_s^{'} / \left(\mu_a + \mu_s^{'}\right), \quad (2.9)$$

$$z_0 = \left[\left(1-g\right)\mu_s\right]^{-1}. \quad (2.10)$$

The time-dependent equation was derived assuming a matched boundary.

2.2 Instrumentation for Measuring Scattering

From diffusion theory, several approaches can be taken towards measuring scattering. Experimental methods are loosely classified into two categories, steady-state methods or time-dependent methods (which are either time-resolved or frequency-resolved).[12, 24, 27, 28]

2.2.1 Steady-State Instruments

Steady-state methods for measuring scattering include a wide variety of instruments, such as goniometers, integrating spheres, and spatial detectors. Goniometers measure the angular scattering intensity, or phase function. Integrating spheres measure the total light reflected or transmitted by the sample. Spatial detectors can measure transmission or reflectance intensities at multiple positions. Different source-detector spacings are sampled using fiber optics or imaging systems. From the spatial gradient patterns in the reflected or transmitted light the scattering coefficient can be estimated.

Steady-state imaging systems typically require less complex electronics than time-resolved instruments. Several methods have been reported that measure the reflectance of laser beams directed onto the surface of turbid media. Point detectors (fiber optics) at multiple source-detector spacings have been used to be sensitive to variations of μ_a and μ'_s.[29] Fiber optic detectors have been reported with radial,[30] linear,[31, 32] and concentric circle[33] arrangements of the detection fiber optics. In addition to point detection methods, imaging methods have been demonstrated for estimation of μ_a and μ'_s.[34-38] Anisotropy has been measured by imaging laser beams at a non-normal angle.[38] Several theories and models for quantification of optical properties from steady-state reflectance have also been investigated.[18, 26, 39, 40]

2.2.2 Time-Resolved Instruments

Time-resolved methods, also called photon time-of-flight methods, take advantage of the finite time taken by a photon to travel through matter. Path length can be estimated from the time-of-flight profile.[41] Light travels approximately $3 \cdot 10^8$ m/s in a vacuum. In biological tissue light travels at approximately $2.1 \cdot 10^8$ m/s, or 21 cm/ns (assuming a refractive index of 1.4). By measuring the time required for photons to move from the source to the detector, the total optical pathlength can be measured. In practice, rapid laser pulses are measured rather than single photons and a pathlength distribution is obtained. This is because unlike in geometric

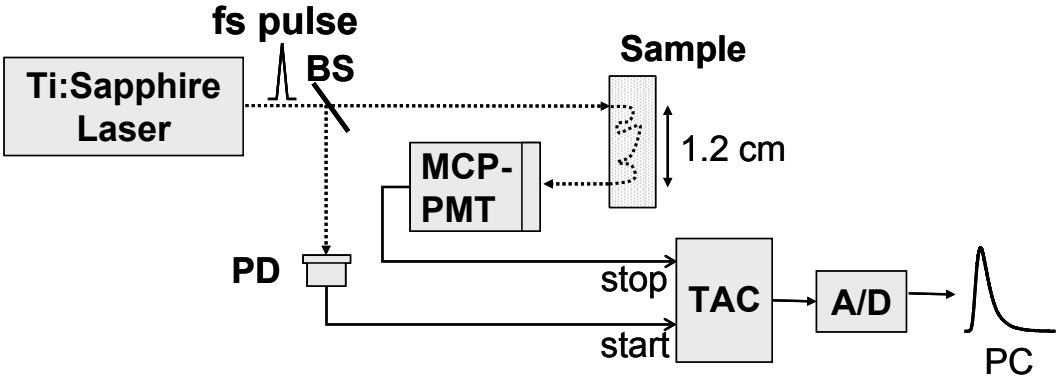

Figure 2.3: Example of a bench scale photon time-of-flight instrument. Components are: Ti-Sapphire Laser, titanium-sapphire laser; BS, beam splitter; PD, photodiode; MCP-PMT, microchannel plate photomultiplier tube; TAC, time-to-amplitude converter; A/D, analog to digital converter; PC, personal computer.

optics, photons do not follow a single predictable path, but rather follow a distribution of paths.

Laser pulses are delayed in time and broadened by scattering because individual photons travel through a distribution of optical paths. An example of a bench-scale photon time-of-flight instrument is presented in Figure 2.3. In this example, a Titanium-sapphire laser is used to generate a brief pulse of light. The pulse is then split by a beam splitter, with one half starting a clock (TAC), and the other half illuminating the sample. A single photon microchannel plate photomultiplier tube (MCP-PMT) detector stops the clock as the first photon exits the sample. By repeatedly recording the time required for the first photon to escape the sample, the distribution of residence times is measured. Time-of-flight profiles have been used to evaluate diffusion theory and Monte Carlo models.[25] Monte Carlo models are described in Appendix G. Time-domain systems have traditionally been non-portable and costly, preventing the routine use of these instruments.[42]

Applications of time-domain systems vary widely, and include such diverse topics as ultra-fast optics,[43] nonlinear optics,[44] continuum-pulse generation,[44] frequency resolved systems,[45, 46] as well as the spatial, confocal and coherent interference systems used for tomographic

reconstruction.[47] Many additional non-chemical applications of time-domain optical methods are widely used, such as laser range-finding and mapping (eg. LIDAR).[48]

Ultra-fast optical laser pulses with very high peak powers generate nonlinear optical effects in condensed matter.[44] Nonlinear optical interactions of light with matter can lead to spectral broadening due to a variety of optical phenomena, such as group velocity dispersion and multi-photon ionization.[44] A common use of nonlinear optics is for generation of white light "continuum" optical pulses (light with continuous wavelength distributions generated from a high intensity single-wavelength source).[44] Traditionally, nonlinear optical broadening required a very high optical power delivered over a short duration to cause broadening effects in condensed matter (typically liquids or glasses). Novel optical fiber structures have recently renewed interest in continuum light generation, because these structures provide stable nonlinear optical cavities. Applications of white-light continuum pulses have included time-resolved spectroscopy in turbid media and broadband optical coherence tomography for tissue characterization.[44, 49-58]

Frequency-resolved systems are similar to time-domain systems, with the difference that frequency-resolved instruments use greater

repetition frequencies and the modulation intensities typically span a smaller contrast range than time-resolved systems. The phase shift and amplitude response of a turbid medium are measured.[45, 46, 59-61] Phase shift, modulation depth, and the integrated intensity of the optical wave are then used to estimate optical properties.[46, 61-63] Frequency domain instruments modulate intensity at megahertz frequencies, and so source and detector requirements have similar temporal requirements as time-of-flight instruments. Advantages of frequency domain instruments include simplifications in electronics because the required sinusoidal waveforms can be easily generated, and because the high duty cycle leads to rapid signal acquisition.[46, 64] Frequency domain measurements have typically been used to acquire scattering and absorption coefficients at multiple wavelengths in series, typically at a single location.[63] Several studies have also used frequency-domain measurements at multiple positions to reconstruct tomographic models of tissue.[45, 47, 64]

In addition to simple point measurements of temporal or frequency domain spectra, spatially variant measurements have been used to reconstruct one, two and three dimensional maps of chemical composition. One example of optical tomography is the use of multiple projections of spectra to reconstruct a three dimensional model of the

specimen.[65] In turbid media, spatial reconstruction is complicated by scattering. Multiple scattering is difficult to accurately model because real systems are strongly heterogeneous, requiring complex simulations of tissue and large numbers of simulated photons to develop accurate predictions. Methods exist to negate scattering by temporally selecting photons with known transit times or spatially selecting photons scattered at a particular location in the sample using confocal optical geometries.[66] Time-domain spectroscopy typically takes advantage of ballistic or snake photons, which pass through a scattering sample without undergoing scattering or undergoing only a small number of scattering events. These photons experience minimal deviations in the optical path and so should follow Beer's law for quantification of analyte. Ballistic photons can be observed in transmission scattering experiments, and have been reported in highly scattering tissue phantoms composed of discrete scatterers. In tissue, rough boundaries with refractive index differences prevent any strictly ballistic photons from transiting tissue, though photons with short transit times (snake photons, with forward directed zig-zag paths) may still be observed.[43] Temporal gating has been used to differentiate between the early-arriving photons and the late-arriving diffusely scattered light.[43] Using finite element modeling, multiple time-domain spectra can be

combined to reconstruct one-, two-, or three-dimensional models of scattering media (with several examples concerned with imaging breast tissue for detection of cancers).[67-70]

Interference patterns of coherent light can also be used to discriminate between the light exiting a turbid medium, in order to select the light escaping from the medium with a particular temporal delay.[71-76] By appropriately positioning the reference beam the depth is selected. Optical Coherence Tomography (OCT) can be used with a single-wavelength, and also been used with broadband continuum white-light pulses to map tissue.[74] The primary advantage of OCT is the extremely fine depth resolution. One limitation of OCT is the sampling depth, which is limited by the exponential decrease of signal intensity with depth and scattering level. Typical sampling depths in tissue are in the hundreds of micrometres, while some studies have reported measurements at up to millimetre depths using infrared light. Confocal Spectroscopy/Microscopy use optical geometries to block scattered photons from being detected.[57] This method has advantages and disadvantages similar to those of OCT, while using spatial rather than temporal means for isolating non-scattering photons. Diffuse Optical Tomography (DOT) uses spectra recorded at various spatial locations or temporal delays to reconstruct the sample,

typically without rejecting the signal from diffusely scattered light.[65, 77] The primary advantage is the dramatic increase in optical signal and simplification of the instrumentation, while the signal processing is more complex and the spatial resolution is very coarse.

Temporal and frequency domain methods along with their tomographic variants have been used in a variety of medical applications. In biological applications the optical power becomes a limiting factor, because high pulse power with short duration pulses can cause damage in tissue.[78] Pulse power must be carefully selected to avoid tissue damage while maximizing signal intensity. A multitude of temporal and frequency domain methods for analysis of biological tissues for medical applications have been explored.[63, 70, 79-83]

2.3 Data Processing for Quantitative Spectroscopy in Scattering Media

Many software approaches have been developed for processing spectral data of scattering samples. Data processing approaches are varied and roughly correlate to the type of available data. There are three main types of available data. Quantification of scattering media is based on data from (1) spectra, (2) optical properties measurements, or (3) a combination of spectra and optical properties measurements. The first category of data analysis is when quantification is based only from spectra

or images; the second category of data sets is from only from measured optical coefficients. The third category is when both spectral and scattering information are used to quantify constituents. A variety of processing methods have been used for each type of data. This section reviews recently reported data processing methods for quantification of components in scattering media. Relevant studies from the past decade have been included to illustrate the various methods.

2.3.1 Quantification from Measured Spectra

The first category, where only spectral information was used for component quantification, involves the majority of reported methods. Near infrared optical quantification via measured reflectance spectra without additional measured scattering information is a simple approach amenable toward clinical applications. Routine tissue analysis by diffuse reflectance NIR spectroscopy is feasible given the availability of high-quality instruments. Scattering measurements are typically not made because of the technological difficulties, but the effects of scattering must be addressed for accurate quantification. This section is further organized according the techniques used to record the data. Data processing for measurements using only a few wavelengths are first discussed, followed by a description of methods using NIR spectra with measurements at

hundreds of wavelengths. Full spectra are processed with either explicit or implicit scatter-correction.

2.3.1.1 Ratiometric Probes and Simple Imaging

The least complex instruments used are probes measuring the reflectance at several discrete wavelengths. Some examples of this are probes calculating the reflectance intensity ratio at two wavelengths to estimate oxygen saturation in tissue.[84-86] Instead of measuring several discrete wavelengths at a single point, colour imaging with red-green-blue (RGB) cameras can be used to perform similar imaging measurements. Digital RGB cameras have been used to estimate tissue oxygenation, again using the intensity ratios of different colours to estimate oxygen saturation.[87, 88] Processing steps for these methods generally consist of a background subtraction and a scaled ratio of intensities at different wavelengths.[89] Fixed-wavelength devices have the advantage of being inexpensive and rugged. Potential disadvantages include a lack of quantification specificity.

2.3.1.2 Processing Full Spectra without Measured Scattering

The most common approach to optical quantification in scattering media uses reflectance spectra measured at a single source-detector separation. Despite the many quantification studies using only spectral information, there is no consensus on the optimal processing method.[90] Spectral processing methods can be split into two main groups, those using explicit scatter-correction, and those using implicit scatter-correction.[91]

Explicit scatter correction methods include various techniques such as dividing by a constant value, taking second derivatives, or fitting the spectra to account for scattering. An example of the first method uses cuvette-based calibrations with a linear-least squares estimation routine to estimate component concentration from spectra scaled by a constant factor of the source-detector separation.[92] Spectral derivatives or discrete differences[93] are often calculated as a data pre-processing step because the wavelength-dependence of scattering is approximately linear (over short wavelength ranges) and scatter-dependence should be eliminated in the derivative spectrum.[94] Subsequent techniques for processing derivative data typically use *in vitro* calibration methods along with inverse least squares or partial least squares.[95-97] These methods use calibrations

determined *in vitro* to estimate properties of the *ex vivo* or *in vivo* tissue, using derivative pre-processing to reduce the effects of scattering. Other methods used to classifying disease states from derivative pre-processed spectra include partial-least-squares logistic-regressions and hierarchal clustering.[98, 99] Other extrinsic methods estimate and correct for scattering directly from the spectrum. Spectral absorption features of water[100] and ratiometric methods based on isosbestic points[90] in the recorded spectra have been used to derive correction measures. However, even for *in vitro* tests, isosbestic spectral points are not always consistent, and this is aggravated by the complicated nature of tissue. Kubelka-Munk theory, diffusion theory and multiplicative scatter correction are also used to correct for scatter prior to least squares or partial least squares estimations.[91, 101] Kubelka-Munk theory describes a sample as a discontinuous set of homogeneous plane-parallel layers. Representative layer theory was developed more recently and is used to describe a sample as a continuous set of heteogeneous plane-parallel layers.[102]

Implicit scatter-correction methods model the spectral data to compensate for scattering rather than explicitly treating scattering. Implicit methods include multivariate curve resolution, principal component analysis,[103] and genetic algorithms.[104-106]

2.3.2 Quantification from Optical Properties Measurements

The second category of data processing methods uses time-domain, spatial-domain, or frequency-domain measurements of samples to estimate the optical properties and the component concentrations. Full spectra are not recorded. Because these measurements usually cover only a few discrete wavelengths, quantification methods are limited to ratios and parametric equations of the various wavelengths recorded. Some examples include: spatially-resolved measurements at 674, 849 and 956 nm;[107] time-domain measurements at 780 and 830 nm for estimating hemoglobin oxygen saturation;[108] and frequency-domain measurements at 674, 811, 849, and 956 nm for estimating hemoglobin, oxyhemoglobin, and water content of cervical tissue.[109] This differs from the spectral-only processing methods because measured absorption coefficients are used to estimate the component concentrations. This difference is important because absorption coefficients are scatter-independent, while measured reflectance as used by spectra-only methods is scatter-dependant. Discrete-wavelength results can also be analyzed with finite-element analysis to map spatial properties of the tissue to subsurface locations. One such example uses a six-wavelength frequency-domain system to measure absorption and scattering

coefficients, which are then used in finite element analysis for volumetric mapping of lesions in breasts.[47]

2.3.3 Quantification from Spectra and Optical Properties Measurements

The third group of processing methods use simultaneously recorded spectra and scattering measurements to quantify tissue components. Although these methods provide the most complete information for tissue quantification, widespread use of this approach is prohibited by the cost and complexity of the instrumentation. While temporal, spatial, and frequency domain measurements have all been demonstrated for spectral correction, the majority of the reported applications have used spatial domain measurements. Correction methods either correct a single spectrum using measured scattering, or use multiple measured spectra to deduce the optical properties at each wavelength.

2.3.3.1 Using One Recorded Spectrum and Diffusion Model Estimation

A single measured diffuse reflectance spectrum can be scatter-corrected using a separately measured scattering coefficient. Examples include use of a frequency domain system[110] and imaging system[111] to measure the scattering coefficient at a few wavelengths, and subsequently correct the measured point spectrum. For the frequency domain system,

reduced scattering coefficients were estimated using a Levenberg-Marquardt algorithm to fit the diffusion model to the recorded frequency domain information. From the scattering coefficients measured at six wavelengths, the scattering power relationship with wavelength was determined. The measured point spectrum was then scatter-corrected using the scattering power relationship and analyzed with a least-squares algorithm.[110] For the spatial domain system, the radial reflectance intensities at three wavelengths were fit to Monte Carlo models to estimate the reduced scattering and absorption coefficients. Absorption coefficients are then used for Beers-law type linear quantifications.

2.3.3.2 Using Many Recorded Spectra

Multi-spectral processing methods are most often used for multiple spectra recorded at different source-detector spacings, though full-spectrum time-domain measurements have also been reported.[31, 112] Spatial methods estimate the scattering and absorption coefficients by fitting the intensities recorded at multiple distances to the diffusion equation.[31, 113] Variations on this method can include taking second differences prior to fitting. Alternately, broadband time-domain measurements have been demonstrated to directly measure the optical properties at many wavelengths simultaneously.[112] These approaches are

elegant and precise. Unfortunately the instrumentation required is complex and not currently practical for routine clinical measurements.

2.4 Tissue Properties and Spectroscopically Active Bioanalytes

Now that light scattering theory, instrumentation, and processing methods have been described, we turn to the crux of the issue: what are the optical properties of tissue and which bioanalytes can be examined? To begin with, a spectral range must be selected. Section 2.4.1 outlines the reasons for which the near-infrared spectral region is used for tissue spectroscopy. Next, some reported optical properties of tissue are listed. Finally, an overview of optically-active metabolic processes and bioanalytes of interest are presented.

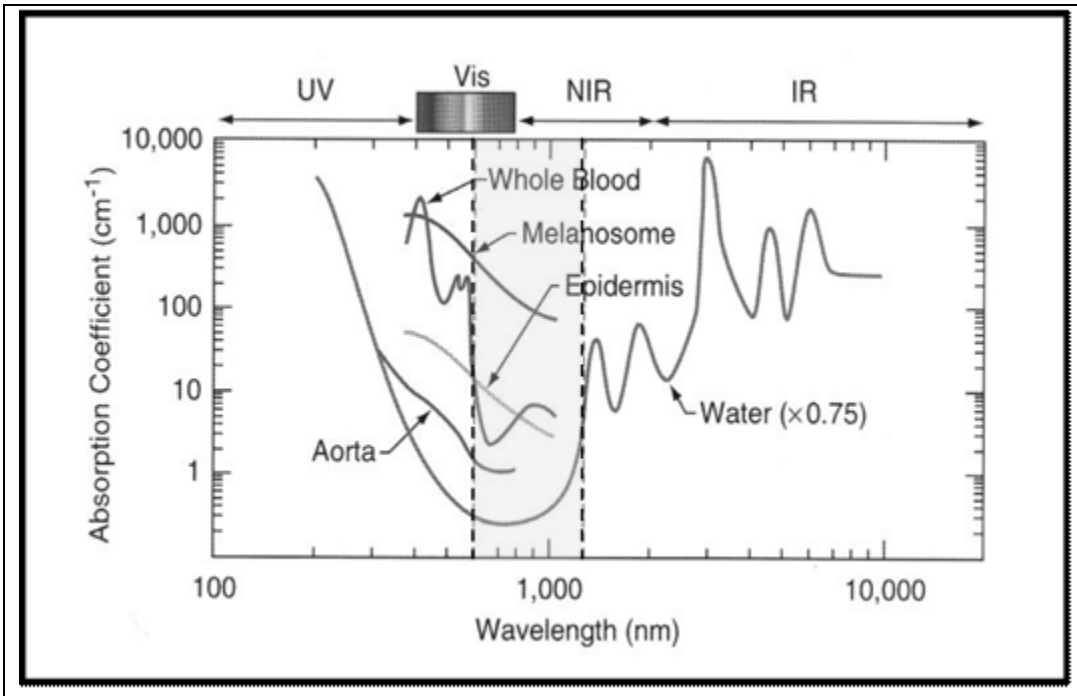

Figure 2.4: The biological window for spectroscopic analysis of tissue spans 600 nm-1100 nm, as marked by dashed lines and highlighted by the shaded area. Copyright 2003 from Biomedical Photonics Handbook by Tuan Vo-Dinh. Reproduced by permission of Taylor & Francis LLC, a division of Informa plc.

2.4.1 Window for Spectroscopic Analysis of Tissue

Several factors limit the wavelength range for non-invasive quantification of constituents in biological tissue: (i) the optical penetration must be sufficient to allow analyses, (ii) the required optical power must not damage the system under study, (iii) the analyte must interact with light and transform the optical signal, and finally (iv) the analyte signal must be sufficiently different from other signals present. With these

constraints in mind, the best region of the electromagnetic spectrum is in the visible to near-infrared (600-1100 nm) region. As seen in Figure 2.4, the spectroscopic window between 600 and 1100 nm is where absorption of hemoglobin, melanin and water is at a minimum, thus enabling NIR measurements of bioanalytes such as hemoglobin, lactate, glucose, or bilirubin. Toward the near-infrared region of the window, light may penetrate several centimetres into tissue, and several bioanalytes have absorption features. Moreover, optical sources and detectors are well-developed for this region. However, absorption features are broad and non-specific. Use of light in the near-infrared region allows non-invasive biomedical measures with lower cost and complexity than other spectral regions.[114] As a result, the near-infrared spectral region is a practical spectral region for the development of simplified instrumentation. However, because of the broad absorption features in near-infrared spectra and interference by light scattering, the potential of *in vivo* near-infrared spectroscopy for clinical purposes has not yet been fulfilled.[115]

2.4.2 Optical Properties of Tissues

As previously discussed, near-infrared quantification of chemical constituents in tissue is complicated by light absorption or scattering in tissue. Optical properties of a variety of biological tissues have been reported.[9, 10, 12, 32, 116, 117] Typical near-infrared optical properties for various tissues are listed in Table 2.1. Most techniques for measuring optical scattering properties require extensive preparation of the sample, which are difficult and may not be reproducible. More importantly, it is unclear if the optical properties of treated tissues (excised, sectioned, preserved)

Tissue Type	Wavelength (nm)	μ_a (mm^{-1})	μ_s' (mm^{-1})	g
Aorta (Human)	632.8	0.052	4.1	0.87
Bladder (Human)	633	0.140	0.264	0.91
Whole Blood (Human)	665	0.130	0.611	0.995
Whole Blood (Human)	960	0.284	0.384	0.992
Brain, White Matter	633	0.158	0.204	0.96
Brain, Gray Matter	633	0.263	0.722	0.88
Heart, Endocardium	1060	0.007	0.367	0.973
Heart, Epicardium	1060	0.035	0.284	0.983
Liver	630	0.32	2.07	0.95
Lung	630	0.84	0.179	0.95
Skin, Dermis	633	0.27	3.55	0.81
Uterus	635	0.035	12.2	0.69

Table 2.1: Measured optical properties of human tissue, adapted to mm^{-1} from Cheong et al.[12]

accurately reflect the optical properties of tissue *in vivo*.

2.4.3 Overview of Spectrally Active Respiratory Metabolic Processes

Living tissues consume nutrients and oxygen to generate

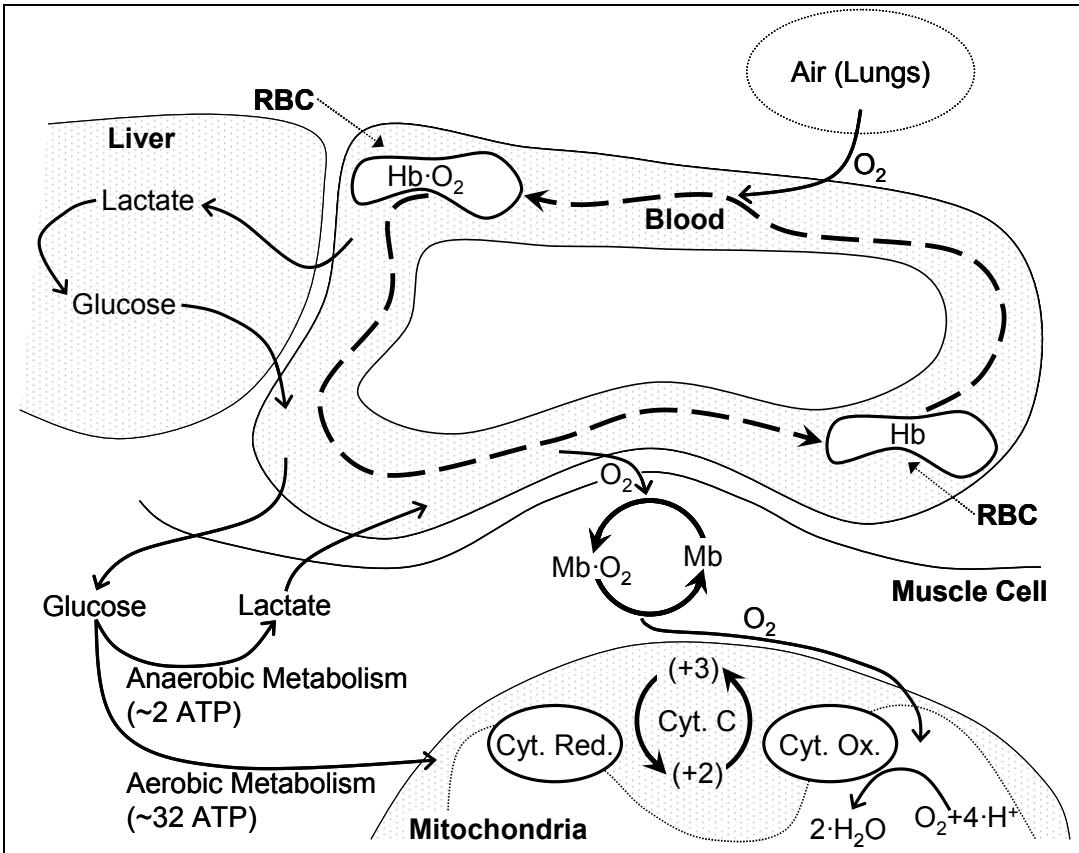

Figure 2.5: A simplified diagram of aerobic and anaerobic respiration. Abbreviations are as follow: RBC, red blood cell; Hb, deoxyhemoglobin; HbO2, oxyhemoglobin; Mb, deoxymyoglobin; Mb O2, oxymyoglobin; Cyt. C, cytochrome c (oxidized state is +3, reduced state is +2); Cyt. Red., cytochrome reductase (Complex III); Cyt. Ox., cytochrome oxidase (Complex IV).

biochemical gradients across cellular membranes. Concentration gradients drive the flow of energy required for many respiratory processes in living organisms. A broad overview of the metabolic pathways for spectrally active oxygen binding proteins, glucose and lactate are shown in Figure 2.5. Proper function of metabolic processes can be examined by measuring oxygen partial pressure or nutrient concentrations. Interruptions to the respiratory system are a prominent cause of metabolic failure and subsequently cellular death. Ultimately, this is summarized by the saying: "if you don't breathe, you die."

Some bioanalytes have spectral features and can serve as indicators of oxygen partial pressure. These bioanalytes can be used to determine the state of oxygen consumption, oxygen delivery, and also metabolic activity. Spectroscopically active indicators of oxygen partial pressure include: hemoglobin in blood, myoglobin in muscle tissue, and cytochromes in mitochondria. These proteins reversibly bind oxygen in proportion to the local oxygen partial pressure. As a result, the ratio of each oxygenated species to the total concentration of that species may function as a localized indicator of oxygen partial pressure. Significant oxygen pressure gradients exist in tissue because oxygen diffuses through blood, tissue and cellular membranes at different rates. The

integrated oxygen saturation of hemoglobin, myoglobin or cytochromes is proportional to the rate of oxygen consumption.

Glucose and lactate concentrations can also be optically measured to gauge the efficiency of metabolic energy flow in tissue. As seen in Figure 2.5, transport of oxygen and production of simple carbohydrates are key functions in aerobic and anaerobic metabolism.[118] Under anaerobic conditions, lactate is produced and builds in tissues during times of high energy demand. Glucose is converted to energy in the form of adenosine 5'-triphosphate (ATP) through the processes of glycolysis and the citric acid cycle. Oxygen supplied to cells is consumed in the conversion of glucose to energy.

Determination of these metabolic indicators *in vivo* is instrumental in further understanding metabolic processes in both healthy and diseased tissue. Respiratory pathways have been studied extensively by NIR spectroscopy because spectra change rapidly in response to its local chemical environment. In particular, NIR spectra of myoglobin and hemoglobin are strongly responsive to oxygenation state. Rapid measurement of myoglobin or hemoglobin oxygenation has important clinical applications of maintaining proper oxygen levels during surgery and monitoring the patient for respiratory failure.

Hemoglobin and myoglobin are metalloproteins found in red blood cells and muscle tissue, respectively. The absolute concentration and relative oxygenation of these proteins can be used to measure the relative ‘health’ of tissues during surgery or as a response to medical treatment. Both proteins function as an oxygen transport and storage network which enhances oxygen transport into tissue in comparison to simple diffusion.[119]

Hemoglobin and myoglobin have iron-containing heme groups, which reversibly bind to oxygen. Heme strongly binds oxygen in an 'end-on bent' geometry, and a distinctly modified NIR spectrum is observed as compared to oxygen-free heme. As seen in Figure 2.6, the NIR spectrum of deoxyhemoglobin is similar to the NIR spectrum of deoxymyoglobin.[120] The myoglobin spectrum is red-shifted by approximately 3 nm with respect to the spectrum of hemoglobin. In the region from 450 to 960 nm, principal features of oxygen-free spectra are maxima at approximately 555, 755 and 910 nm. The corresponding primary feature of the oxy spectra is an incompletely resolved pair of maxima at 545 and 575 nm.

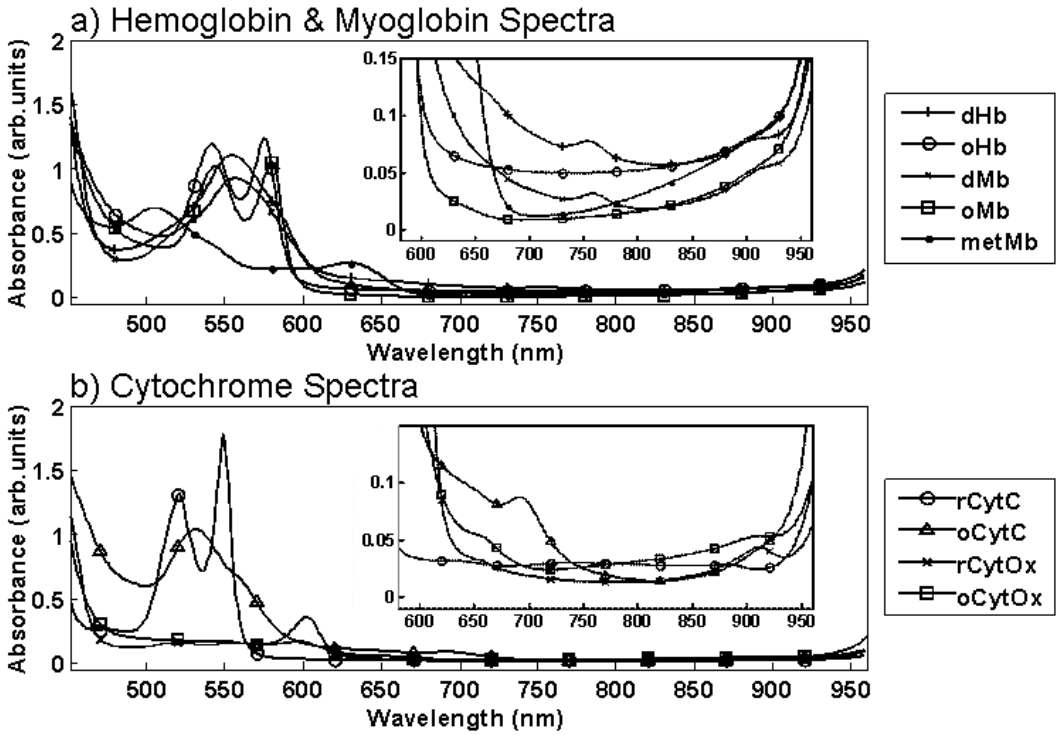

Figure 2.6: NIR spectra of hemoglobin, myoglobin, cytochrome c, and cytochrome oxidase. Species are abbreviated as: dHb, deoxyhemoglobin; oHb, oxyhemoglobin; dMb, deoxymyoglobin; oMb, oxymyoglobin; metMb, metmyoglobin; rCytC, reduced cytochrome c; oCytC, oxidized cytochrome c; rCytOx, reduced cytochrome oxidase; oCytOx, oxidized cytochrome oxidase.

Oxygen partial pressure in tissue can be measured using NIR spectroscopy because the NIR spectra of hemoglobin and myoglobin are modified with oxygenation, and a ratio of oxygenated protein to total protein can be measured. Spectra of cytochrome oxidase and cytochrome c are also shown in Figure 2.6. Cytochrome c is a protein with a heme group at the center, which is bound to a methionine on one face and histidine on the other, which transports electrons in respiration. Spectral features of the cytochromes overlap with spectral features of hemoglobin and myoglobin, and these may interfere with hemoglobin and myoglobin oxygen saturation measurements. Other hemoglobin and myoglobin forms are also present in the body, such as carboxyhemoglobin and metmyoglobin, and may further complicate analysis of NIR spectra.[121, 122] In the ideal case, all spectroscopically active components would be taken into account to better compensate for these optical interferences. In practice, often only the concentrations of the most spectroscopically active species are estimated.

2.4.4 Hemoglobin Oxygen Saturation Measurement

Spectroscopic determination of hemoglobin oxygen saturation is an active area of research.[121, 123-126] Photoplethysmography is the use of optical absorption to measure the cardiovascular pulse wave and

hemoglobin oxygen saturation. In simple implementations, an intensity ratio of the oxyhemoglobin signal is compared to signal at an isosbestic point combining hemoglobin and oxyhemoglobin at a second wavelength. Oxygen saturation in the blood is typically measured from signal ratios, as described in section 2.3.1.1 above.

Improved reliability and imaging modalities are active research areas in photoplethysmography.[87, 127] Pulse-oximetry, another application of optical absorption, was invented early in the twentieth century, and is used to measure blood oxygen saturation.[128, 129] Pulse-oximetry is the most widely-used commercial application of non-invasive NIR biomedical spectroscopy. Pulse-oximetry measures differences in spectra at the maximum and the minimum pulsatile volumes. The pulsatile variation is observed in tissue by rapidly measuring the intensities of two wavelengths (usually 660 and 940 nm) corresponding to deoxy- and oxy-hemoglobin. As the heart beats, blood pulses through tissue capillaries and can be seen as a waveform in the intensities. The DC signal from the tissue background and non-pulsatile blood components is subtracted by taking the difference between the maximum and minimum values in the AC waveform. This process allows for experimental differentiation between the pulsatile component of blood and the non-pulsatile components of

blood and other tissues.[130] The remaining AC signal is attributed to hemoglobin absorption, and hemoglobin oxygen saturation is calculated as the ratio of the two wavelengths. A clear presentation of pulse oximetry is given in "Design of Pulse Oximeters."[131] Oxygen saturation is calculated as the fraction of a species bound to oxygen, and so hemoglobin oxygen saturation is calculated as

$$S_{O_2,Hb} = \frac{[Hb \cdot O_2]}{[Hb \cdot O_2] + [Hb]} \times 100 \qquad (2.7)$$

where [Hb] is the concentration of hemoglobin, [Hb·O_2] is the concentration of oxyhemoglobin, and S is the unitless percent oxygen saturation of hemoglobin. Myoglobin oxygen saturation can be calculated by substituting myoglobin for hemoglobin in the Equation 2.7. Myoglobin concentration does not vary with the heartbeat because it is normally located entirely in muscle tissue. While both pulse-oximetry and photoplethysmography estimate hemoglobin oxygen saturation, neither method measures absolute hemoglobin concentrations.[132] Absolute hemoglobin concentration is about 50 μM in aerobic skeletal muscle, and because hemoglobin contains four heme subunits, the heme concentration should be about 200 μM.[120] Capillary density in cardiac muscle is higher than in skeletal muscle, and the heme concentration should also be higher. [120] Myoglobin concentration in skeletal muscle

should be about 250 μM.[120] In muscle, hemoglobin heme and myoglobin heme should be present in nearly equal proportions. Saturation is typically measured as a difference in saturation compared to an arbitrary starting point. Single-point measures of hemoglobin oxygen saturation can be improved by taking into account light scattering, the presence of myoglobin and cytochromes, and spatial localization of the signal sources.[127] The accuracy of hemoglobin oxygen saturation measurements can also change with absolute concentration.[63] A better understanding of tissue dynamics can be realized by mapping the saturation values to either the surface of the skin or to the subsurface tissue volume.[87, 133] Estimations can be can be further improved by measuring entire spectral profiles and using more complex data analysis techniques instead of measuring saturation from only a few discrete wavelengths.

2.4.5 Myoglobin Oxygen Saturation Measurement

NIR spectroscopy has potential to assess oxygenation of myoglobin in cardiac tissue during surgery, prior to tissue necrosis. However, isolation of spectral features in tissue that can be solely attributed to myoglobin is difficult because of both light scattering and because spectral properties of myoglobin and hemoglobin share similar spectral absorption features.

Nuclear magnetic resonance spectroscopy (NMR) can be used to measure the ^{1}H deoxymyoglobin signal independently from the hemoglobin signal, and several groups have used magnetic resonance imaging (MRI) to study myoglobin oxygen saturation in working muscle.[134] There are many situations where MRI instrumentation is impractical because of the strong ambient magnetic field and constrained working area, for example inside of a surgical suite.

Most optical studies of myoglobin oxygen saturation in biological tissue have experimentally removed hemoglobin prior to measuring the spectra by perfusing the tissue with hemoglobin-free buffer solutions. Elimination of hemoglobin is not feasible when examining tissue *in vivo*. Instead, data reduction techniques can be applied to NIR spectra and estimation of myoglobin oxygen saturation can be obtained.[97, 135, 136] To apply these partial least squares data processing techniques the optical properties of the *in vitro* calibration model must sufficiently represent the optical properties of the working system. Classical least squares (CLS) can also be used to estimate myoglobin oxygen saturation. Classical least squares regressions require the measurement of the 0% and 100% saturation endpoints.

2.4.6 Carbohydrate and Other Spectral Features

Glucose and lactate are spectroscopically active bioanalytes with distinct NIR spectral features. Figure 2.7 shows the NIR spectra of lactate and glucose. Additional components of tissue that can be measured using NIR spectroscopy are melanin, water, adipose tissue, and calcifications. NIR measurements of lactate, melanin, water, and adipose have been shown in tissue, reflecting the applicability of NIR to help diagnose many medical disorders.[24, 86, 95, 137-143] The near infrared spectrum of water is sensitive to temperature because temperature affects hydrogen bonding of water. Tissue temperature can be estimated from water spectra.[104, 144] Of the many spectroscopically active metabolic components, *in vivo* glucose measurements are the most commonly studied. More recently, near infrared measurements of lactate have been increasingly studied.

Non-invasive glucose measurement is of significant medical interest because of the prevalence of diabetes. Current blood glucose measurements require patients to draw blood for analysis, and a non-invasive optical method would be preferable. Despite great interest in non-invasive glucose diagnostics, optical glucometers are not yet readily commercially available. In the near-infrared glucose has a broad spectral absorption band from 1550 to 1850 nm as shown in Figure 2.7b, which

overlaps with NIR spectral features of water and tissue. Spectral overlap and low tissue glucose concentration presents significant challenges in tissue glucose quantification. Progress in near infrared glucose diagnostics has been summarized in many review articles.[91, 145-149] Rapid, non-invasive optical measurement of glucose has potential as a home-based detection system that can be used by diabetes patients to maintain proper insulin levels.[91, 150]

Near infrared tissue lactate measurements can be used to estimate anaerobic exercise thresholds, and may also facilitate monitoring of tissue perfusion in surgery and trauma. Lactate has three near infrared absorption bands at 1675, 1690, and 1730 nm, as shown in Figure 2.7a. These spectral features were used by Lafrance to measure lactate *in vivo*.[95] To the best of our knowledge, this is currently the only study reporting *in vivo* measurement of lactate using the near infrared. Several other studies have reported the measurement of lactate in whole blood, plasma, and other media.[137, 138, 151, 152] In chapter 5, processing models for non-invasive quantification of lactate in tissue are further discussed.

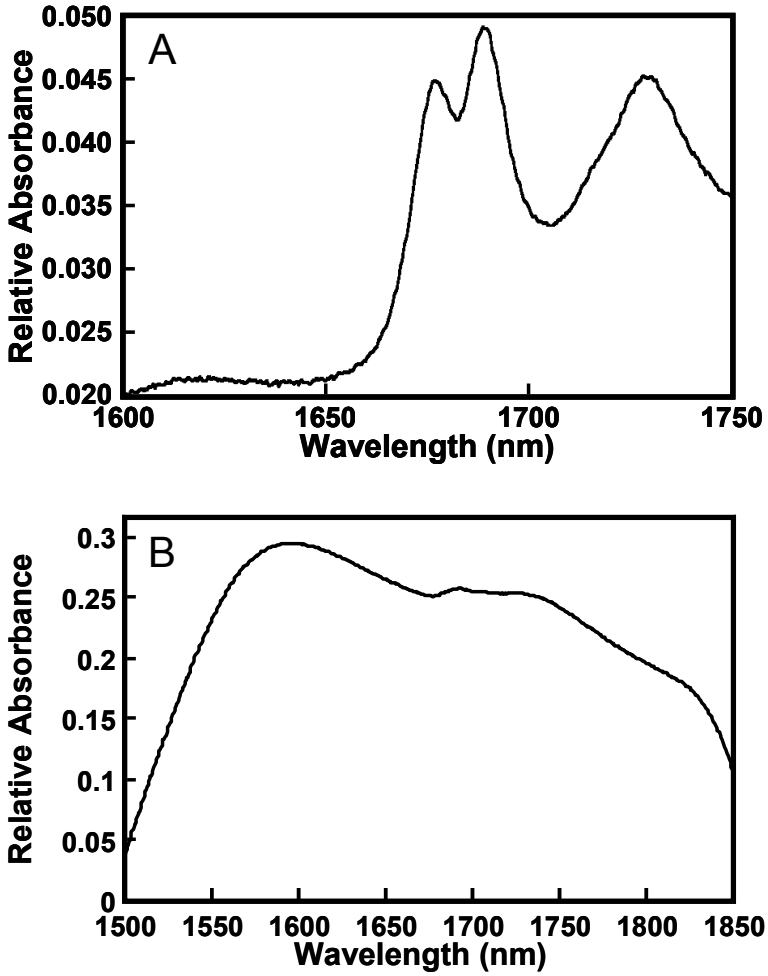

Figure 2.7: NIR spectra of lactate and glucose. Spectra are A) lactate, and B) glucose.

Chapter 3. A Portable Multi-Wavelength Near-Infrared Photon Time-of-Flight Instrument for Measuring Light Scattering

To correct for light scattering, scattering coefficients can be measured and mathematically corrected for. One method of measuring scattering involves measurement of the time required for a pulse of photons to propagate through a medium. Such photon time-of-flight systems have been used to measure scattering coefficients of turbid media. In this chapter, a simplified photon time-of-flight system is described for measuring reduced scattering coefficients and improving chemical quantification in turbid media. Measured scattering coefficients are used to correct near-infrared spectra for quantification. Contemporary photon time-of-flight instruments are impractical for most clinical biomedical problems. The simplified instrument presented here is both cost-effective and practical for use in many fields. This system was developed for measuring scattering coefficients of tissue, with the initial intention of using this pulsed-light system to augment co-measured visible-near infrared spectra of heart tissue.

In the biomedical field, the time-of-flight instrument may be useful for improving measurements of tissues and molecular species such as hemoglobin, myoglobin, cytochrome, glucose, and lactic acid concentrations, water and lipid content, as well as tissue temperature.[28, 47, 91, 137, 144, 153, 154] This photon time-of-flight instrument is practical for correction of reflectance spectra in simple clinical biomedical applications. The time required for measurements, as well as the size and financial cost of the required instrumentation determine the practicality of biomedical measurements. Point-sampling instruments can be built with a minimal cost and complexity, leading to practical applications. Hemoglobin oxygen saturation and temperature are examples of biomedical properties currently measured by doctors using point-sampling optical measurements. This simple method for measuring light scattering can be used to enhance spectral information and improve practical biodiagnostics.

Liquid samples with known optical properties were used to calibrate and test the time-of-flight instrument. The optical properties of biological tissues vary with time and can not be easily controlled. Rather than using biological samples for calibration and testing, dilute Intralipid/dye solutions were used as tissue simulating phantoms. Additional information about

tissue simulating phantoms is provided in Appendix F. Intralipid is a commercially prepared oil-in-water emulsion normally used for intravenous feeding. Intralipid is a practical scattering agent for phantom tissue because it is readily available, has a comparable refractive index to tissue membranes, and can easily be formed into various optical geometries.

3.1 Manuscript

A Portable Multi-Wavelength Near-Infrared Photon Time-of-Flight Instrument for Measuring Light Scattering

Authors:

Francis W.L. Esmonde-White and David H. Burns

3.2 Abstract

Measured light scattering properties can be used to improve quantitative spectroscopic analyses of turbid samples.[155] Instruments currently used to measure scattering coefficients are not optimized for portability. A hand-held, dual-wavelength instrument was developed and validated for rapid measurement of reduced scattering coefficients in tandem with near-infrared spectra. Intralipid/dye tissue simulating phantoms were used to model clinically relevant optical properties. Time-dependent intensity profiles of diffusely reflected near-infrared pulsed laser light were collected from phantoms and processed to

estimate scattering coefficients. In turbid solutions, optical scattering was measured at 850 and 905 nm with coefficients of variation of 14.1% and 11.6% over a clinically-relevant reduced scattering coefficient range from 1 to 6 mm^{-1}. This dual-wavelength scattering measurement provides a practical method for measuring optical scattering. A 35% improvement in quantification of an absorbing dye is shown by incorporating the measured reduced scattering coefficients when processing NIR spectra. We discuss the new instrument, methods for estimating the scattering coefficient from the measured temporal profiles, and finally how the reduced scattering coefficient is used to correct NIR measurements. Correction of near-infrared spectra using optical scattering measurements offers one direction for improving practical non-invasive biomedical quantification techniques.

3.3 Keywords

diffuse reflectance, near-infrared spectroscopy, photon time-of-flight, pulsed laser diode, scattering coefficient, optical transport coefficient, turbid media, biomedical spectroscopy

3.4 Introduction

Near-infrared (NIR) spectroscopy is an established analytical tool in the analysis of goods, such as foods and pharmaceuticals.[155-157] Diffuse

reflectance NIR spectroscopy, in the window from 600 to 1100 nm, has also gained attention as a biomedical diagnostic tool.[28] NIR spectroscopy is attractive because measurements are rapid, non-invasive, low-cost, and the diffuse reflectance sampling geometry is simple to implement. In the biomedical field, NIR spectroscopy has been used to investigate tissues and molecular species such as hemoglobin, myoglobin, cytochrome, glucose, and lactic acid concentrations, water and lipid content, as well as tissue temperature.[28, 47, 91, 137, 144, 153, 154] In some diseases, such as osteoarthritis, treatments are available but there is a lack of simple, rapid and accurate diagnostic tests, in particular for early disease stages. Subtle chemical changes in the cellular matrix or blood provide indications of disease. NIR spectra are sensitive to the local chemical environment, which is modified by disease. Changes in NIR spectra have been shown to accurately diagnose disease in a variety of tissues and biofluids. Identification of cancer in breast and pancreatic tissue using NIR has been demonstrated. Additional applications of NIR spectroscopy include identification of skin-alterations in diabetes and artherosclerotic plaques, examination of dental caries, and detection of burns.[69, 98, 99, 158-161]

Despite promising studies using NIR spectroscopy to examine normal and diseased tissue, widespread use for *in vivo* measurements

has been limited by response variability due to light scattering. In systems with scattering, such as tissue, there is a nonlinear relationship of absorbance to concentration, absorption coefficient, and pathlength. Light scattering adds significant complexity to NIR measurements. Optical scattering properties of tissue are sensitive to variations of the chemical and structural composition of the tissue.[162] Complex structures and dynamics of tissue lead to variations in the optical pathlength even between replicate measurements in a single sampling zone. These pathlength variations alter the reflectance efficiency and result in a wide distribution of observed absorbances.[27] Moreover, light scattering and attenuation is nonlinearly dependent on wavelength. Accurate quantitative measurements are not possible without correction for variations of scattering. Thus, light scattering presents a significant hurdle to robust clinical NIR measurements.

Variation of optical pathlength due to scattering presents a two-fold problem in diffuse reflectance NIR spectroscopy. First, the collection efficiency changes independently of absorption and adds a significant background that is not corrected by traditional reference measurements. Attenuation has different background offsets at different scattering levels. Second, the mean path of light through an absorbing medium will be

changed nonlinearly with scattering, leading to nonlinear attenuation changes.

Approaches have been developed to correct for scattering in attenuation spectra.[155, 163] Scatter correction methods include data-processing (or software techniques) and experimental (or hardware techniques). Data processing methods include using internal standards (e.g. solvent absorption bands), derivative spectroscopy, and multiplicative signal correction. Experimental correction methods measure the reduced scattering coefficient and correct the attenuation spectra for pathlength variations. Scattering varies with wavelength, approximately linearly over short wavelength ranges. Dual-wavelength scattering measurements can be used to improve spectral corrections through a linear interpolation of the scattering background.

Measurements of the reduced scattering coefficient are used to improve estimation of chemical concentrations from NIR spectroscopic measurements. Mean pathlength in the sample is related to the reduced scattering coefficient. Time-resolved instrumentation allows precise measurement of scattering.[41] Typical time-resolved instruments include a picosecond laser source, single photon detectors, and high-speed electronics.[112, 164] Though instrumentation capable of precisely measuring

scattering coefficients is common in academic research institutions, practical instruments are necessary to correct for scattering in clinical NIR spectroscopic applications. We report development of a portable instrument for measuring scattering and absorption coefficients at two wavelengths.

3.5 Method

An instrument was developed to measure reduced scattering coefficients and reflectance spectra. Measuring scattering coefficients in addition to reflectance spectra enables correction for the scattering pathlength. A photon time-of-flight system was developed to measure reduced scattering coefficients. A commercial diode array spectrometer was used to simultaneously measure visible-NIR reflectance spectra. A fiber optic probe was developed for measuring scattering coefficients and spectra over a small tissue region. Finally, software for the processing of the recorded time-of-flight and spectral data was developed.

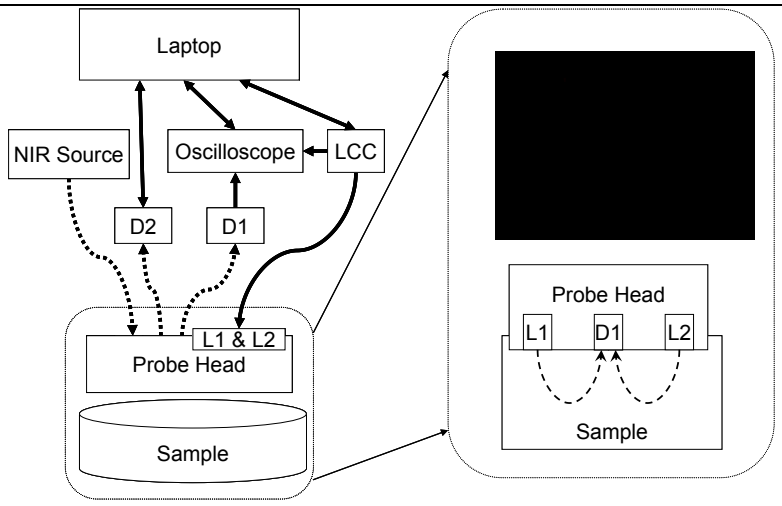

Figure 3.1: Instrument configuration schematic with inset probe diagram. LCC is the laser controller circuit, which is expanded in Figure 3.2. L1 and L2 are the 850 and 905 nm sources, D1 and D2 are fiber optics leading to the fast silicon photodiode (DET210) and the NIR spectrophotometer, NIR Source is the fiber optic leading to the NIR source. The inset at the upper right is a scaled diagram showing the position of elements on the bottom face of the probe. The inset at lower right indicated the orientation of the lasers and collection fibers in contact with the sample. Lasers and fibers face down into the sample and dashed lines indicate the approximate optical collection path.

3.5.1 Temporal Measurements

Generally, time-of-flight systems measure the time required for light to propagate through a medium. Sub-nanosecond pulses of light are used to measure the time shift in the peak optical output, with the shift indicating

the distance light has traveled in the medium. With longer pulses, changes in the optical waveform shape are used to estimate the reduced scattering coefficient. Rising and falling edges change shape with scattering, even when the total time shift is small relative to the duration of the pulse.

In the current system two laser diodes, SPL-LL85 and SPL-LL90 (OSRAM Opto Semiconductors GmbH, Regensburg, Germany), are used to generate nanosecond optical pulses. An oscilloscope (SDS-200, SoftDSP, Seoul, Korea) is then used to record the signal of reflected light as detected with a high speed photodiode. The optical system is shown in Figure 3.1, with details of the optical probe shown inset in the upper right corner. A collection fiber optic spaced 2 mm from the laser diode was used to channel diffusely reflected light to the photodiode. An electronic control system was developed to control the pulse repetition frequency, pulse duration and to choose the output laser wavelength. The electronic control system was integrated onto a printed circuit board measuring 8.3 x 8.3 cm.

Figure 3.2 shows a diagrammatic representation of the control circuit board. This system allowed computer control of a microcontroller through the universal serial bus. The microcontroller produced a trigger signal used to activate a pulse generator (DS1040, Dallas Semiconductor

Corp., Dallas, Texas, USA) and to synchronize the oscilloscope recordings. Pulse repetition frequency was dynamically set in the microcontroller and pulse repetition frequency was configured as 1 kHz. Pulse duration was set to 20 ns using the pulse generator. A high-speed amplifier (EL7104, Intersil, Milpitas, California, USA) was used to amplify the trigger pulse for switching the laser diodes on and off. Laser frequency was selected using transistor switches (2N7002, Digikey) to enable power to only one laser diode at a time.

Characterizing the laser system required measurement of the laser output intensity and pulse shapes. Average power of the 850 nm laser was 182.0 μW +/- 2%. Average power of the 905 nm laser was 187.1 μW +/- 2%. To verify the temporal profile of the laser output, reflectance from a roughened metal surface was recorded as shown in Figure 3.4. Reflectance from the metal surface measures the temporal response profile of the system without diffusion. Optical pulse widths were measured as 24 ns FWHM for both lasers. Temporal response is limited primarily by the oscilloscope, having an analog bandwidth of 200 MHz, a real-time sampling rate of 100 million samples per second and an equivalent sampling rate of 5 billion samples per second through over-sampling with a 200 ps time-to-digital converter.

Pulsed laser signals were detected using a high-speed silicon photodiode (DET210, Thorlabs, Newton, New Jersey, USA), and recorded using the oscilloscope. Each measurement comprised an average optical response from approximately 60 thousand pulses over one minute. Data was recorded using the oscilloscope software. For each sample three measurements were recorded: a dark signal with no laser enabled, a

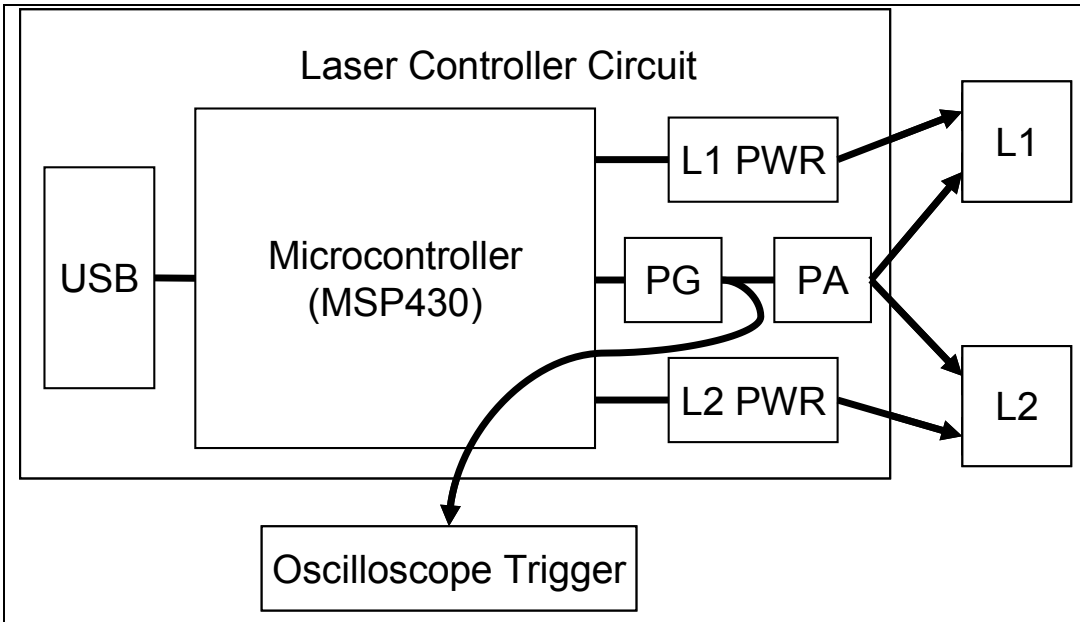

Figure 3.2: Laser controller circuit schematic. USB denotes the USB-to-serial converter (DLP-USB232M), Microcontroller indicates the host microcontroller used to control and trigger the electronic components on the circuit, L1 PWR and L2 PWR indicate the field effect transistors (2N7002) used to enable the laser diode power supplies, PG is the pulse generator (DS1040), PA is the pulse amplifier chip (EL7104), L1 and L2 indicate the 850 and 905 nm laser diodes (SPL-LL85 and SPL-LL90).

response with the 850 nm laser enabled and a response with the 905 nm laser enabled. Ringing signals from inductive coupling of the trigger signal was corrected by subtracting the dark measure from the two laser measures. Time points missing in the individual response profiles were replaced with interpolated values from surrounding data. Data was offset to positive intensity values and a base-10 logarithmic transform was used to linearize the response with respect to scattering and attenuation. These pre-processing steps are consistent with previous work.[23]

3.5.2 Software Processing

Time-series data from pulsed-light measurements was condensed into simple pulse descriptors, which were used to estimate scattering. Programs for processing the spectral and temporal data were written in Matlab (The Mathworks Inc., South Natick, MA). Descriptor properties were calculated from the pre-processed time-of-flight data. Selected descriptors were: the total area, the maximum intensity, the mean slope of the rising edge, the mean slope of the falling edge and the first through fourth statistical moments. Statistical moments describe shape properties of time-series data as numeric values, thus extracting a physical meaning from the data. The use of statistical moments has been previously demonstrated by Leonardi.[165] Details about the calculation of moments

have been described elsewhere.[166] The peak maximum is the maximum value observed from each entire response profile.

3.5.3 Spectroscopic Measurements

Simultaneous visible-NIR spectral measurements were made using a miniature Tungsten-halogen light source (LS-1-LL, Ocean Optics, Dunedin, Florida, USA) and a portable near-infrared spectrometer (BTC 111E, BWTek, Newark, Delaware, USA). A short source-detector separation of 2 mm was selected to ensure adequate reflectance signal intensity from samples with high attenuation. Attenuation spectra were calculated using the spectrum from a dilute 4% solution of Intralipid with no added dye as a reference spectrum. Example diffuse reflectance attenuation spectra are shown in Figure 3.4, along with the spectrum of the Ph. Martin black dye used in the measurements.

3.5.4 Optical Probe

An optical probe was constructed to integrate the photon time-of-flight and spectrometer. Laser diodes and sampling optics for the other system elements were arranged as illustrated in Figure 3.1. For the pulsed-light system, the two laser diodes were fixed in the probe along with an optical fiber. Light was channelled to the high speed photodiode using this first optical fiber. Laser diodes were positioned at 2 mm

distances from high speed detector fiber. Spectroscopic source and detector fibers were positioned at 2 mm increments perpendicular to the high-speed detector fiber. All fiber optics consisted of 600 μm diameter multimodal optical fibers. The fibers were epoxied into the probe head and polished. Transparent epoxy was also used to seal the probe face.

3.6 Materials

To determine the scattering response of the instrument and calibrate for scattering in the presence of absorption, two sets of tissue phantoms were prepared. Aqueous mixtures of Intralipid and black dye were used to model a range of reduced scattering and absorption coefficients corresponding to tissue. Dilution of Intralipid in water has been demonstrated as a practical method for the calibration of scattering in tissue phantoms.[167] Incorporation of a water-soluble dye to the scattering samples results in a known absorption coefficient.[168] Phantoms were prepared by measuring out a mass of dye stock solution, adding a known mass of Intralipid, and diluting to a total solution mass of 100 g. Samples were prepared gravimetrically to avoid error from Intralipid coating of glassware. Optical properties of these solutions were determined from the known concentrations of Intralipid and dye. The first phantom set was a series of 25 dilutions of Intralipid (Intralipid-20%, Fresenius-KABI,

Uppsala, Sweden), with no added absorber. The scattering coefficients and anisotropy were estimated from the measured Intralipid concentrations.[169] Reduced scattering coefficient varied from 0 - 9 mm^{-1}. The second phantom set consisted of 35 samples including 7 dilutions of Intralipid and 5 different concentrations of a black dye (Ph. Martin Black 33, Salis, Florida, USA). Reduced scattering coefficients varied from 0.9 - 6.5 mm^{-1} at 850 nm, and from 0.8 - 6.0 mm^{-1} at 905 nm. Absorption coefficients were determined from the measured dye concentrations and absorptivity. Absorption coefficient varied from 0.003 to 0.013 mm^{-1} at 850 nm, and from 0.002 to 0.010 mm^{-1} at 905 nm. This second phantom tissue set spans the expected range of optical properties in tissue. To avoid correlation with drift, spectral and temporal measures of two separate sets of samples (calibration and validation) were acquired in a random order.

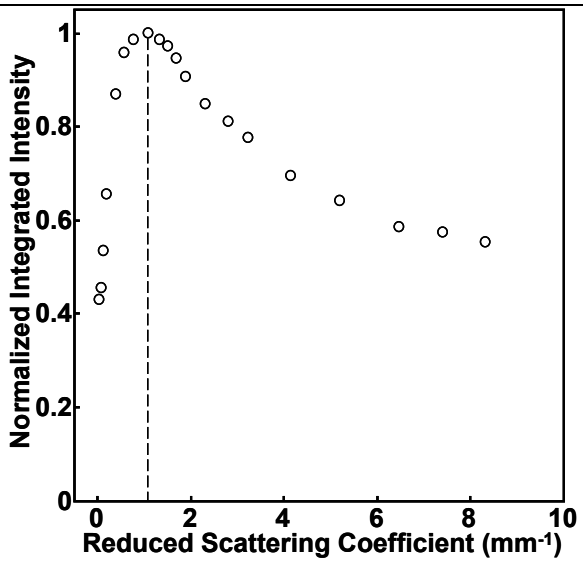

Figure 3.3: Scattering intensity is a non-monotonic function of the reduced scattering coefficient (shown for 905 nm). The dashed line indicates where the intensity relationship inverts from a positive correlation of optical intensity with scattering to a negative correlation.

3.7 Results & Discussion

Time-of-flight profiles were recorded for many scattering levels to determine the functional scattering range over which the simplified instrument could measure scattering. Reflectance intensity changes nonlinearly with scattering, as shown in Figure 3.3. While μ_s' was less than 1 mm^{-1} reflectance intensity increased with increasing scattering. When μ_s' was greater than 1 mm^{-1}, reflectance intensity decreased with increasing scattering. In the high scattering domain photons are progressively constrained to smaller volumes as scattering increases, resulting in decreasing reflectance intensity at the sampled point. The high scattering domain was selected for further work. In practice, the reduced scattering coefficient of human dermis is in the high scattering range.

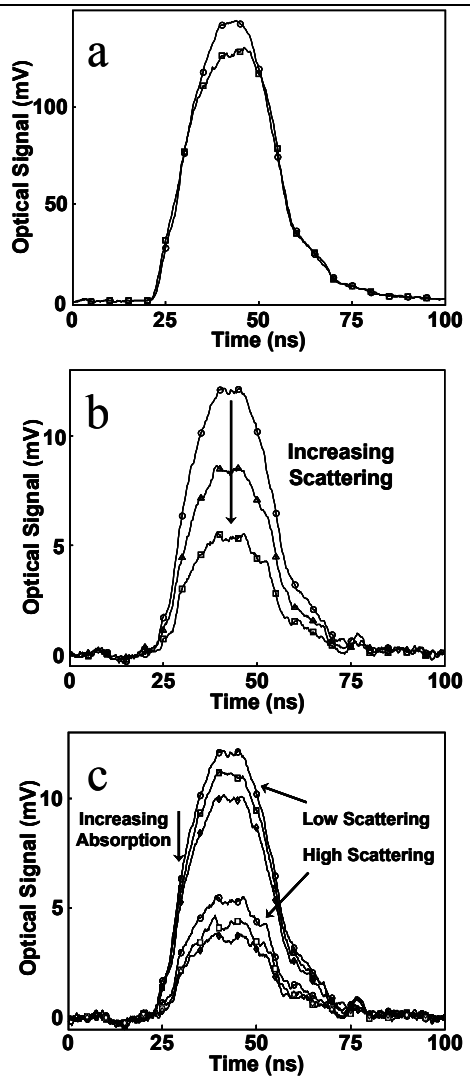

Figure 3.4: Trends in the recorded laser pulse profiles. In a), profiles from the 850 and 905 nm lasers are shown (850 nm is the upper curve). In b), optical intensity decreases with increasing scattering. In c), groups of profiles at low and high scattering levels are shown, intensity decreases with increasing absorption. Attenuation scales nonlinearly to absorption at high scattering.

The instrument was calibrated to measure the reduced scattering coefficient in the presence of varying absorption. Example temporal data is shown in Figure 3.4. Both lasers showed similar pulse shapes. As scattering increased, magnitude of the temporal profiles decreased. As absorption increased, maximum intensity of the profiles decreased.

Linear regressions were used to estimate the reduced scattering coefficients using descriptors of the profile calibration data. Time-of-flight data is determined by simplified descriptors which are less sensitive to temporal jitter. Descriptors were calculated as described in the methods section. Linear regressions were used to estimate μ_s' from each descriptor. Results of these regressions are listed in Table 3.1. Overall, using the second moment resulted in the best μ_s' estimates. This agrees with previous results.[165] Both slope of the falling edge and first moment did not estimate μ_s' well. Error in measurement of the mean pulse time becomes pronounced in wide pulses with a flat maximum intensity. As the first moment is a measure of mean pulse time, and does not estimate scattering in the present system. Estimates of μ_s' were derived from the second moment. Calibration and validation results for the 850 and 905 nm lasers using the second moment are shown in Figure 3.5. Coefficients of

variation (CV) for scattering coefficient estimation were 14% at 850 nm and 12% at 905 nm, for μ_s' from 1- 6 mm^{-1} and μ_a from 0.002-0.013 mm^{-1}.

850 nm laser	Scattering coefficient		
Descriptor	R^2 value	% CV (calibration)	% CV (validation)
first moment	0.67	29%	31%
second moment	0.91	15%	14%
third moment	0.86	18%	17%
fourth moment	0.91	15%	14%
total area	0.85	19%	18%
peak maximum	0.89	17%	15%
rising edge slope	0.88	17%	12%
falling edge slope	0.55	33%	40%
905 nm laser	Scattering coefficient estimation		
Descriptor	R^2 value	% CV (calibration)	% CV (validation)
first moment	0.59	32%	32%
second moment	0.95	12%	12%
third moment	0.85	19%	17%
fourth moment	0.94	12%	11%
total area	0.88	17%	14%
peak maximum	0.92	14%	13%
rising edge slope	0.90	16%	16%
falling edge slope	0.47	36%	40%

Table 3.1: Performance of regression estimation for reduced scattering coefficients using each of the time-of-flight descriptors.

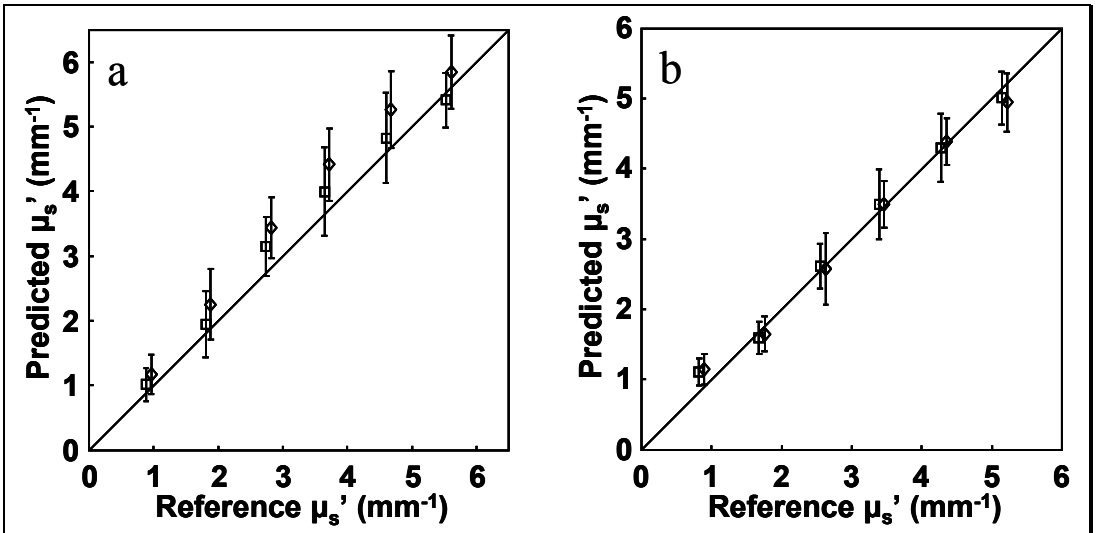

Figure 3.5: Regression plots showing μ_s' estimation using the second moment of the time-of-flight pulses. The results for calibration are shown in a) using the 850 nm laser, and in b) using the 905 nm laser. In both cases, calibration results are plotted as squares, while validation results are plotted as diamonds.

Dye concentration in the phantom tissues was quantified using visible-NIR spectra from 750 - 910 nm. Quantification of the selected dye presented a challenge, as the NIR dye spectra lack sharp spectral features. Pre-processed dye spectra and quantifications using three methods for estimating dye concentration are shown in Figure 3.6. Dye was quantified using only the spectra, and subsequently using two methods of correcting for scattering. In all cases, dye concentration was estimated from partial-least-squares (PLS)[170] analysis of the spectra. In the first case, spectra were processed using only PLS. In the second

case, spectra were corrected for scattering using a single scattering coefficient measure. In the third case, spectra were corrected using scattering coefficients estimated for all wavelengths.

Dye concentration was first estimated using the NIR spectra with no additional corrections applied. To select the number of regression factors the predicted residual error sum of squares (PRESS) was used. A 4 PLS regression was selected. Validation regression estimates degraded after more than 4 PLS terms were included in the model. Using the PLS model with uncorrected spectra, the percent coefficient of variation for the validation was 23%.

In the second method an additional pre-processing step was used where spectra were divided by the square-root of the average measured scattering coefficients. Dividing by the square root of the measured scattering coefficient has previously been demonstrated to reduce error in estimation of analyte concentration where $\mu_s' >> \mu_a$.[1] This correction approach is based on diffusion theory. Over a small wavelength range of less than 100 nm, μ_s' variation is approximately linear with wavelength. Averaging measured μ_s' values at 850 and 905 nm reduced the influence of errors in the measured μ_s' values. Concentration estimates from the single-point scattering corrected spectra improved with respect to the

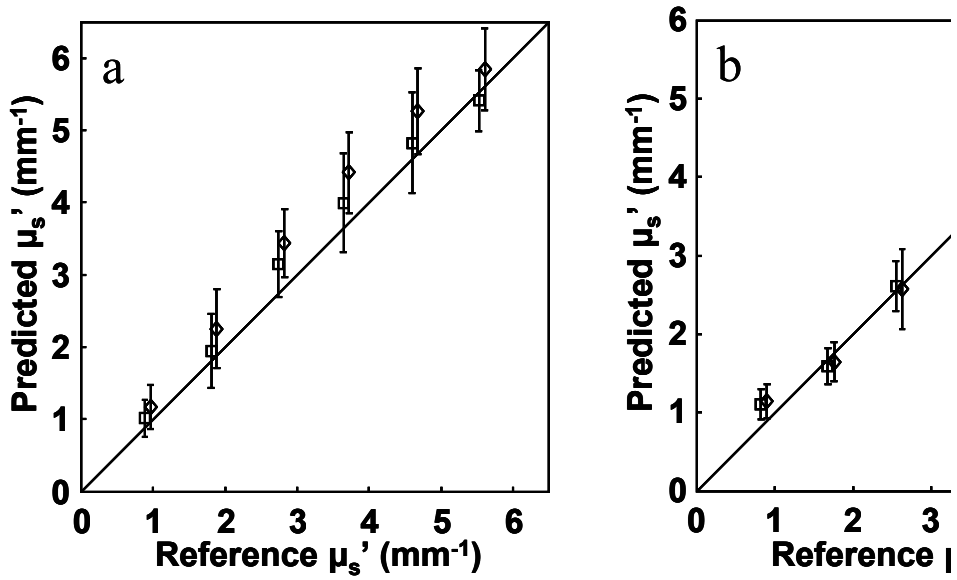

Figure 3.6: Dye concentration estimates with scattering correction. In a), attenuation spectra of the tissue phantoms are shown plotted to the attenuation scale (left axis), with the bolded dye spectrum is plotted to the absorbance scale (right axis). In b), dye concentration was estimated from uncorrected spectral data with a 4-component PLS model. In c), dye concentration was estimated from data corrected by measured μs' values using a 4-component PLS model. In d), dye concentration was estimated from data corrected by known μs' values using a 3-component PLS model. Calibration results are plotted as squares, while validation results are plotted as diamonds.

uncorrected spectra. Spectral correction using wavelength-dependent scattering estimates further improves concentration estimates. From the PRESS, a 4-term PLS model was again selected. Scatter correction using a single scattering value correction resulted in a CV of 21%. Using the measured reduced scattering coefficient improved the CV of dye concentration estimation in comparison to uncorrected spectra.

In the third method, a multi-wavelength scattering correction was used. To correct each spectral wavelength, measured attenuation was divided by the square root of a linear estimate of the μ_s' at each wavelength. Known μ_s' values at 850 and 905 nm were used to generate a linear estimate of μ_s' values from 750 to 910 nm. In the ideal case, a linear trend of scattering with wavelength can be derived from the 2 measured μ_s' values using our simplified instrument. Linear scattering estimates are then applied to spectra over a short wavelength range to correct for scattering. We show this correction based on known μ_s' values rather than directly from the linear estimate of two measured μ_s'. Extrapolating μ_s' values at other wavelengths from a line fitted to two measured points amplifies measurement error. Future improvements to the instrument presented here will allow determination of μ_s' with enough precision to reliably estimate this linear correction factor from measured μ_s' values.

Dividing measured attenuation spectra by the square root of extrapolated μ_s' values improved the validation results. From the PRESS, a 3-term PLS model was selected. Multiwavelength correction resulted in CV of 17%, a 35% improvement over the uncorrected spectral estimate. In addition to the improvement in CV, the selected model used fewer terms. A reduction in the calibration model complexity was possible because scattering had been corrected.

3.8 Conclusions

Improvements to this time-of-flight system will allow more precise quantification of μ_s'. To improve the system, several methods are suggested. Without modifying the current electronics, a shorter pulse can be used without decreasing peak optical-power. Detector rise time can be decreased by increasing the reverse bias applied to the diode. Simplified electronics can be incorporated to replace the oscilloscope. Unpublished results illustrate the utility of decimation of the temporal profiles by electronically windowing the electrical signal from the detector with a delayed trigger pulse using digital delay lines and a high-speed mixer. Future improvements in this portable system will allow for quick, robust multi-wavelength measurement of the reduced scattering coefficients in highly turbid media such as tissue.

It has been shown that the reduced scattering coefficient (μ_s') in the range from 1 – 6 mm^{-1} can be measured at both 850 and 905 nm using a handheld photon time-of-flight instrument. Analytical descriptors were used to compress time-of-flight profiles recorded with the portable instrument. Scattering was then predicted using the descriptors. An inverse least squares linear regression was used to predict the reduced scattering coefficient from the second moment. The coefficients of variation for the measured μ_s' were shown to be 14.1% at 850 nm, and 11.6% at 905 nm. Furthermore, multiwavelength near-infrared estimates of dye concentration were improved by 35% using the scattering correction method. Construction of a miniature device for the measurement of μ_s' represents an important step towards quantitative NIR clinical measurements in turbid media such as tissue. A portable photon time-of-flight device may prove a convenient alternative to costly instrumentation for measuring scattering in tissue and other turbid media.

3.9 Acknowledgements

This work was funded by the National Science and Engineering Research Council (NSERC) of Canada through both research grants and a PGS scholarship. Additional funding was supplied by the Fonds Québécois de la Recherche sur la Nature et les Technologies (FQRNT).

The authors would also like to thank Karen Esmonde-White for editorial comments, as well as Texas Instruments, Dallas Semiconductor Corp., Intersil, and OSRAM Opto Semiconductors for providing samples and technical support in the development of the portable photon time-of-flight device.

Chapter 4. Steady-State Diffuse Reflectance Imaging of an Annular Source Illumination Pattern for Quantifying Scattering and Absorption Coefficients of Turbid Media

To correct for scattering using instrumentation, scattering coefficients can be measured and mathematically corrected for. In Chapter 3, a photon time-of-flight system for measuring and correcting for scattering was described. The multi-wavelength scattering coefficient estimates using the time-of-flight system were shown to improve quantification by 35%. The time-of-flight method is particularly applicable for point-measurements.

In this chapter, a novel reflectance imaging system is described, providing a second method for measuring and correcting scattering in turbid media. A method is presented here for measuring optical scattering and absorption properties using steady-state diffuse reflectance imaging of a ring-shaped laser illumination pattern. By measuring the scattering at the center of an annular illumination pattern, the scattering coefficient is measured at the center of the location of interest. Furthermore, this

method is amenable to measuring scattering even at scattering levels much higher than typically present in tissue.

While the photon time-of-flight instrument presented in the previous chapter is a practical method for measuring and correcting for scattering in a point-measurement, situations arise where it is preferable to measure the scattering coefficients at many locations simultaneously. Though scattering coefficients can be mapped by translating the probe over a sample, this is not practical in dynamic systems. One example is in minimally invasive heart surgery (also known as beating-heart surgery)[171], where operations are performed on the beating heart. Assessment and visualization of tissue oxygen perfusion can help surgeons to monitor tissue viability. Because the heart is beating it is difficult to mechanically align the probe and synchronize the measurements to the beating without introducing errors. Other examples include burn assessment and tumor removal. In burn assessment it is important to quickly determine which burns require grafting.[98] During the excision of tumors, real-time tissue classification helps to guide surgeons in removing only cancerous tissue.[106] This is particularly important in brain surgery, where unnecessarily removing healthy brain matter can have terrible consequences for the patient. In both of these examples, non-contact

imaging can be used to guide medical interventions while avoiding exacerbation of tissue damage. In this chapter a reflectance imaging system is described for measuring scattering properties. The imaging system described here is applicable for measuring scattering in visible and near-infrared imaging spectroscopy.

4.1 Manuscript

Steady-State Diffuse Reflectance Imaging of an Annular Source Illumination Pattern for Quantifying Scattering and Absorption Coefficients of Turbid Media

Authors:

Francis W.L. Esmonde-White and David H. Burns

4.2 Abstract

A novel approach for measuring reduced scattering and absorption coefficients using imaging of lasers was examined. Rather than detecting radial reflectance intensity around an incident point source, intensity can be measured within a small annular pattern projected onto the sample surface. Reversal of the common source-detector geometry arrangement allows measurement of absorption and reduced scattering coefficients from a small surface area. Reduced scattering coefficients were measured over the range $\mu_s' = 0.1 - 40$ mm^{-1}, with a coefficient of variation of 12.6%

using a ring source & imaging detector optical arrangement. Absorption coefficients were measured over the range μ_a = 0 - 0.2 mm^{-1}, with a coefficient of variation of 11.5%, a 50% reduction of error in comparison with non-scatter corrected estimates. This method has the potential to measure scattering coefficients from an array of rings for rapid mapping of reduced scattering coefficients in spectral reflectance imaging. Ultimately, the ring source method has the potential to map optical properties for scatter-correction in spectral imaging.

4.3 Keywords

Scattering, Diffuse Reflectance, Reduced Scattering Coefficient, Spectral Imaging, Absorption, Turbid Media, Phantom Tissue, Computer Generated Holograph, Annular Pattern, Ring Pattern, Orbital Angular Momentum Light, Vortex Light

4.4 Introduction

Diffuse reflectance imaging is a practical modality for recording spectral information in living systems. Recent examples include imaging of hemoglobin oxygen saturation,[87, 133] assessment of burns,[98] and identification of tumors.[106] Tissue is identified or components are quantified based on the light attenuation, typically, as the logarithmic ratio of the light remitted without absorbance (reference) to the light remitted

with the added molecular species (signal). Using transmission geometries the reference intensity can be measured directly. However, in diffuse reflectance imaging spectroscopy the reference intensity can usually not be measured directly, because it is not possible to measure a blank (absorption-free sample) with the appropriate scattering level. The common approach is to instead use reflectance standards or feedback systems, which correct for variations in the intensity of the light source.[27, 172] However, an ideal reference would indicate the reflectance without added absorption so that attenuation could be directly calculated. When scattering is not known, it is difficult to determine the appropriate reference intensity.[40] One solution is to measure the scattering so that reference reflectance intensities can be estimated. Scattering is measured as the reduced scattering coefficient (μ_s'), which measures the effective distance between scattering events and includes the directional dependence of scattering anisotropy. The absorption coefficient (μ_a) is the corresponding measure for describing the absorption of light in terms of inverse propagation distance rather than absolute pathlength.

Continuous intensity methods have been demonstrated for measuring optical properties.[27] Optical properties are estimated from the radial intensity pattern of the reflectance around the point source. In

particular, diffuse reflectance images of point sources such as from a laser has been shown for measuring scattering and absorption coefficients.[26, 33-35, 37, 38] Unfortunately, the point source scattering measurements using imaging techniques require a source detector spacing of many millimetres, and have poor spatial resolution. Reflectance imaging systems collect images from a relatively large scale, and range from a half centimetre to several centimetres. In heterogeneous systems like biological tissue, scattering and absorption coefficients can vary over a few millimetres. Spatial resolution and sampling depths are a function of the source-detector spacing. By reducing the source-detector separation the scattering coefficient is measured with better spatial resolution.

Scattering coefficients have been measured using fiber-optic probes with small source-detector spacings. Examples include probes using a point source and concentric rings of detector fibers,[33] as well as source and detector fibers linearly arranged with total spacings of less than 2 mm.[107] Fiber probes, while having better spatial resolution, are not ideal for use with spectroscopic imaging because they apply pressure to the sample surface. Probe pressure can induce temporary physical deformations, cause changes in the local humidity and optical clearing,[142] and disrupt local circulation by pushing blood out of the tissue of interest.

Similar problems are observed in fluorescence and Raman spectroscopy. The ring/disk geometry has been recently reported for collection of subsurface Raman spectra.[173, 174] In particular, transcutaneous Raman using a similar optical geometry with a ring-shaped source and centrally-positioned detector bundle has been reported.[173, 174] In spatially-offset Raman spectroscopy, larger source ring diameters (greater source-detector separation) have been shown to reduce fluorescence background signal, and improve signal-to-noise ratio of Raman bands.

Several methods have been reported for the generation of annular laser patterns.[175-183] A single ring can be generated using axicon (axial conic) lenses or stepped phase-plates.[173, 178, 184-186] Arrays of ring patterns are also possible using holographic interference filters, either as printed films or using spatial light modulators.[187] Printed films have the advantage of being permanent and inexpensive, while spatial light modulators can be used to dynamically generate arrays of rings.[176, 182, 188, 189] By using arrays of rings rather than a single ring, concurrent measurement of scattering at multiple locations should be possible.

We investigated the feasibility of an annular illumination source to measure scattering at small source-detector separations suitable for an

imaging system. A ring patterned laser source and imaging detector were used to measure reduced scattering and absorption coefficients of tissue phantoms with known optical properties. Using an annular source pattern the spatial location over which the scattering coefficient is measured is small and well-defined, allowing a non-invasive measure of the local properties with fine spatial resolution. We demonstrate use of annular patterns with diffuse reflectance imaging to measure the absorption and reduced scattering coefficients in highly scattering and absorbing tissue phantoms at a single point, with potential applicability for in-vivo tissue diagnostics.

4.5 Material and Methods

A diffuse reflectance system for imaging ring-patterned laser was developed and tested. Image processing methods were developed to estimate reduced scattering and absorption coefficients of Intralipid/dye optical tissue phantoms. Details of the optical system, software, and tissue phantoms are presented in this section.

4.5.1 Instrument Configuration

An annular illumination pattern was generated using a laser, spatial filter and holographic filter. The experimental configuration is illustrated in Figure 4.1. A 5 mW Helium-Neon laser beam (Melles-Griot, Carlsbad,

California, USA) was directed through a spatial filter to improve the symmetry of the Gaussian laser profile and reduce high frequency spatial variations. The spatial filter consisted of two 30 mm lenses and a 12.5 μm pinhole. After the spatial filter, the intensity was 165 μW.

Annular illumination patterns were created using computer generated holographic filters as optical elements to diffract Gaussian laser beams into TEM^{11} beams. Annular profiles are best known for their use in holographic optical trapping, optical tweezers and optical spanners for manipulating particles under a microscope using light.[185, 189-193] Holographic diffraction filters were generated from the theoretical interference pattern between a plane-wave incident and an annular spirally-phased wavefront, and then printed to micrographic film.[194] A holographic interference filter for generating an annular profile is shown in

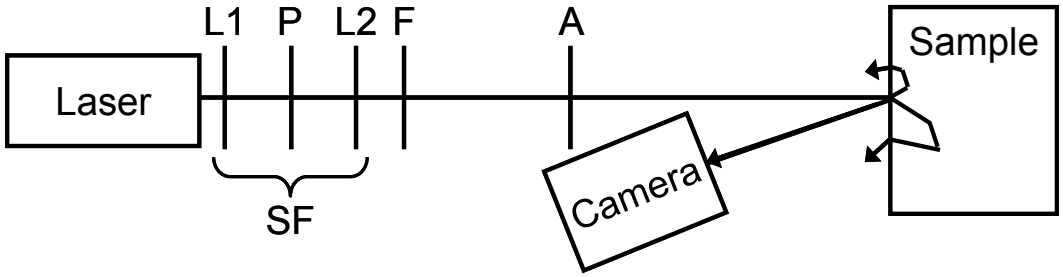

Figure 4.1: Instrumental configuration for imaging reflectance of annular illumination patterns on turbid media. Components are SF, spatial filter; F, vortex filter; A, aperture. The spatial filter consists of L1, lens 1; P, a pinhole; L2, lens 2.

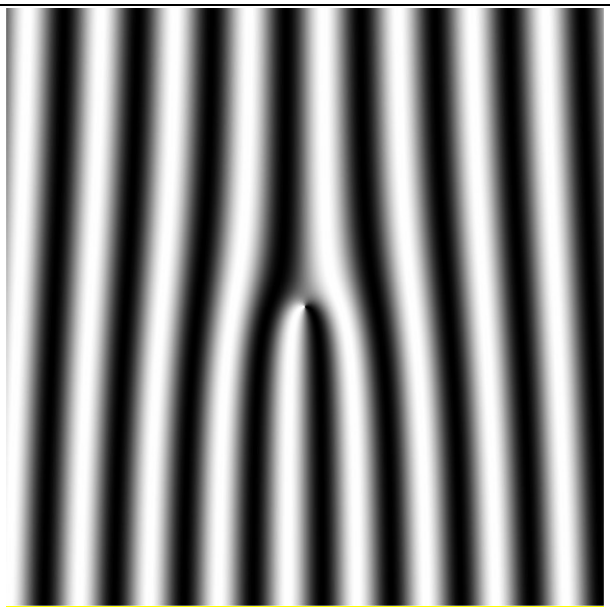

Figure 4.2: Computer generated holographic interference filter.

Figure 4.2. The holographic pattern was printed onto a micrographic film negative (Micromatt Inc., Montreal, Quebec, Canada) and positioned along the optical axis using an X-Y translation stage (HPT1, Thorlabs, Newton, New Jersey, USA). Once the filter was positioned properly in the center of the laser, multiple symmetric diffraction orders were observed as a pattern of multiple rings. Intensity of the zeroth order pattern was 160 μW, and intensity of the first order pattern was 5 μW.

A rectangular plexiglass cuvette used for all measurements was constructed in-house. The cuvette was 20 x 40 x 50 mm (length, width, height). To reduce Fresnel reflections in the recorded image, the front face of the cuvette was replaced by a microscope glass cover slip (45 x 50 x 0.2 mm, Fisher Scientific Co., Ottawa, Ontario, Canada), which

was trimmed to 40 x 50 mm using a ceramic glass cleaving stone. The cuvette was positioned 60 cm from the diffraction filter with annular laser patterns incident at a 90° angle on the surface of the glass cover slip. Sequentially each ring-shaped diffraction order was selected individually using a 35 mm linear translation stage and a variable iris with the diameter adjusted to 1.4 mm. A single diffracted order was permitted to pass through the aperture. Aperture diameter was held constant over the experiment while the aperture was linearly translated to select the proper diffraction order. Results from the second order diffraction beam are presented.

Diffuse reflectance images were recorded using a 14-bit grayscale Sony XCD-V50 digital camera (Sony Corporation, Tokyo, Japan) equipped with a macro lens (Computar M0814-MP, CBC America Corp., Commack, NY, USA). The camera was positioned with the minimum offset required to avoid blocking the incident illumination, and was oriented at an angle of 23° to the front surface of the cuvette.

Images were composite exposures created from 25 captured frames, with each frame having a 10 millisecond exposure time. Resulting images comprised the average of frames acquired over a 0.8 second time interval. Reference dark images were subtracted from the averaged

sample images to remove structured background resulting from the camera digitization electronics.

4.5.2 Software

Images were recorded in Matlab (MATLAB, The MathWorks, Inc., Natick, MA, USA) using the image acquisition toolbox and the Carnegie Mellon University DCAM driver. Radial intensity profiles and integrated annular intensities were measured from each recorded image. Absorption and reduced scattering coefficients were estimated from integrated intensities of rings in the reflectance images. Models for estimating the optical properties of the intralipid phantoms were tested using measured images of replicate samples to estimate the known optical coefficients.

4.5.3 Phantom Tissue Samples

Tissue phantoms were prepared using Intralipid-20 (Fresenius-KABI, Uppsala, Sweden) and green dye (Ph. Martin's Juniper Green 12A, Salis, Florida, USA). Samples were prepared gravimetrically and diluted with deionised water to a final mass of 100g. A gravimetric sample preparation method was used since Intralipid adheres to glassware and can result in inconsistent volume measurements. For each of the 136 phantom tissue samples prepared, scattering and absorption coefficients were calculated from the known Intralipid and dye concentrations.[169]

Samples were prepared so that solutions had optical properties in a biologically relevant range with reduced scattering coefficient between 0.1 and 44 mm^{-1} and absorption coefficient between 0 and 0.34 mm^{-1}. Samples were prepared in batches of ten to reduce the likelihood of false correlation due to systematic error. In each batch, sample concentrations were chosen at random from the predetermined experimental matrix.

Duplicate measurements were made on each Intralipid/dye sample in random order to minimize the effects of cross contamination. Each measurement comprised of first rinsing the cuvette three times with the sample, and then filling the cuvette with the sample. Duplicate measurements were separated into distinct calibration and validation data sets, where the first measurement was used in the calibration set, and the second measurement was used in the validation set.

4.6 Results and Discussion

Diffuse reflectance imaging of annular laser patterns was used to estimate optical properties. Capacity of the imaging system to measure optical properties was tested by imaging a series of tissue simulating phantoms. Diffusion theory suggests an inverse relationship between μ_s' and mean photon propagation distance in scattering materials. This relationship was observed in the measured radial profiles. Different

regions of the radial profiles show different trends with increasing scattering and absorption. Overall the light intensity increases with increasing scattering for all regions except those far away from the source where there is a maximum. This corresponds to estimation by light diffusion theory for point-sources.[18, 26]

When scattering is constant, increased absorption attenuates the ring intensity and also decreases light intensity outside the ring. The effects of scattering and absorption on ring intensity are shown by representative images in Figure 4.3. Ring intensity in Figures 4.3b and 4.3d are diminished, relative to Figures 4.3a and 4.3c. In Figure 4.3d the image shows a sharper intensity decrease around the ring than in Figure 4.3c due to the increased attenuation of diffusely scattered light.

Radial intensity patterns at several scattering and absorption levels are shown in Figure 4.4, along with the areas used for further analysis. Three regions were examined: region A was 0 - 0.30 mm, region B was 0.30 - 0.91 mm and region C was 1.52 - 2.13 mm. The radial profiles demonstrate that with increased absorption the intensity decreased. The intensity decrease was in proportion to the distance from the illuminating ring. Intensity at the center of the illumination ring is strongly affected by the scattering, but not as much by absorption. This is probably due to the

very close source-detector separation used in the measurement resulting in a short path length for the light. At distances further from the source, absorption has a pronounced effect on the intensity.

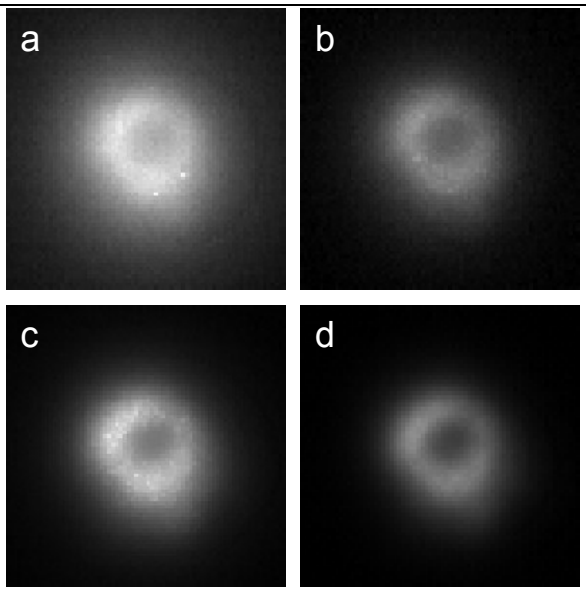

Figure 4.3: Images of the diffuse reflectance patterns for four of the annular patterns show the effect of scattering and absorption on ring intensity. Scattering coefficients increase from the top row to the bottom row (a, b: $\mu_s' = 5.2\ mm^{-1}$; c, d: $\mu_s' = 20.1\ mm^{-1}$). From left to right, absorption coefficients increase (a, c: $\mu_a = 0\ mm^{-1}$; b, d: $\mu_a = 0.21\ mm^{-1}$). If all four images were displayed on a common intensity scale, the upper row would be very dark. Instead, the intensities of the upper row have been displayed at double the true intensity for clarity.

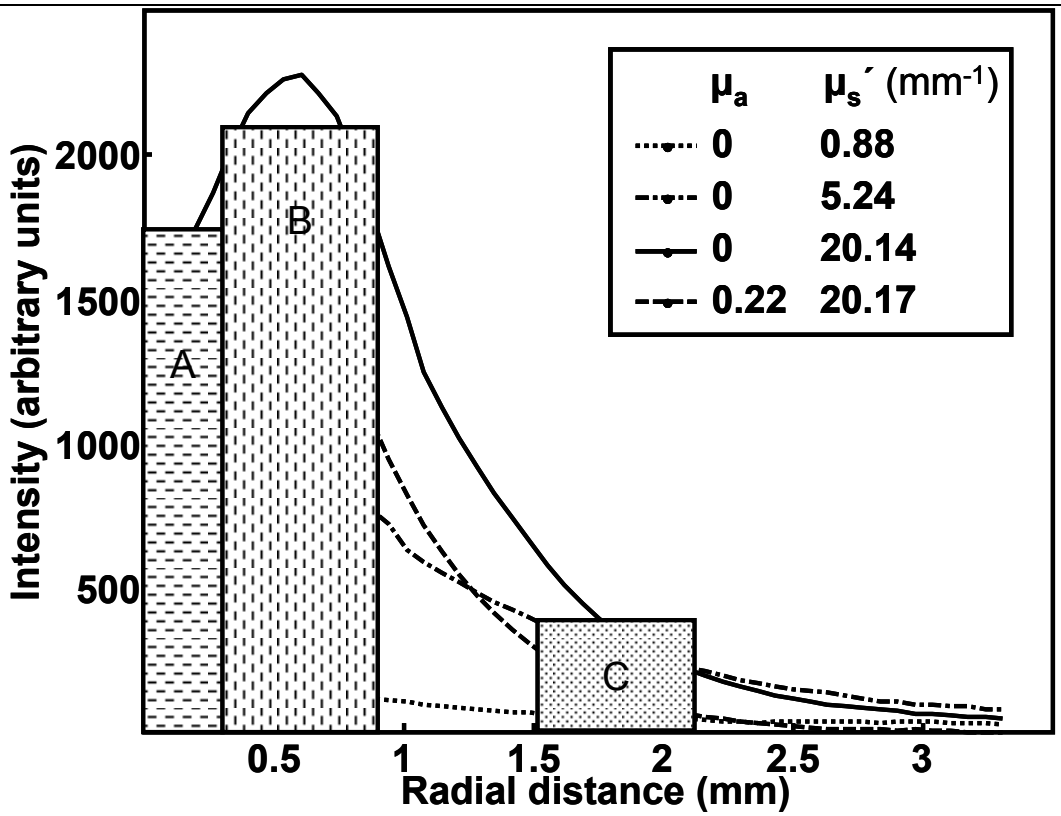

Figure 4.4: Radial reflectance intensity profiles of ring illumination with different reduced scattering and absorption coefficients. Shaded areas indicate the radial areas integrated for estimation of scattering and absorption coefficients. Region A was 0 - 0.30 mm, region B was 0.30 - 0.91 mm, and region C was 1.52 - 2.13 mm.

4.6.1 Estimation of Reduced Scattering Coefficient

Reflectance intensities within radial regions A, B, and C were integrated to estimate absorption and reduced scattering coefficients of the turbid media. As shown in Figure 4.5, reduced scattering coefficients were estimated from the integrated intensities of regions A and B using an inverse least squares calibration of 131 samples. The weighting of the signal for region A was negative in the final calibration and approximately

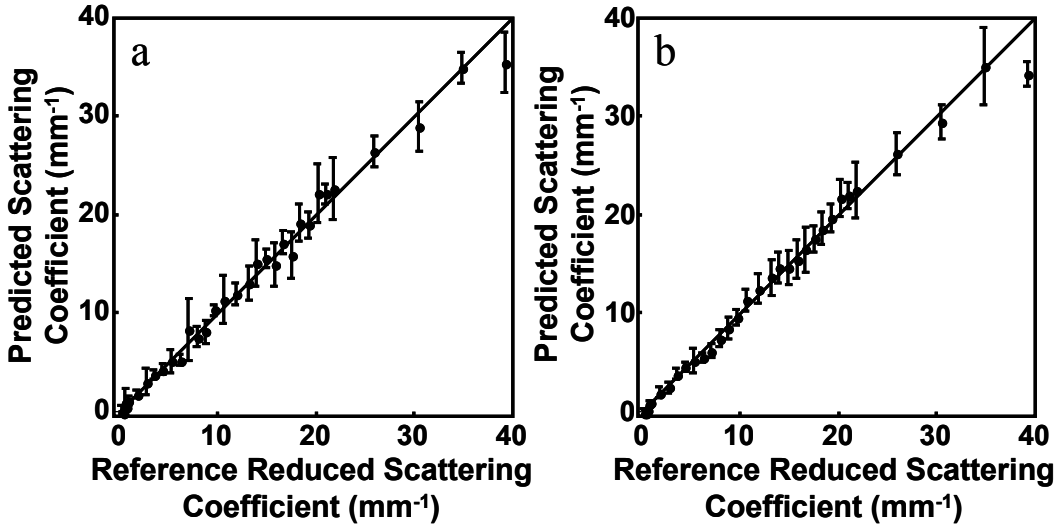

Figure 4.5: Scattering calibration and validation, as estimated from intensity at the disc A and the ring B. In a) calibration estimates are shown, and in b) validation estimates are shown. No differences were observed between calibration and validation estimates. Validation CV = 12.6% and r^2 = 0.97 where μ_s' < 40 mm^{-1}, and μ_a < 0.3 mm^{-1} for 131 samples.

5.8 times greater than the weighting for region B. The magnitudes of the coefficients are approximately equivalent to the ratio of the number of pixels in the respective regions, suggesting a derivative relationship between the regions is linearly proportional to the scattering coefficient. Using the linear model with two terms, reduced scattering coefficients were then estimated for the calibration and validation data sets. Scattering coefficients in the validation data set (n=131) were estimated with a coefficient of variation (CV) of 12.6% and a coefficient of determination (r^2) of 0.97. The results are very encouraging. No direct comparisons can be made with results from other studies because none have been demonstrated over such a large range of scattering and absorption coefficients. Two similar works have been published involving imaging measurements of scattering over short distances. In the first, Kienle et al. reported calibrations of optical properties by imaging radial reflectance patterns 2 to 12 mm from the source.[35] Optical properties of 13 tissue-simulating phantoms were determined over an absorption range of $0.002 < \mu_a < 0.1$ mm^{-1} with a root-mean-square error of ±13.6%, and over a scattering range of $0.5 < \mu_s' < 2.5$ mm^{-1} with a root-mean-square error of 2.6%. Pham et al. reported calibrations of optical properties from hyperspectral images of radial reflectance patterns 0.5 to 2.5 mm from the

source.[37] Optical properties of 15 tissue-simulating phantoms were determined over an absorption range of $0.001 < \mu_a < 0.2$ mm^{-1} with a root-mean-square error of ± 12%, and over a scattering range of $0.3 < \mu_s' < 2.5$ mm^{-1} with a root-mean-square error of 4%. In the present work, scattering coefficients were determined over a much wider range of reduced scattering coefficients, and shorter source-detector separation distances.

Even with short source-detector separations the absorption becomes significant with very high scattering levels. We found that the scattering calibration deviates from linearity when $\mu_s' > 30$ mm^{-1}, and may be a consequence of using only two terms in the calibration model. Estimations at higher scattering levels may be improved by taking into account additional radial regions or by using a nonlinear calibration model.

4.6.2 Estimation of Absorption Coefficient

Several methods were tested to compare the estimation of absorption coefficient using conventional diffuse reflectance imaging and three scattering-correction methods. In diffuse reflectance imaging attenuation (A) is measured according to

$$A = -\log_{10}\left(R/R_0\right) \qquad (4.1)$$

where R is the reflectance intensity and R_0 is the absorption-free reference reflectance. In conventional diffuse reflectance imaging, attenuation is calculated by referencing the diffuse reflectance to a constant value.

Attenuation was first estimated according to the common method using Eq. 4.1 by referencing the integrated reflectance intensity at region C to a constant value. Inverse least squares calibration was used to relate the attenuation to the absorption coefficient, and absorption coefficients were estimated for the validation samples. Best possible μ_a estimates using the conventional method resulted in a CV of 22.8% and r^2 of 0.89 for 45 samples where μ_a = 0 - 0.2 mm^{-1} and μ_s' = 2.7 - 30 mm^{-1}.

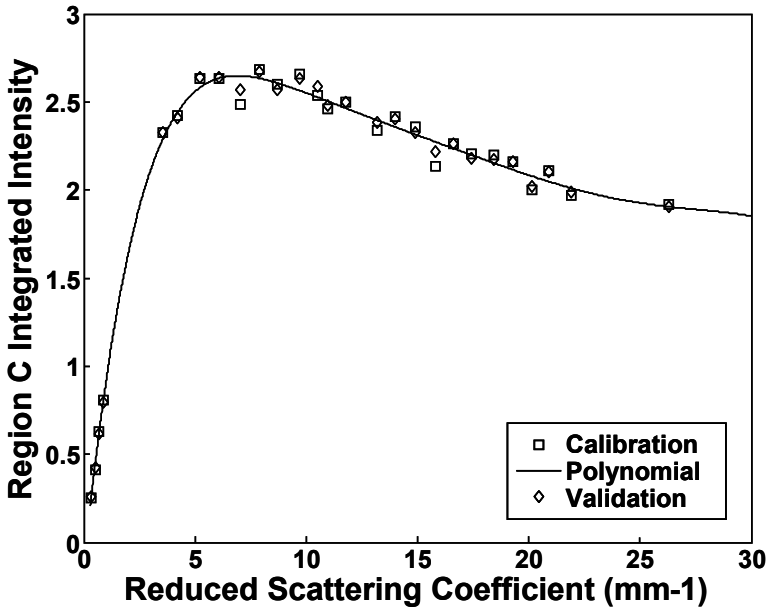

Figure 4.6: Polynomial curve approximation of the reflectance intensity trend in the annular area C for scattering (with $\mu_a = 0$). The solid curve shows the seventh order polynomial between 0.2 and 30 mm^{-1} determined from a polynomial least-squares best fit of the data. From PRESS plots, a seventh order polynomial was selected to best fit the data.

To improve μ_a estimates, absorption-free scattering-dependent reference intensities were estimated. Reference reflectance intensities were a non-monotonic function of the reduced scattering coefficient, as shown in Figure 4.6. Based on the prediction error sum of squares, a seventh-degree polynomial was selected for estimation of the reference reflectance intensity from the reduced scattering coefficient. The polynomial relationship was determined for a series of tissue phantoms with $\mu_a = 0$ mm^{-1} and $0.2 < \mu_s' < 30$ mm^{-1}. Absorption-free reference

reflectance (R_0) was then estimated using the polynomial function and the reduced scattering coefficient measured for each sample as described above. Corrected attenuation was then calculated from Eq. 4.1. Inverse least squares calibration was used to relate the attenuation to the absorption coefficient, results are shown in Figure 4.7a. Using this method and an independent set of validation samples were estimated with a CV of 15.6% and r^2 of 0.95 for 45 samples where $0 < \mu_a < 0.2$ mm^{-1} and $2.7 < \mu_s' < 30$ mm^{-1}.

Integrated reflectance intensity can be estimated using the diffusion equation where:[26]

$$R(\mu_a, \mu_s') = \frac{e^{-\mu_{eff} z_0}}{2}\left(1 + e^{-(4/3)A\sqrt{3(1-a')}}\right) \tag{4.2}$$

and $\mu_{eff} = \left[3\mu_a\left(\mu_a + \mu_s'\right)\right]^{1/2}$, $a' = \mu_s' / \left(\mu_a + \mu_s'\right)$, and $z_0 = \left[(1-g)\mu_s\right]^{-1}$. By simplifying and substituting Eq. 4.2 into Eq. 4.1, the relationship between attenuation and absorption coefficient can be simplified to:

$$A^2 \propto \mu_a \tag{4.3}$$

Inverse least squares calibrations were next tested to relate the squared reference-corrected attenuation to the absorption coefficients, and tested on the separate validation data. Absorption coefficients were estimated from the relationship in Eq. 4.3 for 45 samples where $0 < \mu_a < 0.2$ mm^{-1} and $2.7 < \mu_s' < 30$ mm^{-1}, with a validation CV of 17.7% and r^2 of 0.94. Using the squared attenuation method, the relationship of estimated

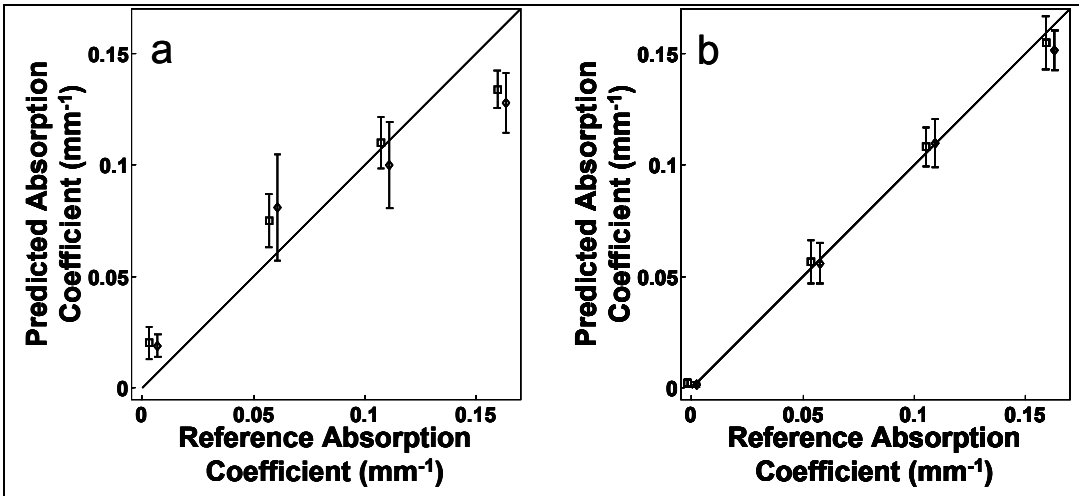

Figure 4.7: Absorption coefficient estimation from integrated reflectance intensities. Absorption coefficient calibration and validation estimates using the intensity in the annular area C are shown. Absorption coefficients are estimated from absorbance (A). In a) μ_a is estimated from A, and in b) μ_a is estimated from $A^{(1.4)}$. Absorption coefficients between $0 < \mu_a < 0.2$ mm^{-1} were estimated in phantoms with $2.7 < \mu_s' < 30$ mm^{-1}. Calibration estimates are shown as squares, and validation estimates are shown as diamonds.

absorption to reference absorption remained nonlinear. The nonlinearity may be due to the approximations made in the derivation of Equations 4.2 and 4.3, or due to the non-zero absorption of light by Intralipid. The diffusion approximation uses a truncation of terms representing anisotropy in a Taylor series expansion. Equations 4.2 and 4.3 are based on the diffusion approximation, and so the relationships are not exact for highly forward scattering media.

To correct the nonlinearity in the attenuation-absorption coefficient relationship, non-integer exponents were tested. From the non-negative experimental attenuation values, the optimal exponent relating attenuation to absorption coefficient was calculated to be 1.4, at which r^2 was maximized and CV minimized. Using this experimentally determined exponent, inverse least squares calibrations were used to relate $A^{1.4}$ to μ_a. Validation results are shown in Figure 4.7b, in which absorption coefficients were estimated for 45 independent validation samples with a CV of 11.5% and an r^2 of 0.96 where $0 < \mu_a < 0.2$ mm^{-1} and $2.7 < \mu_s' < 30$ mm^{-1}. Using scattering correction with the scattering coefficients measured by ring illumination improves both the precision and linearity of estimated absorption coefficients as compared to conventional approaches. Using the scattering-estimated reference when determining

the absorption coefficient, we observed a 30% reduction in CV and an increase in linearity from an r^2 of 0.89 to 0.95. Using the theoretically-derived squared attenuation, validation performance was slightly lower, however with the experimentally determined exponential relationship of $A^{1.4} \propto \mu_a$, the CV was decreased by 50% and the r^2 further increased to 0.96.

4.7 Conclusion

Results show that annular illumination is a viable approach to measuring tissue optical properties. Light diffusion theories, developed for point-sources, can be applied to ring sources. Light intensities of the ring-shaped laser and at distances from the ring were measured using a steady-state diffuse reflectance imaging system. Absorption and reduced scattering coefficients were quantified over short distances, and the quantification results indicate good agreement with previous studies. Optical properties of Intralipid/dye phantom tissue samples with $0 < \mu_a < 0.3$ mm^{-1} and $0 < \mu_s' < 40$ mm^{-1} were quantified. Reduced scattering coefficients were estimated with a CV of 12.6% and r^2 of 0.97 using intensities measured over a disc 0.30 mm in radius, and a ring from 0.30 - 0.91 mm. Absorption coefficients were estimated with a CV of

11.5% and r^2 of 0.96 using intensities measured over a ring from 1.52 - 2.12 mm.

Several features of this method are useful for non-invasive spectroscopic tissue imaging. First, the measurements are made without applying pressure to the sample. When pressure is applied to tissue optical properties can change due to regional blood distribution and tissue compression.[142] Non-contact measurements reduce these sources of pressure-induced variance. Second, the ring-shaped incident pattern spreads light over a ring instead of focusing the laser to a single point. Risk of tissue damage is reduced because incident laser power is spread over a larger area than for a focused point-source of equivalent intensity. For surgical applications, a ceiling mounted imaging device may be practical. With increased collection distances, the f-number of the collection optics becomes very large, and an increase of the source intensity would be required. Higher laser intensities can be safely used with annular patterns as compared to a focused Gaussian laser for imaging scattering coefficients with an equivalent spatial resolution. Increased source power also translates to shorter acquisition times or increased signal-to-noise levels. Third, optical scattering properties are

measured within a small illumination ring, leading to high spatial resolution of the measured properties.

Grier has previously reported using arrays of optical rings for optical trapping of small particles.[189] A potential extension of this method is to generate an array of rings using an active optical element such as a spatial light modulator. Dynamic generation of annular illumination patterns could allow simultaneous mapping of scattering coefficients over a large surface.

4.8 Acknowledgements

This work was funded by the National Science and Engineering Research Council (NSERC) of Canada through both research grants and a PGS scholarship. Additional funding was supplied by the Fonds Québécois de la Recherche sur la Nature et les Technologies (FQRNT). The authors would also like to thank Matthew Schulmerich for feedback, Karen Esmonde-White for editorial comments, and Micromatt Inc. (Montreal, Canada) for providing technical help in printing the microfilm optical filters.

Chapter 5. Generic Parsimony in Genetic Algorithms for Selecting Spectral Processing Models in Regression and Classification

Quantification in turbid media can be augmented by measuring scattering coefficients in addition to spectra. The practical point-source and imaging methods for measuring scattering shown in Chapters 3 and 4 allow for quantification improvements of 35% and 50% over typical methods. Instead of using novel instruments, it is possible to improve quantification using improved data processing methods with conventional instrumentation.

In this chapter a novel method for finding parsimonious spectroscopic data processing models is presented. Spectroscopic measurements of turbid media are often difficult to interpret. Furthermore, spectral properties of samples may change over time, requiring that models be periodically revised. Genetic algorithms have been used to simplify the process of selecting data processing models, with particular applications for processing spectra measured from turbid media. Development of parsimonious models has previously required operator intervention in the crafting of custom penalty weightings. Generic

parsimony penalty functions are presented here for the automated selection of optimal models using genetic algorithms. Matlab source code for the genetic algorithm described in this chapter is provided in Appendix C. To understand the use of parsimony in genetic algorithms, an introduction is given prior to the main body of this chapter.

5.1 Genetic Algorithms

One approach to building optimal processing models uses genetic algorithms to automatically select regression and classification models. Genetic algorithms are nonlinear search algorithms based loosely on simulated evolution.[195] Pre-processing options and wavelengths of interest are coded as a string of binary digits analogous to a genetic code, and optimal models are selected by the GA using a simulated-evolution method akin to 'survival of the fittest'. Model selection is a highly nonlinear process, where selecting slightly different options may result in vastly different model fitness outcomes. Pre-processing options and useful wavelengths can be automatically suggested by genetic algorithms, and expert knowledge is only required in the final selection and application of the models. This allows the expert to reduce time spent in developing processing methods by trial and error. One disadvantage of using genetic algorithms is that the selected processing models can be difficult to

interpret, because no justification is provided by the algorithm as to why particular pre-processing options and wavelengths are selected. In genetic algorithms the choice of an optimal fitness function is crucial, and should include some form of parsimony.

Parsimony is a term meaning to spare complexity. Most commonly parsimony is used to describe the application of Occam's razor. This principle plays an important role in building data processing models. One danger in automated method development is the adoption of complex models which are adapted to noise in the calibration sample, and perform poorly with independent validation and test samples. Model complexity can also have a secondary cost, because complex methods also require unnecessarily complex instrumentation. While the cost of analytical instrumentation is not often prohibitive in research, methods should be oriented towards maximum simplicity to reduce time and cost of routine testing in anticipation of usage under non-laboratory conditions. Development of simplified methods and simplified instrumentation can be guided by automated methods which take into account parsimony. Genetic algorithms which do not penalize for model complexity will evolve very complex models to fit the data as closely as possible. To avoid this, various penalties or constraints are typically applied to model fitness to

emphasize the utility of smaller models. Because the success of genetic algorithms are based on evaluations of processing model fitness, the selection of appropriate fitness functions and associated parsimony penalties are very important.

Fitness functions for regression and classification genetic algorithms vary widely. Standard error[104] and root mean square error[196-200] are often used to evaluate regression model fitness. Regression error is continuous and suitable for genetic algorithm optimizations. Classification fitness functions used in genetic algorithms based on classification accuracy have been reported.[201-204] In this chapter, generic parsimony penalties based on root mean square regression error and Bayesian classification error are examined.

5.2 Manuscript

Generic Parsimony in Genetic Algorithms for Selecting Spectral Processing Models in Regression and Classification

Authors:

Francis W.L. Esmonde-White and David H. Burns

5.3 Abstract

Genetic algorithms have been used to develop models for processing spectroscopic data. Genetic algorithms are able to search a

very large number of possible model types and identify models for closer examination. Unfortunately, very complex models are often developed and techniques for limiting model complexity must be optimized for each particular application in regression and classification. A generalized approach for implementing parsimony was explored by comparing results from a series of regression and classification genetic algorithms incorporating different penalization criteria. Regression models were selected using mean square error and parsimony penalties. Classification models were selected using log-likelihood of correct classification and parsimony penalties. Penalties were based on the number of degrees of freedom, by taking into consideration the number of selected wavelengths and enabled pre-processing steps. Parsimony penalties were found to improve the regression and classification models selected by the genetic algorithm. In particular, the genetic algorithm incorporating parsimony located a simple regression processing method with a lower cross validation error than the optimal expert-developed processing method.

5.4 Keywords

genetic algorithm, regression, quantification, classification, wavelength selection, pre-processing option selection

5.5 Introduction

Spectroscopic measurements are used for non-destructive quantification and classification. However, development of robust spectral processing models can be extremely complex. Spectral data acquired from industrial processes, biological fluids, and biological tissues include significant variability from spectral backgrounds and interference from chemical species other than the analyte of interest. Physical analytical methods such as enzymatic digestion and chromatographic purification can sometimes be used to prepare samples for analysis. However, extra sample preparation steps are costly, require time, and may increase the uncertainty in the spectroscopic measurement by virtue of increased sample handling. Methods for processing spectral data are often a practical alternative, where analytes are measured without pre-treatment steps. Moreover, computational costs are low, even for very complex spectral data analysis. Processing models are composed of pre-processing steps, such as background correction or smoothing, in conjunction with selection of wavelength regions that will best quantify or classify samples. Despite advances in computer hardware, method development for regression or classification based on spectroscopic data is still limited by the selection of pre-processing steps and optimal

wavelength for analysis. Optimization of data processing models is an iterative process and relies partly on chance. Additionally, the spectroscopic background and sample chemical compositions may change over time, requiring experts to periodically revise processing models.

Instead of developing processing methods manually through trial and error, search algorithms are used to select data processing models. Algorithms for optimizing processing methods must search a large, irregular set of solutions. Over the past decade genetic algorithms have been increasingly used to automate selection of regression and classification models for analysis of spectroscopic data.[105, 200-202, 205-212] Genetic algorithms are used to automatically identify processing models, requiring expert knowledge only for selection and application of the final model. A major challenge in using genetic algorithms is the implementation of an appropriate parsimony function.

Complex models generally fit calibration data more closely than do simple models. Because of this, unconstrained automatic model selection algorithms will preferentially select complex models over simple models. However, complex models also adapt to fit noise in calibration data and perform poorly when validated against independent test data. It is

important to use fitness evaluation functions that incorporate penalties to balance data fitting against model complexity.[213] Parsimony is usually implemented as a penalty based on model size. Either system-specific or general parsimony penalties can be implemented. System-specific penalty weights require significant effort to develop and small changes in the assigned weightings can have a dramatic effect on model selection.[212] Alternately, generalized penalties can be implemented using the number of degrees of freedom in the model.[214-216] Degrees of freedom are one method for the representation of model complexity, and are calculated by subtracting the number of coefficients used for processing data from the total number of observations within the data.

In this manuscript, several generalized penalties are examined for parsimonious model selection for regression and classification. Parsimony is implemented based on the model evaluation functions for regression and classification. To evaluate regression model fitness, standard error and root mean square error are commonly used.[196-200] Regression error is continuous and suitable for genetic algorithm optimizations. Different penalty functions based on regression error were examined using *in-vivo* diffuse reflectance NIR spectra of human fingernails to estimate lactate concentration.[95] To evaluate classification model fitness, classification

success rate (also known as accuracy) is commonly used.[201-204] Success rates are determined as a ratio of the number of samples correctly identified to the number of samples incorrectly classified.[217] Precision of the success rate is dependent on the number of samples in the data. In small data sets the success rate is imprecise and cannot be used to discriminate between processing models with small performance differences. This drawback is problematic when developing methods for classification of biomedical samples, where the number of samples is limited by cost or availability of patients. An alternate approach was developed using Bayesian probabilities to classify samples and a Gibbs entropy measure to evaluate processing model fitness.[218-220] Parsimony criteria from information-theory based on penalization of log-likelihood values were then applied to guide model development.[216] Development of models using entropy-based classification fitness parsimony was tested with attenuated total reflectance mid-infrared spectra of starches.[221]

5.6 Methodology

To test the influence of parsimony on model selection, a genetic algorithm was developed and tested with various parsimony functions. The genetic algorithm consists of two portions: a pseudo-evolution based optimization algorithm and a function for evaluation of the fitness of

processing models. Fitness functions were developed for regression and classification of samples using spectral data. Effects of parsimony were tested by examining the performance of the genetic algorithm when using different parsimony criteria as applied to spectral data.

5.6.1 Software

A non-generational genetic algorithm was developed in Matlab (The Mathworks, Inc., Natick, MA) using genetic algorithm techniques as outlined by Luke.[222] Non-generational genetic algorithms are useful because they immediately incorporate optimal solutions into the development of new population members as they are discovered, rather than waiting until an entire generation has been processed. Different fitness functions were implemented in order to evaluate regression models and classification models, where in all cases the underlying genetic algorithm was identical. Effects of parsimony on model selection were examined by comparing several parsimony implementations for regression and classification fitness functions. All fitness functions used a cross-validation approach to measuring model fitness, where data from k samples was divided into n groups of spectra. Each of the n groups was in turn used as validation data while the remaining n-1 groups were used as

calibration data. Results from the n evaluation steps were combined in order to approximate the model fitness.

Steps used in the genetic algorithm were:

1. Randomly initialize the initial population
2. Evaluate the fitness of all population members
3. Generate a new population member using crossover and mutation
4. Evaluate the new population member
5. Selectively replace one population member
6. Repeat steps 3 - 5 for the specified number of evolution steps

To evaluate the fitness of each genetic algorithm population member, each model was tested using a fitness function. Data was first pre-processed according to selected options. Next, coefficients for a linear regression calibration were determined using the wavelengths selected from the calibration data. Properties of the validation data were estimated using the coefficients calculated from the calibration data. For classification, an extra step was included, using the score calculated from the regression to estimate the sample class using a Bayesian probability measure for classification.

5.6.2 Pre-processing Options and Score Calculation

Each solution vector developed by the GA coded a series of steps for pre-processing the spectral data. A maximum of six pre-processing steps were permitted in any processing model. Common pre-processing options were explored, including: removing linear trends in data (using the Matlab function 'detrend'), boxcar smoothing, taking the discrete first difference[93], discrete second difference[93], Haar wavelet transform[211], mean centering, autoscaling, unit scaling, range scale, intensity scaling, area normalizing, and vector normalization. Processing models also included extra parameters for each pre-processing option. Two parameters were generated for each pre-processing option (though used only with certain pre-processing steps): smoothing window, and gap for computation of differences. Smoothing windows were required by the boxcar smoothing and discrete difference methods. Noise in measurements may be reduced by smoothing the data, and a smoothing window parameter specifies the number of spectral values to be used in calculating averages. Derivatives were calculated by taking the difference between data points separated by a number of values specified by the gap parameter. Calibration and validation data were separately pre-processed

for each cross-validation permutation step according to the sequence and options specified in the processing model.

From the vector of selected wavelengths in the pre-processing spectral data, an inverse least squares regression model was developed from the calibration set. Score values estimating the known property (either the concentration or sample class) were calculated for each sample in the calibration and validation sets using the inverse least squares regression model.

5.6.3 Binary Representation of Processing Models

Spectral processing models, pre-processing options and wavelengths of interest were encoded in a string of binary digits. In the first portion six pre-processing steps were encoded. Each pre-processing step was encoded in a sequence of 14 binary digits, using a Gray coding scheme to encode the various required parameters. The bitstring encoding scheme is shown in Figure 5.1. In each pre-processing string: 4 bits were used to select the type of pre-processing function to be applied, 1 bit was used to select the dimension along which the step should be performed (when applicable), 5 bits to encode the width of the smoothing window as an integer number between 1 and 32, and the next 4 bits to encode the derivative gap as an odd integer between 3 and 33. In

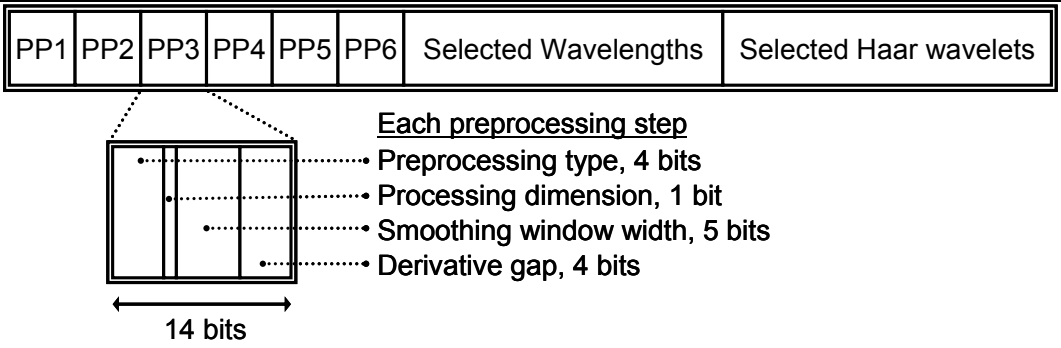

Figure 5.1: Bitstring representation diagram

the next portion of the genetic vector, a bitstring mask was used to select spectral wavelengths for score calculation. The wavelength selection string included one element for each wavelength in the original spectrum, where bits set to 1 indicated that the corresponding wavelength was to be selected. In the final portion of each genetic vector was an alternate bitstring mask to be used for calculating the score value in the place of the spectral bitstring mask when Haar wavelets were enabled in the pre-processing options.

5.6.4 Regression Fitness Function

Regression model fitness was evaluated based on mean square error (MSE), using several penalty functions based on differences in model size.[214] Spectral calibration data with known chemical concentrations were used to build an inverse least squares model for estimation of validation sample concentrations in each cross-validation set. Mean square error was calculated from the difference between known

and estimated validation sample concentrations. Fitness penalty functions incorporated combinations of the number of pre-processing steps and number of wavelengths selected to reduce the number of degrees of freedom when computing MSE. For reference, an initial series of model selection runs applied no model-size penalties. Next, degrees of freedom were decreased by the number of wavelengths included in the model. Finally, both the count of pre-processing options and number of wavelengths were used to penalize the MSE. Statistical distributions of model complexity based on the number of selected wavelengths have previously been examined in this way. However, assignment of penalties based on pre-processing options is not as well developed. For example, consider the use of a smoothing function. Using a smoothing function with a window of 3 effectively triples the number of wavelengths having influence on the regression model estimates. However, model complexity using smoothing does not increase by the same amount as it would with inclusion of three times the number of wavelengths for regression because of spectral collinearity. The statistical distribution and degrees of freedom are not well defined for use with various pre-processing options. Each selected pre-processing option constrains the model, and we opted to

treat each selected pre-processing option as reducing the number of degrees of freedom by one. Equations for the three cases are as follow:[214]

$$MSE = \left(\frac{SSE}{n} \right)^{0.5} \quad (5.1)$$

$$MSE = \left(\frac{SSE}{n - (N_{wl} + 1)} \right)^{0.5} \quad (5.2)$$

$$MSE = \left(\frac{SSE}{n - (N_{wl} + N_{pp} + 1)} \right)^{0.5} \quad (5.3)$$

where MSE is the mean square error, SSE is the validation sum of squared errors, n is the number of validation samples, N_{wl} is the count of wavelengths included in the regression model, and N_{pp} is the number of spectral pre-processing steps employed.

The best models were compiled from the multiple GA runs. In this way, a comparison of best fit results for each parsimony implementation provides a reliable comparison of optimization properties.

5.6.5 Classification Fitness Function

Classification models were based on a Bayesian class assignment using score values (S) determined using an inverse least squares linear regression with pre-processed data at the selected wavelengths the spectral wavelengths selected. Score values were calculated in the same

way that regression models estimated component concentration, except the inverse least squares regression was used to estimate known classification categories (0 or 1) instead of known concentrations.

Gaussian functions were fit to the score estimates of the calibration samples in each known class. The fitted functions were used to approximate the regression score distributions of each class as follows (shown in Figure 5.7):

$$p(S \mid A_i) = e^{-0.5\left(\frac{S - mean(S_i)}{std(S_i)}\right)^2} \qquad (5.4)$$

where $p(S|A_i)$ is the probability of the score given membership in class i, based on the calibration data (S regression score distributions are determined for each class from the calibration data set). Bayesian classification models were constructed from these score distributions. Validation sample classes were independently estimated from the regression scores using Bayes theorem. Bayes theorem states:[218]

$$p(A_i \mid S) = \frac{p(A_i)p(S \mid A_i)}{\sum_i (p(A_i)p(S \mid A_i))} \qquad (5.5)$$

The classification regression scores were used to estimate the class (A_i, either 0 or 1). From the calibration data, the prior probability is determined from the number of samples in each calibration class, $p(A_i)$. The evidence is the sum of all the weighted probabilities in the data, $\sum (p(A_i) \cdot p(S|A_i))$.

Score distributions for each class were estimated using the fitted Gaussian functions. Validation samples were assigned to the class with the highest posterior probability, $p(A_i|S)$, as calculated from Equation 5.5. This approach can was applied for 2-classes, and can be extended to *n*-classes. Posterior probabilities were further used to compute a likelihood measure, according to:

$$L = \sum_i -\ln\left(A_i \cdot p\left(A_i \mid S\right)\right) \qquad (5.6)$$

where L is the log-likelihood, A_i is the known class number (eg. 1 or 0), $p(A_i|S)$ is the probability of membership in class i based on the measured score value. Log-likelihood provides a measure of classification error where likelihood is a positive real number. Smaller likelihood values indicate better model fitness.

To penalize classification models for complexity, three methods were used. Penalties were based on the integrated log-likelihood probability of correct assignment with a general form:[216]

$$\text{fitness} = 2 \cdot L + a(n) \cdot m \qquad (5.7)$$

where L is the log-likelihood of the model, *n* is the number of samples under test, a(n) is a penalty function dependant on the number of samples. The number of model parameters, m, was either set to account for the number of selected wavelengths, or to incorporate both the number

Name	a(n)	Formula
Likelihood	0	2·L
AIC	2	2·L + 2·m
SIC	log(n)	2·L + log(n)·m

Table 5.1: Classification parsimony functions

of wavelengths and pre-processing steps selected. In Table 5.1, the three classification parsimony functions examined are listed.

First, classification models were developed using Likelihood without a parsimony penalty by setting a(n) to 0. Second, Akaike's Information Criterion (AIC) was tested where a(n) was set to 2. Using AIC fitness is penalized by 2 with each additional parameter. Third, Schwarz's Information Criterion (SIC) was examined, where a(n) was set equal to log(n). In this final case, the penalty for each selected parameter was scaled to account for changes in the number of test samples. Scaling the penalty value can be used to compensate for the increase in log-likelihood error with increasing numbers of samples.

5.6.6 Selection of Models

As a quasi-random search process, no single execution of a genetic algorithm is guaranteed to select the best possible model. Instead the genetic algorithm was run several times, and best results for each model size were selected from the aggregated results. To allow direct comparisons, parsimony-free fitness values were calculated and stored in addition to the parsimony-penalized fitness. Statistical methods were applied to select a model for each number of pre-processing steps. Least complex models showing statistically significant improvement over all simpler models were selected. Statistical comparisons for regression models were based on the f-test to compare between MSE values, while classification models were compared using the chi-squared test to evaluate differences between log-likelihood values. Best fit models for each pre-processing scheme were then compared. Among the several models selected for comparison, some use many more or many fewer regression parameters than required and can be rejected. A final processing model is selected from the remaining models based on results of the validation data. Remaining models should also be examined graphically, to ensure that selected wavelengths map to spectral features, and to ensure that cross-validation iterations show consistent results.

Examples of graphical results are shown in Figures 5.3, 5.4, 5.6, 5.7, and 5.8. Figures 5.3 and 5.6 both show the selected regression parameters and calibration weightings along with the pre-processed spectra. Because of shift and transformation in the spectral axis as a result of the various pre-processing options, selected wavelengths may not correspond perfectly to expected spectral features. However, selected wavelengths must correspond to portions of the pre-processed spectrum that contain information about the property under study. Some selected features may represent background offset corrections, and others should map to regions with spectral features. Calibration coefficients weighted inconsistently between cross-validation steps indicate that a model is too large, and may be adapted to noise rather than analyte signal. Figure 5.4 shows results from the optimal processing model for estimating blood lactate content from *in vivo* NIR spectra measured through the fingernail. Figure 5.7 shows the distributions of classes in the calibration and the associated Gaussian probability distributions. Figure 5.8 shows results from the optimal model for assignment of starch class membership from infrared spectra. Models displaying inconsistency were rejected.

5.7 Test Data

Two sets of data were examined to test the use of the regression and classification genetic algorithm.

5.7.1 Regression Data Set

Near-infrared reflectance spectra for in-vivo measurement of lactate were examined.[95] Spectra were recorded from 1000 to 2500 nm with a 16 cm^{-1} resolution, using an FT-NIR spectrometer to sample light diffusely reflected from the fingernails of ten adult subjects.[95] Spectra and reference blood samples were acquired at four intervals before, during and after a 30-second sprint on a modified isokinetic cycle. Reference blood lactate concentrations were measured from the reference blood samples. From partial least squares regression analysis, using the region of the spectrum from 1500 to 1750 nm, lactate concentration was determined with a standard error of cross validation of 2.21 $mmol \cdot l^{-1}$ and a correlation coefficient of 0.74.

5.7.2 Classification Data Set

Mid-infrared spectral data for classification of starches were provided by Dr. Pierre Dardenne and Dr. Juan Antonio Fernández Pierna from the Walloon Agricultural Research Centre in Gembloux (Belgium).[217, 221] Spectra from 215 starch samples were recorded from 4000 to 600 cm^{-1} at a 3.51 cm^{-1} (967 points) resolution using a FTIR spectrometer equipped with an ATR probe. This data was the subject of the 'Chimiometrie 2005' contest. Starches were grouped into 2 classes, with 107 and 108 members in each respective class. As a result, the two classification groups were approximately equal in size.

5.8 Results and Discussion

Multiple linear regression and Bayesian classification models were selected for processing two datasets using the genetic algorithm

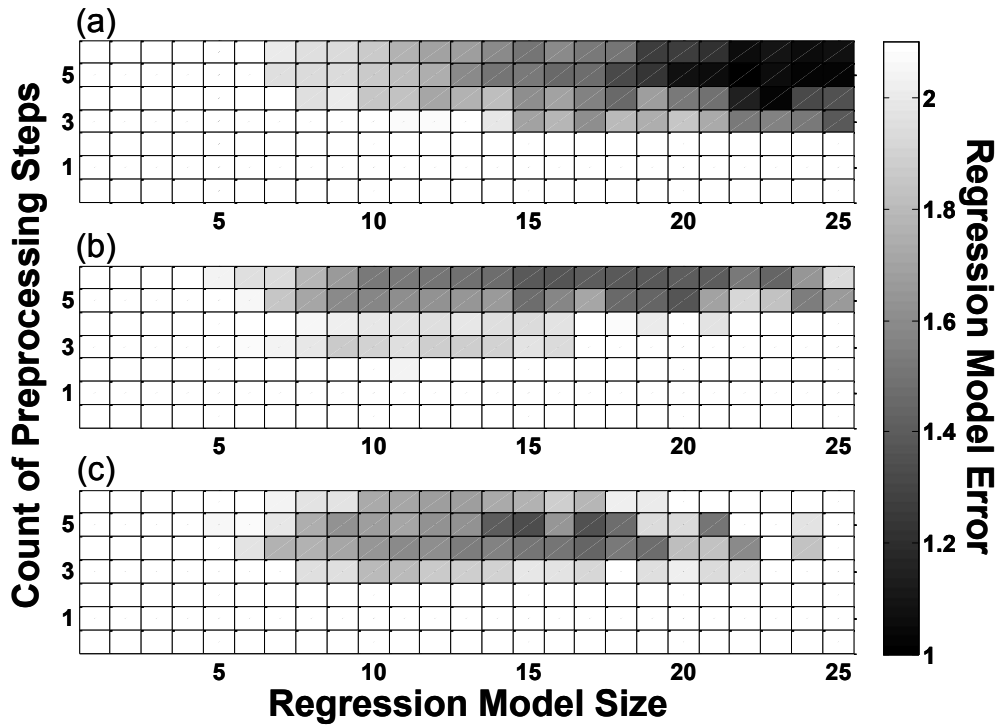

Figure 5.2: Models for determining lactate concentration from NIR spectra were selected by a genetic algorithm. Results are presented as model error (grayscale intensity) for each model size and complexity (position). Dark regions indicate low model error, or good models. Bright regions show high model error and indicate poor models. In the Figures optimization results are shown: (a) without parsimony, (b) using parsimony for the number of wavelengths selected, and (c) using parsimony for both the number wavelengths and pre-processing steps selected.

described above. Different methods of generating parsimonious models were tested to examine effects of parsimony functions on model selection. In each case the genetic algorithm used identical optimization code, with different fitness functions for development of regression and classification models. Classification and regression genetic algorithms sorted and searched based solely on model fitness. Figures 5.2 and 5.5 present results from the genetic algorithm using different parsimony functions with results sorted by model size and complexity. Parsimony methods cause the genetic algorithm to indirectly take into consideration model size. A direct comparison of non-penalized performance measures between different parsimony schemes was used to illustrate differences in optimization.

5.8.1 Regression Model Development

Best-fit models were identified from each parsimony function after the genetic algorithm was run 40 times using each regression parsimony criterion. A parsimony penalty was applied to the mean square error. Figure 5.2 displays the effect of regression variable and pre-processing steps parsimony on model fitness. Results were first obtained (a) without inclusion of parsimony, then (b) parsimony was taken into account through the number of selected regression variables, and finally (c) the number of

selected regression variables was combined with the number of pre-processing steps. As seen in Figure 5.2a, when parsimony penalties were not included the genetic algorithm selected models with many regression variable and pre-processing steps. The parsimony-free search resulted in large models, which also have the lowest error of all the methods explored. However, when the large models were examined, they were observed to fit noise in the data. Examining the cross-validation plots of selected regression parameters, similar to those shown in Figure 5.4, demonstrated that for large models selected parameters did not correspond to regions containing signal or differences in signal. Parsimonious models were developed using a penalty for the number of regression parameters based on traditional multivariate linear regression statistical analysis.[214] When parsimony was added to constrain the number of regression variables, as seen in Figure 5.2b, models with fewer regression variables were selected but the model retained many pre-processing steps. There was a slight increase in the global model error but a decrease in error for models with few regression parameters. Finally, parsimony for both the number of regression parameters and the number of pre-processing steps was used. Figure 5.2c shows the optimal model size was further reduced when the parsimony accounted for the number of

both regression variables and pre-processing steps. In this final case, models with fewer pre-processing steps were preferentially explored by the genetic algorithm because of the parsimony penalties. Larger models were also examined; however, parsimony penalties emphasized the development of small models. Use of both parsimony criteria constrained the algorithm to small models. As a result, the genetic algorithm did not search for solutions with large numbers of regression variables and pre-processing steps. Large models selected when using both parsimony criteria had higher error than models of corresponding size selected in the parsimony-free algorithm. In contrast, small models selected when using both parsimony criteria had lower error than models of corresponding size selected in the parsimony-free algorithm. The large models selected without parsimony had the lowest total error of all the models developed. However, these models were unnecessarily complicated. One potential disadvantage of using parsimony is a decrease in the selection of complex models with low error. This can be a problem because complex models can serve as intermediate steps in the evolution of simple models. Nonetheless, the most efficient model with fewest pre-processing steps, regression parameters, and lowest error was located using the parsimony

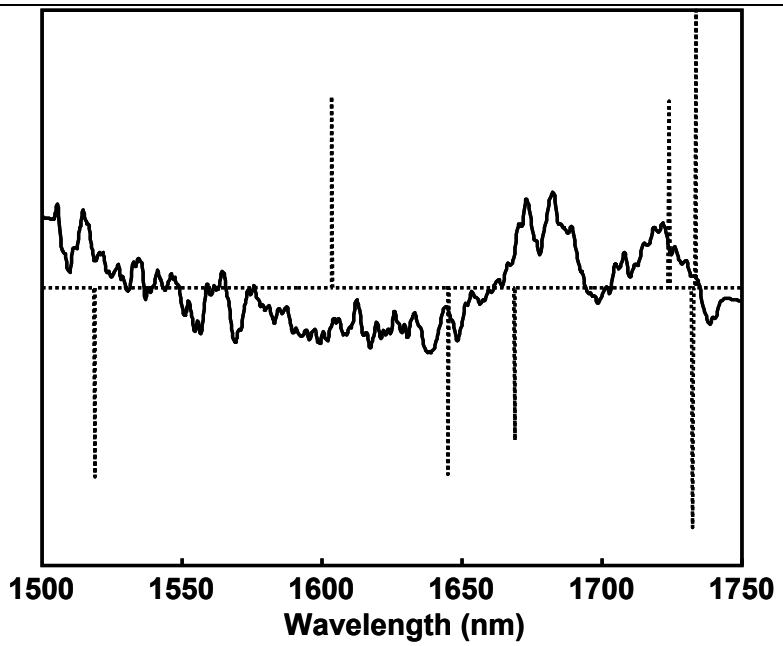

Figure 5.3: Pre-processed NIR spectra for lactate estimation from in-vivo fingernail reflectance spectra. Dashed lines mark wavelengths selected for regression and corresponding regression coefficient magnitudes. Four pre-processing options were selected: (1) derivatives were taken with smoothing window 10 and derivative gap 5, (2) spectra were normalized to area 1, (3) a linear detrend, and (4) spectra were scaled to a maximum value of one.

method taking into account both model size and pre-processing complexity.

Selected wavelengths and relative coefficient magnitudes are shown in Figure 5.3, overlaid on the pre-processed spectrum. We examined the best fit solutions at all combinations of wavelength and pre-processing step parsimony constraints on model error. There were 7

possible combinations of pre-processing step complexity (no steps to all six steps enabled), and 25 possible regression model sizes (inclusion of 1-25 wavelengths). Use of more than 25 wavelengths resulted in fitting of noise. A matrix of 7 by 25 models was compared. For each combination of pre-processing steps, a single model was selected. A statistical f-test was used to determine a statistical difference in regression error at a 95% confidence level, between models with increasing number of wavelengths. For each of the seven pre-processing step categories, one model was selected as significant Comparison of the absolute regression error, linearity, model size and consistency of regression coefficients was used to manually select the optimum model from among the 7 final models. A processing model using 7 wavelengths and 4 pre-processing options was selected. Results of the selected model are shown in Figures 5.3 and 5.4. Pre-processing steps were: (1) second derivative operation on each spectrum with a smoothing window of 10 and derivative gap of 5, (2) a normalization of each spectrum to a unit area, (3) a linear detrend of each spectrum, and (4) scaling to a maximum intensity of one of each spectrum. Wavelengths selected for analysis correspond to the primary lactate spectral features near 1670 and 1720 nm and regions of background intensity between 1550 and 1650 nm.

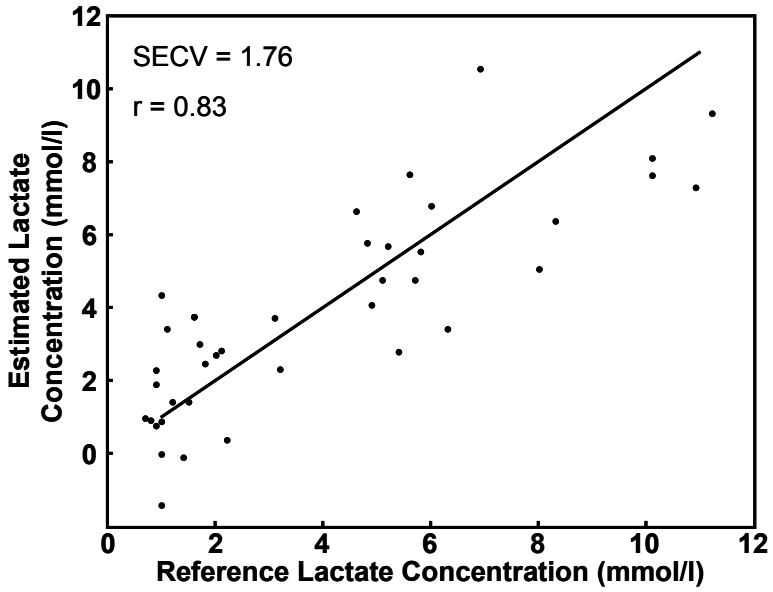

Figure 5.4: Lactate was estimated for 10 subjects using in-vivo NIR spectra versus a reference measure of lactate. Cross-validation using a 7-component multilinear regression model was used to estimate the lactate concentrations from spectral data between 1500 and 1750 nm; n = 40, r = 0.83, SECV = 1.76 mmol•l^{-1}. Regression estimates were determined from data at 1519, 1604, 1645, 1669, 1724, 1733 and 1734 nm.

Results using the linear calibration model selected by the genetic algorithm for estimation of lactate concentration are shown in Figure 5.4. Lafrance showed a 5-component partial least squares model to best estimate lactate concentration.[95] In comparison, the model selected by the genetic algorithm performed better, the standard error of cross validation decreased and coefficient of regression increased. Standard error decreased from 2.21 to 1.76 mmol·l^{-1} and the correlation coefficient

increased from 0.74 to 0.83. Sagacious use of parsimony constraints enabled selection of an improved model using a genetic algorithm. As shown in the estimation of lactate concentration from NIR spectra, a generic parsimony penalty incorporating both number of wavelengths and pre-processing complexity resulted in an improved model.

5.8.2 Development of Classification Models

The effect of using different parsimony measures on the selection of classification models is presented in Figure 5.5. Results for each parsimony method were determined by selecting the best models identified from fifteen executions of the genetic algorithm. Parsimony criteria were based on penalization of log-likelihood for the model size using either the Akaike Information Criteria (AIC) or Schwarz' information criteria (SIC), as previously explained in the methods section. Maps of log-likelihood for models with different numbers of included regression parameters and pre-processing options are shown in Figure 5.5, where non-penalized log-likelihood values are displayed for comparison.

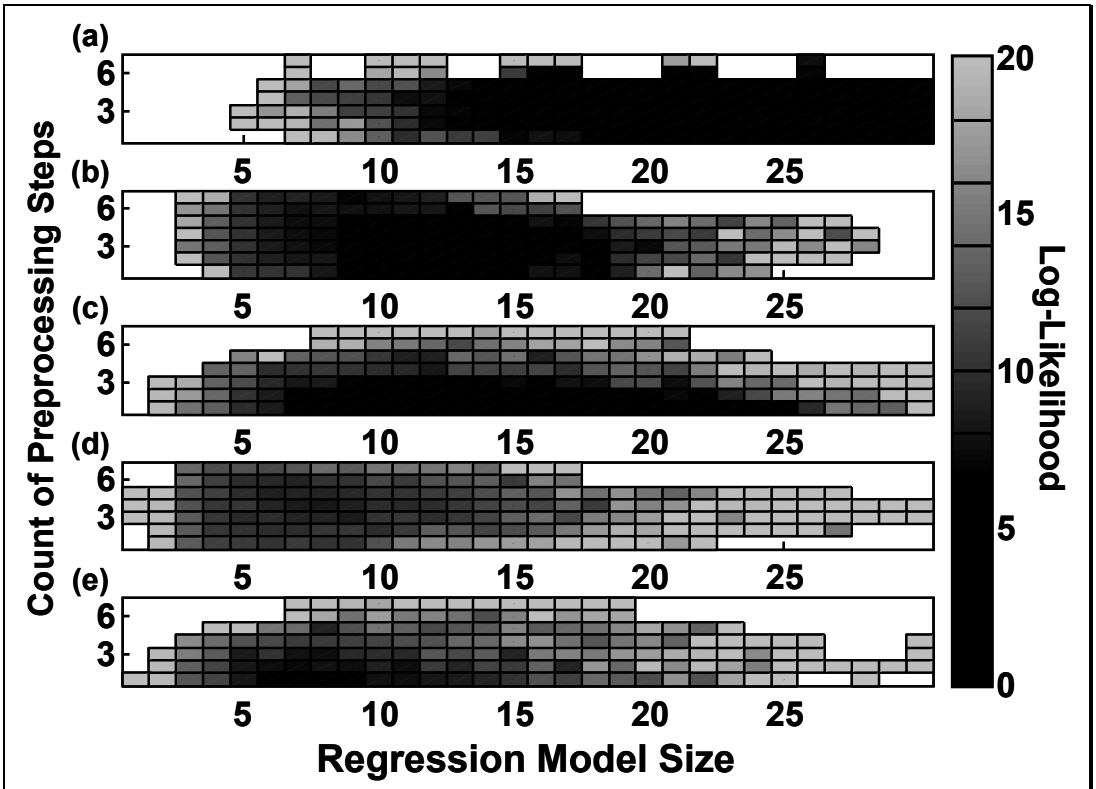

Figure 5.5: Regions with different model properties were optimized by the genetic algorithm based on the implementation of parsimony. Dark regions indicate low log-likelihood, or good models. Bright regions show high log-likelihood and indicate poor models. Genetic algorithms with no penalties on model size develop complex models to find models with the lowest possible error. In the Figures optimization results are shown (a) without parsimony, (b) using AIC parsimony for the number of wavelengths selected, (c) using AIC parsimony for both the number wavelengths and pre-processing steps selected, (d) using SIC parsimony for the number of wavelengths selected, (e) using SIC parsimony for both the number wavelengths and pre-processing steps selected.

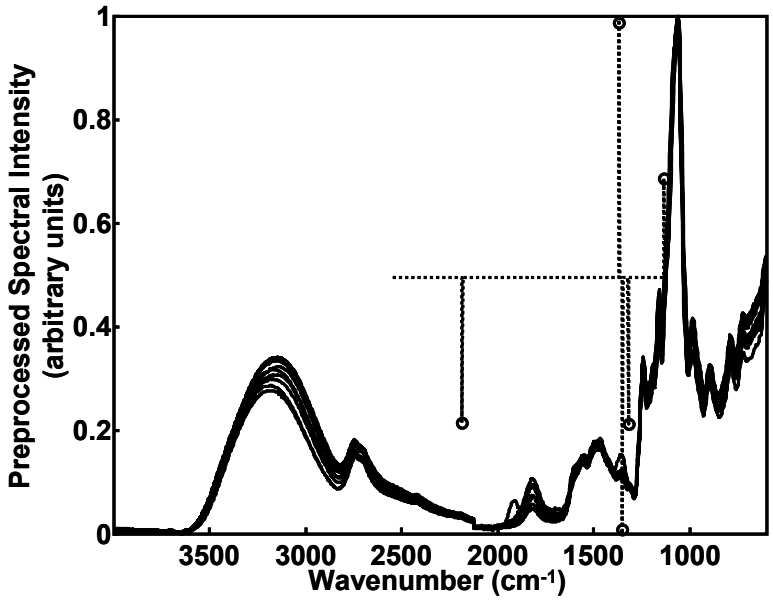

Figure 5.6: Pre-processed starch spectral data, with the normalized regression coefficients shown as dashed lines to indicate the portions of the spectrum selected for analysis. No pre-processing options were selected in the optimal model. Data at 1133, 1329, 1352, 1369 and 2185 cm^{-1} were selected for developing the classification score.

Similar to the comparisons for the regression model penalties, classification models were initially developed without penalization for model size (as measured by the number of wavelengths) and complexity (as measured by the number of pre-processing steps). Classification models were also developed using AIC to penalize fitness based on only the model size or a combination of the model size and complexity, as shown in Figures 5.5b and 5.5c respectively. Finally, classification models were developed using SIC, using either the model size or a combination of the model size and complexity, as shown in Figures 5.5d and 5.5e.

Schwartz's information criterion uses a penalty scaled by the number of samples used for testing the model. This penalty biased the search towards the selection of small models and prevented models with moderate complexity from being fully exploited. Using the Akaike information criteria small models were emphasized over very large models, while still exploring intermediate models. In the fitness maps in Figure 5.5, shifts in model exploration result in shifts in the dark basin representing the best models located. Without parsimony, large complex models are selected. When parsimony measures based on model size are included in the genetic algorithm, optimal models requiring fewer wavelengths are found. When constrained with both model size and

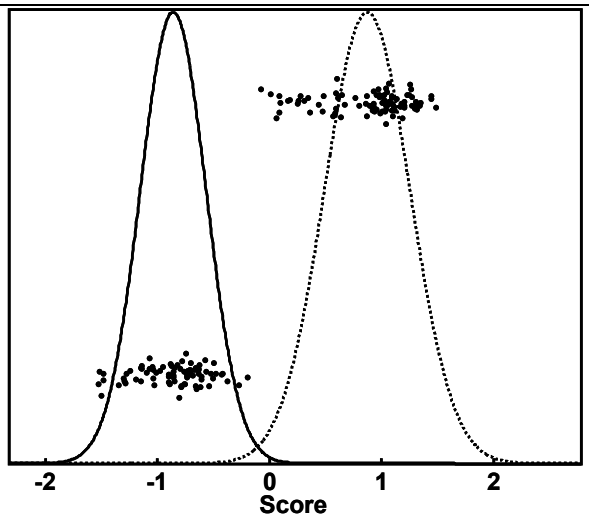

Figure 5.7: Gaussian functions fitted to the score values in the calibration data. Score values developed from spectra of two classes of modified starches are shown. Score estimates from the multilinear regression are plotted along the x-axis, with the first class plotted as a solid line, and the second class plotted as a dashed line. Points are offset vertically to indicate known classifications.

complexity, the genetic algorithm finds optimal solutions requiring fewer pre-processing steps.

Models selected by the genetic algorithm under different parsimony constraints were examined. As was done for the regression model, a matrix of 7 by 30 models was compared. An optimal model was found for each number of enabled pre-processing steps by comparing models using different numbers of wavelengths. Chi-squared statistical comparison was used to select the most complex model with a significantly lower log-

likelihood than all the less complex models. Using AIC parsimony less complex processing models were selected than without parsimony. The best fit model was determined using AIC to implement parsimony penalizing for both the number of selected wavelengths and pre-processing options. Pre-processing steps were not required for sample classification. A subset of the raw spectra is shown in Figure 5.6, along with the wavelengths selected for evaluation of score values and the relative coefficient weightings of the wavelengths. Spectral intensities and coefficient weightings have been scaled for display purposes. From the score values associated with the calibration data, Bayesian classification probabilities were developed.

Figure 5.7 shows Gaussian functions fitted to the score values for data in each known class. From the two Gaussian functions and the number of data points in each class, the class membership probability distribution was developed. Figure 5.8 shows the classification assignment using the score value to determine the probability. From the 215 samples examined by cross-validation, three were incorrectly classified, as indicated by arrows. Samples were classified with an accuracy of 98.6%. Selection of a simple model using the genetic algorithm was improved by

the application of the AIC parsimony method taking into account both the number of selected wavelengths and pre-processing steps.

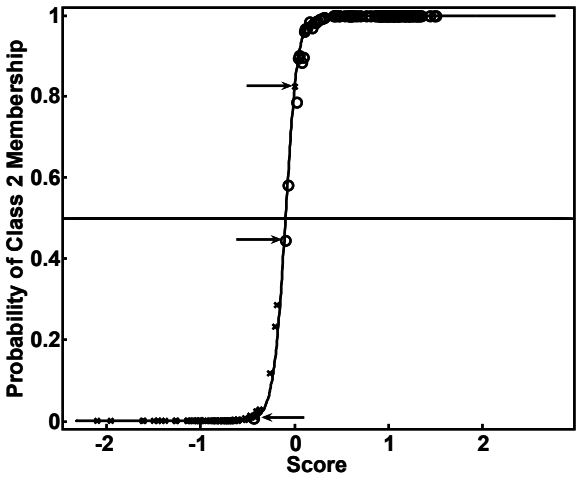

Figure 5.8: Bayesian class estimates, showing the estimated likelihood that a given test sample belongs to class 2. Two samples are incorrectly estimated as belonging to class 1, and one sample is incorrectly estimated as belonging to class 2. Incorrectly classified cross-validation samples are indicated with arrows. In the plot classifications class assignments for the 215 samples are shown as calculated using cross-validation with 5 groups of 43 samples.

5.9 Conclusions

Incorporation of generalized parsimony constraints in a non-generational genetic algorithm was demonstrated for spectroscopic data in quantification and classification modeling. Generalized parsimony for selection of regression models was implemented using an adjusted

RMSE, while parsimony for selection of classification models was implemented using penalized log-likelihood. Model size was measured by the number of wavelengths, and model complexity was measured by the number of pre-processing steps. When unconstrained, the genetic algorithm was shown to search for large, complex models. Single parsimony using only the number of wavelengths was effective in directing the search algorithm towards exploration of smaller models. Likewise, dual parsimony using both the number of wavelengths and pre-processing steps resulted in optimization of models with fewer wavelengths and also fewer pre-processing steps. The constrained algorithm returned solutions with slightly more error, but successfully located smaller models not identified without parsimony constraints. The quality of small models is very important for practical reasons, while much larger models are less useful. Other than as intermediate solutions, very complex models will not likely find practical application. We found that dataset independent parsimony functions affected these two data sets in a similar manner, resulting in the selection of simple processing models.

5.10 Acknowledgements

Funding for this research was provided by the National Science and Engineering Research Council of Canada (NSERC). The authors thank

Dr. Pierre Dardenne and Dr. Juan Antonio Fernández Pierna from the Walloon Agricultural Research Centre in Gembloux (Belgium) for providing the starch data,[217] and Dr. Royston Goodacre of the Institute of Biological Sciences, University of Wales, Aberystwyth for additional data used in testing the algorithm.[212] Finally, the authors would also like to thank Karen Esmonde-White for editorial comments.

Chapter 6. Estimation of Myoglobin Oxygen Saturation from Spectra of Cardiac Tissue using Multivariate Curve Resolution

Improvements to spectroscopic quantification in turbid media have been demonstrated using novel instrumentation and data processing methods. In the previous chapter, a novel method for applying parsimony in the selection of processing models using a genetic algorithm was demonstrated. In particular, a regression-based data processing model was identified with a 41% reduction in regression error as compared to the best user-developed model. Genetic algorithm based development of data processing models are most useful where calibration conditions are consistent with validation and usage conditions.

In systems where the chemical environment is expected to vary from the initial calibration conditions, self-adapting methods can be used to compensate for changes. Multivariate curve resolution techniques are one such example of self-adapting methods. In multivariate curve resolution the measured data is used to directly estimate the signal response and sample composition.

In this chapter a method for adaptively modelling tissue spectra is presented. Spectral features in biological systems are not identical to spectral features of the isolated components. Reasons for this include the pH of the chemical environment, the multitude of interactions, and the spectral transformations caused by light scattering. To improve quantification in biological systems, multivariate curve resolution can recover the analyte concentrations and pure component spectral profiles. In this chapter we describe a novel application of multivariate curve resolution for estimating myoglobin oxygen saturation in cardiac tissue. Matlab code for the MCR routine described here is provided in appendix D. A brief introduction to multivariate curve resolution is presented prior to the main manuscript.

6.1 Multivariate Curve Resolution

Multivariate curve resolution (MCR) refers to a family of data processing techniques used for simultaneous determination of concentrations and pure spectra of mixtures based on perturbations in the data.[223] One member of the MCR family is alternating least-squares multivariate curve resolution (MCR-ALS), based on an alternating series of least squares concentration and spectral profile estimates.[224] Central to the alternating least squares algorithm are constraints for bounding

solutions within physically relevant limits. Constraints are used to mathematically resolve the chemical components.[225, 226] MCR algorithms typically use constraints such as closure, non-negativity, selectivity, normalization, and equality.[227, 228] Selections and implementations of constraints are the primary differences between MCR-ALS algorithms.[224] Spectral data is normally assumed to be non-negative, as are chemical concentrations. However, in tissue spectroscopy second derivatives are commonly taken as a data pre-treatment step. When derivatives are taken, spectral intensities can assume negative values. Non-negativity cannot be used as a constraint when processing derivative spectra. Likewise concentration closure is no longer applicable when spectral backgrounds are subtracted because some spectral contribution from each species may be lost. Pre-processing steps must be carefully selected to ensure that constraints chosen for the MCR remain applicable.

An initial starting point must be supplied to MCR algorithms. The similarity of the starting guess to the true component is important, and influences the results of the MCR algorithm. Suitable starting points can include principal component spectra as derived from singular value decompositions, or better yet, measured spectra of the isolated components. In addition to estimated spectra, the total number of

components present in the mixture must be supplied to the MCR algorithm. Methods suggested in the literature include use of prediction error sum of squares plots (scree plots) examining the residual error from fitting varying numbers of principal components to the experimental data. MCR algorithms use systematic variations in the data to isolate signal contributions from different species, and so data should include independent variations between components. If components have spectra or concentration profiles that are too similar, a lack of selectivity can lead to significant ambiguity in the MCR solutions.[229]

Multivariate curve resolution techniques allow for the determination of both the concentrations and the spectral profiles for each component in a mixture, given a suitable starting point. By allowing an MCR routine to determine the optimal spectra directly from measured data, pure component spectra are estimated for the relevant chemical environment. Absolute chemical concentrations are not determined from the MCR algorithm because of scaling constraints. Instead, relative composition is determined and can be related to absolute concentration using known system properties.

6.2 Manuscript

Estimation of Myoglobin Oxygen Saturation from Spectra of Cardiac Tissue using Multivariate Curve Resolution

Authors:

Francis W.L. Esmonde-White, Lorilee S.L. Arakaki,

Kenneth A. Schenkman, Wayne A. Ciesielski, David H. Burns

6.3 Abstract

A method for adaptive modeling of spectra from tissue for myoglobin oxygen saturation was developed. The multivariate curve resolution (MCR) technique was compared with a classical least squares method for estimation of myoglobin oxygen saturation in simulated and biological cardiac tissue. Tissue simulations with fixed and variable hemoglobin concentrations were examined to compare the performance of the techniques under different conditions. Myoglobin saturation estimates using MCR with variable hemoglobin composition were shown to decrease estimation error by 75% compared to least squares estimates. The range of myoglobin saturation required for MCR to function was examined. Results show that the spectral data set must include myoglobin saturation values that vary from at least 85% to 100% for myoglobin oxygen saturation calibration using MCR. Myoglobin oxygen saturation endpoints

in 9 guinea pig hearts were estimated from spectra using MCR and classical least squares. Results showed saturation estimates using MCR to be better than estimates using classical least squares. Endpoints at the 100% level were estimated to be 89 +/- 4% using MCR as compared to 199 +/- 54 % using classical least squares. MCR provides a means for practical measurements in clinical settings.

6.4 Keywords

Multivariate curve resolution, MCR, self-modeling curve resolution, SMCR, myoglobin oxygen saturation

6.5 Introduction

Visible and near-infrared spectroscopic measurements in living tissue are routinely used to measure blood oxygenation.[128-130] Pulse oximetry uses distinctions between the absorption spectra of deoxyhemoglobin (Hb) and oxyhemoglobin (HbO_2) to rapidly measure blood oxygen saturation. Spectroscopic difference measurements between the systolic and diastolic moments, while the heart is beating and at rest, enable a hemoglobin-selective oxygen saturation measurement. However, pulse oximetry measurements cannot be used to measure oxygen saturation within cells, where oxygen is ultimately consumed.

Myoglobin is present in skeletal muscle and the heart. Measurement of myoglobin oxygen saturation in cardiac tissue has the potential to provide information about intracellular oxygenation during surgical procedures. Standard imaging modalities, such as magnetic resonance imaging, that are widely used to measure oxygen content in blood or tissue may not be compatible with the small spaces in a surgical suite or may not adequately discriminate tissue from blood. Visible-near-infrared (VIS-NIR) spectroscopy is currently explored as a measurement of myoglobin oxygen saturation. Spectroscopic systems are relatively small and resulting spectra can be used to quantify oxygen content in blood, tissue or both. The high spatial resolution and specificity of VIS-NIR spectra can be used to distinguish normal arterial perfusion from regional ischemia and show areas of low, medium, and high deoxygenation during reperfusion of cardiac tissue.[88]

Spectroscopic methods for measuring hemoglobin oxygen saturation noninvasively have widely been reported.[125, 134, 230] Hemoglobin oxygen saturation in arterial blood can be measured by taking the spectral difference between points of maximum and minimum blood volume during the cardiac pulse to isolate the spectral contribution of red blood cells from surrounding tissue. However, the same method cannot be applied to

spectral measurements of myoglobin oxygen saturation in cardiac and skeletal muscle because myoglobin concentration does not change rapidly within muscle cells. The similarity of myoglobin and hemoglobin NIR spectra further complicates measurements of myoglobin oxygen saturation (S_{Mb}). More complex processing methods than used in pulse oximetry are utilized for determination of relative deoxymyoglobin (Mb) and oxymyoglobin (MbO_2) concentrations. Myoglobin oxygen saturation within tissue can be calculated from the relative deoxymyoglobin and oxymyoglobin concentrations, indicating the intracellular oxygen partial pressure.

Methods have been reported for spectroscopic measurement of S_{Mb} in the presence of hemoglobin *in vitro* both without scattering,[120] and also in the presence of scattering.[153, 231] In addition to *in vitro* studies, myoglobin oxygen saturation has been measured spectroscopically under *ex vivo* and *in vivo* conditions by perfusing tissue with a buffer solution to remove hemoglobin interference.[101, 232, 233] Calibration spectra are required with classical least squares (CLS) and partial least squares (PLS) to determine S_{Mb} for samples at intermediate oxygen saturations. Unfortunately, calibration spectra cannot be measured in tissue. Instead, *in vitro* calibrations developed with PLS can be transferred and used for *ex*

vivo and *in vivo* measurements with scattering and hemoglobin interference.[97, 234] Using PLS, calibrations require spectra to be collected at 0% and 100% O_2 saturation for scaling the data to account for differences between samples.[97] Physical manipulations such as occlusion of blood flow to tissue and manipulations of the inspired air oxygen content have been performed to reach 0% and 100% O_2 saturations. Manipulations for calibration such as these are impractical for measurements in a surgical setting because myoglobin oxygen saturation should not reach the limit values under normal physiological conditions.

Spectroscopic measurement of S_{Mb} is further complicated because spectra of individual components are imperfectly known, because reference S_{Mb} calibration values are not available, and because light scattering causes nonlinear transformations between spectra measured with and without scattering.[235] Reference spectra are measured from purified samples and can include a scatterer. Differences in scattering between spectra of reference and test samples lead to fitting errors in the data processing. Light scattering varies between individuals, and over time also varies within each individual.[236] Because of these variations, scattering is problematic even when calibrations are obtained directly from

tissue. Spectra for each individual subject may be acquired over short time periods to minimize temporal variations in light scattering.

Multivariate curve resolution (MCR) is used to isolate pure component spectra and pure component compositions from a series of spectra.[237, 238] MCR allows scattering-transformed spectra to be estimated directly from *ex vivo* or *in vivo* tissue spectra. Estimation of component concentrations using scattering-transformed spectra, instead of using reference spectra measured *in vitro* as in CLS and PLS, should improve least squares estimates of component concentrations. MCR has been demonstrated to mathematically isolate pure component spectra from mixtures of multiple components with varying sample composition in recorded spectral data.[223, 239, 240] Components are isolated by MCR using constraints such as closure, non-negativity and normalization to limit the range of valid solutions.[239, 241] MCR is particularly useful in systems where physical limitations prohibit measurement of isolated pure component spectra. Examples include species present in equilibria which can never be completely isolated and living tissue where reference spectra may be inaccurate if recorded outside the scattering environment.[237, 238, 242]

In this paper, we report the application of MCR to measurement of myoglobin oxygen saturation using VIS-NIR spectra of cardiac tissue

perfused with red blood cells. Pure spectra and relative concentrations of Mb and MbO_2 were estimated by the MCR algorithm, using *in vitro* spectra of myoglobin and hemoglobin measured at 0 % and 100 % oxygen saturations for initial estimates of pure component spectra. Estimated myoglobin concentrations were then used to calculate S_{Mb}. Analysis using the MCR method was compared to a classical least-squares (CLS) analysis method by examining simulated tissue spectral data and spectra acquired from cardiac tissue. Simulated tissue data were also used to examine effects of the sampled oxygen saturation span on MCR analysis accuracy.

6.6 Theory

Multivariate curve resolution refers to a family of data processing techniques used for simultaneous determination of concentrations and pure spectra of mixtures based on perturbations in the data.[223] One member of the MCR family is alternating least-squares multivariate curve resolution (MCR-ALS), based on a series of alternating least squares estimates of composition and spectral components.[224] Constraints are used to mathematically isolate the chemical components by providing boundaries to limit the possible solutions.[225, 226] Constraints typically used in MCR algorithms include closure, non-negativity, selectivity,

normalization, and equality.[227, 228] Selections and implementations of constraints are the primary differences between MCR-ALS algorithms.[224] Spectral data are normally assumed to be non-negative, as are chemical concentrations. However, in tissue spectroscopy, second derivatives are commonly taken as a data pre-treatment step. When derivatives are taken, spectral intensities can assume negative values and non-negativity cannot be used as a constraint. Likewise, concentration closure is no longer applicable when spectral backgrounds are subtracted because some spectral contribution from each species may be lost. Pre-processing steps must be carefully selected to ensure that constraints chosen for the MCR remain applicable.

We have adapted MCR for analysis of myoglobin oxygen saturation from visible spectral data. Three general algorithm components are required. A core alternating least squares algorithm is necessary for repeatedly estimating concentrations and spectral profiles. This algorithm must maintain component ordering and determine when to terminate the optimization. A non-negativity constraint for limiting solutions to chemically relevant values is also necessary. Non-negativity is not applicable to spectral component estimates because second derivatives were taken as a data pre-processing step. Last, closure is used to relate the final

chemical composition estimates to relative concentration values. S_{Mb} is then calculated from the relative concentrations.

Relative myoglobin and oxymyoglobin concentrations were first estimated using an MCR-ALS routine, based in part on the algorithm by Tauler et al.[227, 243] Spectral profiles and concentrations were repeatedly estimated through a series of alternating least-squares computations with constraints applied at each iteration. Classical least squares estimations based on Eq. 6.1 are central to MCR-ALS algorithms:[224]

$$\mathbf{X} = \mathbf{CS} + \mathbf{E} \qquad (6.1)$$

Concentration (**C**) and spectral (**S**) estimates in MCR-ALS are repeatedly estimated from recorded spectral data (**X**), while minimizing the error matrix (**E**). In order to determine concentrations from spectral estimates and the measured data, Eq. 6.1 can be rearranged as:

$$\mathbf{C} = \mathbf{XS}(\mathbf{SS}^{T})^{-1} \qquad (6.2)$$

Equation 6.1 can also be rearranged to solve for spectral estimates using concentration estimates and the measured data:

$$\mathbf{S} = \mathbf{X}^{T}\mathbf{C}(\mathbf{C}^{T}\mathbf{C})^{-1} \qquad (6.3)$$

To begin the ALS routine, initial pure component spectral estimates must be provided. Convergence of MCR is dependent on both the selection of an appropriate number of components and similarity of initial

spectral estimates to the true spectra. Random guesses, principal components, or measured pure spectra may be used to initialize MCR routines. When random guesses are used, spectral ordering is undetermined and MCR is more likely to become trapped in local minima. Principal component analysis will yield orthogonal component estimates, and is not suitable for estimating spectra of highly collinear components such as hemoglobin and myoglobin. Throughout the present work, pure component spectra measured in the presence of scattering were taken as initial spectral estimates.

Spectral profiles from each component, as estimated from Eq. 6.3 during iterations of the ALS routine, were normalized to unit vector length to avoid intensity ambiguities. To ensure that the ordering of pure spectral components did not change, estimated spectra were compared to the initial spectra using a similarity measure.[227, 242] If necessary, spectra were reordered to preserve the relationship between chemical component and position in the initial spectral estimates. If component ordering was not maintained, components in the final algorithm solution would not have a defined correspondence to the pure chemical components.

While chemical concentrations are always positive, mathematical least squares estimates of concentration (Eq. 6.2) are not necessarily

positive. To constrain estimated concentrations to positive values, a soft non-negativity constraint was implemented. Several methods are commonly used to implement non-negativity, including non-negative least squares (NNLS), hard constraints, and soft constraints. We implemented a novel hard non-negativity boundary constraint, where concentrations approaching negative values were constrained to positive numbers. A transformation threshold (t) was calculated as the maximum magnitude of the concentration vector divided by the total number of values. All regions in the concentration profile with magnitudes below the threshold were exponentially transformed, thereby constraining all concentrations to positive numbers:

$$C' = t \times 10^{(C-t)} \qquad (6.4)$$

Sequentially, all rows of the concentration matrix **C** were constrained to positive values by selecting each row (chemical species) as a concentration vector C. This transformation retained a shape similar to the original concentration profile, where t indicates the lower bound, and C is the concentration vector to be constrained to positive values (C').

Residual errors were calculated after each iteration of the MCR routine to determine when the MCR algorithm was to be terminated. Residual error was calculated as the difference between the original data

and data reconstructed from spectral and concentration estimates. Using singular value decomposition (SVD), a reference error was determined for the selected number of components to establish the minimum error attainable. Residual error of the least-squares estimates was normalized to the SVD-derived minimum error to provide a measure of convergence independent of the particular data used. As the algorithm converged, the residuals no longer changed appreciably between steps. The algorithm was stopped when the change in normalized residual error was less than 10^{-5}. Optimizing the four component myoglobin/hemoglobin system, the MCR algorithm typically terminated in less than 40 iterations, requiring a few seconds of computational time on a portable computer equipped with a dual-core 2.0 GHz processor and 2 GB of random access memory.

After the ALS optimization terminated, a closure constraint was used to scale the concentration estimates determined by the MCR to relative concentrations. Scaling is necessary for closure because of spectral normalization, which results in spectral magnitudes having undetermined concentration scaling. As a result, concentration estimates from different chemical species are seldom equally weighted. Closure constraints are used to determine relative concentrations between the chemical species using known relationships. Myoglobin concentration is

assumed to be constant over each experiment because myoglobin is contained within muscle cells and the total concentration should not change. Cytochromes might be treated similarly, but closure cannot be used for hemoglobin as blood flow varies in response to physiological events. A single positive non-zero closure constant (k) was calculated for each data set for which sum of the oxymyoglobin and deoxymyoglobin concentrations varied the least. The closure constraint, k, which minimized E(k) was selected:

$$E(k) = \text{std}(k \cdot [Mb] + [MbO_2]) \qquad (6.5)$$

E(k) is a measure of the variation in total myoglobin concentration. Myoglobin oxygen saturation (S_{Mb}) was calculated using:

$$S_{Mb} = [MbO_2] / (k \cdot [Mb] + [MbO_2]), \qquad (6.6)$$

Where k is the closure constant, $[MbO_2]$ is the estimated oxymyoglobin concentration, and [Mb] is the estimated deoxymyoglobin concentration. Because scattering transformed spectra are determined directly by MCR and because concentration is related using closure, tissue-specific endpoint spectra are not required for calibration or normalization.

6.7 Experimental

To evaluate the use of the MCR method for measurement of myoglobin oxygen saturation, both simulated and cardiac tissue spectra were examined. Tissue simulations, where oxygen saturation could be controlled, were developed to compare MCR and CLS estimates of S_{Mb}. The oxygen saturation range required for accurate MCR estimates of S_{Mb} was determined using tissue simulations. To demonstrate applicability in cardiac tissue, S_{Mb} was evaluated from spectra of guinea pig hearts measured *ex vivo* using the MCR method.

6.7.1 Simulated Data

Simulated data sets were created to investigate the performance of algorithms for estimation of myoglobin oxygen saturation under conditions applicable in tissue. Simulated tissue spectra were developed by summing second derivative diffuse reflectance spectra of Hb, HbO_2, Mb, and MbO_2 solutions recorded in scattering conditions.[135, 153, 231] Spectra from 450 to 950 nm with 1 nm resolution were recorded with addition of 2% Intralipid to simulate scattering.[135] The wavelength range from 450-650 nm was used in the analyses. Simulated tissue spectra comprised linear additions of oxygenated and deoxygenated myoglobin and hemoglobin spectra to obtain spectra with known intermediate saturations, with 1% added noise.

Hemoglobin Concentration	Processing Technique	S_{Hb}		S_{Mb}	
		RMSEP	r^2	RMSEP	r^2
Constant	MCR	0.15	0.95	0.13	0.88
	CLS	0.15	0.95	0.33	0.93
+/- 10%	MCR	0.13	0.96	0.08	0.97
	CLS	0.13	0.96	0.32	0.93

Table 6.1: Residual error (RMSEP) and linearity (r^2) for estimations of hemoglobin (S_{Hb}) and myoglobin (S_{Mb}) oxygen saturations determined using Multivariate Curve Resolution (MCR) and Classical Least Squares (CLS) from simulated spectra. Hemoglobin concentration was held constant and was varied in two separate tests.

One hundred simulated tissue spectra with randomized and known myoglobin and hemoglobin saturations were generated for the cases listed in Table 6.1. Hemoglobin concentration was first kept fixed and then varied randomly. Random changes in sampled blood volume were simulated by allowing total hemoglobin concentration to vary from 1 according to a normal distribution with a standard deviation of 0.1. Myoglobin concentration was constant in all simulated data sets. Hemoglobin concentration was approximately equal to the myoglobin concentration. Where hemoglobin concentration varied, the mean concentration of hemoglobin was approximately equal to the myoglobin concentration. Hemoglobin concentration is expressed as heme concentration, four times the concentration of molecular hemoglobin.

A third series of tissue simulation spectra were developed to determine the minimum oxygen saturation range required for accurate estimation of myoglobin oxygen saturation. The data set must contain some perturbation in order for MCR to successfully separate the spectral components. Simulated spectral data included fixed total myoglobin concentration, and allowed total hemoglobin concentration to vary by 10%. Since it is expected that normal S_{Mb} values in the heart are close to 100%,[97] each set of simulated tissue spectra spanned a range from 100 % to a lower bound which varied from 99% to 60% in increments of 1%. Hemoglobin saturation was varied over the same saturation range as myoglobin. Results for each saturation range were evaluated from the average performance over 10 tissue simulation data sets, each containing 100 spectra.

6.7.2 Cardiac Tissue Data

All animal protocols were approved by the Institutional Animal Care and Use Committee at the University of Washington. Optical spectroscopic measurements of guinea pig hearts (n = 9) were recorded between 450 and 950 nm. Excised hearts were perfused with red blood cells at 5% hematocrit under conditions of varying oxygen saturation according to the Langendorff method. Diffuse reflectance spectra were

recorded from the left ventricular wall using a custom bifurcated fiber optic probe having a 1.75 mm separation between source and detector fibers. Spectra of cardiac tissue were collected as previously described in detail.[232, 244] Spectra were recorded for each excised heart while oxygen saturation of the blood was controlled using a gas-exchange perfusion system to control the oxygen, nitrogen and carbon dioxide concentrations. Each heart was exposed to a hypoxic ramp over 20 minutes, a linear reduction in perfusate oxygen content. Maximum myoglobin oxygen saturation was produced experimentally by perfusion with oxygenated buffer, infusion of adenosine to maximally vasodilate the coronary arteries, and infusion of potassium chloride to arrest the heart and thus lower myocardial oxygen consumption. Maximal deoxygenation was produced by infusion of sodium dithionite (Na_2SO_4) at the end of each experiment.[244] Guinea pig heart spectra were pre-processed by taking second derivatives with the same settings as used for tissue simulation spectra. All spectral analyses were done in the range from 450 to 650 nm.

6.8 Results & Discussion

To evaluate the use of the MCR method for measuring myoglobin oxygen saturation, both simulated and cardiac tissue spectra were examined. Estimates of oxygen saturation using MCR and CLS were

compared with and without variation in hemoglobin concentration. Simulated tissue spectra were also used to estimate the required oxygen saturation range for accurate *in vivo* S_{Mb} estimates. Cardiac tissue was examined using MCR and CLS to demonstrate applicability of the MCR technique to biological tissue.

6.8.1 Simulated Tissue Measurements

To compare MCR and CLS, simulations with constant hemoglobin concentration were examined. Prediction error was measured as the root mean square error (RMSE) between estimated and known values of S_{Hb} and S_{Mb}. Calibration linearity was measured using correlation coefficients (r^2) between estimated and known values of S_{Hb} and S_{Mb}. Corresponding experimental results are shown in Table 6.1. When hemoglobin concentration was held constant, estimates of hemoglobin oxygen saturation were equivalent for both CLS and MCR. However, estimates of myoglobin oxygen saturation using MCR were better than the corresponding CLS estimates. Prediction error for S_{Mb} using MCR was half that using CLS because constraints used in the MCR algorithm limit myoglobin concentration to chemically relevant values. Collinearity between hemoglobin and myoglobin spectral profiles leads to negative myoglobin concentration estimates using CLS.

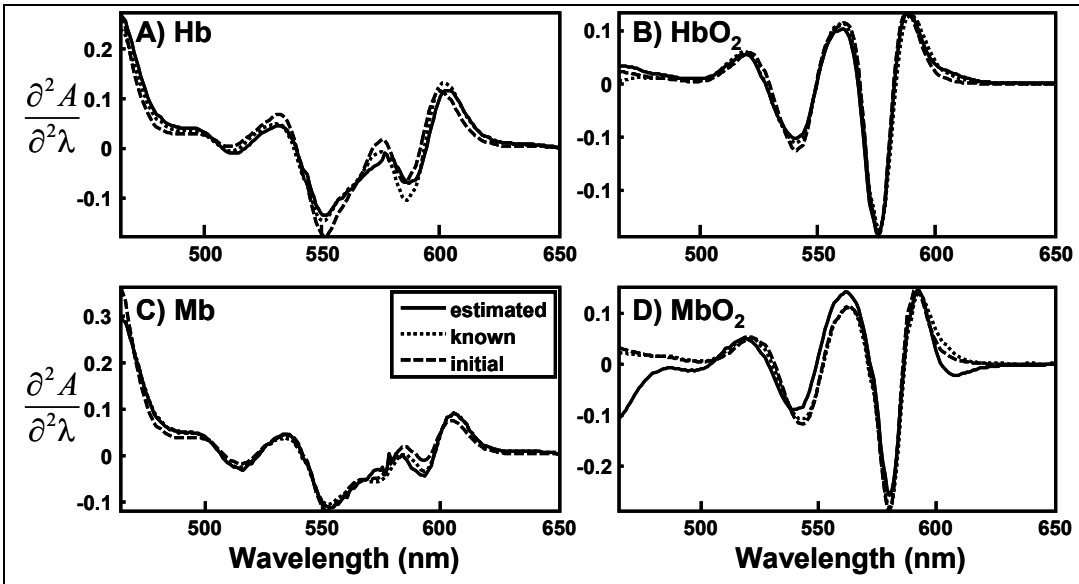

Figure 6.1: Spectral components estimated from MCR processing of simulated tissue spectra. Spectra are displayed as: a) deoxyhemoglobin, Hb, b) oxyhemoglobin, HbO_2, c) deoxymyoglobin, Mb, and d) oxymyoglobin, MbO_2. Solid lines indicate MCR spectral estimates, dotted lines indicate known component spectra and dashed lines indicate initial guesses. Simulated tissue spectra were composed from component spectra at one scattering level (known), while the MCR was initiated with component spectra measured at a different scattering level (initial).

In addition, spectra of the pure components as estimated by MCR better conform to spectral components present in the data than the *in vitro* reference spectra used in CLS. Output spectral profiles correspond closely to the known spectral profiles, as illustrated in Figure 6.1. Using MCR, pure component spectral profiles are determined *in situ* from measured

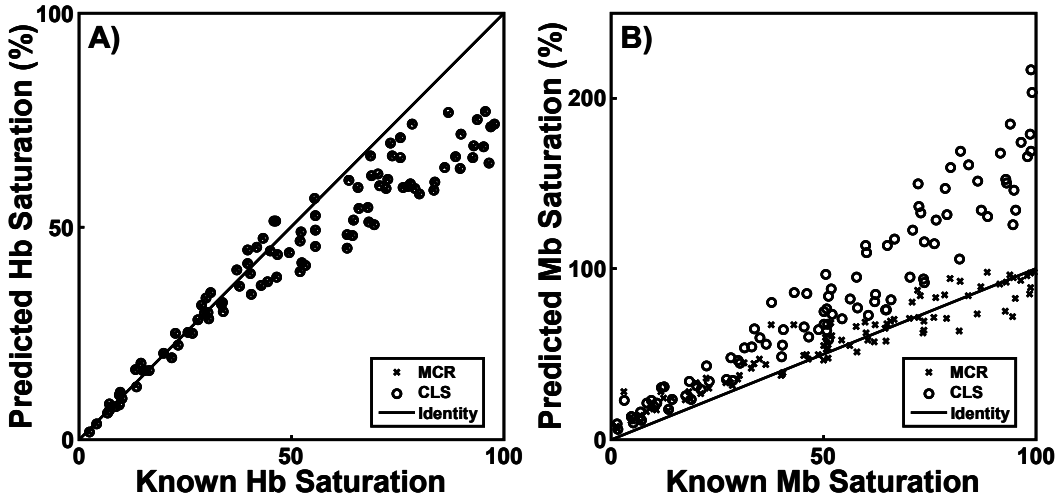

Figure 6.2: Calibration plots comparing tissue oxygen saturation estimated using MCR and CLS to known values. Calibrations of: a) hemoglobin oxygen saturation, and b) myoglobin oxygen saturation. Hemoglobin estimates are nearly identical using both MCR and CLS, and as such the plot symbols overlap. Myoglobin estimates are improved using MCR as compared to CLS estimates. Hemoglobin and myoglobin concentrations were the same in all spectra.

spectra during an experiment rather than from purified external calibration solutions. Optical scattering leads to a transformation of measured spectra, but spectral shifts arising from light scattering are corrected by the MCR. By determining spectra *in situ*, concentration estimates can be improved.

Calibration and validation results are shown in Figure 6.2. As shown in Figure 6.2a, hemoglobin oxygen saturation is consistently

estimated by both CLS and MCR. However, as shown in Figure 6.2b, the CLS method overestimates myoglobin oxygen saturation. Using the closure constraint, MCR corrects the overestimates. Hemoglobin spectral intensity in the measured pure components is about 30% greater than the myoglobin spectral intensity. Noise added to the simulation degrades myoglobin concentration estimates more than the hemoglobin concentration estimates because of the difference in the spectral weightings. In cases where the total spectral intensity from myoglobin is much greater than from hemoglobin, hemoglobin concentration estimates become worse than the myoglobin concentration estimates. Regardless of the relative component magnitudes, oxygen saturation estimates are improved when using the MCR routine.

When hemoglobin concentration was varied in the simulated spectra, the error in MCR estimates of S_{Mb} was less than when hemoglobin concentration was fixed, and linearity increased slightly. In contrast, when using CLS for estimation of S_{Mb}, error and linearity were constant regardless of hemoglobin variation. These results indicate that variation of hemoglobin perfusion improves the capacity for the MCR algorithm to adapt pure spectra to data. This is fortuitous, as hemoglobin perfusion varies naturally with both time and oxygenation. It appears that

the natural variation in hemoglobin concentration improves MCR resolution of nearly collinear spectra.

Saturation must vary in the data set in order for MCR to successfully determine the underlying spectral components. However, acquiring spectral data at extreme variations such as at 0% and 100% oxygen saturation endpoints *in vivo* is challenging. To determine the range required to accurately estimate S_{Mb}, a series of simulated tissue spectra were examined with progressively increasing oxygen saturation spans. Each span had a maximum of 100% oxygen saturation and a minimum saturation of (100-x) %, where x is the range of saturation values included. Values for x varied from 1-40%. Simulation data was developed allowing total hemoglobin concentration to vary by 10%. Correlation coefficients and root mean square error for each calibration over the span were compared. Linearity and error trends from this experiment are shown in Figure 6.3. Values along the abscissa of the plot correspond to oxygen saturation ranges used in simulations. Linearity increased until the calibration range spanned the upper 15% of saturation values (100% - 85% S_{Mb}), after which point linearity did not improve appreciably with increasing calibration range. Validation error as indicated by the root mean square error of prediction (RMSEP) decreased as the calibration range

increased. Saturation ranges greater than 15% did not show appreciable improvement of RMSEP. These results suggest that a minimum calibration range spanning from 85% to 100% S_{Mb} should be sampled for calibration of S_{Mb} by MCR in cardiac tissue. This range of oxygen content is feasible, and S_{Mb} values such as these should be attainable by variation of the oxygen content of inspired air.[134]

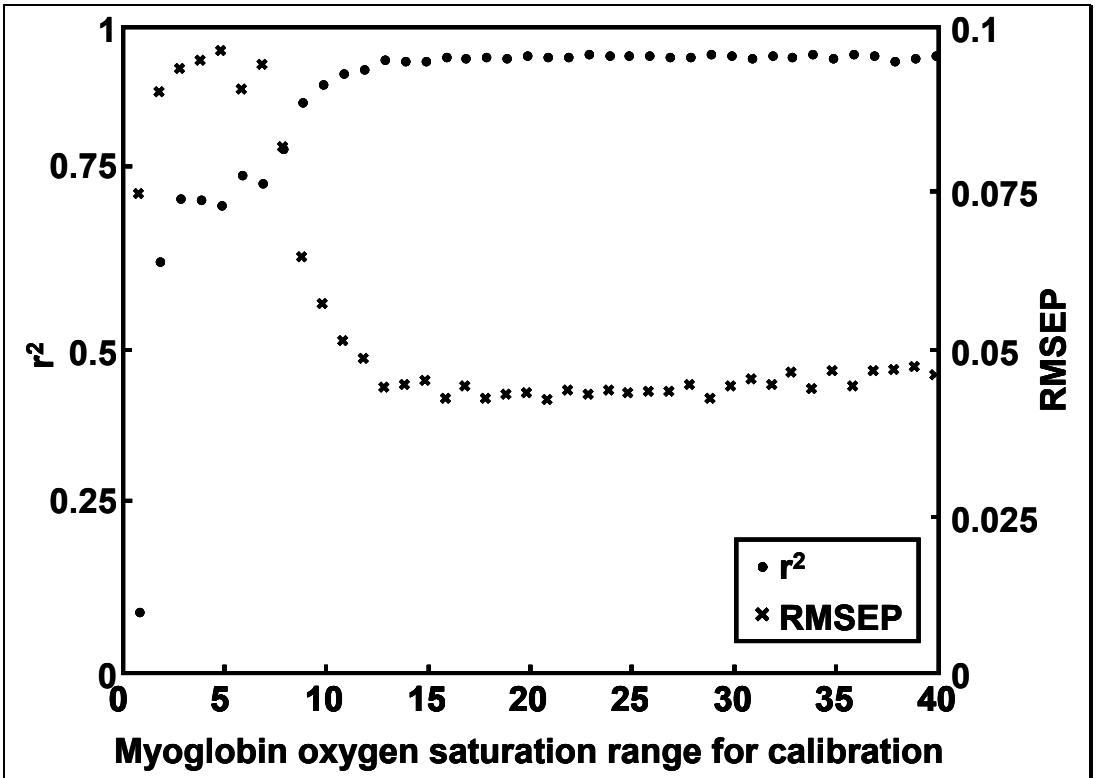

Figure 6.3: Simulated tissue processing validation results for the determination of an adequate calibration range. Abscissa values indicate the range of oxygen saturation range used in the calibration, varying from a maximum of 100% to a lower bound of (100 – range). Correlation coefficient values (r2) are drawn as points, and root mean squared error of prediction (RMSEP) values are drawn as 'x's. Each point represents the averaged results from 10 simulations, each comprised of 100 spectra.

	MCR		CLS	
Heart	100(%)	0(%)	100(%)	0(%)
1	97	11	165	17
2	91	11	157	17
3	89	13	327	40
4	88	10	198	17
5	96	15	200	24
6	87	15	206	30
7	85	8	139	14
8	86	23	183	24
9	85	8	217	14
Mean	89.4	12.6	199.2	21.8
Std.Dev.	4.4	4.7	54.3	8.8

Table 6.2: Myoglobin oxygen saturation (S_{Mb}) measured in guinea pig myocardium at the experimental 100% and 0% oxygen saturation endpoints using multivariate curve resolution (MCR) and classical least squares (CLS).

6.8.2 Measurements of Guinea Pig Hearts

Myoglobin oxygen saturation was estimated in isolated perfused guinea pig hearts. Spectral data from each guinea pig heart was processed using the MCR method in the range 450-650 nm. Myoglobin oxygen saturation was estimated for all of the data, including the hypoxic ramp and fully oxygenated and deoxygenated endpoints. Since there was no reference measurement of S_{Mb} during the hypoxic ramp, estimation of accuracy is undefined over intermediate saturations. However, as a test of accuracy, we assume that myoglobin was fully oxygenated and fully deoxygenated at the experimental endpoints and that S_{Mb} is 100% and

0%, respectively, during these periods. Saturation estimates for nine hearts using MCR and CLS are displayed in Table 6.2. CLS values at the 100% S_{Mb} endpoint were physically impossible because they exceeded 100% saturation. This artifact was caused by negative deoxymyoglobin concentration estimates. Using MCR, concentration estimates were constrained to a physically possible range using non-negativity constraints. Concentrations were related using closure (Eq. 6.5) to compute S_{Mb} (Eq. 6.6). Typical values of the closure constraint, k, ranged from 1 to 4 when processing guinea pig heart spectra. Composition of deoxymyoglobin and oxymyoglobin components after scaling for closure is shown in Figure 6.4 for one heart. In a typical hypoxic ramp, MCR estimates showed decreases in oxymyoglobin concentration and increases in deoxymyoglobin concentration. Values measured at the 0% and 100% saturation values are plotted as the two final points. Endpoint saturations estimated by MCR are nearer to the ideal saturations than CLS estimates (Table 2).

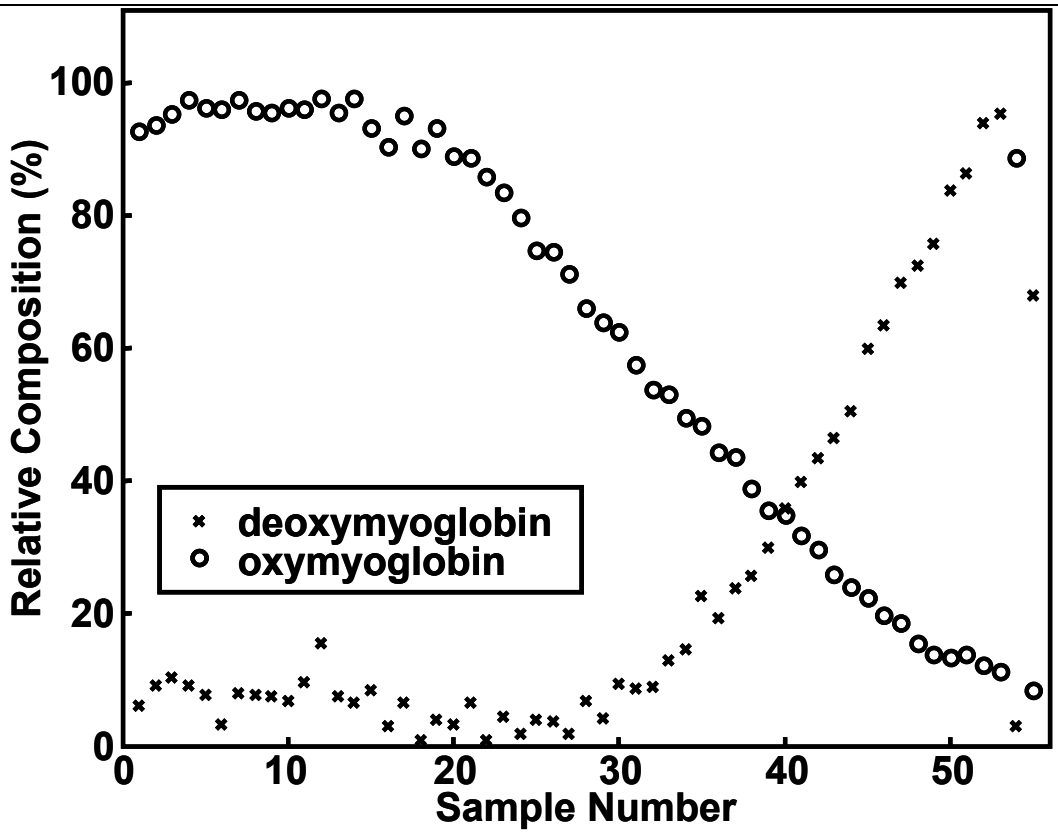

Figure 6.4: Myoglobin composition estimate from MCR using the closure constraint. Composition estimates are plotted for the first heart listed in Table 6.2. Samples labelled 1-53 were recorded during the hypoxic ramp, where oxygen content of the perfusate was gradually decreased. Oxygen saturation was maximized at sample 54 and minimized at sample 55.

Selected spectral components for the first heart listed in Table 6.2 are shown in Figure 6.5. Pure spectra estimated using the MCR differ from the input spectra, having adapted to the data to compensate for scattering and the presence of other constituents. Adaptation of the spectra to the data can be observed by examining the residual between the recorded data and data reconstructed using the estimated spectra and

concentrations. Using MCR, residuals are less than 1% of the magnitude of residuals observed using CLS. Periodic oscillations observed in estimated spectra may arise from several sources. Thin layers within cardiac tissue may lead to interference pattern effects in recorded tissue spectra or from adaptation of the spectra to additional components present in tissue (such as cytochromes) which vary in relation to the oxygen saturation. In tissue, many chemical constituents are present in addition to hemoglobin and myoglobin. Spectral features of other chemical constituents having some collinearity, such as cytochromes, may be incorporated into pure component spectra of hemoglobin and myoglobin. While spectral profiles corresponding to the data were approximated by MCR, ideal pure component spectra for the hearts are not known. No tissue endpoint measurements are required for use of the MCR method, as compared to using partial least squares. Results indicate that MCR estimates of S_{Mb} are more accurate than using similar CLS methods.

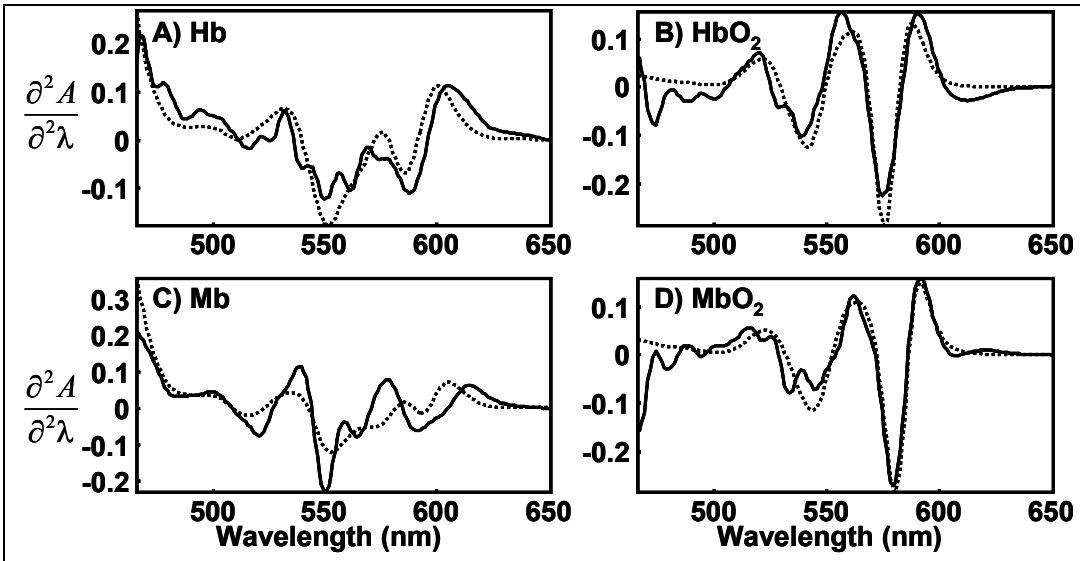

Figure 6.5: Spectral profiles estimated for the first guinea pig heart listed in Table 2 using the MCR algorithm. Estimated spectral profiles are shown as solid curves, while the initial spectra input to the MCR are shown as dotted curves. Spectra are displayed as: a) deoxyhemoglobin, Hb, b) oxyhemoglobin, HbO_2, c) deoxymyoglobin, Mb, and d) oxymyoglobin, MbO_2.

6.9 Conclusions

Myoglobin oxygen saturation (S_{Mb}) is more accurately measured from visible spectra using multivariate curve resolution (MCR) than by classical least squares (CLS). Pure spectral profiles were estimated using the MCR algorithm, and quantification was improved through application of constraints tailored to the system under study. Incorporation of pre-processing steps may yield constraints that are invalid, and

pre-processing steps should be optimized against physical constraints. In particular, MCR is useful when known pure spectral profiles are modified by scattering or when they cannot be measured in isolation. Myoglobin oxygen saturation in tissue can be estimated without recording endpoint spectra for calibration and normalization in each data set. Instead, a closure constraint is automatically determined from recorded data to determine the proper scaling of component concentrations for S_{Mb} estimates. Simulations indicate that in order to use the MCR technique, the spectral data set must include myoglobin saturation values that vary from at least 85% to 100%. Suitable oxygen saturation ranges should be possible under normal physiological conditions through manipulations of inspired oxygen content. Finally, results showed that variations in hemoglobin concentration seem to improve myoglobin oxygen saturation measurements.

Chapter 7. Conclusions and Future Work

Spectroscopy is a powerful method for analyzing a variety of materials, through which chemically specific information can be obtained non-invasively. Despite the large body of research into non-invasive tissue measurements using diffuse-reflectance NIR spectroscopy, it is not yet commonly used. One of the main limitations is the lack of optimal correction for light scattering. This dissertation has described four practical methods for correcting light scattering in order to better quantify analyte concentrations in turbid media.

As explained throughout this thesis, light scattering is deleterious to accurate *in situ* diffuse-reflectance measurements. The theory and practice of diffuse-reflectance is difficult because the most commonly used spectroscopic model of light absorbance, the Lambert-Beer law, does not account for light scattering. More complex models of photon transport, such as the radiative transport equation and its diffusion approximation treat multiple scattering. These models serve as a theoretical basis to correct for scattering effects. Experimental approaches have been developed to measure optical properties, such as the absorption coefficient, and to use measured reduced scattering coefficients for improving spectroscopic quantification in turbid media.

7.1 Conclusions

This thesis has focused on four methods for improving spectroscopy in scattering media. These practical methods are applicable to biomedical spectroscopy for point and imaging measurements. Depending on the particular application, either point measurements or imaging measurements are used.

Point measurements are appropriate for the evaluation of chemical composition at a single location of interest or in cases where concentrations change relatively slowly. Applications which use point measurements include studies for identifying lesions or tissue damage, and studies for quantifying lactate, glucose, or oxygen saturation. An advantage of point measurements is that relatively simple instruments can be built to fulfil these applications. Single-point spectroscopic measures can be improved using photon time-of-flight instruments. For example, the photon time-of-flight instrument described in chapter 3 is appropriate for point measurements of the reduced scattering coefficient.

In chapter 3, a rapid handheld time-of-flight spectrometer was demonstrated for measuring the scattering coefficient. A spectrum recorded with a commercially available handheld spectrometer was corrected using the scattering coefficient measured with the photon time-

of-flight instrument. This was shown to improve quantification of dye in a turbid sample using a single-point optical measure by 35%. This instrument is practical for improving point-spectroscopy measures in tissue.

In chapter 5, a method was described for incorporating generic parsimony or simplicity measures into genetic algorithms for automated data processing method development. This approach is useful for developing simplified spectroscopic systems, and might be incorporated with the photon time-of-flight instrument to develop optimal point-measurement devices. Potential applications for handheld medical devices include measurement of hemoglobin and myoglobin oxygen saturation, lactate and glucose concentration, and evaluation of burns, edema and other disease states. Parsimonious genetic algorithms are useful for identifying important wavelength regions and for guiding the development of optimal devices. By combining a readily available portable spectrometer and the portable photon time-of-flight instrument, the parsimonious genetic algorithm can be used to efficiently develop new analytical spectroscopy methods. The genetic algorithm was shown to improve quantification of lactate *in vivo* by 20% as compared to the best method developed by an expert.

Imaging spectral measurements are appropriate for measurements of heterogeneous systems such as: to identify regions of interest, for measuring rapidly varying concentrations, and for measuring the properties of tissues in motion (in cardiac tissue for example).

To improve spectroscopic imaging, a novel instrument was demonstrated using images of an annular illumination pattern projected onto a sample surface to estimate the reduced scattering coefficient. Imaging annular laser patterns to estimate scattering holds several advantages with respect to imaging Gaussian beams. Most important is the short source-detector separation distance (ρ) used in this method. Illumination intensity is distributed over a larger area as compared to Gaussian beam imaging methods, decreasing the flux while maintaining the same illumination power. In order to measure the optical absorbance of components within the scattering medium, reference reflectance intensity must be determined. Reflectance is a function of the scattering coefficient, and the reference reflectance can be estimated from the measured scattering coefficient. Chapter 4 describes how reflectance at the center and edges of the annular laser pattern can be used to first measure the scattering coefficient, and also how to use the scattering coefficient to estimate the reference reflectance intensity. Finally, the

absorption coefficient can be estimated using the measured reflectance (with absorbance) and the estimated reference reflectance (absorbance-free). Using the annular beam imaging method, error in the estimation of absorption coefficients was reduced by 50% as compared to conventional imaging.

In chapter 6, multivariate curve resolution method is used to estimate constituent concentrations and spectra directly from the spectra of a series of mixtures. This approach is applicable towards modelling of imaging data, and might be incorporated into the annular imaging system to develop improved spectroscopic imaging systems. Multivariate curve resolution leverages the variance within a data set to estimate underlying spectral components. In imaging spectroscopy the composition may vary with position in the image. The rapid multivariate curve resolution algorithm shows promise for real-time spectral processing and adaptive modelling. In chapter 6 we demonstrated that over the clinically relevant oxygen saturation range of 85-100% the multivariate curve resolution approach estimated myoglobin oxygen saturation more accurately than the classical least squares approach.

7.2 Future Work

Potential avenues of future research are proposed in this section, where improvements can be made to each technique individually. Moreover, the various techniques can be combined to achieve further improvements. Improvements in efficiency, accuracy, and ease-of-use would advance the use of clinical non-invasive reflectance spectroscopy.

7.2.1 Future Work using the Photon Time-of-Flight Instrument

With improvements to this portable time-of-flight system, more accurate estimations of μ_s' will enable more precise quantification of components in highly scattering media. Several methods are proposed here for improving upon the current system, these include improvements using the current system, and improvements through modification of the current electronics.

Without any modification of the current electronics, a shorter pulse can be used. The current system can be reconfigured in software to output a 5 or 10 nanosecond pulse. Using a 10 nanosecond pulse should not decrease the peak intensity. With a 5 nanosecond pulse, optical intensity would decrease, though the temporal shift would be even more pronounced, likewise, skew and kurtosis would be more prominent. An increase in the pulse rate should also permit faster measurements by

allowing for decreased signal-averaging times. A second set of improvements requiring changes to the electronics of the device would be to use higher charge and gate voltages to the laser diodes. The optical output of the laser diodes may be increased three- or four-fold by optimizing the charge and gate voltages. A third method would involve improvement of the detection system. The rise time of the detector could be decreased by increasing the reverse bias applied to the diode. Likewise, the use of a high-speed amplifier could increase the absolute magnitude of the detected electrical signal and thus improve the signal-to-noise ratio of the time-of-flight profiles. The bandwidth of the oscilloscope was only 200 MHz, and coupling between the channels was observed to cause ringing. Simplified electronics could be incorporated to replace the oscilloscope. Previously unpublished results illustrate the utility of decimation of the temporal profiles by electronically windowing the electrical signal from the detector with a delayed trigger pulse using digital delay lines and a high-speed mixer. Likewise the oscilloscope used an 8-bit analog-to-digital converter, whereas a 12- or 16-bit analog-to-digital converter would improve the precision of the digitization. Finally, it should be noted that voltages for the laser control circuitry were chosen for convenience of design and construction. This system was designed to run

for several hours from two 9 V batteries. Using an increased source voltage or some voltage-boost circuitry, performance of the lasers and detector could be improved. Future improvements in this portable system will allow for quick, robust multi-wavelength measurement of the reduced scattering coefficients for the correction of spectra in highly turbid media such as tissue.

In particular, preliminary tests have shown the simplified detector system should improve results. A simplified detection scheme was tested

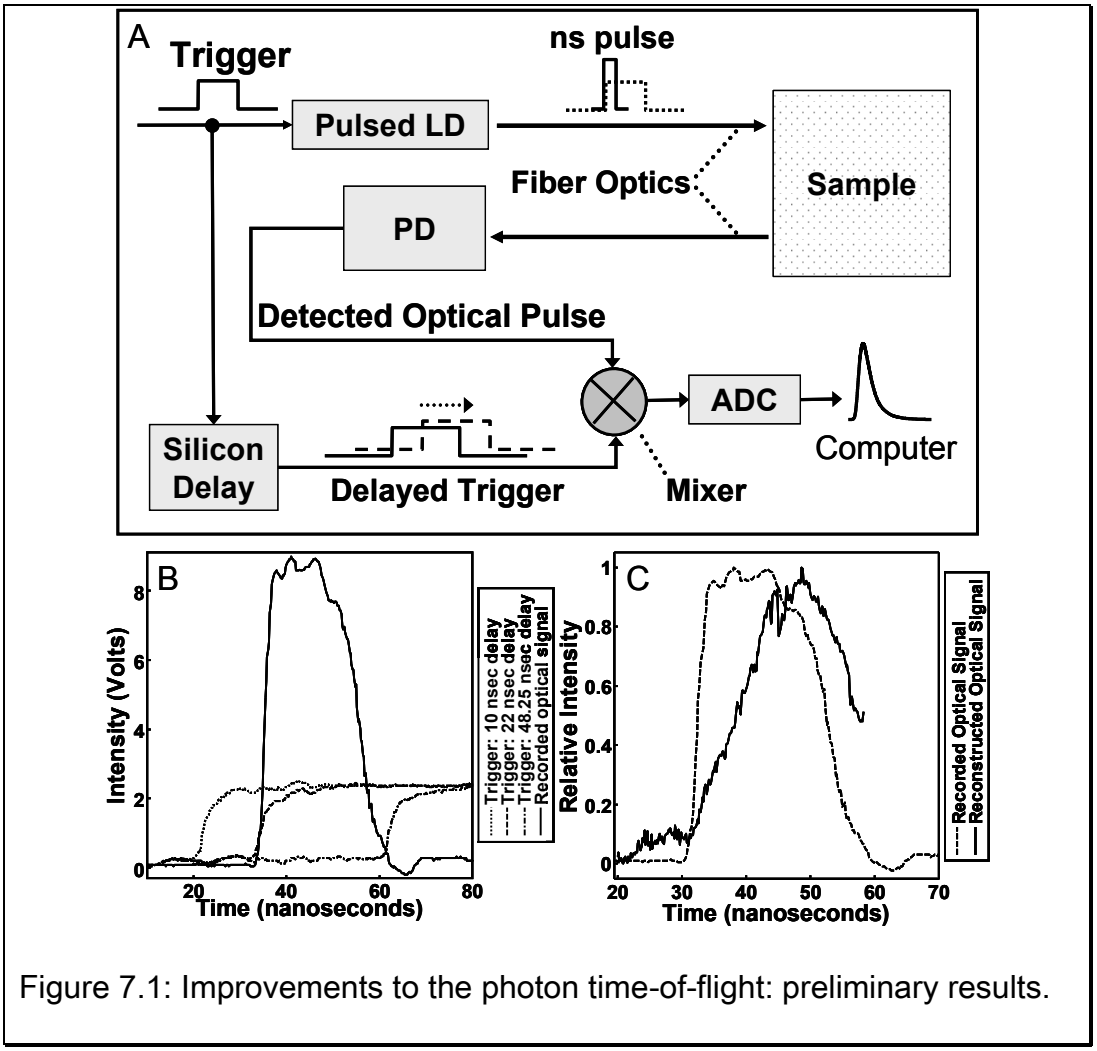

Figure 7.1: Improvements to the photon time-of-flight: preliminary results.

using a variable delay line (DS1040, Maxim Integrated Products, Inc., CA, USA) and a signal mixer (ZAD-1, Mini-Circuits, New York, USA) to transform the optical signal output from the high speed silicon photodiode. A diagram of the simplified detector system is shown in Figure 7.1. For testing purposes, the output was recorded using the high speed oscilloscope. The digital delay line was fed with the laser trigger pulse, and the delayed trigger selected a temporal window from the optical signal. The mixer transforms (inverts) the detected optical pulse using the delayed trigger. Signal from the mixer was recorded for each of the 256 time-steps of the delay line, as shown in Figure 7.1. The detected signal includes a background ringing signal caused by the laser module. By taking the sum of intensity in each trace, the integrated signal was estimated for each time delay. Integrated signal was plotted against delay time and reconstructed of the directly measured optical pulse. Preliminary results are shown in Figure 7.1, where the reconstructed pulse is shown along with the directly measured pulse. While distortion is present, major features of the time-of-flight profile are present. Initial tests were laboriously carried out by manually selecting the delay-time and recording the oscilloscope trace. In the next iteration of the simplified photon time-of-flight instrument, the delay-time will be digitally selected using a

microcontroller that will also record the signal magnitude as averaged across a capacitor. The automated system should allow a complete measurement of the photon time-of-flight profile in a quarter of a second with a temporal resolution of 150 picoseconds. Furthermore, the intensities would be recorded using 12- or 16-bit analog to digital converters rather than an 8-bit analog to digital converter. As a result, the next iteration of the time-of-flight instrument should have a two order of magnitude improvement in signal resolution. With these improvements, a portable biomedical instrument should be feasible.

7.2.2 Future Work using the Ring-Light System

A natural extension of the ring imaging technique is to examine the effects of a variable ring diameter. Source-detector separation distance is known to change the optical sampling depth.[245, 246] Variation of ring diameter may allow depth-resolved non-invasive measurement of scattering properties. In the current work, reduced scattering coefficients were measured within the ring source pattern. In future experiments, ring diameter can be dynamically controlled using a spatial light modulator or adjustable conical lenses to measure scattering at different sampling depths. In the recently reported subsurface Raman ring/disk spectroscopy, ring patterns were formed using conical lenses to transform the incident

Gaussian laser beam into a ring-shape.[173, 174] Illumination ring diameter was varied by adjusting the position of the conic lens, or using adjustable telescopic lenses.[173, 174] This combination has shown sensitivity to depth.[247, 248] Combinations of ring arrays and dynamic diameter selection have the potential to map subsurface scattering properties. Depth penetration increases as ρ increases, as does the sampling volume, which scales approximately as the cube of the source-detector separation. Using computer-generated holograms arrays of annular patterns can be produced. Arrays of rings might be used to measure the optical properties at many positions over a surface. Imaging annular arrays would allow scattering properties to be measured at many spatial positions concurrently. This imaging technique should ultimately allow non-invasive tomographic imaging spectroscopy of highly turbid media.

Aspects to examine for improving the annular measurements should include verification of the effects of changing anisotropy, testing the accuracy when mapping scattering coefficients using an array of rings, and testing whether variations of the ring diameter can be used to measure depth-resolved scattering coefficients. One experimental method for controlling anisotropy is to vary the refractive index of the solution, while using a constant scattering particle size and concentration. By using

polystyrene/latex microspheres and different solvents the anisotropy can be controlled, while keeping the scattering coefficient constant. Experimental methods for testing imaging with multiple rings and depth-dependence could use scattering spheres embedded in thin slices of polymer. Additionally, the system should be tested with the camera at greater distances, particularly for any future medical applications.

7.2.3 Future Work using the Genetic Algorithm

Genetic algorithms are well suited for the selection of data processing methods which can be used to guide the design of portable instruments. Future directions for improving genetic algorithms in processing method selection should consider better ways of incorporating preprocessing step complexity into parsimony penalties, better ways of determining optimal cross-validation group sizes, and improved methods for selecting between the final solutions presented by the GA. Metrics for improving the assessment of model complexity include the time or memory required for processing, algorithm complexity using 'O-notation', or a financial cost for building a simplified instrument using the specified model (by including instrument costs for component such as specialized optical filters and the number of detectors). Ideally, non-parametric statistical methods should be used for comparing model size and

preprocessing step complexity, along with different complexity metrics. Cross-validation group sizes need to be better studied so that the accuracy of cross-validated model performance metrics is better understood. Statistical properties of cross-validated results are difficult to prove. Similarly, improved statistical methods for comparing the results of models with different sizes should be developed.

Incorporation of scatter-correction directly into the GA should allow improved quantification. Such methods can be implemented either by scatter-correcting spectra before the GA is run, or by supplying the scattering coefficient to the GA and allowing an automatic scatter-correction method to be selected. The second method would allow for more flexibility and should be more easily generalized to new systems, however, measurements of scattering would be necessary in all such systems. Simplified instruments, such as the scattering coefficient measurements demonstrated in this thesis would be appropriate for supplementing commonly measured absorption or reflectance spectra.

7.2.3 Future Work using Multivariate Curve Resolution

Multivariate curve resolution algorithms are well suited for diffuse reflectance spectroscopy because they adaptively model the system based on recorded data. Several methods might be explored as

extensions for improving MCR processing of reflectance spectroscopy data. Potential areas for improvement include the integration of an inverse-scattering-transform to use estimated or measured scattering coefficients to inversely transform the measured spectra to compensate for scattering. By combining the MCR with the scattering measurements from annular patterns, the scattering coefficients could be measured throughout an imaging system, with regional scattering corrections applied to different portions of the spectral image. This could be implemented in two ways, by either transforming the initial guesses for the underlying pure component spectra of each sub region, or by transforming the data set. Because of the structure of the MCR algorithm, transformation of the data set would be less complicated to implement. However, transformation of the initial guesses would allow the MCR to correct for imperfections in the inverse scattering correction.

A second way to improve multivariate curve resolution is to develop constraints which can be applied more easily to imaging data. One example is in real-time imaging of hemoglobin and myoglobin in cardiac tissue. Real-time video imaging has three dimensions: spectral band, position, and time. By constructing the appropriate dimensional collapsing

scheme, and appropriate constraints, variability within each of these dimensions can be used to improve MCR solutions.

7.3 Conclusion

In summary, the techniques demonstrated in this thesis have been demonstrated to improve quantitative diffuse reflectance spectroscopy. Results of this thesis show promise for practical non-invasive measurements in turbid media. Several future directions have been suggested to improve quantification so that a wider variety of problems can be approached. Non-invasive biomedical measurements have a potential to greatly improve current clinical practice by providing physicians precise and timely diagnostic information.

Appendix A: TOF Device

The photon Time-of-Flight instrument consisted of both electronic hardware and software. Details of the electronics developed are listed, including: electronic schematics, the list of required electronic components, Printed Circuit Board layout, and C code for programming the control board. Finally, a brief explanation is given of the mathematics used for estimating statistical moments from time-of-flight profiles.

A.1 Time-of-Flight Control Electronics Schematic

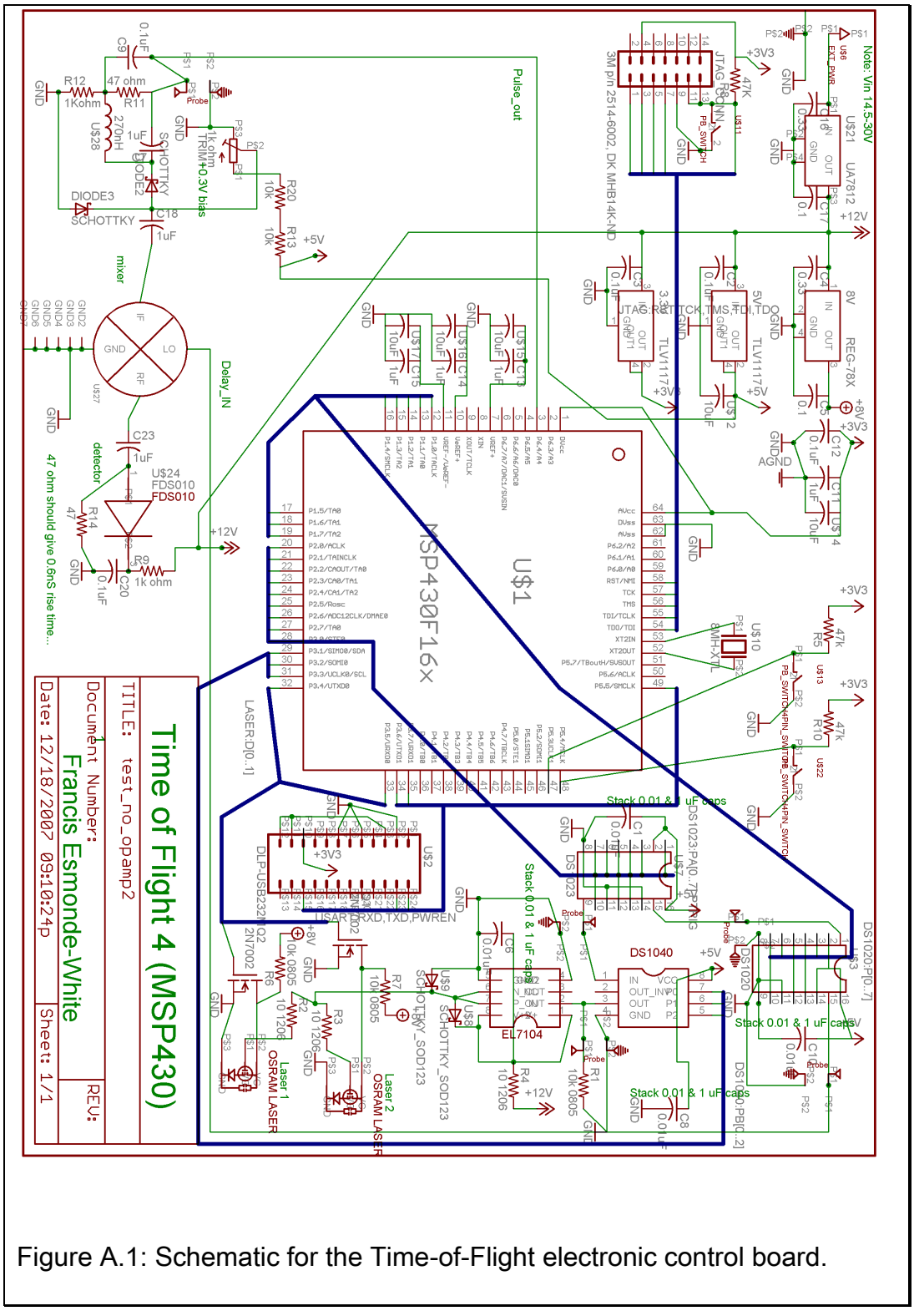

Figure A.1: Schematic for the Time-of-Flight electronic control board.

A.2 Time-of-Flight Control Electronics Part List

Component [Package Type]

Voltage Regulators:

- 1xTLV1117-3.3 3.3 volt regulator [SOT223]
- 1xTLV1117-5 5 volt regulator [SOT223]
- 1xLM7808 8 volt regulator [SOT223]
- 1xUA7812 12 volt regulator [PFM-KTE]

Capacitors:

- 4x0.01 μF [C0603K]
- 7x0.1 μF [C0603K]
- 2x0.33 μF [C0603K]
- 7x1 μF [C0805K]
- 5x10 μF [cylindrical]

Resistors:

- 3x10 ohm 1206
- 2x47 ohm, M1206
- 1x1K ohm, R0603
- 1x1k ohm, M1206
- 5x10k ohm 0805
- 3x47K ohm, M1206
- 1x1k ohm variable resistor (potentiometer)

Inductor:

- 270 nH inductor, M0603 package

Diodes:

- 4 Schottky diodes [SOD-123]

Transistors:

- 2x2N7002 FET transistor [SOT23]

Microcontroller:

- MSP430 F1611 microcontroller [PQFP64](Texas Instruments)

- 8MHz crystal oscillator [HCM49]

Integrated Circuits:

- USB-to-serial converter (DLP-USB232M) (DLP Design)
- DS1020 Delay line [SO16W] (Dallas Semiconductor)
- DS1023 Timing element [SO16W] (Dallas Semiconductor)
- DS1040 Pulse generator [SOIC8] (Dallas Semiconductor)
- EL7104 Power MOSFET driver [SOIC8] (Elantec/Intersil)
- MCA-12G mixer (Minicircuits)

Laser Diodes:

- SPL-LL85, 850 nm pulsed laser diode
- SPL-LL90, 905 nm pulsed laser diode

(OSRAM Opto Semiconductors)

Detector:

- FDS010 silicon photodiode [TO5]

Mechanical Pieces and Connectors:

- JTAG programming port (Digi-Key# MHB14K-ND)
- 0.1" spacing 2-wire screw terminal
- push-button reset switch
- 2 bush-button switches (4 pin)

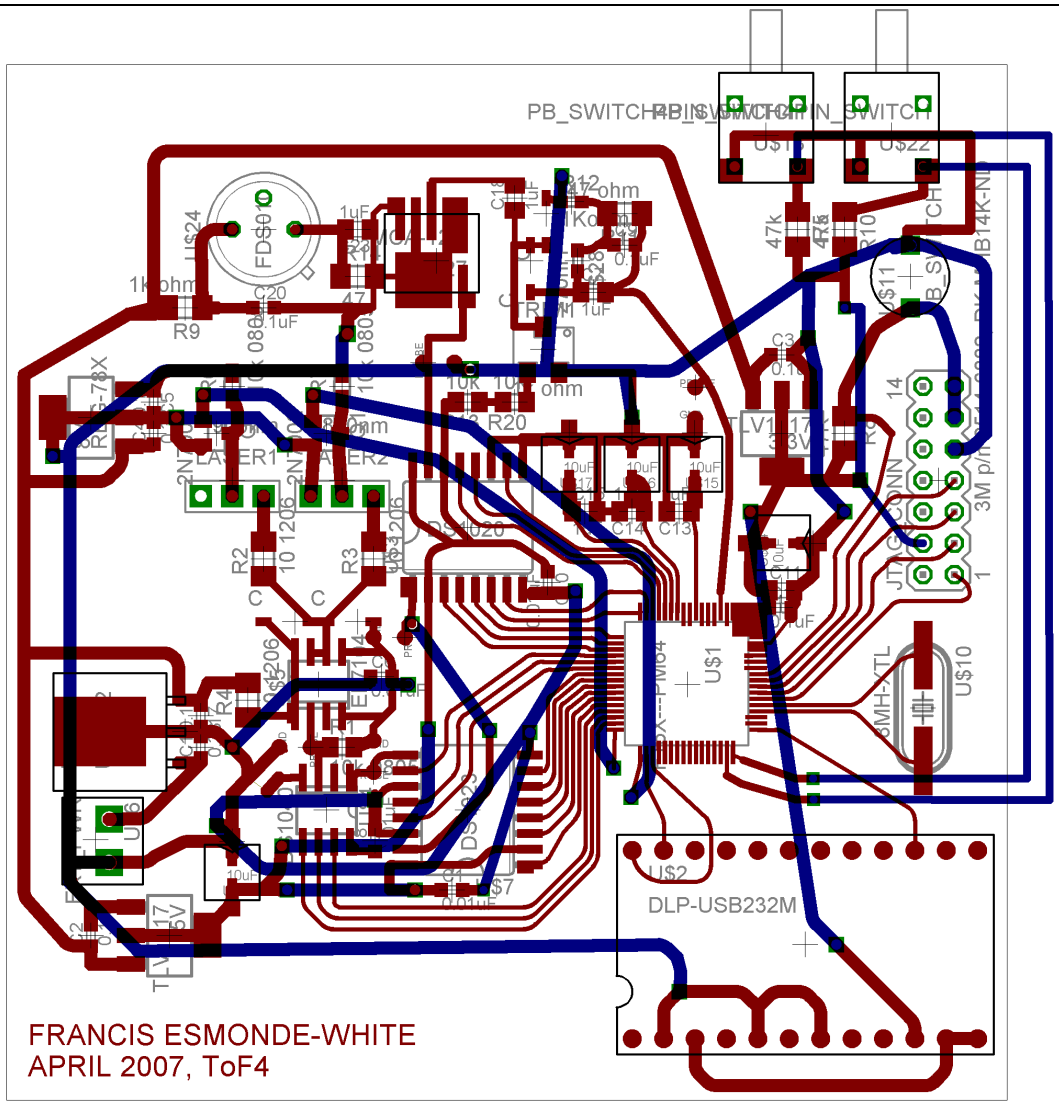

Figure A.2: Printed circuit board layout for the Time-of-Flight electronic control board. Not to scale. Both top and bottom layers are shown overlapped.

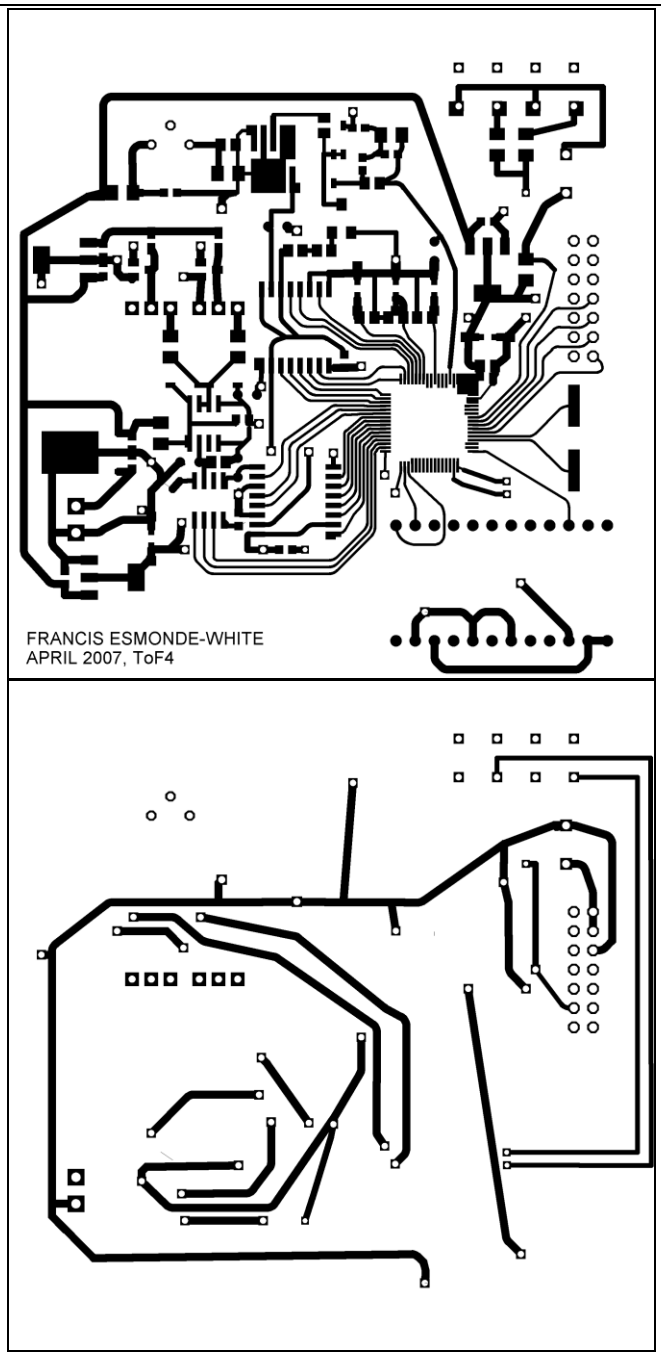

Figure A.3: Printed circuit board traces, with the top surface in the upper pane and the bottom surface in the lower pane. The boxes should be 3.36 inches wide and 3.48 inches tall. Units are presented in inches corresponding to the original Eagle PCB software.

A.3 Photon Time-of-Flight Electronic Control System C Code

```
//////////////
// main.c
#include "msp430.h"
#include "IO_ports.h"
#include "USART1_lib.h"
#include "ADC12_lib.h"

#include "IO_ports.c"
#include "USART1_lib.c"
#include "ADC12_lib.c"

#define IRQ_DELAY 1000
// 1 millisecond handing period.

int wakeup_for_pulsing = 0;
int current_laser = 0;
int startup_delay = 0;

void main( void )
{
  int i;
  char j;
  // Stop watchdog timer to prevent time out reset
  WDTCTL = WDTPW + WDTHOLD;

  BCSCTL1 &= ~XT2OFF;                       // XT2on
  // Wait for the 8MHz clock to start.
  do
  {
    IFG1 &= ~OFIFG;                         // Clear OSCFault flag
    for (i = 0xFF; i > 0; i--);             // Time for flag to set
  }
  while ((IFG1 & OFIFG));                   // OSCFault flag still set?
  BCSCTL2 |= SELM_2 + SELS;                 // MCLK = SMCLK = XT2 (safe)

  // Initialize Timer B for the polling loops.
  TBCCTL0 = CCIE;                           // CCR0 interrupt enabled
  TBCCR0 = IRQ_DELAY;
  TBCTL = TBSSEL_2 + BIT6 + BIT7 + MC_2;    // SMCLK / 8, contmode

 while(startup_delay < 500)
 {
  _BIS_SR(LPM0_bits + GIE);                 // Enter LPM0 w/ interrupt
 }

  init_IOports();
  initUART1();


  // laser_select('0');
  // set_DS1040(4);
//  P3OUT &= ~(DS1040_PB1); // zero the masked pins
//  P3OUT |= (DS1040_PB0&DS1040_PB2);

  while(1)
  {
    // Do the important stuff, while there is stuff to be done.

        put_message("Settings:\n\r");
        put_message("Both lasers selected.\n\r");
        put_message("Pulse width 15nS.\n\r");
        put_message("Offset delay 0nS selected (DS1023).\n\r");
        IntDegC = ADC12_read_temp();
        put_message(tempstr);
        putchar('0'+((IntDegC/10)%10)); // tens
        putchar('0'+(IntDegC%10));      // ones
        putchar('.');
        putchar('0'+((IntDegC*10)%10)); // decimal
        put_message("\n\r");

        j=47;
        wakeup_for_pulsing=1;
        // while (++j<58)
        while (1)
        {
            //putchar(j);
            //put_message("\n\r");
```

```
            Laser_Pulse();
            ADCVal_to_ADC_resultHEX();
            put_message(ADC_result);
            put_message("\n\r");

            _BIS_SR(LPM0_bits + GIE);
        }
        wakeup_for_pulsing=0;

    // Enter LPM0 while waiting for stuff to do.
    _BIS_SR(LPM0_bits + GIE);               // Enter LPM0 w/ interrupt
  }

  _BIS_SR(LPM0_bits + GIE);                 // Enter LPM0 w/ interrupt
}

// Timer B0 interrupt service routine
#pragma vector=TIMERB0_VECTOR
__interrupt void Timer_B (void)
{
  TBCCR0 += IRQ_DELAY; // Add Offset to CCR0 to maintain interrupt timing.

  // Periodic output check
  if (TXCount>0)
    // if there is any data to be transmitted, transmit will be started.
    if (!(IFG2 & UTXIFG1)) //(TXBusy==0)
    {
      // Disable TX interrupt
      // _BIC_SR( GIE); // bit clear
      TXBUF1=TXBUF[TXRead++];
      TXCount--;
      // enable TX interrupt
      // _BIS_SR( GIE); // bit set.
    }

  if ((~P5IN) & BUTTON_1) // check if BUTTON_1 is low.
    Debounce_Count_1++;
  else if(Debounce_Count_1>0)
  {
    if (Debounce_Count_1>=40) // was the button low for at least 40mS?
    {
      //_NOP(); // if it was, then perform the button actiond.
      // _BIC_SR_IRQ(LPM0_bits); // wake the uC
      current_laser = ( (current_laser==2)?1:2 );
      // toggle between laser2 and laser1
      if ( current_laser==1)
        laser_select('1');
      else
        laser_select('2');
    }
    // clear the Debounce_Count
    Debounce_Count_1=0;
  }

  if (startup_delay<=500)
    startup_delay++;
  else
    wakeup_for_pulsing=1;

   if (wakeup_for_pulsing)
    _BIC_SR_IRQ(LPM0_bits); // wake the uC

  // otherwise go back to sleep
}

//////////////
// ADC12_lib.c

void ADC12init(void)
{
  // Initialize the ADC12.

  P6SEL |= 0x10;    // Enable A/D channel A4, pin 6.4

  ADC12CTL0 &=  !ENC; // DISABLE ADC12
  ADC12CTL1 = SHS_0 + SHP + CONSEQ_0 + ADC12SSEL_2 + ADC12DIV_1;
  // Trigger Source is ADC12SC bit
  // SAMPCON is sourced from the sampling timer
  // Single-Channel, Single-Conversion
  // The ADC12 clock is sourced from MCLK, and divided by 2 (4MHz clock)
  ADC12MCTL0 = SREF_1 + INCH_4;                 // Channel A4, Vref+/AVss
```

```
  ADC12CTL0 = SHT0_1 + SHT1_1 + REFON + ADC12ON; // Config ADC12
  // 8 clocks for sampling, reference on at 1.5V, ADC on, ADC enabled
  // 2 us sampling period based on 4MHz ADC12CLK
  // I'm not sure about the interrupt usage
  ADC12IE = 0xFF;                           // Enable ADC12IFG.0
  // I'm not triggering on Timer_A, so ignore the following 2 lines.
  // TACCTL1 = OUTMOD_4;                    // Toggle on EQU1 (TAR = 0)
  // TACTL = TASSEL_2 + MC_2;               // SMCLK, cont-mode
  ADC12CTL0 |=  ENC ;   // Enable the ADC

  ADC_result[3]=0;

}

void ADCVal_to_ADC_resultHEX(void)
{
  for (int i=2; i>=0; i--)
  {
    // convert from ADCval (uint, 12 bit digit) to hex (signed char[3])
    ADC_result[2-i]= hextable[((ADCVal >> i*4) & 0xF)];
    // ADC_result[i]= "0123456789ABCDEF"[((ADCVal >> i*4) & 0xF)];
    // if hextable is unused elsewhere, then we don't use the lookup table.
  }
}

// Pulse Laser
// ADC value read is stored in ADCVal, and can be extracted to hex using
//    ADCVal_to_ADC_resultHEX();
void Laser_Pulse(void)
{
    // Disable Interrupts
  _BIC_SR( GIE);
    // bit clear, clear the register bits according to the bit mask.


  // Start the ADC12 (2uS sampling time),
  //Turn on and then turn off the laser line.
//  ADC12CTL0 &=  !ENC; // DISABLE ADC12
//  ADC12CTL1 = SHS_0 + SHP + CONSEQ_0 + ADC12SSEL_2 + ADC12DIV_1;
// Setup ADC12
//  ADC12CTL0 |=  ENC ;                 // Enable the ADC
  ADC12CTL0 |= ADC12SC;                 // Sampling and conversion start
  // Turn on the Laser line             // rising edge triggers the laser
  P3OUT = P3OUT|DS1023_PTRIG;

  while (!(0x01 & ADC12IFG));           // ((ADC12IFG & BIT0)==0);
  _NOP();                               // SET BREAKPOINT HERE

  //    while (!(0x01 & ADC12IFG));     // Conversion done?
  ADCVal = ADC12MEM0;                   // Read out 1st ADC value

   // Enable Interrupts
  _BIS_SR( GIE);
   // bit set, set the register bits according to the bit mask.
   //  Turn off the laser line. This prepares for the next pulse.
  P3OUT = P3OUT&(~DS1023_PTRIG);
  return;
}

// read Temperature
int long ADC12_read_temp(void)
{
  _BIC_SR( GIE);
  ADC12CTL0 &=  !ENC; // DISABLE ADC12
  ADC12CTL1 = SHS_0 + SHP + CONSEQ_0 + ADC12SSEL_2 + ADC12DIV_1;
  // Trigger Source is ADC12SC bit,
  // SAMPCON is sourced from the sampling timer
  // Single-Channel, Single-Conversion
  // The ADC12 clock is sourced from MCLK, and divided by 2 (4MHz clock)
  ADC12MCTL0 = SREF_1 + INCH_10;    // Channel A10 (temp sens), Vref+/AVss
  ADC12CTL0 = SHT0_7 + SHT1_7 + REFON + ADC12ON; // Config ADC12
  // 128 clocks for sampling, reference on at 1.5V, ADC on, ADC enabled
  // 30 us sampling period based on 4MHz ADC12CLK
  ADC12IE = 0xFF;                           // Enable ADC12IFG.0
  ADC12CTL0 |=  ENC ;   // Enable the ADC
  // Start the ADC12 (30uS sampling time)
  // Enable the ADC
  ADC12CTL0 |= ADC12SC;                    // Sampling and conversion start
  while (!(0x01 & ADC12IFG));        // Conversion done? (wait until done)
  temp = ADC12MEM0;                  // Read out 1st ADC value
  _BIS_SR( GIE);
```

```
  IntDegC = (temp - 2692) * 423; // Calibration is probably necessary
  IntDegC = IntDegC / 4096;
  _NOP();                       // << SET BREAKPOINT HERE for calibration
  /*
  while (cout_busy); // wait until cout is ready.
  strcopy(tempstr, str_out); // copy temp string
  sz_str_out = strlen(str_out); // measure string length
  num2str(IntDegC, tmpstr1); // convert a number to a decimal string
  strcopy(tmpstr1,&str_out[sz_str_out]);
        // add the decimal string onto the str_out
  sz_str_out = strlen(str_out); // measure string length
  while (cout_uart0()); // wait until cout has taken the transmission
string.
  */

  // cout the temperature + ,10,13 (nl,cr)

  ADC12init(); // reset the ADC12 for Pulse Sampling
  /*
  ADC12CTL0 &=  !ENC; // DISABLE ADC12
  ADC12CTL0 = SHT0_1 + SHT1_1 + REFON + ADC12ON; // Config ADC12
  // 8 clocks for sampling, reference on at 1.5V, ADC on, ADC enabled
  // 2 us sampling period based on 4MHz ADC12CLK
  ADC12MCTL0 = SREF_1 + INCH_5;            // Channel A5, Vref+/AVss

  ADC12CTL0 |=  ENC ;   // Enable the ADC
 */
  return IntDegC;
}

//////////////
// ADC12_lib.h

unsigned int ADCVal;
int long temp;
int long IntDegC;

char ADC_result[4];

void ADC12init(void);
void ADCVal_to_ADC_resultHEX(void);
void Laser_Pulse(void);
int long ADC12_read_temp(void);


//////////////
// IO_ports.c

void init_IOports(void)
{
  volatile unsigned int i;
  volatile double j;
  // Set the ports for output
  P1DIR = 0xFF; // enable all bits in P1 as outputs
  P1SEL = 0x00; // set all pins as I/O
  P1OUT = 0x00;
  P2DIR = 0xFF; // enable all bits in P2 as outputs
  P2SEL = 0x00; // set pins as I/O
  P2OUT = 0x00;
  P3DIR |= 0x3F; // enable all non-USART bits in P3 as outputs
  // P3SEL = 0x00; // set pins as I/O
  P3OUT = 0x38; // set all pins to ground except lasers...

  P4DIR = 0x00;
  P5DIR = 0x00;

 // P5DIR = 0x20; // enable the P5.5 as an input
 // P5SEL = 0x00; // set pins as I/O
 // P5OUT = 0x00; // Set all pins to gnd

  // Set the delay to 00
  set_DS1020('0','0');

  // Set the delay to 00
  set_DS1023('0','0');

  // Ensure both lasers are on to begin.
  laser_select('0');

  P3OUT = P3OUT&(~DS1023_PTRIG);
        // set the pulse pin low so that it's ready to pulse
```

```
  // Set DS1040 to the desired pulse (15nS)
  set_DS1040(4);

}

void set_DS1040(int i)
  // P5OUT = P5OUT^((P5OUT^pulse_table[4])&DS1040Mask);
  // Abbreviated command to swap mask-selected bits into the P5OUT pins
  // 100 ms power-up time.
  // 5 ns programming time
  // 0-10 ns delay
{
  // signed int i;
//  volatile unsigned int tmp1, tmp2;
  // unsigned int setoutp=0;
  // i=a-'0';
  if ((i<=4)&&(i>=0))
  {
    P3OUT &= ~(0x0E); // zero the masked pins
    P3OUT |= pulse_table[i]; // set the proper pins on.
    // the pulse_table index chooses pulse length

 //   tmp2 = P3OUT;
 //   tmp1 = (tmp2 ^ (pulse_table[i]));
 //   tmp1 = tmp1 & DS1040Mask;
 //   P3OUT = ((tmp2) ^ (tmp1));

 /*   setoutp=~(DS1040_PB0+DS1040_PB1+DS1040_PB2);
    P3OUT &= setoutp; // set laser pins to 0.

    setoutp |= (i1&0x01)?DS1040_PB0:0x00;
    setoutp |= (i1&0x02)?DS1040_PB1:0x00;
    setoutp |= (i1&0x04)?DS1040_PB2:0x00;
    P3OUT |= setoutp;
    P3OUT &= ~setoutp;
    */

  }
}

void set_DS1023_int(signed int i1)
{
  unsigned int setoutp=0;
  if ((i1>=0)&&(i1<=255))
  {
    setoutp |= (i1&0x01)?DS1023_PA0:0x00;
    setoutp |= (i1&0x02)?DS1023_PA1:0x00;
    setoutp |= (i1&0x04)?DS1023_PA2:0x00;
    setoutp |= (i1&0x08)?DS1023_PA3:0x00;
    setoutp |= (i1&0x10)?DS1023_PA4:0x00;
    setoutp |= (i1&0x20)?DS1023_PA5:0x00;
    setoutp |= (i1&0x40)?DS1023_PA6:0x00;
    setoutp |= (i1&0x80)?DS1023_PA7:0x00;
    P2OUT = setoutp;
  }
}

void set_DS1023(signed char a1, signed char a2)
{
  signed int i1=0, i2=0;
  unsigned int setoutp=0;
  // a1 is the Low byte
  // a2 is the High byte

  if (a1!=32) // if it's a space, ignore it.
  {
    if (a1<58)
      i1=a1-48;
    else
      i1=a1-55;
  }
  if (a2!=32) // if it's a space, ignore it.
  {
    if (a2<58)
      i2=a2-48;
    else
      i2=a2-55;
  }
  i1=i1+16*i2;
```

```
  if ((i1>=0)&&(i1<=255))
  {
    setoutp |= (i1&0x01)?DS1023_PA0:0x00;
    setoutp |= (i1&0x02)?DS1023_PA1:0x00;
    setoutp |= (i1&0x04)?DS1023_PA2:0x00;
    setoutp |= (i1&0x08)?DS1023_PA3:0x00;
    setoutp |= (i1&0x10)?DS1023_PA4:0x00;
    setoutp |= (i1&0x20)?DS1023_PA5:0x00;
    setoutp |= (i1&0x40)?DS1023_PA6:0x00;
    setoutp |= (i1&0x80)?DS1023_PA7:0x00;
    P2OUT = setoutp;
  }
}

void set_DS1020_int(signed int i1)
{
  unsigned int setoutp=0;
  if ((i1>=0)&&(i1<=255))
  {
    setoutp |= (i1&0x01)?DS1020_P0:0x00;
    setoutp |= (i1&0x02)?DS1020_P1:0x00;
    setoutp |= (i1&0x04)?DS1020_P2:0x00;
    setoutp |= (i1&0x08)?DS1020_P3:0x00;
    setoutp |= (i1&0x10)?DS1020_P4:0x00;
    setoutp |= (i1&0x20)?DS1020_P5:0x00;
    setoutp |= (i1&0x40)?DS1020_P6:0x00;
    setoutp |= (i1&0x80)?DS1020_P7:0x00;
    P1OUT = setoutp;
  }
}

void set_DS1020(signed char a1, signed char a2)
{
  signed int i1=0, i2=0;
  unsigned int setoutp=0;
  // a1 is the Low byte
  // a2 is the High byte

  if (a1!=32) // if it's a space, ignore it.
  {
    if (a1<58)
      i1=a1-48;
    else
      i1=a1-55;
  }
  if (a2!=32) // if it's a space, ignore it.
  {
    if (a2<58)
      i2=a2-48;
    else
      i2=a2-55;
  }
  i1=i1+16*i2;

  if ((i1>=0)&&(i1<=255))
  {
    setoutp |= (i1&0x01)?DS1020_P0:0x00;
    setoutp |= (i1&0x02)?DS1020_P1:0x00;
    setoutp |= (i1&0x04)?DS1020_P2:0x00;
    setoutp |= (i1&0x08)?DS1020_P3:0x00;
    setoutp |= (i1&0x10)?DS1020_P4:0x00;
    setoutp |= (i1&0x20)?DS1020_P5:0x00;
    setoutp |= (i1&0x40)?DS1020_P6:0x00;
    setoutp |= (i1&0x80)?DS1020_P7:0x00;
    P1OUT = setoutp;
  }

  //    P1OUT = i1;


}

  /*
  // Set DS1020
  delay_time=0x00; // specify a delay time
  P4OUT = delay_time; // set the DS1020 delay time.
  // 100 ms power-up time
  // 50 us programming time
  // 10-48.25 ns propagation delay
  //// NOTE: It may be necessary to use the Enable (E) pin of the DS1020,
  //   though it seems that it is only truly necessary to latch a data bus.
```

```
  */
//}

void laser_select(unsigned char a)
{
  // Valid commands:
  // Value in a:      Laser 1 Status:   Laser 2 Status:
  // '0'              OFF               OFF
  // '1'              ON                OFF
  // '2'              OFF               ON
  // '3'              ON                ON

  // 20ns delay in turning on/off

  switch (a)
  {
  case '0':
    // Clear Laser 1
    P3OUT = P3OUT|LASER_D0;
    // Clear Laser 2
    P3OUT = P3OUT|LASER_D1;
    break;
  case '1':
    // Set Laser 1
    P3OUT = P3OUT&(~LASER_D0);
    // Clear Laser 2
    P3OUT = P3OUT|LASER_D1;
    break;
  case '2':
    // Clear Laser 1
    P3OUT = P3OUT|LASER_D0;
    // Set Laser 2
    P3OUT = P3OUT&(~LASER_D1);
    break;
  case '3':
    // Set Laser 1
    P3OUT = P3OUT&(~LASER_D0);
    // Set Laser 2
    P3OUT = P3OUT&(~LASER_D1);
    break;
  default:
    _NOP();
  }
  return;
}

void full_scan(void)
{
  unsigned int setoutp=0;
  unsigned int pause_counter=0;
  unsigned char Delay1023=0;
        // We will use this when scanning the delay times
  unsigned char Delay1020=0;
        // We will use this when scanning the delay times.
  char outstr[7];
//  char outval[6]; // the output value string is stored in ADC_result

  // let the user know that the scan has begun:
  put_message("/n/rBegin scan./n/r");

  Delay1023=0;
  Delay1020=0;
  outstr[2]=',';
  outstr[5]=',';
  outstr[6]=0;
  /*
  outval[3]='\n';
  outval[4]='\r';
  outval[5]=0;
  */
  do
  {
    // set DS1023 delay.
    setoutp=0;
    setoutp |= (Delay1023&0x01)?DS1023_PA0:0x00;
    setoutp |= (Delay1023&0x02)?DS1023_PA1:0x00;
    setoutp |= (Delay1023&0x04)?DS1023_PA2:0x00;
    setoutp |= (Delay1023&0x08)?DS1023_PA3:0x00;
    setoutp |= (Delay1023&0x10)?DS1023_PA4:0x00;
    setoutp |= (Delay1023&0x20)?DS1023_PA5:0x00;
    setoutp |= (Delay1023&0x40)?DS1023_PA6:0x00;
```

```
    setoutp |= (Delay1023&0x80)?DS1023_PA7:0x00;
    P2OUT = setoutp;

    do
    {
      // set DS1020 delay.
      setoutp=0;
      setoutp |= (Delay1020&0x01)?DS1020_P0:0x00;
      setoutp |= (Delay1020&0x02)?DS1020_P1:0x00;
      setoutp |= (Delay1020&0x04)?DS1020_P2:0x00;
      setoutp |= (Delay1020&0x08)?DS1020_P3:0x00;
      setoutp |= (Delay1020&0x10)?DS1020_P4:0x00;
      setoutp |= (Delay1020&0x20)?DS1020_P5:0x00;
      setoutp |= (Delay1020&0x40)?DS1020_P6:0x00;
      setoutp |= (Delay1020&0x80)?DS1020_P7:0x00;
      P1OUT = setoutp;

      // pause
      for (pause_counter=0; pause_counter<1000; pause_counter++) {_NOP();};

      // pulse the laser
      Laser_Pulse();

      // convert the recorded value to a string
      ADCVal_to_ADC_resultHEX();
      // display current delay combination
      outstr[0]= hextable[Delay1020>>4]; // upper byte of 1020 delay
      outstr[1]= hextable[Delay1020&0x0F]; // lower byte of 1020 delay
      // comma separated, comma statically added as byte 2
      outstr[3]= hextable[Delay1023>>4]; // upper byte of 1023 delay
      outstr[4]= hextable[Delay1023&0x0F]; // lower byte of 1023 delay
      // comma separated, comma statically added as byte 5
      put_message(outstr);
      // Output ADC_result
      put_subs(ADC_result,3); // output 3 hex digits.

      put_message("\n\r"); // line terminators
    }
    while ((Delay1020++)<255);
    // CAUTION: I'm using the uchar 255 rollover to terminate both while
loops here.
  }
  while ((Delay1023++)<255);
}

////////////
// IO_ports.h

// DEFINE DEVICE PINS

#define DS1020_P5 0x01
#define DS1020_P6 0x02
#define DS1020_P7 0x04
#define DS1020_P4 0x08
#define DS1020_P3 0x10
#define DS1020_P2 0x20
#define DS1020_P1 0x40
#define DS1020_P0 0x80

#define DS1023_PA5 0x01
#define DS1023_PA6 0x02
#define DS1023_PA7 0x04
#define DS1023_PA4 0x08
#define DS1023_PA3 0x10
#define DS1023_PA2 0x20
#define DS1023_PA1 0x40
#define DS1023_PA0 0x80
#define DS1023_PTRIG 0x01

#define DS1040_PB0 0x02
#define DS1040_PB1 0x04
#define DS1040_PB2 0x08

#define LASER_D0 0x10
#define LASER_D1 0x20

#define USART_PWREN 0x20

#define BUTTON_1 BIT4

int Debounce_Count_1; // Used for debouncing the button.
```

```
unsigned int delay_time; // delay time is set using the DS1020
// Hex   Binary     Time (nS)
// 0x00  0000 0000  10
// 0x01  0000 0001  10.15
// 0x02  0000 0010  10.30
// 0x03  0000 0011  10.45
//  //    //   //    //
// 0xFE  1111 1110  48.10
// 0xFF  1111 1111  48.25

unsigned int pulse_width; // Pulse width is set using the DS1040

// DS1040-A15, ToF2 rev 2
// Hex   Binary     Time (nS)
// 0x00  0000 0000  15
// 0x20  0010 0000  5
// 0x40  0100 0000  7.5
// 0x60  0110 0000  10
// 0x80  1000 0000  12.5
// 0xA0  1010 0000  15

const unsigned char pulse_table[5] = { DS1040_PB0, DS1040_PB1,
(DS1040_PB0+DS1040_PB1), DS1040_PB2, (DS1040_PB0+DS1040_PB2) };
// this is a lookup table for setting the pulse width

// DS1040-A20:
//  pulse_table[0]->10nS, [1]->12.5nS, [2]->15nS, [3]->17.5nS, [4]->20nS

// for DS1040-A15
// using this, pulse_table[0] gives 5nS, pulse_table[1] gives 7.5nS...

// const unsigned int DS1020Mask=0xFF;
// No DS1020 Mask is needed, since it uses the whole port
/*
const unsigned int DS1040Mask = 0xE0;
const unsigned int Laser1Mask = 0x02;
const unsigned int Laser2Mask = 0x08;
*/
//  DS1020Mask=0xFF; // all 8 bits used
//  Laser1Mask=0x01; // bit 0 used
//  Laser2Mask=0x02; // bit 1 used
//  DS1040Mask=0xE0; // bits 5-7 used

// const unsigned int PulsePin = 0x01;
// the pin to toggle to pulse the laser

void init_IOports(void);

void laser_select(unsigned char);
void set_DS1040(int);
void set_DS1023_int(signed int);
void set_DS1023(signed char, signed char);
void set_DS1020_int(signed int);
void set_DS1020(signed char, signed char);

// Francis USART0 Cyclic Buffer Module

#define IOBufferLen 256
// I'm using a character buffer of 256, with char position counters
// 0xFF overflows to 0x00, and 0x00 underflows to 0xFF automatically.

char TXBUF[IOBufferLen];
char TXCount, TXWrite, TXRead, TXBusy;
// Program always writes to the XXWrite, and reads from XXRead.
// XXCount is always >=0 and < (IOBufferLen-1)

void initUART1(void)
{
  int i=0;
  // Enable 115kbps communication

  P3SEL |= BIT6;                          // P3.6,7 = USART1 TXD/RXD select
  P3DIR |= BIT6; // UTXD1 as output

  U0CTL |= CHAR + SWRST;
  U1CTL |= CHAR + SWRST;                  // 8-bit character
  ME2 |= UTXE1;                       // Enable USART1 TXD/RXD
  U1TCTL |= SSEL1;                        // UCLK = SMCLK
 // U1RCTL |= URXWIE; // URX Wake up enable
  U1BR0 = 0x45;                           // 8Mhz/115200 - 69.44
```

```
  U1BR1 = 0x00;                             //
  U1MCTL = 0xAA;                            // modulation
  U1CTL &= ~SWRST;                          // Initialize USART state machine
  IE2 |= UTXIE1;                            // Enable USART1 RX interrupt
  // Setup Communication Library
  for (i=0; i<IOBufferLen; i++)
  {
    TXBUF[i]=0;
  }
  TXCount=0;
  TXWrite=0;
  TXRead=0;
  TXBusy=0;

  /*
  while ( USART_PWREN & P5IN ) // Wait for DLP-USB232M windows enumeration
    _NOP();
  */

  _BIS_SR(GIE);
}

signed char putchar(char a)
{
  if (TXCount<255)
  {
    // disable TX interrupt
    _BIC_SR( GIE); // bit clear
    TXBUF[TXWrite++]=a;
    TXCount++;
    // enable TX interrupt
    _BIS_SR( GIE); // bit set.
    return a;
  }
  else
    return -1;
}

static void put_subs(char *s, int sz_s)
{
  int i=sz_s;
  while (i--)
    putchar(*s++);
}

static void put_message(char *s)
{
  while (*s)
    putchar(*s++);
}

#pragma vector=USART1TX_VECTOR
__interrupt void usart1_tx(void)
{
  if (TXCount>0) {
// do this if there is still data in the buffer and the TX buffer is ready.
    U1TXBUF=TXBUF[TXRead++];
    TXCount--;
  }
}

//////////////
// USART_lib.h

unsigned const char
hextable[]={'0','1','2','3','4','5','6','7','8','9','A','B','C','D','E','F'
};

char hellostr[]="\n\rToF 3 rev.1 Bootup Complete.\n\r\n\r\n\r";

char tempstr[]="Temp (C): ";

char StrProc[80];

void initUART1(void);
signed char putchar(char);
static void put_subs(char*, int);
static void put_message(char*);
```

A.4 Mellin Transform for Estimating Statistical Moments

To estimate scattering from pulsed-light measurements, analytical descriptors may be used to distil the data into terms which can be measured using simplified electronics in the future. The use of statistical moments has been previously demonstrated by Leonardi.[166, 249, 250] Moments may be mapped to properties of the response profile curvature. The moments of the temporal distribution are calculated in several steps. First, the Mellin transform, $\Gamma^*(s)$, is calculated from the optical pulse intensities, $\Gamma(t)$:

$$\Gamma^*(s) = M[\Gamma(t); s] = \int_0^\infty t^{s-1}\Gamma(t)\partial t \tag{A.1}$$

Next, the moments are calculated using the Mellin transformed data from the following functions, where the nth moment is represented as σ_n (with n from 1 to 4).

$$\langle t^n \rangle = \frac{\int_0^\infty t^n \Gamma(t)\partial t}{\int_0^\infty \Gamma(t)\partial t} = \frac{\Gamma^*(n+1)}{\Gamma^*(1)} \tag{A.2}$$

$$\sigma_0 = \Gamma^*(1),$$

$$\sigma_1 = \langle t \rangle,$$

$$\sigma_n = \langle t^n \rangle = \frac{\int_0^\infty (t - \langle t \rangle)^n \Gamma(t)\partial t}{\int_0^\infty \Gamma(t)\partial t} \tag{A.3}$$

The zeroth moment of the Mellin transform is the integrated intensity. Mean time of a pulse is calculated from the first moment.

Standard deviation is calculated as the square root of the second moment. Skew is calculated as the third moment divided by the second moment to the power 3/2. Finally, kurtosis is calculated from the fourth moment divided by the square of the second moment minus 3. The moments were taken as defined by Arridge.[166]

Appendix B: Ring-Light Device

Source code for three different Matlab functions have been included here for generating amplitude filters for making the ring patterned lasers. Ring-patterned light is used in mathematics, physics, engineering and chemistry. Each field uses different terminology, including: vortex light, orbital angular momentum light, spirally phased light, and phase singularities. Several methods for generating the ring patterns were examined. Three such approaches are included here. In the first, OAMmask.m, a real-valued plane phase mask is generated to emphasize a single phase-spiral order. In the second, squareOAMmask.m, a binarized plane phase mask is generated to produce multiple phase-spiral orders. In the third, rotOAMmask.m, a real-valued plane phase mask is generated in which the planar wave is incident at an angle in order to produce a spiral phase wave normal to the filter.

```
function [mask]=squareOAMmask( angle, orders, masksize)

% function squareOAMmask, used to make a thresholded
%  spiral phase function image pattern (vortex light).
%
% Usage: [mask]=squareOAMmask( angle, orders, masksize) where angle is
    the
% angle of incidence of the reference beam relative to the main planar
% beam. (also the angle at which the generated OAM beam propagates)
    orders
% determines the number of passes used to create the square-wave pattern.
% Make this a number such as 20 or 30 to see a very well thresholded
% pattern. Masksize is the number of pixels for both the x and y axes.
%(final mask is of size 2*masksize+1, over both x & y directions)
%
% Example call:
%   [mask]=squareOAMmask( 5, 5, [500,500]);
%       To generate a large binary mask.
```

```
%   [mask]=squareOAMmask( 5, 1, [50,50]);
%       To generate a small fuzzy mask.
%
% This squareOAMmask function is derived from the following paper:
   Optical
% and Quantum Electronics, 24 (1992) S951-S962 Laser beams with phase
% singularities, N.H. Heckenberg, R. McDuff, C.P. Smith, H.
% Rubinsztein-Dunlop, and M.J. Wegener Department of Physics, the
% University of Queensland, Brisbane, Australia see page S954, equation
   (8)

% calculate the kx for the incident reference beam, from the angle of
% interference.
kx=sin(pi*angle/180);

% % generate a matrix of x-positions and y-positions for each pixel.
xpositions=[-masksize(1):masksize(1)]'*ones(1,1+2*masksize(2));
ypositions=[[-masksize(2):masksize(2)]'*ones(1,1+2*masksize(1))]';

% determine the phase angles for each pixel relative to the center of the
% Gaussian beam.
[theta,r]=cart2pol(xpositions,ypositions);

% % plot the phase angles figure; imagesc(theta);

% % generate the OAM filter as a 2d array of intensities
mask=0.5*ones(size(theta));
% % the triple-commented code is to show the mask being built, as each
   new
% % layer is added % % figure; % % mesh(mask) % % pause
for i=1:orders;
    mask = mask - (sin(i*pi/2)/(i*pi/2))*cos( i*(kx*ypositions-theta) );
% If xpositions is used in the mask instead of ypositions, then the mask
   is
% completely different. % %     mesh(mask) % %     pause
end

% % display the OAM filter.
figure;
imshow(mask)
```

```
function [mask]=OAMmask( angle, masksize)

% function OAMmask, generate a non-binarized vortex light holograph.
%
% Usage: [mask]=OAMmask( angle, masksize)
% with angle being the angle of incidence for the reference beam
%   (and the angle at which the generated OAM beam propagates)
% and masksize being used to determine the number of pixels for both the
x
% and y axes.
%   (the final mask size will be of size 2*masksize+1, over both
directions)
%
% Example call:
%   [mask]=OAMmask( 5, [500,500]);
%
% This OAMmask function is derived from the following paper:
% Optical and Quantum Electronics, 24 (1992) S951-S962
% Laser beams with phase singularities, N.H. Heckenberg, R. McDuff,
% C.P. Smith, H. Rubinsztein-Dunlop, and M.J. Wegener
% Department of Physics, the University of Queensland, Brisbane,
Australia
% see page S954, equation (5)

% % calculate the kx for the incident reference beam, based on the angle
of interference.
kx=sin(pi*angle/180);
```

```
% % generate a matrix of x-positions and y-positions for each pixel.
xpositions=[-masksize(1):masksize(1)]'*ones(1,1+2*masksize(2));
ypositions=[[-masksize(2):masksize(2)]'*ones(1,1+2*masksize(1))]';

% % determine the phase angles for each pixel relative to the center of
the
% % Gaussian beam.
[theta,r]=cart2pol(xpositions,ypositions);

% % plot the phase angles
% figure; imagesc(theta);

% % generate the OAM filter as a 2d array of intensities
mask = 0.5*(1-cos(kx*xpositions-theta));
% % If xpositions is used in the mask instead of ypositions, then the
mask is
% % completely different.

% % display the OAM filter.
figure;
imshow(mask)
```

```
function [mask]=rotOAMmask( omega, masksize, wavenum)

% function rotOAMmask, to generate OAM beams from a plane wave incident
at
% an angle omega from the filter normal, such that the final
annular/vortex
% beam propagates normal to the filter rather than at an angle.
%
% Usage: [mask]=rotOAMmask( angle, masksize, wavelength) with angle being
% the angle of incidence for the reference beam
%   (and the angle at which the generated OAM beam propagates)
% and masksize being used to determine the number of pixels for both the
x
% and y axes.
%   (the final mask size will be of size 2*masksize+1, over both
%   directions)
%
% Example usage:
%   [mask]=rotOAMmask( 30, [1000, 1000], 650);
%
% This OAMmask function is derived from the following paper: Optical and
% Quantum Electronics, 24 (1992) S951-S962 Laser beams with phase
% singularities, N.H. Heckenberg, R. McDuff, C.P. Smith, H.
% Rubinsztein-Dunlop, and M.J. Wegener Department of Physics, the
% University of Queensland, Brisbane, Australia see page S954, equation
(5)
% Additional modifications by Francis Esmonde-White to rotate the
computed
% filter plane.

% % calculate the kx for the incident reference beam, based on the angle
of
% interference.
kx=sin(pi*omega/180);

% % generate a matrix of x-positions and y-positions for each pixel.
xpositions=[-masksize(1):masksize(1)]'*ones(1,1+2*masksize(2));
ypositions=[[-masksize(2):masksize(2)]'*ones(1,1+2*masksize(1))]';


% the interference plane
zpositions=xpositions*kx;
xpositions=xpositions*cos(pi*omega/180);
```

```
% % determine the phase angles for each pixel relative to the center of
the
% % Gaussian beam.
[theta,r]=cart2pol(xpositions,ypositions);
% figure; imagesc(theta)

% the plane wave has intensity 1 everywhere
mask=0.5*(1-cos(3/2*pi-theta+2*pi*zpositions/wavenum));

% for each theta, we need to add the change due to the difference in the
z
% plane position (which z=0 has become z*cos(theta)+x*sin(theta)=0)

% % plot the phase angles figure; imagesc(theta);

% % generate the OAM filter as a 2d array of intensities mask =
% 0.5*(1-cos(kx*xpositions-theta)); % If xpositions is used in the mask
% instead of ypositions, then the mask is % completely different.

% display the OAM filter.
figure;
imshow(mask)
```

Appendix C: Genetic Algorithm Code

```
function thesis_GA(savefile)
warning off

% Thesis GA

% load lactate data
% wlrange=find((wave>=1500)&(wave<=1750));
load lactate

numtot=10; % ten samples total
numval=1; % choose 4 validation samples
numspec=4; % 4 spectra per sample
numwl=size(data,2); % 987 wavelengths
sampleset=1:numspec:numtot*numspec;
comb=nchoosek(sampleset,numval); % permutation combinations
pop_sz=200; % 200 population members
N=6; % maximum possible number of pre-processing steps.

% Size information for the genetic bitstring representation of models
numbits_preproc=N*14; % number of bits required for the pre-processing
    option
numbits_HT=2^ceil(log2(numwl)); % number of bits required for Haar
    transform selection
numbits=numbits_preproc+numwl+numbits_HT; % total number of bits required

GA_iter_max=pop_sz*50; % number of evolution iterations
saveinterval=50; % interval (in evolution steps) at which to save the
    results

maxmodelsz=numtot*numspec; % choose a maximum number of wavelengths to
    allow in a solution

% initialize matrix sizes
bestmodels=false(maxmodelsz,N+1,numbits); % store the best population
    members
bestmodelsres=NaN(maxmodelsz,N+1); % store indeces to results for the
    best members
bestmodelfit=NaN(maxmodelsz,N+1); % fitness values of the best members
modelcount=zeros(maxmodelsz,N+1); % number of models built in each
    category
popfitness=zeros(1,pop_sz); % vector of population fitnesses
popres=zeros(1,pop_sz); % indeces pointing to results for each of the
    current population members

% randomly generate an initial GA population
% total number of bits:
% pre-processing options + wavelength selection + FWT component selection
% N*14+numwl+ (1:(2^ceil(log2(numwl))))
pop=[(rand(pop_sz,numbits_preproc)<0.5),
    (rand(pop_sz,numwl)<((numtot*numspec)/(5*numwl))),
    (rand(pop_sz,numbits_HT)<((numtot*numspec)/(5*numbits_HT)))];

init_mut_rate=0.10; % initial mutation rate
mut_rate=0.10; % 10% mutation rate

% big matrix in which to store results for all evaluate strings
%       (indexed by popres and bestmodelsres)
result=zeros(GA_iter_max,10);

% begin the GA
for GA_iter=1:GA_iter_max

    disp(['Iteration: ',num2str(GA_iter)]) % let the user know how things
    are progressing

    if mod(GA_iter,saveinterval)==0 % periodically save based on the
    selected interval
```

```
     save(savefile) % the savefile is selected in the GA function
call.
     mut_rate=mut_rate+0.004; % increase the mutation rate as the
evolution progresses
 end

 % select the genetic vector to evaluate for fitness (by copying to
"bitstring")
 if GA_iter<=pop_sz  % Fitnesses of the randomly initialized
population are first
     % evaluated. By taking the vector from the population at the
current index.
     bitstring=pop(GA_iter,:);

 else % Make a new vector from the existing population and process it.
     [popfitness,popind]=sort(popfitness,'ascend'); % sort the
population according to fitness
     % This depends on the type of fitness value used. (examples in
brackets)
     % Ascending fitness sorting will leave small values at the top.
(residual, cost)
     % Descending fitness sorting will leave big values at the top.
(linearity, probability)

     % popfitness=popfitness(1:ev_pop_size); % Already sorted
     pop=pop(popind,:); % sort the population members according to the
fitness
     popres=popres(popind); % keep the results vector correctly
indexed

     % FITNESS ORDERING/SCALING
     scaled_fitnesses = cumsum(1./popfitness);

     % scale the fitnesses between zero and one
%      minfit = min(scaled_fitnesses);
     maxfit = max(scaled_fitnesses);
%      scaled_fitnesses = (scaled_fitnesses-minfit)/(maxfit-
minfit+eps);
     scaled_fitnesses = (scaled_fitnesses)/(maxfit+eps);

     % find the first parent based on the scaled fitness
     parent1 = find(scaled_fitnesses<=rand(1),1,'last');
     if isempty(parent1)  % if no first parent is selected yet
         parent1=1;
     end

     % crossover & mutation
     mut = rand(1)<mut_rate; % mutation?

     if (mut) % if performing a mutation evolution step
         mut_count=ceil(5*abs(randn(1)).^1.5); % number of mutations
         % distribution of mutation counts so there are some rare
         % mutations of many bits and many mut's with few bits

         bits_to_mutate=1+ceil(rand(1,mut_count)*(numbits-1));% bit
positions to mutate

         % perform the mutation
         bitstring = pop(parent1,:); % copy the original vector
         bitstring(bits_to_mutate)=~bitstring(bits_to_mutate); %
invert the selected bits

     else % if performing a crossover evolution step
         n_cx=ceil((rand(1)^3)*4); % initial number of crossover
points

         cx_ind=unique(1+ceil(rand(1,n_cx)*(numbits-1))); % choose the
crossover points
         n_cx=numel(cx_ind); % count of unique crossover steps

         % find the second parent based on the scaled fitness
         parent2 = find(scaled_fitnesses<=rand(1),1,'last');
```

```
        % index of the second parent selected (the first is selected
above)

        % Error checking
        if isempty(parent2) % if no second parent is selected yet
            parent2=2; % default second parent.
        end
        % if the same parent is selected for both parents
        if parent1==parent2;
            parent2=mod(parent1+1,pop_sz-1)+1; % select a different
second parent
        end

        % Perform the crossover
        % at least one crossover point must be present
        bitstring =
[pop(parent1,1:cx_ind(1)),pop(parent2,(cx_ind(1)+1):end)];
        if (n_cx>=2) % if two cx points, then add next segment.
            bitstring((cx_ind(2)+1):end) =
pop(parent1,(cx_ind(2)+1):end);
            if (n_cx>=3) % if 3 cx points, then add next segment.
                bitstring((cx_ind(3)+1):end) =
pop(parent2,(cx_ind(3)+1):end);
                if (n_cx==4) % if 4 cx points, then add next segment.
                    bitstring((cx_ind(4)+1):end) =
pop(parent1,(cx_ind(4)+1):end);
                end
            end
        end
    end
end


% initialize result vectors for the permutation fitness evaluation
    ctrue=[]; % known calibration concentrations
    cest=[]; % estimated calibration concentrations
    vtrue=[]; % known validation concentrations
    vest=[]; % estimated validation concentrations
    sens=[]; % sensitivity from each calibration
    tic; % start the timer

for permut=1:size(comb,1); % choose the permutation iteration
    % process all permutations of the data using the model bitstring.

    % initialize the temporary calibration and validation data
    cal=zeros((numtot-numval)*numspec,987); % calibration spectra
    cal_known=zeros(1,(numtot-numval)*numspec); % calibration
reference values
    val=zeros(numval*numspec,987); % validation spectra
    val_known=zeros(1,numval*numspec); % validation reference values

    % select data for calibration (not already selected for
validation)
    comb_compl=setdiff(sampleset,comb(permut,:));
    % comb is initialized at the beginning of the function, and
    % contains the nchoosek() permutation orderings
    for i=1:(numtot-numval);
        % r and r2 just get the correct indeces
        r=(1:numspec)+numspec*(i-1);
        r2=(1:numspec)+comb_compl(i)-1;
        cal(r,:)=data(r2,:); % select the calibration data
        cal_known(r)=known(r2); % select the calibration reference
values
    end

    % copy the validation data into the temporary matrices
    for i=1:numval;
        r=(1:4)+4*(i-1);
        r2=(1:4)+comb(permut,i)-1;
        val(r,:)=data(r2,:); % select the validation data
        val_known(r)=known(r2); % select the validation reference
values
```

```
    end

    % Evaluate the fitness of the current bitstring

[tmp,ce,ck,ve,vk]=GA_processing(cal,cal_known,val,val_known,bitstring
,numwl,N);

    % store the temporary results
    ctrue=[ctrue,ck];
    cest=[cest,ce];
    vtrue=[vtrue,vk];
    vest=[vest,ve];
    sens=[sens,tmp(5)];

end

% check that the fitness function returned the right number of total
% values (when the model fails, it will not return consistent
numbers)
if (numel(ctrue)==numel(cest))&(tmp(6)<numel(vtrue))

    % MSE(Mean Square Error)
    % from:
    %   Probability and Statistics for engineering and the sciences,
    %   Jay L. Devore, Sixth Edition. Brooks/Cole - Thomson learning.
2004
    %   Chapter 13 (13.4 in particular)
    % n is the number of y-values or equations.
    n(1)=numel(ctrue); % n for calibration
    n(2)=numel(vtrue); % n for validation

    % This is where PARSIMONY is applied. Either define MSE as:
    %
    % No parsimony
    % SSE/(n) for no parsimony
    %
    % Parsimony with # wavelengths
    % SSE/(n-(k+1)) where k is # of wavelengths for parsimony by WL
    %
    % Parsimony with # wavelengths & # pre-processing options
    % SSE/(n-(k+1)) where k is # of wl & # of pre-processing options

    k=tmp(6); % k is the number of wavelengths used in the model

    % Use the following line for WL & PP option penalty
    k=k+tmp(7); % k is now additionally penalized for the number of
pp options used in the model

    SST(1)=sum(ctrue.^2)-(sum(ctrue)^2)/n(1);
    SSE(1)=sum((cest-ctrue).^2);
    SST(2)=sum(vtrue.^2)-(sum(vtrue)^2)/n(2);
    SSE(2)=sum((vest-vtrue).^2);

    MSE(1)=SSE(1)/(n(1)-(k+1)); % p. 594 of Devore's book
    MSE(2)=SSE(2)/(n(2)-(k+1));

    result(1)=MSE(1);
    result(2)=MSE(2);

    R2(1)=1-SSE(1)/SST(1);
    R2(2)=1-SSE(2)/SST(2);

    R2adj(1)=((n(1)-1)*R2(1)-k)/(n(1)-(k+1));
    R2adj(2)=((n(2)-1)*R2(2)-k)/(n(2)-(k+1));

    result(GA_iter,1)=MSE(1);
    result(GA_iter,2)=MSE(2);
    result(GA_iter,3)=R2adj(1);
    result(GA_iter,4)=R2adj(2);

    % Non-parsimony penalized results for storage & later comparison.
    result(GA_iter,9)=sqrt(sum((ctrue-cest).^2)/numel(ctrue)); % RMSE
```

```
    result(GA_iter,10)=sqrt(sum((vtrue-vest).^2)/numel(vtrue));
         % RMSE

    % Alternate measure (RMSE, MSE, or SDEP are equivalent)
    %   result(GA_iter,1)=sqrt(sum((ctrue-cest).^2)/numel(ctrue));
    %   result(GA_iter,2)=sqrt(sum((vtrue-vest).^2)/numel(vtrue));
    %   % Corresponds to SDEP of R. Todescini et al., p. 160, Nature
    %   % inspired methods in chemometrics:... (2003 Leardi book)
else
    % if invalid model, result is set to not-a-number
    result(GA_iter,1:4)=NaN;
end

% store model details in the results matrix
result(GA_iter,5)=mean(sens); % mean sensitivity
result(GA_iter,6)=tmp(6); % store # wavelengths selected
result(GA_iter,7)=tmp(7); % store # pre-processing options selected
result(GA_iter,8)=toc; % store total processing time

% Display model processing time (allows a rough estimate of the
% required time for a complete algorithm run.
disp(['     Mean/total model processing time: ',
      num2str([result(GA_iter,8)/permut,result(GA_iter,8)])]);

% determine the statistical properties of the model.
if (result(GA_iter,6)>0)&~sum(isnan(result(GA_iter,:)));
   % if the model is properly evaluated
    % select the fitness property to use: this allows different
results to be chosen.
    str_fitness=result(GA_iter,2); % MSE adjusted for model size

else % otherwise the model fitness is set to not-a-number
    str_fitness=NaN;
end

% if the new model is succesfully evaluated and has suitably good
fitness,
% and there is no current best model or the model is better than the
current best model... then
% store it for later comparison in the 'bestmodels' arrays.
tmp_wlcount=result(GA_iter,6);
tmp_ppcount=result(GA_iter,7);
if ~isnan(str_fitness)&(tmp_wlcount<=maxmodelsz)

modelcount(tmp_wlcount,tmp_ppcount+1)=modelcount(tmp_wlcount,tmp_ppco
unt+1)+1;
    if
isnan(bestmodelfit(tmp_wlcount,tmp_ppcount+1))|(str_fitness<bestmodel
fit(tmp_wlcount,tmp_ppcount+1))
       bestmodels(tmp_wlcount,tmp_ppcount+1,:)=bitstring;
       bestmodelsres(tmp_wlcount,tmp_ppcount+1)=GA_iter;
       bestmodelfit(tmp_wlcount,tmp_ppcount+1)=str_fitness;
    end
end

if GA_iter<=pop_sz % if evaluating the population for the first time,
then store all the results
    popfitness(GA_iter)=str_fitness;
    popres(GA_iter)=GA_iter;
else % if evaluating evolution members, then compare & replace a
suitable member.

    % either replace the first parent, or the last bitstring in the
    % population, depending if the new bitstring is better than the
    % parent1 or the pop(end) members.
    if ~isnan(str_fitness)
        if
isnan(popfitness(parent1))|(str_fitness<=popfitness(parent1))
            % Replace the first parent
            popfitness(parent1)=str_fitness;
            pop(parent1,:)=bitstring;
            popres(parent1)=GA_iter;
```

```
            else
                % replace the first unsuccesful member of the population
                % (where fitness is 'NaN')
                ind=find(isnan(popfitness),1,'first');
                if (~isempty(ind)) % if there is a NaN member, replace
    it.
                    popfitness(ind)=str_fitness;
                    pop(ind,:)=bitstring;
                    popres(ind)=GA_iter;
                else % otherwise find the last member with lower fitness
                    ind=find(popfitness>=str_fitness,1,'last');
                    if (~isempty(ind)) % if there is a lower member,
    replace it.
                        popfitness(ind)=str_fitness;
                        pop(ind,:)=bitstring;
                        popres(ind)=GA_iter;
                    else % if none of these is replaced, then keep the
    member anyways
                        % replace one of the 20% worst members anyways
                        % (serves to keep some randomized members &
    maintain genetic diversity)
                        ind=ceil((.8+rand(1)/5)*pop_sz);
                        popfitness(ind)=str_fitness;
                        pop(ind,:)=bitstring;
                        popres(ind)=GA_iter;
                    end
                end
            end
        end
    end

end
warning on



%%%%% Support Functions %%%%%
%%%%%%%%%%%%%%%%%%%%%%%%%%%%%

%%%% Function graytoreal
function realval=graytoreal(bitstring)
% convert the gray coded bitstring into a real value and return as
    realval

binstr = bitstring;
% convert gray code to binary
for k=2:numel(bitstring)
    if (binstr(k-1))
        binstr(k)= ~binstr(k);
    end
end
% convert the binary string to a real value
realval = polyval(binstr, 2);

%%%% Function second_deriv
function [modeldata, testdata] = second_deriv(modeldata, testdata,
    window, gap, v)
% Second derivative function

window=2*round((window-0.1)/2)+1; % an odd integer
gap=2*round((gap-0.1)/2)+1; % an odd integer

gapderiv=zeros(1,gap);
gapderiv((gap-1)/2)=-2;
gapderiv([1,end])=1;
filter=conv(conv(ones(1,window),ones(1,window)),gapderiv/gap);
ends = (numel(filter)-1)/2;

modeldata=conv2(modeldata,filter);
cutoff1 = round((size(modeldata,2)-v)/2);
cutoff2 = size(modeldata,2)-v-cutoff1;
```

```
modeldata(:,[1:cutoff1, (end-cutoff2+1):end])=[];
modeldata(:,1:ends)=repmat(modeldata(:,ends+1),[1,ends]);
modeldata(:,(end-ends+1):end)=repmat(modeldata(:,end-ends),[1,ends]);

testdata=conv2(testdata,filter);
testdata(:,[1:cutoff1, (end-cutoff2+1):end])=[];
testdata(:,1:ends)=repmat(testdata(:,ends+1),[1,ends]);
testdata(:,(end-ends+1):end)=repmat(testdata(:,end-ends),[1,ends]);

%%%%% Function first_deriv
function [modeldata, testdata] = first_deriv(modeldata, testdata, window,
   gap, v)
% First Derivative function

window=2*round((window-0.1)/2)+1; % an odd integer
gap=2*round((gap-0.1)/2)+1; % an odd integer

% double smooth

gapderiv=zeros(1,gap);
gapderiv(1)=1;
gapderiv(end)=-1;
filter=conv(conv(ones(1,window),ones(1,window)),gapderiv/gap);
ends = (numel(filter)-1)/2;

modeldata=conv2(modeldata,filter);
cutoff1 = round((size(modeldata,2)-v)/2);
cutoff2 = size(modeldata,2)-v-cutoff1;
modeldata(:,[1:cutoff1, (end-cutoff2+1):end])=[];

modeldata(:,1:ends)=repmat(modeldata(:,ends+1),[1,ends]);
modeldata(:,(end-ends+1):end)=repmat(modeldata(:,end-ends),[1,ends]);

testdata=conv2(testdata,filter);
testdata(:,[1:cutoff1, (end-cutoff2+1):end])=[];
testdata(:,1:ends)=repmat(testdata(:,ends+1),[1,ends]);
testdata(:,(end-ends+1):end)=repmat(testdata(:,end-ends),[1,ends]);

%%%%% Function haar1d
function Dout=haar1d(Din)
% Take the 1D Haar Transform along the second dimension:
%  based on http://www.cs.ucf.edu/~mali/haar/
%
% The algorithm pads the data with the last datapoint in each vector to a
% length of 2^ceil(log2(size(data,2))).
%
% Usage: Dout=haar1d(Din);
%
% Francis Esmonde-White, July 2007

n=2^ceil(log2(size(Din,2)));
w=n;
[sz1,sz2]=size(Din);

Dout=zeros(sz1,n);
% D=zeros(1,n);
D=repmat(Din(:,end),[1,n]);
D(:,1:sz2)=Din;
sqrt2=sqrt(2);
while (w>1);
    w=w/2;
    for i=0:(w-1);
        Dout(:,i+1)=(D(:,2*i+1)+D(:,2*i+2))/sqrt2;
        Dout(:,i+w+1)=(D(:,2*i+1)-D(:,2*i+2))/sqrt2;
    end
    for i=1:(w*2)
        D(:,i)=Dout(:,i);
    end
end

%%%%% Function GA_processing (regression fitness function)
```

```
function [result,cal_est,cal_known,val_est,val_known] =
    GA_processing(cal,cal_known,val,val_known,bitstring,numwl,N)
% GA_processing function
%
% Takes the calibration and validation data, along with the known
% assignments, and estimates the fitness of the model specified by
% bitstring.
%
% numwl is the number of wavelengths.
% N is the number of pre-processing options.
%
% The output is a vector 'result' that contains the desired model
% performance information.

is_HWT = false; % by default we assume that we do not use the HWT
is_badmodel = false; % by default we assume that the model is good
result=zeros(1,5); % initialize the result array

opt_count=0; % initialize the count of pre-processing options to use

% initialize the calibration and validation estimate vectors
cal_est=NaN;
val_est=NaN;

% First we check to ensure that the current model has some wavelengths
    selected!
for preproc_N=1:N; % iterate through the pre-processing options
    Pbits=bitstring((1:14)+(preproc_N-1)*14); % select the relevant pre-
    processing option string
    Pvals(1)=graytoreal(Pbits(1:4)); % convert the pre-processing string
    to a real value
    if (Pvals(1)>=1)&(Pvals(1)<=12) % Does the selected option value
    specify a pre-processing step?
        opt_count=opt_count+1;
    end

    % is the haar transform option selected?
    if (Pvals(1)==12)
        % FWT
        is_HWT=true;
    end
end

% we need to check to ensure that some parameters are used in the
    regression.
if is_HWT
    % ensure that at least one HWT parameter is selected for regression
    if (sum(bitstring(N*14+(1:numwl)))==0)
        % model has no selected wavelengths
        is_badmodel=true;
    end
else
    if sum(bitstring(N*14+numwl+ (1:(2^ceil(log2(numwl))))))==0
        % model has no selected wavelengths
        is_badmodel=true;
    end
end

% if the model doesn't use any wavelengths, it's a bad model and should
    be skipped.
if is_badmodel
    result(1:7)=NaN;
    return;
end

for preproc_N=1:N; % For each pre-processing option

    % First chop the bitstring into a series of Pbits, for each allowed
    option
    Pbits=bitstring((1:14)+(preproc_N-1)*14); % preproc_N specifies the
    index of the current pre-processing option
```

```
% Next decode Pbits into Pvals
% Pbits is stored as Grey code, and must be decoded to real values.

% Pvals(1) is the selected technique, between 0 and 15
% 4 bits
Pvals(1)=graytoreal(Pbits(1:4));
% Pvals(2) selects wavelength axis (0) or sample axis (1)
% 1 bit
Pvals(2)=Pbits(5);
% Pvals(3) specifies smoothing window, an integer between 1 and 32.
% 5 bits
Pvals(3)=graytoreal(Pbits(6:10))+1;
% Pvals(4) specifies derivative gap, an odd integer between 3 and 34.
% 4 bits
Pvals(4)=2*graytoreal(Pbits(11:14))+3;

% Allow N spaces for pre-processing to enable that many options and
allow
% them to self-order.
switch Pvals(1)
    case 0
        % do nothing, the option is disabled.
    case 1
        % mean centering
        % Pvals(2)==0 by wavelength
        if (Pvals(2)==0)
            val=val-repmat(mean(cal),[size(val,1),1]);
            cal=cal-repmat(mean(cal),[size(cal,1),1]);
        % Pvals(2)==1 by sample
        elseif (Pvals(2)==1)
            val=val-repmat(mean(val,2),[1,size(val,2)]);
            cal=cal-repmat(mean(cal,2),[1,size(cal,2)]);
        end
    case 2
        % autoscaling
        % Pvals(2)==0 by wavelength
        %   mean center by wavelength and scale by wavelength
variance
        if (Pvals(2)==0)
            val=val-repmat(mean(cal),[size(val,1),1]);
            cal=cal-repmat(mean(cal),[size(cal,1),1]);

            val=val./repmat(std(cal),[size(val,1),1]);
            cal=cal./repmat(std(cal),[size(cal,1),1]);
        % Pvals(2)==1 by sample
        %   mean center by sample and scale by sample variance
        elseif (Pvals(2)==1)
            val=val-repmat(mean(val,2),[1,size(val,2)]);
            cal=cal-repmat(mean(cal,2),[1,size(cal,2)]);

            val=val./repmat(std(val,0,2),[1,size(val,2)]);
            cal=cal./repmat(std(cal,0,2),[1,size(cal,2)]);
        end
    case 3
        % scale to variance
        % Pvals(2)==0 per wavelength
        if (Pvals(2)==0)
            val=val./repmat(std(cal),[size(val,1),1]);
            cal=cal./repmat(std(cal),[size(cal,1),1]);
            % Pvals(2)==1 per sample
        elseif (Pvals(2)==1)
            val=val./repmat(std(val,0,2),[1,size(val,2)]);
            cal=cal./repmat(std(cal,0,2),[1,size(cal,2)]);
        end
    case 4
        % scale range to 0-1
        % Pvals(2)==0 per wavelength
        if (Pvals(2)==0)
            minc=min(cal);
            rangec=max(cal)-minc;
            val=(val-
repmat(minc,[size(val,1),1]))./repmat(rangec,[size(val,1),1]);
```

```
            cal=(cal-
repmat(minc,[size(cal,1),1]))./repmat(rangec,[size(cal,1),1]);

            % Pvals(2)==1 per sample
        elseif (Pvals(2)==1)

            minc=min(val,[],2);
            rangec=max(val,[],2)-minc;
            val=(val-
repmat(minc,[1,size(val,2)]))./repmat(rangec,[1,size(val,2)]);
            minc=min(cal,[],2);
            rangec=max(cal,[],2)-minc;
            cal=(cal-
repmat(minc,[1,size(cal,2)]))./repmat(rangec,[1,size(cal,2)]);

        end
    case 5
        % scale to max 1
        % Pvals(2)==0 per wavelength
        if (Pvals(2)==0)
            rangec=max(cal);
            val=val./repmat(rangec,[size(val,1),1]);
            cal=cal./repmat(rangec,[size(cal,1),1]);

            % Pvals(2)==1 per sample
        elseif (Pvals(2)==1)
            rangec=max(val,[],2);
            val=val./repmat(rangec,[1,size(val,2)]);
            rangec=max(cal,[],2);
            cal=cal./repmat(rangec,[1,size(cal,2)]);

        end
    case 6
        % normalize to area 1
        % Pvals(2)==0 per wavelength
        if (Pvals(2)==0)
            rangec=sum(cal);
            val=val./repmat(rangec,[size(val,1),1]);
            cal=cal./repmat(rangec,[size(cal,1),1]);

            % Pvals(2)==1 per sample
        elseif (Pvals(2)==1)
            rangec=sum(val,2);
            val=val./repmat(rangec,[1,size(val,2)]);
            rangec=sum(cal,2);
            cal=cal./repmat(rangec,[1,size(cal,2)]);

        end
    case 7
        % normalize to norm 1
        % Pvals(2)==0 per wavelength
        if (Pvals(2)==0)
            normc=zeros(1,size(cal,2));
            for i=1:size(cal,2);
                normc(i)=norm(cal(:,i));
            end
            val=val./repmat(normc,[size(val,1),1]);
            cal=cal./repmat(normc,[size(cal,1),1]);

            % Pvals(2)==1 per sample
        elseif (Pvals(2)==1)
            normc=zeros(size(val,1),1);
            for i=1:size(val,1);
                normc(i)=norm(val(i,:));
            end
            val=val./repmat(normc,[1,size(val,2)]);
            normc=zeros(size(cal,1),1);
            for i=1:size(cal,1);
                normc(i)=norm(cal(i,:));
            end
            cal=cal./repmat(normc,[1,size(cal,2)]);
```

```
            end
        case 8
            % linear detrend by sample
            val=detrend(val')';
            cal=detrend(cal')';
        case 9
            % smoothing along sample
            % Pvals(3) specifies smoothing window

            sm=2*Pvals(3)+1; % calculate the smoothing window
            tmp=conv2(val,ones(1,sm)); % smooth the data
            val=tmp(:,(1+Pvals(3)):(end-Pvals(3))); % chop the ends off
            val(:,1:Pvals(3))=repmat(val(:,Pvals(3)+1),[1,Pvals(3)]); %
    adjust the first end
            val(:,(end-Pvals(3)+1):end)=repmat(val(:,end-
    Pvals(3)),[1,Pvals(3)]); % adjust the second end

            tmp=conv2(cal,ones(1,sm));
            cal=tmp(:,(1+Pvals(3)):(end-Pvals(3)));
            cal(:,1:Pvals(3))=repmat(cal(:,Pvals(3)+1),[1,Pvals(3)]);
            cal(:,(end-Pvals(3)+1):end)=repmat(cal(:,end-
    Pvals(3)),[1,Pvals(3)]);

            % intrinsic smoothing function sometimes stalls in infinite
    loops
%             for i=1:size(val,1);
%                 val(i,:)=smooth(val(i,:),Pvals(3));
%             end
%             for i=1:size(cal,1);
%                 cal(i,:)=smooth(cal(i,:),Pvals(3));
%             end

        case 10
            % first deriv along sample
            % Pvals(3) specifies smoothing window
            % Pvals(4) specifies derivative gap
            sm=2*(Pvals(3)-1)+1;
            [cal, val] = first_deriv(cal, val, sm, Pvals(4),
    size(cal,2));
            % v is the original number of wavelengths
        case 11
            % second deriv along sample
            % Pvals(3) specifies smoothing window
            % Pvals(4) specifies derivative gap
            sm=2*(Pvals(3)-1)+1;
            [cal, val] = second_deriv(cal, val, sm, Pvals(4),
    size(cal,2));
        case 12
            % FWT
            is_HWT=true;
            cal=haar1d(cal);
            val=haar1d(val);

%         case 13 % NO SVD IMPLEMENTED YET
%             % SVD
        otherwise
            % do nothing
    end
end

if (is_HWT)

    wlstring=bitstring(N*14+numwl+ (1:(2^ceil(log2(numwl)))));
    % determine the activated FWT components from the selected
    % wavelengths.

    selwl=find(wlstring);

    beta=cal_known/[ones(size(cal,1),1),cal(:,selwl)]';
    cal_est=beta*[ones(size(cal,1),1),cal(:,selwl)]';
    val_est=beta*[ones(size(val,1),1),val(:,selwl)]';
```

```
else

    wlstring=bitstring(N*14+(1:numwl));
    selwl=find(wlstring);

    beta=cal_known/[ones(size(cal,1),1),cal(:,selwl)]';
    cal_est=beta*[ones(size(cal,1),1),cal(:,selwl)]';
    val_est=beta*[ones(size(val,1),1),val(:,selwl)]';

end

% % Plot cal/val results
% figure
% plot(cal_known,cal_est,'b.')
% hold on;
% plot(val_known,val_est,'r.')
% pause;

% RMSE (error)
result(1)=sqrt(sum((cal_known-cal_est).^2)/numel(cal_known));
result(2)=sqrt(sum((val_known-val_est).^2)/numel(val_known));

% linearity
% r value (correlation coefficient)
mcal_known=cal_known-mean(cal_known);
mcal_est=cal_est-mean(cal_est);
result(3)=sum(mcal_est.*mcal_known)/sqrt(sum(mcal_known.^2)*sum(mcal_est.
   ^2));

mval_known=val_known-mean(val_known);
mval_est=val_est-mean(val_est);
result(4)=sum(mval_est.*mval_known)/sqrt(sum(mval_known.^2)*sum(mval_est.
   ^2));

% sensitivity
%   Olivieri, p.648
%   1.  Olivieri, A. C. Uncertainty estimation and figures of merit for
   multivariate calibration (IUPAC Technical Report). Pure and Applied
   Chemistry 78, no. 3 2006.
result(5)=1/norm(beta);

% wavelength count complexity
result(6)=numel(selwl);

% number of pre-processing options enabled
result(7)=opt_count;
```

Appendix D: MCR Code

```
function [conc, spec, resid, bestconc, bestspec, bestresid] =
      als_mcr_deriv_clos( data, ncomp, guess, niter);

% als_mcr
%
% Alternating least squares multivariate curve resolution
%
% inputs:
%   data is of size [m,n]
%   ncomp is the number of components to work with
%   guess is of size [m,p] or [p,n]
% (if [m,p] it's a spectral guess, otherwise a concenctration guess)
%   niter is the number of iterations to use
%
% outputs:
%   conc is of size [p,n] - The estimated concentrations
%   spec is of size [m,p] - The estimated spectra
%   resid stores the residual of the estimated data
%
% Francis Esmonde-White, updated June 2007
%

% enable/disable plotting during optimization.
ploten=false; %true;
plotpause=0.5; % pause length in seconds for each plot step.

[m,n]=size(data);

if(~exist('ncomp'))
    error('Please specify the number of components required.');
end

if (exist('guess'))
    [j,k]=size(guess);
else
    j=0;
    k=0;
end

if (~exist('niter'))
    niter=400;
end

[u,s,v] = svd(data,0);
% the SVD finds the minimum error solution for the n-component linear estimate
best_err =
    sqrt(sum(sum( [data-u(:,1:ncomp)*s(1:ncomp,1:ncomp)*v(:,1:ncomp)'] .^2 )));

% set up the initial inputs
if (j==m) % guess is spectra
    sest=guess;
    p=k;
    c_iter=1;
elseif (k==n) % guess is concentration
    cest=guess;
    p=j;
    c_iter=0;
elseif (k==m) % guess is spectra
    sest=guess';
    p=j;
    c_iter=1;
elseif (j==n) % guess is concentration
    cest=guess';
    p=k;
    c_iter=0;
else % no valid guess
    % Use an SVD estimate
```

```
    sest=u(:,1:ncomp);
    p=ncomp;
    c_iter=1;
    clear u s v;
end

zz1=1:10;zz2=11-zz1; % used in determining the slope

% c_iter determines if the next iteration is to be concentration estimation
% step (c_iter == 1) or a spectral estimation step (c_iter == 0)

% check that everything is a reasonable size
if ncomp>p
    error('maximum number of components allowed is limited by the guess')
elseif p>ncomp
    if (c_iter==1)
        sest=sest(:,1:ncomp);
        p=ncomp;
    elseif (c_iter==0)
        cest=cest(1:ncomp,:);
        p=ncomp;
    end
end

% Make a copy of initial (original) spectral estimate for the reordering of
% the spectral components during the ALS routine.
if (exist('sest'))
    [sest]=sest./repmat(diag(sest'*sest)',[m,1]); % normalize spectrum length
    sorig=sest;
else
    sorig=data/cest';
    [sorig]=sorig./repmat(diag(sorig'*sorig)',[m,1]); % normalize spectrum len.
end

resid=zeros(1,niter-1);
improving=true;

% Begin the ALS routine
itercount=0;
while ((itercount<niter)&&improving)
    if (~c_iter); % if citer == 0
        %         disp('spec est')
        sest=data/cest'; % estimate spectral component

        limit=max(sest(:))/prod(size(sest));
%         [sest]=nn(sest,limit); % force non-negativity
% we don't constrain the derivative spectra to non-negative values.

        [sest] = sest./repmat(sqrt(diag(sest'*sest)'),[m,1]);
             % normalize the spectrum length

        similarity=-1*ones(p);

        % check that the ordering of the components has not changed.
        for i=1:p;
            for j=i:p;
               similarity(i,j) =
                ( sorig(:,i)'*sest(:,j)) / (norm(sorig(:,i))*norm(sest(:,j)) );
            end
        end

        % reorder the components using similarity
        for i=1:p-1;
            % check that the ordering of the components has not changed.
            [y,j]=max(similarity(:));
               % find the most similar spectrum to the ith original spectrum
            rowindex=mod(j-1,p)+1; % find the row index
            colindex=floor((j-1)/p)+1; % find the column index
            similarity(rowindex,:)=-1;
            similarity(:,colindex)=-1;
            if (colindex==rowindex)
                % do nothing (the spectrum is in the correct position)
```

```
        else
            sest(:,[rowindex,colindex])=sest(:,[colindex,rowindex]);
        end
    end

    % check that none of the components has inverted to negative
    % spectra
    for i=1:p;
        sim_a=(sorig(:,i)'*sest(:,i))/(norm(sorig(:,i))*norm(sest(:,i)));
        sim_b=(sorig(:,i)'*(-sest(:,i)))/(norm(sorig(:,i))*norm(-
  sest(:,i)));
        if (sim_b>sim_a);
            sest(:,i)=-sest(:,i);
        end
    end

    if (ploten)
        %            pause(plotpause);
        subplot(2,2,1);
        cla;
        plot(sest);
        title('Spectral Estimate');
    end

    itercount=itercount+0.5;
    c_iter=~c_iter;

elseif (c_iter); % if citer == 1
    %         disp('conc est')
    cest=data'/sest'; % estimate concentration component

    limit=max(cest(:))/prod(size(cest));
    [cest]=nn(cest,limit); % force non-negativity

    % try to force a closure between (1 & 2) and (3 & 4)
    [cest(:,[1,2])]=clos(cest(:,[1,2]));
    [cest(:,[3,4])]=clos(cest(:,[3,4]));

    if (ploten)
        subplot(2,2,2);
        cla;
        plot(cest);
        title('Concentration Estimate');
        pause(plotpause);
    end

    itercount=itercount+0.5;
    c_iter=~c_iter;
    current=ceil(itercount);

    % we always compute the residual after estimating the
    % concentrations
    tmp=data-sest*cest';
    resid(current)=sqrt(sum(tmp(:).^2))/best_err;

    if (current==1)
        bestresid=resid(1);
    end

    if (resid(current)<bestresid)
        bestspec=sest;
        bestconc=cest;
        bestresid=resid(current);
        if (ploten)
            subplot(2,2,3);
            cla;
            plot(sest);
            title('Best Spectral Estimate');
            subplot(2,2,4);
            cla;
            plot(cest);
            title('Best Concentration Estimate');
```

```
            end
        end

        if (current>12)
          slope = abs( [resid(current) - ([zz1]*resid(current-(zz2))')/55] );
           % weighted average of the last 10 iterations
          if (slope<0.00001);
            disp( ['MCR terminated, the slope change was ', num2str(slope)] )
             % we have reached a period of little change... end the routine
             % things are neither getting much worse nor getting much better
            improving=false;
             % disp('stopped improving')
          end
        end

    end
end

conc=cest;
spec=sest;
% resid=resid/best_err;
% return the residual ratioed with respect to the minimal possible error for a
       n-component estimate

resid=resid(find(resid)); % get rid of any non-allocated residual values

if ~exist('bestconc')
    bestspec=sest;
    bestconc=cest;
    bestresid=resid(current);
end


function [data]=nn(data,limit)
% apply an exponential non-negativity constraint to all data points with a
% magnitude <= limit.
% (this forces all negative values to a constrained positive domain)

i=find(data<=limit);
data(i)=limit*10.^(data(i)-limit);


function [data]=clos(data);
% try to find a coefficient so that the
% std(coef*data(:,1)+data(:,2)) is minimized.
e=zeros(100,1);
for i=1:100;
    e(i)=std((i/2)*data(:,1)+data(:,2));
end
[y,t]=min(e);
t1=(t-1)/2;
% t2=(t+1)/2;
for i=1:100;
    e(i)=std( (t1+ (i/100))*data(:,1)+data(:,2));
end
[y,t2]=min(e);
t2=t1+((t2)/100);

if ((t2>0) & (t2<50))
    data(:,1)=t2*data(:,1);
end
```

Appendix E: N-Way Visualization Manuscript Reprint

As part of the course of study exploring spectroscopy in turbid media, methods for visualizing complex multidimensional data were developed. One such visualization method was published, and a reprint of the manuscript as published has been included here with permission from Elsevier. This reprint has been included partly because this is an efficient way of exploring n-way data sets, and partly because the work was completed as part of the course of study described in this thesis. The n-way visualization method is complementary to the work presented, because prior to the application of any data processing method, the unprocessed data should be examined to confirm that chemically significant changes can be observed. Whether 2-D (images, spectra) or N-D data is recorded, n-way visualization of correlation is a straightforward way to observe trends in complex datasets. The n-way visualization method is not used to correct for light-scattering, and so it is included as an appendix rather than in the main body of the thesis.

Available online at www.sciencedirect.com
SCIENCE DIRECT
Vibrational Spectroscopy 36 (2004) 287–292
VIBRATIONAL SPECTROSCOPY
www.elsevier.com/locate/vibspec

Visualization of *N*-way data using two-dimensional correlation analysis

Francis L.W. Esmonde-White, David H. Burns*

Department of Chemistry, McGill University, Montreal, Que., Canada H3A 2K6

Received 11 November 2003; received in revised form 26 February 2004; accepted 27 February 2004

Abstract

A method for applying two-dimensional correlation analyses to *N*-way data is presented, which compactly displays trends in the data. Interpreting large multi-dimensional data sets obtained from hyphenated instruments is difficult. Several methods of applying two-dimensional correlation analyses to *N*-way data are examined. To visualize trends occurring along the original parameters, data are stacked lexicographically according to $N-1$ parameters in preparation for synchronous and asynchronous correlation analyses (2D COSY). Correlation analysis comparing a first physical parameter to all other parameters indicates trends. The average correlation intensity indicates significance of the correlation. It does not indicate variation between axes. Standard deviation of correlation intensity is used to determine the magnitude of variation about the mean. This shows the extent correlation changes with other parameters. Pearson correlation coefficients are computed. The sign of correlation coefficients indicates trend direction. Combining the sign of Pearson correlation coefficients with standard deviation magnitudes indicates magnitude and direction of correlation changes. These visualization methods are used to investigate mathematically generated three-way data. Results show that a small number of figures can illustrate variation in the signal and isolate the components causing signal variation. This provides a rapid means for initial trend-screening of large multi-dimensional data sets. Rapid trend screening is important for both data acquisition and data analysis.

Keywords: *N*-way correlation spectroscopy; 2D correlation spectroscopy; Visualization

1. Introduction

Increasingly sophisticated instrumentation has led to *N*-way data sets becoming more commonly encountered. Trend screening is difficult with *N*-way data. Hyphenated techniques such as HPLC-UV-MS that acquire three-way data sets in real time [1], resulting in *N*-way data, are now frequently encountered. Likewise, in environmental monitoring, it is common that several species are sampled from several geographic locations over a time period of interest, again leading to three-way data [2]. Variation of any two perturbation parameters while recording spectroscopic data results in a three-way data set.

Analysis of *N*-way data presents many challenges. It is difficult to visualize trends occurring along several perturbations. Traditional methods of trend screening often involve visual analysis. In visual analysis, 2D plots are made and looked at as a time series. Unfortunately, subjective viewer-dependent conclusions often result. An alternative in visual analysis is to position 2D graphs next to each other, so that differences are evident. Once again, observers do not always concur on the nature of trends when data are viewed in this manner. Three-dimensional plots of data may also help clarify some ambiguity, by grouping data together into clusters or emphasizing differences. Conclusions drawn from three-dimensional plots will be influenced by both the angle from which the data are examined and the media used to display the plots.

Analytic computational methods such as *N*-way principal component analysis (PCA) [3] can discern trend information in data without observer bias. While *N*-way PCA allows underlying trends to be estimated, the correct number of underlying species must be known for it to be used optimally. Parallel factor analysis (PARAFAC) [4] and multivariate self-modeling curve resolution (MCR) [5] are both techniques operating on *N*-way data to estimate pure component spectra and relative contributions of the components found. Both MCR and PARAFAC techniques are based on a constrained iterative least squares algorithm. One drawback for these techniques is the time required for the optimization to the final solution. A second drawback is that MCR may optimize to solutions with rotation ambiguity.

For two decades, two-dimensional correlation spectroscopy (2D COSY) has been used to determine relationships

* Corresponding author. Fax: +1-514-398-2382.
E-mail address: david.burns@mcgill.ca (D.H. Burns).

0924-2031/$ – see front matter © 2004 Published by Elsevier B.V.
doi:10.1016/j.vibspec.2004.02.012

between spectral channels and perturbations [6]. The first use employed 2D COSY to work out effects of external perturbations on vibrational spectra. Effects of perturbations are easily visualized through this method [7]. Synchronous and asynchronous correlations determined by 2D COSY are usually displayed as contour or surface plots, which indicate regions influenced by perturbations.

Conventional 2D COSY is limited because it cannot be applied directly to three-way data. Modification of COSY analysis to visualize trends in *N*-way data would provide a means of simple visual analysis. By reshaping *N*-way arrays of data, 2D COSY can be used for analysis. The goal of this manuscript is to investigate ways in which *N*-way COSY can help visualize trends that are traditionally difficult to observe in *n* dimensions. The results are then analyzed for statistical trends. This is called *N*-way COSY. Contrary to conventional 2D COSY, *N*-way COSY plots represent change of correlation with respect to a perturbation, and not the correlation with the perturbation itself.

Initial trend screening is one use of *N*-way COSY. Preliminary use of the method indicates that subtle trends may be revealed and displayed in a compact manner. Changes in COSY intensities through the data series may be correlated to a single parameter. Changes can be shown to vary statistically for a single perturbation independently of the remaining perturbations. For each perturbation, synchronous and asynchronous trends can be visualized in a single figure. This is an expansion of the use of traditional 2D COSY.

2. Theory

2.1. Two-dimensional correlation spectroscopy

Many ways of computing 2D COSY intensities have been proposed. All of these computational methods isolate synchronous or asynchronous [8] changes between two spectral variables as a result of an external perturbation. Of the many methods for computing 2D COSY values, the most commonly employed method is based on Fourier transforms, as described below. Other methods have been proposed to decrease the time required for computations [9].

Correlation intensities from 2D COSY are computed using dynamic spectra. Dynamic spectra are calculated by centering the original spectra about a chosen reference spectrum. Reference spectra are often chosen from one of two sources. Arbitrarily chosen static spectra are commonly used as a reference. Alternately, mean spectra may also be chosen as a reference spectrum [10,11].

Computation of dynamic spectra is done by subtracting the reference spectra from the data, yielding spectral intensity changes. For a wavelength (λ) and a perturbation (τ), spectral intensities can be expressed as $\gamma(\lambda, \tau)$, as observed over a period *T*. The dynamic spectra would then be expressed as

$$\Delta\gamma(\lambda, \tau) = \gamma(\lambda, \tau) - \gamma(\lambda, 0). \quad (1)$$

Fourier transform 2D COSY was employed as the method for computing the COSY intensities described in this manuscript. Spectra, which vary due to a perturbation, are recorded along a perturbation domain, analogous to how data may be recorded along a time domain. Dynamic spectra along the perturbation domain are first converted into the frequency domain using a Fourier transform to obtain generalized 2D correlation spectra. Intensities are calculated as complex 2D correlation, defined as

$$\Phi(\lambda_1, \lambda_2), i\Psi(\lambda_1, \lambda_2) = \frac{1}{\pi T}\int_0^\infty \bar{Y}_1(\omega)\bar{Y}_2^*(\omega)\partial\omega. \quad (2)$$

With $\bar{Y}_1$ and $\bar{Y}_2^*$ being the Fourier transform and the conjugate of the Fourier transform of $\bar{\gamma}(\lambda_1, \tau)$ and $\bar{\gamma}(\lambda_2, \tau)$, respectively. The real part (Φ) is the synchronous 2D correlation intensity, while the imaginary part (Ψ) is the asynchronous 2D correlation intensity [6].

2.2. Compact 2D COSY graphs

Synchronous and asynchronous 2D COSY plots are usually presented as two contour plots. Synchronous and asynchronous correlation intensities are plotted separately. However, the two plots contain redundant information. Synchronous correlation intensities are symmetric about the diagonal. Asynchronous correlation intensities are antisymmetric about the diagonal. As shown in Fig. 1, information may be displayed in a compact form by plotting only the upper triangle of the synchronous correlation intensities, and the lower triangle of the asynchronous correlation intensities. This preserves the information contained and eliminates redundancy, as information is not repeated in the plot. All subsequent 2D COSY plots presented in this manuscript are portrayed in this form. Attention must be paid to the manner in which these matrices are joined. Diagonal values for the synchronous correlation are meaningful, and must be preserved. Contrarily, asynchronous diagonal intensities may be discarded without losing information. Diagonal asynchronous values are insignificant, as no spectral signal varies out of phase with itself.

2.3. N-way data compression

Current algorithms for 2D COSY are designed to process two-way data matrices. These matrices consist of rows of

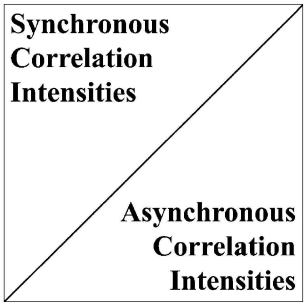

Fig. 1. Novel 2D COSY display.

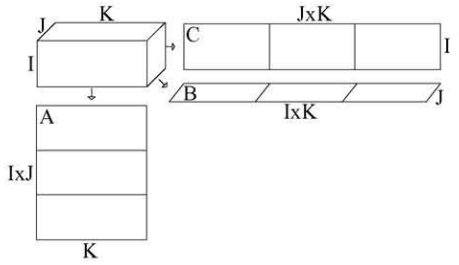

Fig. 2. Methods for collapsing three-way data.

independent measurements, such as spectroscopic measurements that vary with a perturbation. Two-dimensional matrices of correlation intensities result from 2D COSY, and are displayed as either contour or surface plots. Relationships along more than one mode cannot be determined directly with 2D COSY. Unfolding of a three-mode data set into a two-mode matrix allows use of common 2D COSY methods. Data are unfolded such that the spectroscopic mode will always lie along the rows of the new 2D array. This is done in three distinct ways, all shown in Fig. 2, and referred to as arrangements 'A', 'B', and 'C'. Arrangement 'A' is the IJ × K stacking, while arrangements 'B' and 'C' are the J × IK and I × JK stackings, respectively. Unfolding of a three-way array is done by lexicographically stacking two modes into a single matrix axis, thus reducing the effective shape of the data to two ways. One of the axes in the new matrix will be the same as one of the original modes and the other axis will contain both of the two remaining original modes. Two-dimensional correlation intensities are then calculated for the newly formed two-way array.

For three-way arrays, data are stored as an I × J × K three-way array, and the three modes are labeled M_i, M_j, and M_k respectively. In this ordering, mode M_k is chosen to represent the spectroscopic mode. Stacking of the three-way array to a two-way array is done by assembly of horizontal or frontal slices, and yields a J × IK or I × JK lexicographically stacked matrix. Fig. 2 illustrates these combinations as arrangements 'B' and 'C'. A third arrangement exists, where an IJ × K matrix is formed, emphasizing correlations for all perturbations simultaneously, illustrated as arrangement 'A' in Fig. 2.

Note that in all three cases, the Kth mode (M_k) of the three-way array is mapped onto the second way of the new two-way array. This approach of stacking may be extended more generally to N-way arrays, as is done for other N-way techniques [12]. N-way arrays are unfolded, so the spectroscopic mode is collapsed with at most one other mode. This results in a matrix formed of $N-2$ modes nested along one way of the array, and two modes nested together on the other way. The nesting is done so that the spectroscopic mode and the perturbation mode of interest are together along one way in the new array.

This can be expressed mathematically as taking an array with N modes, M_1 through M_N, and unfolding it into a two-mode array where the first way holds M_1 through $M_{(N-2)}$ and the second way holds $M_{(N-2)}$ and M_N. Traditional 2D correlation intensities are then calculated for the new matrix.

2.4. N-way data visualization by 2D COSY

Correlation matrices computed for reshaped N-way data introduce a new problem. Similar-looking spectroscopic correlation sub-matrices are repeated. Each sub-matrix is a set of 2D correlation intensities, where there are two values of one perturbation used for each correlation. Utility of such collapsed sub-matrices of correlations is not immediately evident. Statistical analysis is used to make sense of the results. Simple statistical descriptors of the sub-matrices are possible, such as mean values, standard deviations, and Pearson correlation coefficients. A fourth descriptor is also possible, which combines Pearson correlation coefficients and standard deviations.

A first method involves taking the mean correlation spectrum. To obtain the mean, correlation values from all sub-matrices along non-spectroscopic modes are averaged into a single K × K correlation matrix. This leads to a general correlation spectrum. Mean values indicate the average relationship between spectral points over the perturbation. Of greater interest is the relationship between the perturbation and changes in COSY intensities.

To obtain a clearer picture of the relationship between the perturbation and COSY intensity changes, a second method is introduced. This second method displays standard deviations of the correlation spectra. Standard deviations indicate where correlation changes are occurring, showing that there is variation of correlation along the perturbation of interest that is not due to other parameters. Though deviation from the mean is described by this graph, trends are not isolated. Both random deviations and perturbation-induced deviations will be present. However, correlations with noise are reduced by the sheer volume of data that has been used to generate the standard deviations. Though displaying deviations from the means is possible, no sense is made of the coherence of variation by this method.

To visualize the direction of the relationship between the COSY intensities and the perturbation, Pearson correlation coefficients (r) can be used as a third method of analyzing the 2D COSY sub-matrices. For the N-way COSY data, correlation can be expressed as

$$r(K_1, K_2) = \frac{\sum_{i-1}^{I}\sum_{j-i}^{I}\Phi_{ij}D_{ij}}{(N-1)S_\Phi S_D} \tag{3}$$

where r is the Pearson correlation coefficient determined for wavelengths K_1 and K_2. The summation terms select the upper triangle, with 'I' being the maximum index along the perturbations. In the numerator, the Φ matrix contains the synchronous or asynchronous correlation values. The D matrix contains the Euclidean distances from the rest state. In the denominator, S_Φ and S_D represent the standard

deviations of the upper triangular synchronous or asynchronous correlation matrices and the perturbation distances, respectively. For each of these values, there are N values in the upper triangle.

A link between variation of the perturbation and the correlation spectra variations is indicated by the r values. The perturbation of interest is used as the independent axis. Each sub-matrix comprises a combination of two values of the perturbation of interest, while r values must be computed with a single independent variable. To determine a single measure of perturbation intensity from the two levels of the mode of interest, Euclidean distances along the perturbation mode can be used as the independent variable. Manhattan or Mahalanobis distances may prove to be more useful indicators of perturbation magnitude (as the independent variable). Each sub-matrix represents two distances along perturbation d, expressed as D_{ij}, a combination of both positions along the perturbation mode. These distances can be expressed as

$$D_{ij} = \sqrt{d_i^2 + d_j^2}. \tag{4}$$

By combining the magnitude of standard deviations and the sign from r values, a fourth method of displaying the variation of COSY intensities is obtained. The r values indicate whether the correlations are positive or negative. If there is very little correlation, the coefficient will be near 0. Unfortunately, r values do not indicate magnitude of underlying variation. This means that while correlation sign is useful, correlation magnitude is not as interpretable.

Table 1
Parameters of sinusoidal intensity variations along each mode for the Gaussian functions

Gaussian function	Mode 1		Mode 2	
	Phase shift (degrees)	Relative frequency	Phase shift (degrees)	Relative frequency
1	0	2	90	2
2	180	2	0	2
3	180	4	45	2
4	0	4	0	1
5	90	2	90	1

Change in correlation intensity along a single perturbation mode is visualized by combining the sign of the r value with the magnitude of the standard deviation. Any r values below a correlation threshold are set to 0. This is done to avoid suggesting that any region with a large standard deviation and a small r value is of interest.

2.5. Simulations

Simulated data was used to test the N-way COSY method. Five equally spaced Gaussian functions were used to generate a three-way data set. These functions are labeled 1 through 5 on all plots. Intensities of the Gaussian functions were varied along two distinct modes with sinusoidally varying magnitudes, the phases and frequencies of which are listed in Table 1. Variations were constructed to have different phase shifts and frequencies, such that synchronous and asynchronous trends would vary differently along each mode.

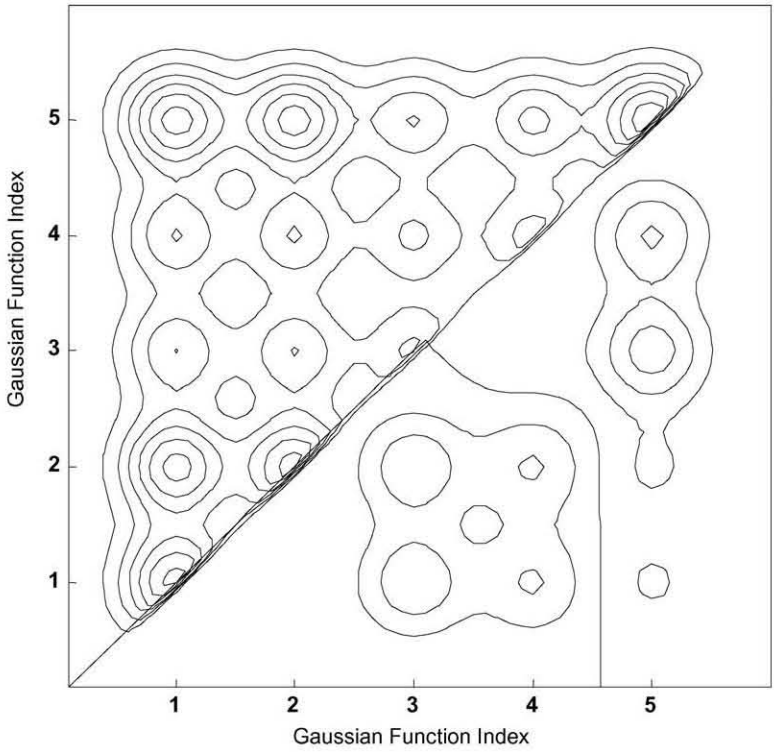

Fig. 3. N-way COSY of simulated data, both modes collapsed for correlation.

All of the computations described in this manuscript made use of the Matlab™ (The MathWorks Inc., Natick, MA, USA, release 6.121) programming language.

3. Results and discussion

Application of *N*-way COSY is illustrated by use with a simulated data set. From the simulated data set it is shown that correlation intensity changes can be isolated to a single mode. In all figures derived from the simulated data, numbers on the axes correspond to positions of the Gaussian functions. The label '1' shows the maximum of the first Gaussian function and each of the other numbers corresponds to maxima of the other Gaussian functions.

Results from three-way COSY analysis may be displayed in three sets of plots. Two of the three sets of plots are presented. The third set of plots generates results analogous to the second set of plots, so we have excluded it. Each set of plots shows results from a different data stacking. Each stacking isolates correlation changes that result from either a single perturbation or a combination of several perturbations. The first of these results are shown in Fig. 3. Data collapsed into the IJ × K form result in 2D COSY intensities showing correlation changes due to both perturbations. Autocorrelations in Fig. 3 are large for the first, second, and fifth Gaussian functions. This indicates that they all increase synchronously. Synchronous correlation intensities are highest for correlations between functions [1, 2], [1, 5], and [2, 5]. Although correlations are observed, the correlation cannot be attributed

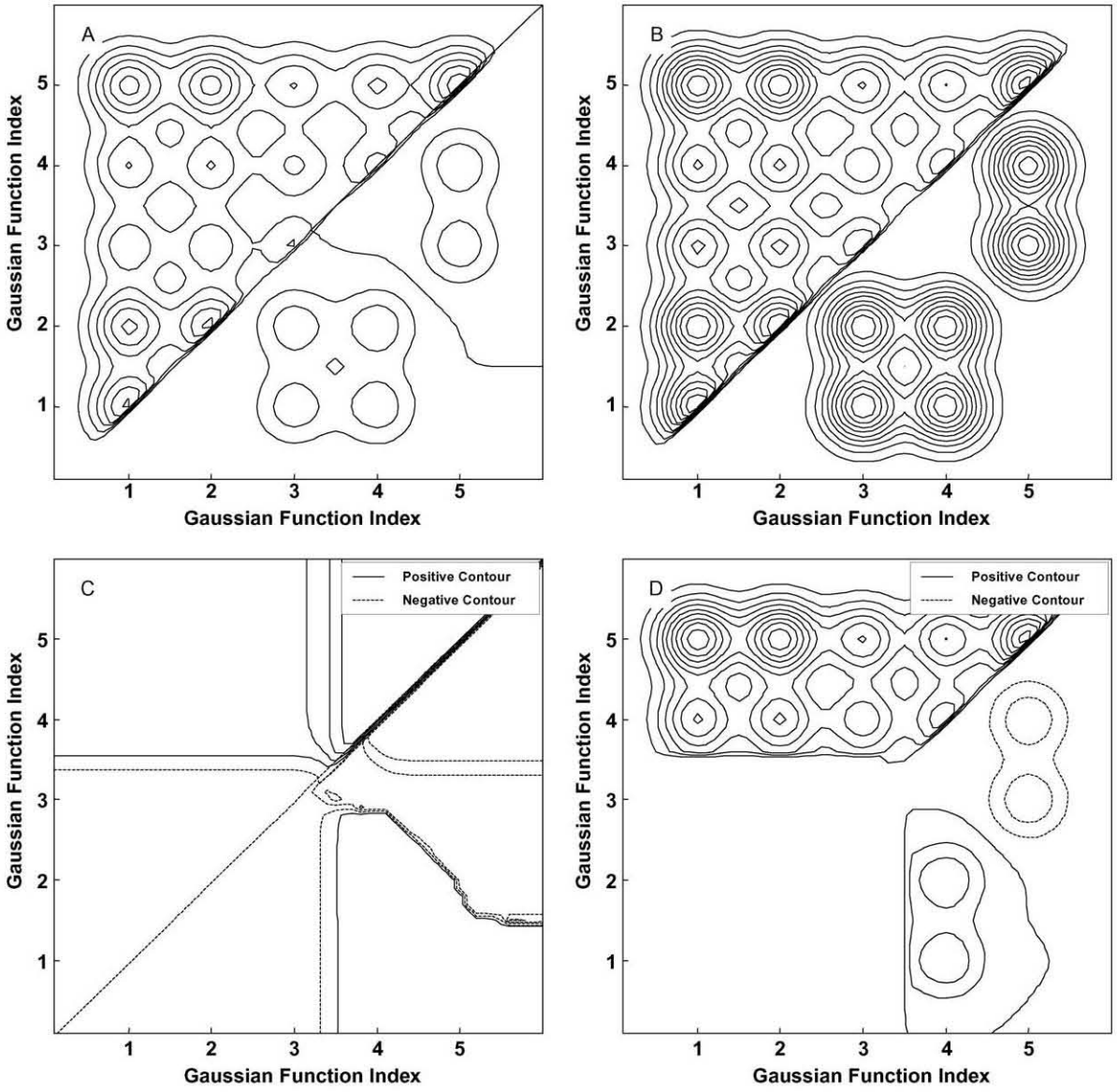

Fig. 4. *N*-way COSY of simulated data, second sinusoidal mode collapsed for correlation. (A) is mean of correlation, (B) is for S.D. of correlation, (C) is *r* values, and (D) is sign of *r* values with magnitude of S.D. Both axes are labeled with the positions of the contributing Gaussian functions.

to a particular perturbation mode. Combinations of correlations from multiple perturbations cause difficulty in determining whether contribution from any particular perturbation dominates in the results. The number of samples taken along each perturbation influences the effective weighting of a particular perturbation on calculated correlation intensity, complicating interpretation of this plot.

The *N*-way correlation results are shown in Fig. 4 for the unfolding, which computes COSY values along the second perturbation mode, and then looks at variance of COSY intensities along the first perturbation mode. This is an example of *N*-way COSY using the J × IK collapsed form of three-way data.

Mean correlation values are shown in Fig. 4A. These results are very similar to those of Fig. 3. Using *N*-way COSY, more information can be retrieved.

Standard deviations along mode M_i are determined, indicating correlation changes due to the *I*th mode. These standard deviations are shown in Fig. 4B. Maximum variation in amplitude occurs where frequencies of the perturbations are not equal. Amplitude variations are more informative than mean values, because intense mean COSY correlations are of little value if very little deviation of COSY intensities results from a perturbation. Thus, although correlation is present, it is not affected by the *I*th mode.

The reverse can also occur, where regions of small mean intensity may result from intense variation in the correlation whose average is a low value. The importance of this variance depends on correlation to a single perturbation mode. Only regions with large *r* values are actually correlated to a perturbation, as shown in Fig. 4C, in which functions 4 and 5 correlate with the second perturbation mode though function 3 does not. This reflects the relationship between the linear axis of perturbation and the one quarter of one sinusoidal wave by which the intensities vary. So long as magnitude of an *r* value is above a threshold, sign is important and magnitude is not. Not all regions with significant standard deviations are strongly enough correlated to the perturbation to justify describing them as regions that vary due to a perturbation.

Magnitude of the COSY standard deviation combined with the sign of *r* results in Fig. 4D. In the synchronous region, regions of significant correlation variation all change in concert. In the asynchronous region, correlations between functions [1, 4] and [2, 4] increase, while correlations between functions [3, 5] and [4, 5] decrease. No significant relationship exists between variations at [1, 3] and [2, 3] with respect to the perturbation mode. It is this difference between Figs. 3 and 4D that illustrates the usefulness of *N*-way correlation spectroscopy, as compared to 2D COSY.

4. Conclusions

Application of *N*-way 2D COSY isolates results from different perturbation modes in a way that no other technique does. By collapsing *N*-way data into a two-way array, it is possible to obtain COSY intensities for *N*-way data. Statistical analysis on the resulting 2D correlation intensities allows a compact display of the complex trends. Properties such as mean, standard deviation, Pearson correlation, and a combination of the sign of *r* and the magnitude of standard deviations are all used to discover trends.

The *N*-way COSY method promotes a straight forward, convenient means to visualize complex relationships of underlying components in *N*-way data. With the sinusoidally varying test data, it was shown that correlation can be made specific to a single perturbation mode. Application of the *N*-way method could allow rapid prescreening of trends in systems such as hyphenated techniques and imaging spectrometers.

Acknowledgements

The authors thank the Natural Sciences and Engineering Research Council of Canada (NSERC) and the Fonds Québécois de la Recherche sur la Nature et les Technologies (FQRNT) for support of this research.

References

[1] O.Y. Al-Dirbashi, K. Nakashima, Biomed. Chromatogr. 14 (2000) 406.
[2] J.W. Edwards, K.S. Edyvane, V.A. Boxall, M. Hamann, K.L. Soole, Mar. Pollut. Bull. 42 (2001) 389.
[3] R. Henrion, Chemometr. Intell. Lab. Sys. 25 (1994) 1.
[4] R. Bro, Chemometr. Intell. Lab. Sys. 38 (1997) 149.
[5] J.R. Schoonover, R. Marx, S.L. Zhang, Appl. Spectrosc. 57 (2003) 154A.
[6] D. Lafrance, Ph.D. Dissertation. McGill University, Montreal, Canada, 2003.
[7] I. Noda, AIP Conf. Proc. 503 (2000) 3.
[8] S. Sasic, Y. Ozaki, Anal. Chem. 73 (2001) 2294.
[9] I. Noda, A.E. Dowrey, C. Marcott, Appl. Spectrosc. 47 (1993) 1317.
[10] Y. Ozaki, S. Sasic, T. Tanaka, I. Noda, Bull. Chem. Soc. Jpn. 74 (2001) 1.
[11] V.H. Segtnan, S. Sasic, T. Isaksson, Y. Ozaki, Anal. Chem. 73 (2001) 3153.
[12] H.A.L. Kiers, J. Chemometrics 14 (2000) 105.

Appendix F: Tissue Simulating Phantoms

Because of the difficulties inherent in measuring optical properties of tissues, calibration materials made from synthetic or natural component can be used to develop or validate spectroscopic methods used to analyze scattering media. Optical properties of these calibration materials, also called tissue phantoms, optical properties can be changed to suit the requirements of the application. Tissue phantoms can be prepared as either a liquid or a solid. Properties of tissue phantoms were reviewed by Pogue and Patterson.[251] Several materials are suitable for scattering calibration method development. Briefly, scattering agents include lipid emulsions, polymer microspheres, and small particles. Various absorbing species can be added to the scattering agent, including dyes, inks, molecular probes, or biological constituents like hemoglobin. One difference between solid and liquid phantoms is the absence of laser speckle in the liquid phantoms. Scattering from biological tissue yields speckle, and some instrumentation uses speckle, while with other instrumentation speckle may deleteriously influence results.

Lipid emulsions, such as oil-in-water emulsions, milks, and creams,[252] are commonly used as light scattering standards because lipid bilayers are a primary source of light scattering. Lipid emulsions are

popular because the chemical and optical properties of lipid droplets are similar to lipid bilayers. Moreover, the optical scattering properties of Intralipid under storage conditions is stable over a long time period because the polydispersity does not appreciably change.[253] However, once removed from packaging, lipid solutions degrade via oxidation over a period of hours to days.[254] As a result, mixtures containing emulsions must be prepared immediately before each experiment. Optical properties of Intralipid are difficult to characterize because particle sizes and distributions are difficult to measure and widely vary among .[255] Due to pharmaceutical applications and risks of lung embolism from large droplets, pharmaceutical preparations have well regulated droplet size distributions. Instruments used for characterizing particle size distributions of complex mixtures such as oil in water emulsions show variations between instrument manufacturers and methods.[256]

Intralipid™ is a commercially available lipid emulsion used for intravenous feeding. Optical properties of Intralipid have been reported for a variety of concentrations,[113, 167, 169, 257-259] and they demonstrate that tissue simulating phantoms can be prepared from Intralipid solutions to accurately describe the optical properties of tissue.

The main advantages of using Intralipid as a scattering standard are the low cost, widespread availability, and the ease of preparing liquid scattering phantoms into which water-soluble dyes can be incorporated. The main disadvantages are potential batch-to-batch variations of optical coefficients, and the limited stability of samples in ambient conditions.

Several other tissue phantoms have been developed, including solid polyurethane TiO_2 phantoms,[260] solid glass spheres in polyester resin,[261] aqueous suspensions of polystyrene spheres,[262] and Intralipid in an agar matrix.[263] Plastic resin samples can be machined to particular shapes, and may be particularly suitable for preparing standards that last for a long time.

Appendix G: Numerical Models of Light Scattering

Aside from the purely theoretical approaches used in radiative transfer theory, diffusion theory, and the 2-flux theories, numerical models are commonly used to give approximate solutions for scattered light intensity. The two common methods, finite element analysis and Monte Carlo simulations are described here.

G.1 Finite Element Analysis

Finite-element analysis is a theoretical approach for modelling light transport according to a mesh-based diffusion system with nodes through which photon transport can be calculated.[166] Finite-element analysis systems are used to solve both the forward and inverse problems.[166, 264] The forward problem is to calculate how light will propagate through a system of known properties. The inverse problem is to estimate the properties of a system using the measured optical response. Results have shown that this type of analysis can be used to estimate the optical properties of systems.[166] For optimal results, *a priori* spatial information (i.e. spatial priors, or estimates of the sample geometry) are incorporated into the calculations, and require extra information not typically available, such as geometric mesh-models of the physical system.[265, 266] Geometric models of tissue can be obtained, using optical computed tomography for

very shallow tissues, or x-ray computed tomography for deep tissues Finite element analysis is also computationally expensive.

G.2 Monte Carlo Simulations

Monte Carlo simulations are another approach to estimating the propagation of light in turbid media using numerical simulation methods.[41, 267-270] Photon migration is modeled stochastically in Monte Carlo simulations by simulating large numbers of photons travelling through the medium and integrating the results. This is a tractable method for simulating the motion of light in situations which are too complex to be solved mathematically. Trajectories for each photon are simulated according to the transmission and absorption properties of the medium. Simulations consist of a series of events where individual photons can be: consumed by absorption, transmitted at a new angle by scattering events, or escape the simulation boundaries.

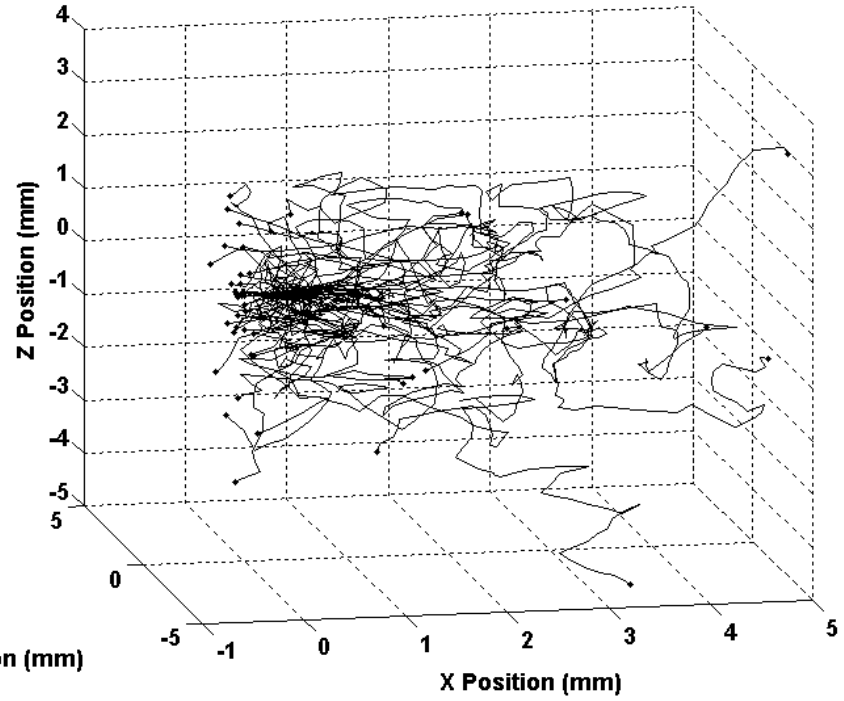

Figure G.1: Example results from a Monte Carlo simulation.

Results of a Monte Carlo simulation are shown in Figure G.1. In this example, photon trajectories were simulated, recorded, and finally plotted as curves. Photons were injected into the simulation at (x=0, y=0, z=0), facing in the positive x direction. The photon injection point is where the highest density was observed. While most photons were constrained to regions near the source, some traveled much further and exited through the simulation boundaries. Points plotted at the end of the traces indicate the location at which a photon was absorbed or escaped from the simulation boundaries (at the planes where x = -0.05, x = 5, y = -5, y = 5, z = -5, and z = 5, measured in millimetres). This example simulation

shows the results of only 50 photons, while complete simulations might average the results of 10^4 or 10^6 simulated photons.

Accuracy of Monte-Carlo simulations depends greatly on the quality of the underlying statistical model and the number of photons used in the simulation. Flux densities, temporal and spatial reflectance profiles, and sample heating can be also modeled using this type of simulation. Despite the accuracy of Monte Carlo simulations for estimating how light propagates, they cannot easily be used to estimate optical properties from a set of measured experimental results. This “inversion problem” has been approached by fitting measured distributions to libraries of pre-determined fluence distributions.[271] Libraries consist of a large number of Monte Carlo models generated with various optical properties for a particular geometry.

Bibliography

1. L. Leonardi, and D. H. Burns, "Quantitative Multiwavelength Constituent Measurements Using Single-Wavelength Photon Time-of-Flight Correction," Applied Spectroscopy **53,** 637-646 (1999).
2. J. D. Ingle, and S. R. Crouch, *Spectrochemical analysis* (Prentice Hall, Englewood Cliffs, N.J., 1988).
3. D. A. Skoog, F. J. Holler, and S. R. Crouch, *Principles of instrumental analysis* (Thomson Brooks/Cole, Belmont, CA, 2007).
4. A. K. Popp, M. T. Valentine, P. D. Kaplan, and D. A. Weitz, "Microscopic Origin of Light Scattering in Tissue," Applied Optics **42,** 2871-2880 (2003).
5. P. C. Waterman, "Matrix formulation of electromagnetic scattering," Proceedings of the IEEE **53,** 805-812 (1965).
6. A. Ishimaru, *Wave propagation and scattering in random media* (IEEE Press; Oxford University Press, New York; Oxford, 1997).
7. T. Vo-Dinh, ed. *Biomedical photonics handbook* (CRC Press, Boca Raton, Fla., 2003).
8. C. F. Bohren, and D. R. Huffman, *Absorption and scattering of light by small particles* (Wiley, New York, 1983).
9. M. S. Patterson, B. C. Wilson, and D. R. Wyman, "The propagation of optical radiation in tissue. II: Optical properties of tissues and resulting fluence distributions," Lasers in Medical Science **6,** 379-390 (1991).
10. S. J. Matcher, M. Cope, and D. T. Delpy, "In vivo measurements of the wavelength dependence of tissue-scattering coefficients between 760 and 900 nm measured with time-resolved spectroscopy," Applied Optics **36,** 386-396 (1997).
11. M. Born, and E. Wolf, *Principles of optics: electromagnetic theory of propagation, interference and diffraction of light* (Cambridge University Press, Cambridge ; New York, 1999).

12. W. F. Cheong, S. A. Prahl, and A. J. Welch, "A review of the optical properties of biological tissues," Quantum Electronics, IEEE Journal of **26,** 2166-2185 (1990).

13. A. Liebert, H. Wabnitz, D. Grosenick, M. Möller, R. Macdonald, and H. Rinneberg, "Evaluation of Optical Properties of Highly Scattering Media by Moments of Distributions of Times of Flight of Photons," Applied Optics **42,** 5785-5792 (2003).

14. G. W. Faris, "Diffusion equation boundary conditions for the interface between turbid media: a comment," J. Opt. Soc. Am. A **19,** 519-520 (2002).

15. G. N. K. Y. Tatsuya Nakai, "Expression of optical diffusion coefficient in high-absorption turbid media," Electronics and Communications in Japan (Part II: Electronics) **81,** 34-41 (1998).

16. I. V. Yaroslavsky, A. N. Yaroslavsky, V. V. Tuchin, and H.-J. Schwarzmaier, "Effect of the scattering delay on time-dependent photon migration in turbid media," Applied Optics **36,** 6529-6538 (1997).

17. C. A. Thompson, K. J. Webb, and A. M. Weiner, "Diffusive media characterization with laser speckle," Applied Optics **36,** 3726-3734 (1997).

18. A. Kienle, and M. S. Patterson, "Improved solutions of the steady-state and the time-resolved diffusion equations for reflectance from a semi-infinite turbid medium," J. Opt. Soc. Am. A **14,** 246-254 (1997).

19. R. Model, R. Huenlich, D. Richter, H. H. Rinneberg, H. Wabnitz, and M. Walzel, "Imaging in random media: simulating light transport by numerical integration of the diffusion equation," in *Photon Transport in Highly Scattering Tissue*, (SPIE, Lille, France, 1995), pp. 11-22.

20. R. C. Haskell, L. O. Svaasand, T.-T. Tsay, T.-C. Feng, M. S. McAdams, and B. J. Tromberg, "Boundary conditions for the diffusion equation in radiative transfer," J. Opt. Soc. Am. A **11,** 2727- (1994).

21. G. Yoon, A. Welch, M. Motamedi, and M. v. Gemert, "Development and application of three-dimensional light distribution model for laser

irradiated tissue," Quantum Electronics, IEEE Journal of **23,** 1721-1733 (1987).

22. M. Keijzer, W. M. Star, and P. R. M. Storchi, "Optical diffusion in layered media," Applied Optics **27,** 1820 (1988).

23. M. S. C. Patterson, B.; Wilson, Brian C., "Time resolved reflectance and transmittance for the noninvasive measurement of tissue optical properties," Applied Optics **28,** 2331-2336 (1989).

24. V. V. Tuchin, "Light scattering study of tissues," Physics-Uspekhi **40,** 495-515 (1997).

25. S. J. Madsen, B. C. Wilson, M. S. Patterson, Y. D. Park, S. L. Jacques, and Y. Hefetz, "Experimental tests of a simple diffusion model for the estimation of scattering and absorption coefficients of turbid media from time resolved diffuse reflectance measurements," Applied Optics **31,** 3509-3517 (1992).

26. T. J. Farrell, M. S. Patterson, and B. Wilson, "A diffusion theory model of spatially resolved, steady-state diffuse reflectance for the noninvasive determination of tissue optical properties in vivo," Medical Physics **19,** 879-888 (1992).

27. D. T. Delpy, and M. Cope, "Quantification in tissue near-infrared spectroscopy," Philosophical Transactions of the Royal Society B: Biological Sciences **352,** 649-659 (1997).

28. R. Richards-Kortum, and E. Sevick-Muraca, "Quantitative optical spectroscopy for tissue diagnosis," Annual Review of Physical Chemistry **47,** 555-606 (1996).

29. R. A. J. Groenhuis, J. J. Ten Bosch, and H. A. Ferwerda, "Scattering and absorption of turbid materials determined from reflection measurements. 2: Measuring method and calibration," Applied Optics **22,** 2463 (1983).

30. M. G. Nichols, E. L. Hull, and T. H. Foster, "Design and testing of a white-light, steady-state diffuse reflectance spectrometer for determination

of optical properties of highly scattering systems," Applied Optics **36,** 93-104 (1997).

31. R. M. P. Doornbos, R. Lang, M. C. Aalders, F. W. Cross, and H. J. C. M. Sterenborg, "The determination of in vivo human tissue optical properties and absolute chromophore concentrations using spatially resolved steady-state diffuse reflectance spectroscopy," Physics in Medicine and Biology**,** 967 (1999).

32. S. Nickell, M. Hermann, M. Essenpreis, T. J. Farrell, U. Kramer, and M. S. Patterson, "Anisotropy of light propagation in human skin," Physics in Medicine and Biology**,** 2873 (2000).

33. J. Swartling, J. S. Dam, and S. Andersson-Engels, "Comparison of Spatially and Temporally Resolved Diffuse-Reflectance Measurement Systems for Determination of Biomedical Optical Properties," Applied Optics **42,** 4612-4620 (2003).

34. L. Wang, and S. L. Jacques, "Use of a laser beam with an oblique angle of incidence to measure the reduced scattering coefficient of a turbid medium," Applied Optics **34,** 2362-2366 (1995).

35. A. Kienle, L. Lilge, M. S. Patterson, R. Hibst, R. Steiner, and B. C. Wilson, "Spatially resolved absolute diffuse reflectance measurements for noninvasive determination of the optical scattering and absorption coefficients of biological tissue," Applied Optics **35,** 2304-2314 (1996).

36. L. Gobin, L. Blanchot, and H. Saint-Jalmes, "Integrating the Digitized Backscattered Image to Measure Absorption and Reduced-Scattering Coefficients in vivo," Applied Optics **38,** 4217-4227 (1999).

37. T. H. Pham, F. Bevilacqua, T. Spott, J. S. Dam, B. J. Tromberg, and S. Andersson-Engels, "Quantifying the absorption and reduced scattering coefficients of tissuelike turbid media over a broad spectral range with noncontact Fourier-transform hyperspectral imaging," Applied Optics **39,** 6487-6497 (2000).

38. N. Joshi, C. Donner, and H. W. Jensen, "Noninvasive measurement of scattering anisotropy in turbid materials by nonnormal incident illumination," Optics Letters **31,** 936-938 (2006).

39. R. A. J. Groenhuis, H. A. Ferwerda, and J. J. Ten Bosch, "Scattering and absorption of turbid materials determined from reflection measurements. 1: Theory," Applied Optics **22,** 2456 (1983).

40. M. E. Arnoldussen, D. Cohen, G. H. Bearman, and W. S. Grundfest, "Consequences of scattering for spectral imaging of turbid biologic tissue," Journal of Biomedical Optics **5,** 300-306 (2000).

41. D. T. Delpy, M. Cope, P. v. d. Zee, S. Arridge, S. Wray, and J. Wyatt, "Estimation of optical pathlength through tissue from direct time of flight measurement," Physics in Medicine and Biology **33,** 1433-1442 (1988).

42. M. S. Patterson, J. D. Moulton, B. C. Wilson, and B. Chance, "Applications of time-resolved light scattering measurements to photodynamic therapy dosimetry," in *Photodynamic Therapy: Mechanisms II*, (SPIE, Los Angeles, CA, USA, 1990), pp. 62-75.

43. F. Liu, K. M. Yoo, and R. R. Alfano, "Ultrafast laser-pulse transmission and imaging through biological tissues," Appl. Opt. **32,** 554-558 (1993).

44. D. Mathur, "Matter in strong fields: from molecules to living cells," Journal of Physics: Conference Series**,** 012048 (2007).

45. B. J. Tromberg, N. Shah, R. Lanning, A. Cerussi, J. Espinoza, T. Pham, L. Svaasand, and J. Butler, "Non-invasive in vivo characterization of breast tumors using photon migration spectroscopy," Neoplasia **2,** 26-40 (2000).

46. B. W. Pogue, and M. S. Patterson, "Frequency-domain optical absorption spectroscopy of finite tissue volumes using diffusion theory," Physics in medicine & biology **39,** 1157-1180 (1994).

47. B. W. Pogue, S. Jiang, H. Dehghani, C. Kogel, S. Soho, S. Srinivasan, X. Song, T. D. Tosteson, S. P. Poplack, and K. D. Paulsen, "Characterization of hemoglobin, water, and NIR scattering in breast tissue: analysis of intersubject variability and menstrual cycle changes," Journal of Biomedical Optics **9,** 541-552 (2004).

48. F. Blais, "Review of 20 years of range sensor development," Journal of electronic imaging **13,** 231 (2004).

49. S. Yamaguchi, "Convenient Method of Measuring the Chirp Structure of Femtosecond White-Light Continuum Pulses," Applied Spectroscopy **49,** 1513 (1995).

50. A. M. Zheltikov, "Let there be white light: supercontinuum generation by ultrashort laser pulses," Physics-Uspekhi**,** 605 (2006).

51. G. r. Genty, "Supercontinuum generation in microstructured fibers and novel optical measurement techniques," (Helsinki University of Technology, Espoo, 2004).

52. R. L. Fork, C. V. Shank, C. Hirlimann, R. Yen, and W. J. Tomlinson, "Femtosecond white-light continuum pulses," Opt. Lett. **8,** 1-3 (1983).

53. S. Andersson-Engels, R. Berg, A. Persson, and S. Svanberg, "Multispectral tissue characterization with time-resolved detection of diffusely scattered white light," Opt. Lett. **18,** 1697-1699 (1993).

54. S. A. Trushin, W. Fuss, K. Kosma, and W. E. Schmid, "Widely tunable ultraviolet sub-30-fs pulses from supercontinuum for transient spectroscopy," Applied Physics B: Lasers and Optics **85,** 1-5 (2006).

55. R. R. Alfano, "Emission in the Region 4000 to 7000 Å Via Four-Photon Coupling in Glass," Physical Review Letters **24,** 584 (1970).

56. J. K. Ranka, R. S. Windeler, and A. J. Stentz, "Visible continuum generation in air-silica microstructure optical fibers with anomalous dispersion at 800 nm," Optics letters **25,** 25-27 (2000).

57. K. Lindfors, T. Kalkbrenner, P. Stoller, and V. Sandoghdar, "Detection and Spectroscopy of Gold Nanoparticles Using

Supercontinuum White Light Confocal Microscopy," Physical Review Letters **93,** 037401 (2004).

58. T. A. Birks, W. J. Wadsworth, and P. S. Russell, "Supercontinuum generation in tapered fibers," Optics letters **25,** 1415-1417 (2000).

59. T. H. Pham, O. Coquoz, J. B. Fishkin, E. Anderson, and B. J. Tromberg, "Broad bandwidth frequency domain instrument for quantitative tissue optical spectroscopy," Review of Scientific Instruments **71,** 2500-2513 (2000).

60. B. Chance, "Time-resolved spectroscopy and imaging," in *Optical Tomography, Photon Migration, and Spectroscopy of Tissue and Model Media: Theory, Human Studies, and Instrumentation*, (SPIE, San Jose, CA, USA, 1995), pp. 122-139.

61. S. J. Madsen, E. R. Anderson, R. C. Haskell, and B. J. Tromberg, "Portable, high-bandwidth frequency-domain photon migration instrument for tissue spectroscopy," Opt. Lett. **19,** 1934-1936 (1994).

62. S. R. Arridge, M. Cope, and D. T. Delpy, "The theoretical basis for the determination of optical pathlengths in tissue: temporal and frequency analysis," Physics in Medicine and Biology**,** 1531 (1992).

63. E. M. Sevick, B. Chance, J. Leigh, S. Nioka, and M. Maris, "Quantitation of time- and frequency-resolved optical spectra for the determination of tissue oxygenation," Analytical Biochemistry **195,** 330-351 (1991).

64. S. Fantini, "Frequency-domain multichannel optical detector for noninvasive tissue spectroscopy and oximetry," Optical engineering **34,** 32 (1995).

65. D. H. Burns, "Optical Tomography for Three-Dimensional Spectroscopy," Applied Spectroscopy **48,** 12 (1994).

66. W. F. Long, C. E. W. Gributs, and D. H. Burns, "Quantification in highly scattering/absorbing layered samples using photon time-of-flight

measurements and confocal optical geometry," Vibrational Spectroscopy **30,** 121-129 (2002).

67. G. Boverman, Q. Fang, S. A. Carp, E. L. Miller, D. H. Brooks, J. Selb, R. H. Moore, D. B. Kopans, and D. A. Boas, "Spatio-temporal imaging of the hemoglobin in the compressed breast with diffuse optical tomography," Physics in Medicine and Biology**,** 3619 (2007).

68. S. Srinivasan, B. W. Pogue, S. Jiang, H. Dehghani, C. Kogel, S. Soho, J. J. Gibson, T. D. Tosteson, S. P. Poplack, and K. D. Paulsen, "Interpreting hemoglobin and water concentration, oxygen saturation, and scattering measured in vivo by near-infrared breast tomography," Proceedings of the National Academy of Sciences **100,** 12349-12354 (2003).

69. T. O. McBride, B. W. Pogue, S. Poplack, S. Soho, W. A. Wells, S. Jiang, U. L. Osterberg, and K. D. Paulsen, "Multispectral near-infrared tomography: a case study in compensating for water and lipid content in hemoglobin imaging of the breast," Journal of Biomedical Optics **7,** 72-79 (2002).

70. D. A. Benaron, M. Lennox, and D. K. Stevenson, "Two-dimensional and 3-D images of thick tissue using time-constrained times-of-flight and absorbance spectrophotometry," in *Physiological Monitoring and Early Detection Diagnostic Methods*, (SPIE, Los Angeles, CA, USA, 1992), pp. 35-45.

71. D. Huang, E. A. Swanson, C. P. Lin, J. S. Schuman, W. G. Stinson, W. Chang, M. R. Hee, T. Flotte, K. Gregory, and C. A. Puliafito, "Optical coherence tomography," Science **254,** 1178-1181 (1991).

72. A. M. Rollins, and J. A. Izatt, "Optimal interferometer designs for optical coherence tomography," Optics letters **24,** 1484-1486 (1999).

73. J. M. Schmitt, "Optical coherence tomography (OCT): a review," IEEE journal of selected topics in quantum electronics **5,** 1205 (1999).

74. W. Watanabe, Y. Masuda, and K. Itoh, "Coherence Spectrotomography of Layered Medium with White-Light Continuum," Optical Review **6,** 71-76 (1999).

75. A. F. Fercher, "Optical coherence tomography-principles and applications," Reports on Progress in Physics **66,** 239 (2003).

76. W. Drexler, "Ultrahigh-resolution optical coherence tomography," Journal of biomedical optics **9,** 47 (2004).

77. D. A. Boas, D. H. Brooks, E. L. Miller, C. A. DiMarzio, M. Kilmer, R. J. Gaudette, and Z. Quan, "Imaging the body with diffuse optical tomography," Signal Processing Magazine, IEEE **18,** 57-75 (2001).

78. J.-L. Boulnois, "Photophysical processes in recent medical laser developments: A review," Lasers in Medical Science **1,** 47-66 (1986).

79. B. C. Wilson, "Time-dependent optical spectroscopy and imaging for biomedical applications," Proceedings of the IEEE **80,** 918 (1992).

80. B. C. Wilson, "Optical reflectance and transmittance of tissues: principles and applications," IEEE journal of quantum electronics **26,** 2186 (1990).

81. S. Andersson-Engels, J. Axelsson, A. Johansson, J. Johansson, S. Svanberg, and T. Svensson, "Time-of-flight laser spectroscopy in biomedical diagnostics," in *Optical Fiber Communication and Optoelectronics Conference, 2007 Asia*, (2007), pp. 236-238.

82. R. R. Alfano, "Advances in Optical Imaging of Biomedical Media," Annals of the New York Academy of Sciences **820,** 248 (1997).

83. S. J. Matcher, "Performance Comparison of Several Published Tissue Near-Infrared Spectroscopy Algorithms," Analytical Biochemistry **227,** 54 (1995).

84. R. X. Xu, B. Qiang, J. J. Mao, and S. P. Povoski, "Development of a handheld near-infrared imager for dynamic characterization of in vivo biological tissue systems," Applied Optics **46,** 7442-7451 (2007).

85. T. Shiga, K. Yamamoto, K. Tanabe, Y. Nakase, and B. Chance, "Study of an algorithm based on model experiments and diffusion theory for a portable tissue oximeter," Journal of Biomedical Optics **2,** 154-161 (1997).

86. B. Grassi, V. Quaresima, C. Marconi, M. Ferrari, and P. Cerretelli, "Blood lactate accumulation and muscle deoxygenation during incremental exercise," J Appl Physiol **87,** 348-355 (1999).

87. N. J. Crane, Z. D. Schultz, and I. W. Levin, "Contrast Enhancement for in Vivo Visible Reflectance Imaging of Tissue Oxygenation," Appl. Spectrosc. **61,** 797-803 (2007).

88. S. P. Nighswander-Rempel, V. V. Kupriyanov, and R. A. Shaw, "Regional cardiac tissue oxygenation as a function of blood flow and pO_2: a near-infrared spectroscopic imaging study," Journal of Biomedical Optics **11,** 054004-054010 (2006).

89. P. Rolfe, "In vivo near-infrared spectroscopy," Annual Review of Biomedical Engineering **2,** 715-754 (2000).

90. J. Gade, D. Palmqvist, P. Plomgard, and G. Greisen, "Diffuse reflectance spectrophotometry with visible light: comparison of four different methods in a tissue phantom," Physics in Medicine and Biology **51,** 121-136 (2006).

91. R. J. McNichols, and G. L. Cote, "Optical glucose sensing in biological fluids: an overview," Journal of Biomedical Optics **5,** 5-16 (2000).

92. A. D. McGown, H. Makker, C. Elwell, P. G. Al Rawi, A. Valipour, and S. G. Spiro, "Measurement of Changes in Cytochrome Oxidase Redox State During Obstructive Sleep Apnea Using Near-Infrared Spectroscopy," Sleep **26,** 1-7 (2003).

93. L. S. L. Arakaki, "An Optical Method for Myoglobin Oxygenenation Measurements in the Blood-Perfused Rat Hind Limb," in *Center for Bioengineering*, (University of Washington, Seattle, 1995), p. 161.

94. H. Xu, B. W. Pogue, H. Dehghani, K. D. Paulsen, R. Springett, and J. F. Dunn, "Absorption and scattering imaging of tissue with steady-state second-differential spectral-analysis tomography," Optics Letters **29,** 2043-2045 (2004).

95. D. Lafrance, L. C. Lands, and D. H. Burns, "In vivo lactate measurement in human tissue by near-infrared diffuse reflectance spectroscopy," Vibrational Spectroscopy **36,** 195-202 (2004).

96. D. J. Marcinek, W. A. Ciesielski, K. E. Conley, and K. A. Schenkman, "Oxygen regulation and limitation to cellular respiration in mouse skeletal muscle in vivo," Am J Physiol Heart Circ Physiol **285,** H1900-1908 (2003).

97. K. A. Schenkman, Marble, D.R., Burns, D.H., Feigl, E.O., "Optical Spectroscopic Method for in Vivo Measurement of Cardiac Myoglobin Oxygen Saturation," Applied Spectroscopy **53,** 332-338 (1999).

98. M. G. Sowa, L. Leonardi, J. R. Payette, K. M. Cross, M. Gomez, and J. S. Fish, "Classification of burn injuries using near-infrared spectroscopy," Journal of Biomedical Optics **11,** 054002-054006 (2006).

99. J. Wang, Y.-J. Geng, B. Guo, T. Klima, B. N. Lal, J. T. Willerson, and W. Casscells, "Near-infrared spectroscopic characterization of human advanced atherosclerotic plaques," J Am Coll Cardiol **39,** 1305-1313 (2002).

100. M. M. Tisdall, I. Tachtsidis, T. S. Leung, C. E. Elwell, and M. Smith, "Near-infrared spectroscopic quantification of changes in the concentration of oxidized cytochrome c oxidase in the healthy human brain during hypoxemia," Journal of Biomedical Optics **12,** 024002-024007 (2007).

101. J. Hoffmann, D. W. Lubbers, and H. M. Heise, "Applicability of the Kubelka-Munk theory for the evaluation of reflectance spectra demonstrated for haemoglobin-free perfused heart tissue," Physics in Medicine and Biology **43,** 3571-3587 (1998).

102. D. J. Dahm, and K. D. Dahm, "Representative Layer Theory for Diffuse Reflectance," Applied Spectroscopy **53,** 647-654 (1999).

103. B. O. Budevska, S. T. Sum, and T. J. Jones, "Application of Multivariate Curve Resolution for Analysis of FT-IR Microspectroscopic Images of in Situ Plant Tissue," Applied Spectroscopy **57,** 124-131 (2003).

104. C. E. W. Gributs, and D. H. Burns, "Parsimonious calibration models for near-infrared spectroscopy using wavelets and scaling functions," Chemometrics and Intelligent Laboratory Systems **83,** 44-53 (2006).

105. B. M. Smith, and P. J. Gemperline, "Wavelength Selection and Optimization of Pattern Recognition Methods Using the Genetic Algorithm," Analytica Chimica Acta **423,** 167-177 (2000).

106. C. Beleites, G. Steiner, M. G. Sowa, R. Baumgartner, S. Sobottka, G. Schackert, and R. Salzer, "Classification of human gliomas by infrared imaging spectroscopy and chemometric image processing," Vibrational Spectroscopy **38,** 143-149 (2005).

107. F. P. Bevilacqua, D. Piguet, P. Marquet, J. D. Gross, B. J. Tromberg, and C. D. Depeursinge, "In-vivo local determination of tissue optical properties," in *Photon Propagation in Tissues III*, (SPIE, San Remo, Italy, 1998), pp. 262-268.

108. T. Hamaoka, T. Katsumura, N. Murase, S. Nishio, T. Osada, T. Sako, H. Higuchi, Y. Kurosawa, T. Shimomitsu, M. Miwa, and B. Chance, "Quantification of ischemic muscle deoxygenation by near infrared time-resolved spectroscopy," Journal of Biomedical Optics **5,** 102-105 (2000).

109. R. Hornung, T. H. Pham, K. A. Keefe, M. W. Berns, Y. Tadir, and B. J. Tromberg, "Quantitative near-infrared spectroscopy of cervical dysplasia in vivo," Hum. Reprod. **14,** 2908-2916 (1999).

110. A. Cerussi, N. Shah, D. Hsiang, A. Durkin, J. Butler, and B. J. Tromberg, "In vivo absorption, scattering, and physiologic properties of 58

malignant breast tumors determined by broadband diffuse optical spectroscopy," Journal of Biomedical Optics **11,** 044005-044016 (2006).

111. T. J. Beck, W. Beyer, T. Pongratz, W. Stummer, R. M. Waidelich, H. Stepp, S. Wagner, and R. Baumgartner, "Clinical determination of tissue optical properties in vivo by spatially resolved reflectance measurements," in *Photon Migration and Diffuse-Light Imaging*, (SPIE, Munich, Germany, 2003), pp. 96-105.

112. F. Chauchard, S. Roussel, J. M. Roger, V. Bellon-Maurel, C. Abrahamsson, T. Svensson, S. Andersson-Engels, and S. Svanberg, "Least-squares support vector machines modelization for time-resolved spectroscopy," Applied Optics **44,** 7091-7097 (2005).

113. T. Xu, C. Zhang, X. Wang, L. Zhang, and J. Tian, "Measurement and Analysis of Light Distribution in Intralipid-10% at 650 nm," Applied Optics **42,** 5777-5784 (2003).

114. H. Owen-Reece, M. Smith, C. E. Elwell, and J. C. Goldstone, "Near infrared spectroscopy," Br. J. Anaesth. **82,** 418-426 (1999).

115. G. Greisen, "Is near-infrared spectroscopy living up to its promises?," Seminars in Fetal and Neonatal Medicine **11,** 498-502 (2006).

116. G. Zaccanti, A. Taddeucci, M. Barilli, P. Bruscaglioni, and F. Martelli, "Optical properties of biological tissues," in *Optical Tomography, Photon Migration, and Spectroscopy of Tissue and Model Media: Theory, Human Studies, and Instrumentation*, (SPIE, San Jose, CA, USA, 1995), pp. 513-521.

117. M. J. C. Van Gemert, S. L. Jacques, H. J. C. M. Sterenborg, and W. M. Star, "Skin optics," Biomedical Engineering, IEEE Transactions on **36,** 1146-1154 (1989).

118. L. Stryer, *Biochemistry* (W.H. Freeman, New York :, 1995).

119. J. B. Wittenberg, "Myoglobin-facilitated oxygen diffusion: role of myoglobin in oxygen entry into muscle," Physiol. Rev. **50,** 559-636 (1970).

120. L. S. L. Arakaki, and D. H. Burns, "Multispectral Analysis for Quantitative Measurements of Myoglobin Oxygen Fractional Saturation in the Presence of Hemoglobin Interference," Applied Spectroscopy **46,** 1919-1928 (1992).

121. S. J. Matcher, P. J. Kirkpatrick, K. Nahid, M. Cope, and D. T. Delpy, "Absolute quantification methods in tissue near-infrared spectroscopy," in *Optical Tomography, Photon Migration, and Spectroscopy of Tissue and Model Media: Theory, Human Studies, and Instrumentation*, (SPIE, San Jose, CA, USA, 1995), pp. 486-495.

122. K. A. Schenkman, D. R. Marble, D. H. Burns, and E. O. Feigl, "Myoglobin oxygen dissociation by multiwavelength spectroscopy," J Appl Physiol **82,** 86-92 (1997).

123. J. C. Maxwell, C. H. Barlow, J. E. Spallholz, and W. S. Caughey, "The utility of infrared spectroscopy as a probe of intact tissue: determination of carbon monoxide and hemeproteins in blood and heart muscle," Biochem Biophys Res Commun **61,** 230-236 (1974).

124. F. Costes, J. C. Barthelemy, L. Feasson, T. Busso, A. Geyssant, and C. Denis, "Comparison of muscle near-infrared spectroscopy and femoral blood gases during steady-state exercise in humans," J Appl Physiol **80,** 1345-1350 (1996).

125. R. A. Blasi, M. Cope, C. Elwell, F. Safoue, and M. Ferrari, "Noninvasive measurement of human forearm oxygen consumption by near infrared spectroscopy," European Journal of Applied Physiology **67,** 20-25 (1993).

126. R. Boushel, H. Langberg, J. Olesen, J. Gonzales-Alonzo, J. Bulow, and M. Kjaer, "Monitoring tissue oxygen availability with near infrared spectroscopy (NIRS) in health and disease," Scandinavian Journal of Medicine & Science in Sports **11,** 213-222 (2001).

127. M. J. Hayes, and P. R. Smith, "Artifact Reduction in Photoplethysmography," Applied Optics **37,** 7437-7446 (1998).

128. G. A. Millikan, "The Oximeter, an Instrument for Measuring Continuously the Oxygen Saturation of Arterial Blood in Man," Review of Scientific Instruments **13,** 434-444 (1942).

129. G. Zonios, U. Shankar, and V. K. Iyer, "Pulse oximetry theory and calibration for low saturations," Biomedical Engineering, IEEE Transactions on **51,** 818-822 (2004).

130. J. E. Sinex, "Pulse oximetry: Principles and limitations," The American Journal of Emergency Medicine **17,** 59-66 (1999).

131. J. G. Webster, ed. *Design of Pulse Oximeters* (Institute of Physics Publishing, Bristol and Philadelphia, 1997).

132. A. C. Ralston, R. K. Webb, and W. B. Runciman, "Potential errors in pulse oximetry. I. Pulse oximeter evaluation," Anaesthesia **46,** 202-206 (1991).

133. K. Humphreys, T. Ward, and C. Markham, "Noncontact simultaneous dual wavelength photoplethysmography: A further step toward noncontact pulse oximetry," Review of Scientific Instruments **78,** 044304 (2007).

134. D. M. Mancini, J. R. Wilson, L. Bolinger, H. Li, K. Kendrick, B. Chance, and J. S. Leigh, "In vivo magnetic resonance spectroscopy measurement of deoxymyoglobin during exercise in patients with heart failure. Demonstration of abnormal muscle metabolism despite adequate oxygenation," Circulation **90,** 500-508 (1994).

135. K. A. Schenkman, and W. A. Ciesielski, "Improved Myoglobin Saturation Measurement Made by Partial Least-Squares Analysis of Optical Reflectance Spectra," Applied Spectroscopy **56,** 1215-1221 (2002).

136. D. J. Marcinek, K. A. Schenkman, W. A. Ciesielski, and K. E. Conley, "Mitochondrial coupling in vivo in mouse skeletal muscle," Am J Physiol Cell Physiol **286,** C457-463 (2004).

137. D. Lafrance, L. C. Lands, L. Hornby, and D. H. Burns, "Near-Infrared Spectroscopic Measurement of Lactate in Human Plasma," Applied Spectroscopy **54,** 300-304 (2000).

138. D. Lafrance, L. C. Lands, and D. H. Burns, "Measurement of lactate in whole human blood with near-infrared transmission spectroscopy," Talanta **60,** 635-641 (2003).

139. N. Kollias, "The physical basis of skin color and its evaluation," Clinics in Dermatology **13,** 361-367 (1995).

140. G. N. Stamatas, B. Z. Zmudzka, N. Kollias, and J. Z. Beer, "Non-Invasive Measurements of Skin Pigmentation In Situ," Pigment Cell Research **17,** 618-626 (2004).

141. I. Nishidate, Y. Aizu, and H. Mishina, "Estimation of melanin and hemoglobin in skin tissue using multiple regression analysis aided by Monte Carlo simulation," Journal of Biomedical Optics **9,** 700-710 (2004).

142. A. N. Bashkatov, E. A. Genina, V. I. Kochubey, and V. V. Tuchin, "Optical properties of human skin, subcutaneous and mucous tissues in the wavelength range from 400 to 2000 nm," Journal of Physics D: Applied Physics**,** 2543 (2005).

143. W. Shen, Z. Wang, M. Punyanita, J. Lei, A. Sinav, J. G. Kral, C. Imielinska, R. Ross, and S. B. Heymsfield, "Adipose Tissue Quantification by Imaging Methods: A Proposed Classification," Obesity Res **11,** 5-16 (2003).

144. J. J. Kelly, K. A. Kelly, and C. H. Barlow, "Tissue temperature by near-infrared spectroscopy," in *Optical Tomography, Photon Migration, and Spectroscopy of Tissue and Model Media: Theory, Human Studies, and Instrumentation*, (SPIE, San Jose, CA, USA, 1995), pp. 818-828.

145. O. S. Khalil, "Spectroscopic and Clinical Aspects of Noninvasive Glucose Measurements," Clin Chem **45,** 165-177 (1999).

146. O. S. Khalil, "Non-invasive glucose measurement technologies: an update from 1999 to the dawn of the new millennium," Diabetes Technol Ther **6,** 660-697 (2004).
147. J. C. Pickup, F. Hussain, N. D. Evans, and N. Sachedina, "In vivo glucose monitoring: the clinical reality and the promise," Biosensors and Bioelectronics **20,** 1897-1902 (2005).
148. M. A. Arnold, and G. W. Small, "Noninvasive Glucose Sensing," Anal. Chem. **77,** 5429-5439 (2005).
149. M. A. Arnold, "Non-invasive glucose monitoring," Current Opinion in Biotechnology **7,** 46-49 (1996).
150. M. R. Robinson, R. P. Eaton, D. M. Haaland, G. W. Koepp, E. V. Thomas, B. R. Stallard, and P. L. Robinson, "Noninvasive glucose monitoring in diabetic patients: a preliminary evaluation," Clin Chem **38,** 1618-1622 (1992).
151. J. Chen, M. A. Arnold, and G. W. Small, "Comparison of Combination and First Overtone Spectral Regions for Near-Infrared Calibration Models for Glucose and Other Biomolecules in Aqueous Solutions," Anal. Chem. **76,** 5405-5413 (2004).
152. K. H. Hazen, M. A. Arnold, and G. W. Small, "Measurement of glucose and other analytes in undiluted human serum with near-infrared transmission spectroscopy," Analytica Chimica Acta **371,** 255-267 (1998).
153. L. S. L. Arakaki, M. J. Kushmerick, and D. H. Burns, "Myoglobin Oxygen Saturation Measured Independently of Hemoglobin in Scattering Media by Optical Reflectance Spectroscopy," Applied Spectroscopy **50,** 697-707 (1996).
154. M. Egawa, T. Fukuhara, M. Takahashi, and Y. Ozaki, "Determining Water Content in Human Nails with a Portable Near-Infrared Spectrometer," Applied Spectroscopy **57,** 473-478 (2003).
155. M. Cope, P. van der Zee, M. Essenpreis, S. R. Arridge, and D. T. Delpy, "Data analysis methods for near-infrared spectroscopy of tissue:

problems in determining the relative cytochrome aa_3 concentration," in *Time-Resolved Spectroscopy and Imaging of Tissues*, (SPIE, Los Angeles, CA, USA, 1991), pp. 251-262.

156. B. G. Osborne, "Near-infrared spectroscopy in food analysis," in *Encyclopedia of Analytical Chemistry*, R. A. Meyers, ed. (John Wiley & Sons Ltd., Chichester, 1986), pp. 1-14.

157. M. Blanco, J. Coello, A. Eustaquio, H. Iturriaga, and S. Maspoch, "Development and validation of a method for the analysis of a pharmaceutical preparation by near-infrared diffuse reflectance spectroscopy," Journal of Pharmaceutical Sciences **88,** 551-556 (1999).

158. B. D. S. Venz, "NIR-spectroscopic investigation of water sorption characteristics of dental resins and composites," Journal of Biomedical Materials Research **25,** 1231-1248 (1991).

159. A. E. Cerussi, D. Jakubowski, N. Shah, F. Bevilacqua, R. Lanning, A. J. Berger, D. Hsiang, J. Butler, R. F. Holcombe, and B. J. Tromberg, "Spectroscopy enhances the information content of optical mammography," Journal of Biomedical Optics **7,** 60-71 (2002).

160. J. Nyström, B. Lindholm-Sethson, L. Stenberg, S. Ollmar, J. Eriksson, and P. Geladi, "Combined near-infrared spectroscopy and multifrequency bio-impedance investigation of skin alterations in diabetes patients based on multivariate analyses," Medical and Biological Engineering and Computing **41,** 324-329 (2003).

161. V. R. Kondepati, J. Zimmermann, M. Keese, J. Sturm, B. C. Manegold, and J. Backhaus, "Near-infrared fiber optic spectroscopy as a novel diagnostic tool for the detection of pancreatic cancer," Journal of Biomedical Optics **10,** 054016-054016 (2005).

162. D. J. Faber, M. C. G. Aalders, E. G. Mik, B. A. Hooper, M. J. C. van Gemert, and T. G. van Leeuwen, "Oxygen Saturation-Dependent Absorption and Scattering of Blood," Physical Review Letters **93,** 028102-028104 (2004).

163. H. Martens, J. P. Nielsen, and S. B. Engelsen, "Light Scattering and Light Absorbance Separated by Extended Multiplicative Signal Correction. Application to Near-Infrared Transmission Analysis of Powder Mixtures," Analytical Chemistry **75,** 394-404 (2003).

164. M. Miwa, Y. Ueda, and B. Chance, "Development of time-resolved spectroscopy system for quantitative noninvasive tissue measurement," in *Optical Tomography, Photon Migration, and Spectroscopy of Tissue and Model Media: Theory, Human Studies, and Instrumentation*, (SPIE, San Jose, CA, USA, 1995), pp. 142-149.

165. L. Leonardi, and D. H. Burns, "Quantitative constituent measurements in scattering media from statistical analysis of photon time-of-flight distributions," Analytica Chimica Acta **348,** 543-551 (1997).

166. S. R. Arridge, and M. Schweiger, "Direct calculation of the moments of the distribution of photon time of flight in tissue with a finite-element method," Applied Optics **34,** 2683-2687 (1995).

167. S. T. Flock, S. L. Jacques, B. C. Wilson, W. M. Star, and M. J. C. v. Gemert, "Optical properties of intralipid: A phantom medium for light propagation studies," Lasers in Surgery and Medicine **12,** 510-519 (1992).

168. S. J. Madsen, M. S. Patterson, and B. C. Wilson, "The use of India ink as an optical absorber in tissue-simulating phantoms," Physics in Medicine and Biology **37,** 985 (1992).

169. H. J. van Staveren, C. J. M. Moes, J. van Marle, S. A. Prahl, and M. J. C. van Gemert, "Light scattering in Intralipid-10% in the wavelength range of 400-1100 nm," Applied Optics **30,** 4507-4514 (1991).

170. P. Geladi, and B. R. Kowalski, "Partial least-squares regression: a tutorial," Analytica Chimica Acta **185,** 1-17 (1986).

171. W. R. Chitwood, Jr., C. L. Wixon, J. R. Elbeery, J. F. Moran, W. H. H. Chapman, and R. M. Lust, "VIDEO-ASSISTED MINIMALLY INVASIVE MITRAL VALVE SURGERY," J Thorac Cardiovasc Surg **114,** 773-782 (1997).

172. K. A. Schenkman, and S. Yan, "Propofol impairment of mitochondrial respiration in isolated perfused guinea pig hearts determined by reflectance spectroscopy," Crit Care Med **28,** 172-177 (2000).

173. M. V. Schulmerich, K. A. Dooley, M. D. Morris, T. M. Vanasse, and S. A. Goldstein, "Transcutaneous fiber optic Raman spectroscopy of bone using annular illumination and a circular array of collection fibers," Journal of Biomedical Optics **11,** 060502-060503 (2006).

174. P. Matousek, "Inverse Spatially Offset Raman Spectroscopy for Deep Noninvasive Probing of Turbid Media," Appl. Spectrosc. **60,** 1341-1347 (2006).

175. D. Rozas, "Generation and Propagation of Optical Vortices," in *Physics*, (Worcester Polytechnic Institute, Worcester, MA, 1999), p. 176.

176. D. Ganic, X. Gan, M. Gu, M. Hain, S. Somalingam, S. Stankovic, and T. Tschudi, "Generation of doughnut laser beams by use of a liquid-crystal cell with a conversion efficiency near 100%," Optics Letters **27,** 1351-1353 (2002).

177. D. McGloin, N. B. Simpson, and M. J. Padgett, "Transfer of orbital angular momentum from a stressed fiber-optic waveguide to a light beam," Applied Optics **37,** 469-472 (1998).

178. G.-H. Kim, J.-H. Jeon, K.-H. Ko, H.-J. Moon, J.-H. Lee, and J.-S. Chang, "Optical vortices produced with a nonspiral phase plate," Applied Optics **36,** 8614-8621 (1997).

179. L. Allen, M. W. Beijersbergen, R. J. C. Spreeuw, and J. P. Woerdman, "Orbital angular momentum of light and the transformation of Laguerre-Gaussian laser modes," Physical Review A **45,** 8185 (1992).

180. M. S. Soskin, and M. V. Vasnetsov, "Nonlinear singular optics," Pure and Applied Optics: Journal of the European Optical Society Part A **7,** 301-311 (1998).

181. J. Arlt, K. Dholakia, L. Allen, and M. J. Padgett, "Parametric down-conversion for light beams possessing orbital angular momentum," Physical Review A **59,** 3950 (1999).

182. Q. Wang, X. W. Sun, P. Shum, and X. J. Yin, "Dynamic switching of optical vortices with dynamic gamma-correction liquid crystal spiral phase plate," Optics Express **13,** 10285-10291 (2005).

183. J. Lin, X.-C. Yuan, and S. H. Tao, "Variable-radius focused optical vortex with suppressed sidelobes," Optics Letters **31,** 1600- (2006).

184. P.-A. Belanger, and M. Rioux, "Ring pattern of a lens-axicon doublet illuminated by a Gaussian beam (TE)," Appl. Opt. **17,** 1080 (1978).

185. C.-S. Guo, X. Liu, J.-L. He, and H.-T. Wang, "Optimal annulus structures of optical vortices," Optics Express **12,** 4625-4634 (2004).

186. V. V. Kotlyar, A. A. Kovalev, and V. A. Soifer, "Sidelobe contrast reduction for optical vortex beams using a helical axicon," Optics Letters **32,** 921-923 (2007).

187. M. D. Levenson, T. Ebihara, G. Dai, Y. Morikawa, N. Hayashi, and S. M. Tan, "Optical vortex masks for via levels," Journal of Microlithography, Microfabrication, and Microsystems **3,** 293-304 (2004).

188. N. R. Heckenberg, R. McDuff, C. P. Smith, H. Rubinsztein-Dunlop, and M. J. Wegener, "Laser beams with phase singularities," Optical and Quantum Electronics **24,** S951-S962 (1992).

189. D. G. Grier, "A revolution in optical manipulation," Nature **424,** 810-816 (2003).

190. N. B. Simpson, K. Dholakia, L. Allen, and M. J. Padgett, "Mechanical equivalence of spin and orbital angular momentum of light:an optical spanner," Optics Letters **22,** 52-54 (1997).

191. M. E. J. Friese, T. A. Nieminen, N. R. Heckenberg, and H. Rubinsztein-Dunlop, "Optical alignment and spinning of laser-trapped microscopic particles," Nature **394,** 348-350 (1998).

192. W. L. Power, L. Allen, M. Babiker, and V. E. Lembessis, "Atomic motion in light beams possessing orbital angular momentum," Physical Review A **52,** 479 (1995).

193. M. Babiker, W. L. Power, and L. Allen, "Light-induced Torque on Moving Atoms," Physical Review Letters **73,** 1239 (1994).

194. A. A. Ivanovskyy, I. V. Basistiy, and M. S. Soskin, "Synthesis, recording and metrology of laser beams with phase singularities," Semiconductor physics, Quantum electronics & optoelectronics **6,** 249-253 (2003).

195. T. M. Mitchell, *Machine Learning* (WCB/McGraw-Hill, Boston, 1997).

196. A. Niazi, A. Soufi, and M. Mobarakabadi, "Genetic Algorithm Applied to Selection of Wavelength in Partial Least Squares for Simultaneous Spectrophotometric Determination of Nitrophenol Isomers," Analytical Letters **39,** 2359 - 2372 (2006).

197. R. Leardi, M. B. Seasholtz, and R. J. Pell, "Variable selection for multivariate calibration using a genetic algorithm: prediction of additive concentrations in polymer films from Fourier transform-infrared spectral data," Analytica Chimica Acta **461,** 189-200 (2002).

198. R. Leardi, "Application of genetic algorithm-PLS for feature selection in spectral data sets," Journal of Chemometrics **14,** 643-655 (2000).

199. Q. Ding, G. W. Small, and M. A. Arnold, "Genetic Algorithm-Based Wavelength Selection for the Near-Infrared Determination of Glucose in Biological Matrixes: Initialization Strategies and Effects of Spectral Resolution," Analytical Chemistry **70,** 4472-4479 (1998).

200. D. Broadhurst, R. Goodacre, A. Jones, J. J. Rowland, and D. B. Kell, "Genetic algorithms as a method for variable selection in multiple linear regression and partial least squares regression, with applications to pyrolysis mass spectrometry," Analytica Chimica Acta **348,** 71-86 (1997).

201. J. Yang, and V. Honavar, "Feature subset selection using a genetic algorithm," IEEE Intelligent Systems **13,** 44-49 (1998).

202. B. K. Lavine, C. E. Davidson, A. J. Moores, and P. R. Griffiths, "Raman Spectroscopy and Genetic Algorithms for the Classification of Wood Types," Applied Spectroscopy **55,** 960-966 (2001).

203. K. Raghuraj Rao, and S. Lakshminarayanan, "Partial correlation based variable selection approach for multivariate data classification methods," Chemometrics and Intelligent Laboratory Systems **86,** 68-81 (2007).

204. M. L. Raymer, W. F. Punch, E. D. Goodman, L. A. Kuhn, and A. K. Jain, "Dimensionality reduction using genetic algorithms," Evolutionary Computation, IEEE Transactions on **4,** 164-171 (2000).

205. R. Leardi, R. Boggia, and M. Terrile, "Genetic algorithms as a strategy for feature selection," Journal of Chemometrics **6,** 267-281 (1992).

206. D. Jouan-Rimbaud, D.-L. Massart, R. Leardi, and O. E. De Noord, "Genetic Algorithms as a Tool for Wavelength Selection in Multivariate Calibration," Analytical Chemistry **67,** 4295-4301 (1995).

207. A. S. Bangalore, R. E. Shaffer, G. W. Small, and M. A. Arnold, "Genetic Algorithm-Based Method for Selecting Wavelengths and Model Size for Use with Partial Least-Squares Regression: Application to Near-Infrared Spectroscopy," Analytical Chemistry **68,** 4200-4212 (1996).

208. M. J. Arcos, M. C. Ortiz, B. Villahoz, and L. A. Sarabia, "Genetic-algorithm-based wavelength selection in multicomponent spectrometric determinations by PLS: application on indomethacin and acemethacin mixture," Analytica Chimica Acta **339,** 63-77 (1997).

209. U. Depczynski, K. Jetter, K. Molt, and A. Niemoller, "Quantitative analysis of near infrared spectra by wavelet coefficient regression using a genetic algorithm," Chemometrics and Intelligent Laboratory Systems **47,** 179-187 (1999).

210. J. M. Roger, and V. Bellon-Maurel, "Using Genetic Algorithms to Select Wavelengths in Near-Infrared Spectra: Application to Sugar Content Prediction in Cherries," Applied Spectroscopy **54,** 1313-1320 (2000).

211. C. E. Gributs, and D. H. Burns, "Haar transform analysis of photon time-of-flight measurements for quantification of optical properties in scattering media," Applied Optics **42,** 2923-2930 (2003).

212. R. M. Jarvis, and R. Goodacre, "Genetic algorithm optimization for pre-processing and variable selection of spectroscopic data," Bioinformatics **21,** 860-868 (2005).

213. M. B. Seasholtz, and B. Kowalski, "The parsimony principle applied to multivariate calibration," Analytica Chimica Acta **277,** 165-177 (1993).

214. J. L. Devore, *Probability and statistics for engineering and the sciences* (Duxbury Press Pub, Pacific Grove, Calif., 2004).

215. A. D. Lanterman, "Schwarz, Wallace, and Rissanen: Intertwining Themes in Theories of Model Selection," (2000).

216. S. Sclove, "Application of model-selection criteria to some problems in multivariate analysis," Psychometrika **52,** 333-343 (1987).

217. J. A. Fernandez Pierna, and P. Dardenne, "Chemometric contest at 'Chimiometrie 2005': A discrimination study," Chemometrics and Intelligent Laboratory Systems **86,** 219-223 (2007).

218. I. T. Nabney, *NETLAB: algorithms for pattern recognition* (Springer, London, 2004).

219. M. L. Raymer, T. E. Doom, L. A. Kuhn, and W. F. Punch, "Knowledge discovery in medical and biological datasets using a hybrid Bayes classifier/evolutionary algorithm," IEEE Transactions on Systems, Man and Cybernetics, Part B: Cybernetics **33,** 802-813 (2003).

220. K. L. Mello, and S. D. Brown, "Novel 'hybrid' classification method employing Bayesian networks," Journal of Chemometrics **13,** 579-590 (1999).

221. J. A. Fernandez Pierna, P. Volery, R. Besson, V. Baeten, and P. Dardenne, "Classification of Modified Starches by Fourier Transform Infrared Spectroscopy Using Support Vector Machines," J. Agric. Food Chem. **53,** 6581-6585 (2005).

222. R. Leardi, ed. *Nature-inspired methods in Chemometrics: Genetic Algorithms and Artificial Neural Networks* (Elsevier, Amsterdam, 2003).

223. J.-H. Jiang, and Y. Ozaki, "Self-Modeling Curve Resolution (SMCR): Principles, Techniques, and Applications," Applied Spectroscopy Reviews **37,** 321 - 345 (2002).

224. J.-H. Jiang, Y. Liang, and Y. Ozaki, "Principles and methodologies in self-modeling curve resolution," Chemometrics and Intelligent Laboratory Systems **71,** 1-12 (2004).

225. M. N. Leger, and P. D. Wentzell, "Dynamic Monte Carlo self-modeling curve resolution method for multicomponent mixtures," Chemometrics and Intelligent Laboratory Systems **62,** 171-188 (2002).

226. R. Tauler, "Calculation of maximum and minimum band boundaries of feasible solutions for species profiles obtained by multivariate curve resolution," Journal of Chemometrics **15,** 627-646 (2001).

227. R. Tauler, A. Smilde, and B. Kowalski, "Selectivity, local rank, three-way data analysis and ambiguity in multivariate curve resolution," Journal of Chemometrics **9,** 31-58 (1995).

228. C. Young, J. R. Gould, A. de Juan, Y. V. Heyden, R. Tauler, and D. L. Massart, "Assessment of new constraints applied to the alternating least squares method," Analytica Chimica Acta **346,** 307-318 (1997).

229. A. de Juan, Y. V. Heyden, R. Tauler, and D. L. Massart, "Assessment of new constraints applied to the alternating least squares method," Analytica Chimica Acta **346,** 307-318 (1997).

230. F. F. Jobsis, "Noninvasive, Infrared Monitoring of Cerebral and Myocardial Oxygen Sufficiency and Circulatory Parameters," Science **198,** 1264-1267 (1977).

231. K. A. Schenkman, D. R. Marble, E. O. Feigl, and D. H. Burns, "Near-Infrared Spectroscopic Measurement of Myoglobin Oxygen Saturation in the Presence of Hemoglobin Using Partial Least-Squares Analysis," Applied Spectroscopy **53,** 325-331 (1999).

232. K. A. Schenkman, "Cardiac performance as a function of intracellular oxygen tension in buffer-perfused hearts," Am J Physiol Heart Circ Physiol **281,** H2463-2472 (2001).

233. B. De Groot, C. J. Zuurbier, and J. H. G. M. van Beek, "Dynamics of tissue oxygenation in isolated rabbit heart as measured with near-infrared spectroscopy," Am J Physiol Heart Circ Physiol **276,** H1616-1624 (1999).

234. L. S. L. Arakaki, D. H. Burns, and M. J. Kushmerick, "Accurate Myoglobin Oxygen Saturation by Optical Spectroscopy Measured in Blood-Perfused Rat Muscle," Appl. Spectrosc. **61,** 978-985 (2007).

235. D. J. J. Fraser, and P. R. Griffiths, "Effect of Scattering Coefficient on Diffuse Reflectance Infrared Spectra," Applied Spectroscopy **44,** 193-199 (1990).

236. V. V. Tuchin, *Tissue optics: light scattering methods and instruments for medical diagnosis* (SPIE, Bellingham, Washington, 2000).

237. W. H. Lawton, and E. A. Sylvestre, "Self Modeling Curve Resolution," Technometrics **13,** 617-633 (1971).

238. J. C. Hamilton, and P. J. Gemperline, "Mixture analysis using factor analysis. II: Self-modeling curve resolution," Journal of Chemometrics **4,** 1-13 (1990).

239. R. Tauler, B. Kowalski, and S. Fleming, "Multivariate curve resolution applied to spectral data from multiple runs of an industrial process," Analytical Chemistry **65,** 2040-2047 (1993).

240. M. Esteban, C. Arino, J. M. Daz-Cruz, M. S. Daz-Cruz, and R. Tauler, "Multivariate curve resolution with alternating least squares optimisation: a soft-modelling approach to metal complexation studies by

voltammetric techniques," Trends in Analytical Chemistry **19,** 49-61 (2000).

241. M. H. Van Benthem, M. R. Keenan, and D. M. Haaland, "Application of equality constraints on variables during alternating least squares procedures," Journal of Chemometrics **16,** 613-622 (2002).

242. J. Jaumot, R. Gargallo, and R. Tauler, "Noise propagation and error estimations in multivariate curve resolution alternating least squares using resampling methods," Journal of Chemometrics **18,** 327-340 (2004).

243. J. Jaumot, R. Gargallo, A. de Juan, and R. Tauler, "A graphical user-friendly interface for MCR-ALS: a new tool for multivariate curve resolution in MATLAB," Chemometrics and Intelligent Laboratory Systems **76,** 101-110 (2005).

244. K. A. Schenkman, D. A. Beard, W. A. Ciesielski, and E. O. Feigl, "Comparison of buffer and red blood cell perfusion of guinea pig heart oxygenation," Am J Physiol Heart Circ Physiol **285,** H1819-1825 (2003).

245. I. V. Meglinski, and S. J. Matcher, "Estimation of the optical sampling volume for skin reflectance measurements," in *Photon Migration, Diffuse Spectroscopy, and Optical Coherence Tomography: Imaging and Functional Assessment*, (SPIE, Amsterdam, Netherlands, 2000), pp. 233-241.

246. W. F. Long, and D. H. Burns, "Optical tomographic reconstruction from diffuse remittance in scattering media using partial least squares estimation," Analytica Chimica Acta **348,** 553-563 (1997).

247. M. V. M. V. Schulmerich, W. F. W. F. Finney, R. A. R. A. Fredricks, and M. D. M. D. Morris, "Subsurface Raman spectroscopy and mapping using a globally illuminated non-confocal fiber-optic array probe in the presence of Raman photon migration," Applied Spectroscopy **60,** 109-114 (2006).

248. M. V. Schulmerich, W. F. Finney, V. Popescu, M. D. Morris, T. M. Vanasse, and S. A. Goldstein, "Transcutaneous Raman spectroscopy of

bone tissue using a non-confocal fiber optic array probe," in *Photonics West*, M.-J. Anita, and H. P. Wolfgang, eds. (SPIE, San Jose, California, 2006), p. 60930O.

249. L. Leonardi, and D. H. Burns, "Quantitative Measurements in Scattering Media: Photon Time-of-Flight Analysis with Analytical Descriptors," Applied Spectroscopy **53,** 628-636 (1999).

250. E. Kreyszig, *Advanced Engineering Mathematics* (John Wiley & Sons, Inc., New York, 1999).

251. B. W. Pogue, and M. S. Patterson, "Review of tissue simulating phantoms for optical spectroscopy, imaging and dosimetry," Journal of Biomedical Optics **11,** 041102-041116 (2006).

252. R. J. P. Shulman, Sarah, "Parenteral Nutrition in Infants and Children," Journal of Pediatric Gastroenterology and Nutrition **36,** 587-607 (2003).

253. J.-C. Desport, B. Hoedt, V. Pelagatti, A. Lagarde, F. Lorieul, D. Chalmel, F. Sultan, and P. Feiss, "Twenty-nine day study of stability for six different parenteral nutrition mixtures," Critical Care **1,** 41 (1997).

254. H. T. Osborn, and C. C. Akoh, "Effect of emulsifier type, droplet size, and oil concentration on lipid oxidation in structured lipid-based oil-in-water emulsions," Food Chemistry **84,** 451-456 (2004).

255. D. G. Dalgleish, S. J. West, and F. R. Hallett, "The characterization of small emulsion droplets made from milk proteins and triglyceride oil," Colloids and Surfaces A: Physicochemical and Engineering Aspects **123-124,** 145-153 (1997).

256. D. F. Driscoll, F. Etzler, T. A. Barber, J. Nehne, W. Niemann, and B. R. Bistrian, "Physicochemical assessments of parenteral lipid emulsions: light obscuration versus laser diffraction," International Journal of Pharmaceutics **219,** 21-37 (2001).

257. I. Driver, J. W. Feather, P. R. King, and J. B. Dawson, "The optical properties of aqueous suspensions of Intralipid, a fat emulsion," Physics in Medicine and Biology **34,** 1927-1930 (1989).

258. S. L. Jaques, "Optical properties of Intralipid, an aqueous suspension of lipid droplets.," Internet**,** (1998).

259. M. Autiero, R. Liuzzi, P. Riccio, and G. Roberti, "Determination of the concentration scaling law of the scattering coefficient of water solutions of Intralipid at 832 nm by comparison between collimated detection measurements and Monte Carlo simulations," Lasers in Surgery and Medicine **36,** 414-422 (2005).

260. T. Moffitt, Y.-C. Chen, and S. A. Prahl, "Preparation and characterization of polyurethane optical phantoms," Journal of Biomedical Optics **11,** 041103-041110 (2006).

261. U. Sukowski, F. Schubert, D. Grosenick, and H. Rinneberg, "Preparation of solid phantoms with defined scattering and absorption properties for optical tomography," Physics in Medicine and Biology **41,** 1823–1844 (1996).

262. E. L. Hull, M. G. Nichols, and T. H. Foster, "Quantitative broadband near-infrared spectroscopy of tissue-simulating phantoms containing erythrocytes," Physics in Medicine and Biology **43,** 3381-3404 (1998).

263. M. Bartlett, and H. Jiang, "Measurement of particle size distribution in multilayered skin phantoms using polarized light spectroscopy," Physical Review E **65,** 031906 (2002).

264. S. R. Arridge, and M. Schweiger, "Photon-measurement density functions. Part 2: Finite-element-method calculations," Applied Optics **34,** 8026-8037 (1995).

265. S. Srinivasan, B. W. Pogue, H. Dehghani, S. Jiang, X. Song, and K. D. Paulsen, "Improved quantification of small objects in near-infrared diffuse optical tomography," Journal of Biomedical Optics **9,** 1161-1171 (2004).

266. A. Douiri, M. Schweiger, J. Riley, and S. R. Arridge, "Adaptive diffusion regularization method of inverse problem for diffuse optical tomography," in *Photon Migration and Diffuse-Light Imaging II*, (SPIE, Munich, Germany, 2005), pp. 585916-585911.

267. S. A. Prahl, M. Keijzer, S. L. Jacques, and A. J. Welch, "A Monte Carlo Model of Light Propagation in Tissue," Dosimetry of Laser Radiation in Medicine and Biology (SPIE Institute Series Vol. IS 5) **5,** 102-111 (1989).

268. D. Boas, J. Culver, J. Stott, and A. Dunn, "Three dimensional Monte Carlo code for photon migration through complex heterogeneous media including the adult human head," Optics Express **10,** 159-170 (2002).

269. A. Sassaroli, C. Blumetti, F. Martelli, L. Alianelli, D. Contini, A. Ismaelli, and G. Zaccanti, "Monte Carlo procedure for investigating light propagation and imaging of highly scattering media," Applied Optics **37,** 7392-7400 (1998).

270. E. Berrocal, D. L. Sedarsky, M. E. Paciaroni, I. V. Meglinski, and M. A. Linne, "Laser light scattering in turbid media Part I: Experimental and simulated results for the spatial intensity distribution," Optics Express **15,** 10649-10665 (2007).

271. A. Pifferi, P. Taroni, G. Valentini, and S. Andersson-Engels, "Real-Time Method for Fitting Time-Resolved Reflectance and Transmittance Measurements with a Monte Carlo Model," Applied Optics **37,** 2774-2780 (1998).